INTERNATIONAL DOCTORAL
SCHOOL OF THE USC

Iván
Martínez Suárez

PhD Thesis

Lagrangian formulation and numerical simulation of multiphysics models. Application to electric upsetting

Santiago de Compostela, 2025

Doctoral Programme in Mathematical Modelling and Numerical Simulation in Engineering and Applied Sciences

INTERNATIONAL DOCTORAL SCHOOL OF THE USC

DOCTORAL THESIS

LAGRANGIAN FORMULATION AND NUMERICAL SIMULATION OF MULTIPHYSICS MODELS. APPLICATION TO ELECTRIC UPSETTING

Author

Iván Martínez Suárez

Supervisors: Alfredo Bermúdez de Castro López-Varela, María del Pilar Salgado Rodríguez

Tutor: María del Pilar Salgado Rodríguez

DOCTORAL PROGRAMME IN MATHEMATICAL MODELLING AND NUMERICAL SIMULATION IN ENGINEERING AND APPLIED SCIENCES

SANTIAGO DE COMPOSTELA

2025

Declaration of competing interest

The doctoral candidate, **Iván Martínez Suárez**,

declares no conflicts of interest related to his thesis

Lagrangian formulation and numerical simulation of multiphysics models. Application to electric upsetting.

Santiago de Compostela, 30 October 2025

Agradecementos

En primeiro lugar, quérolles dar as grazas a Alfredo Bermúdez de Castro e a Pilar Salgado pola oportunidade de facer esta tese e por toda a dedicación que puxeron en dirixila.

Tamén me gustaría agradecerlles a Marta Benítez e a Pedro Fontán as innumerables reunións e o seu admirable xeito de facer as cousas.

Moitas grazas á miña familia, amizades, compañeiras e compañeiros polo apoio e polos momentos compartidos.

Grazas tamén á empresa CIE Galfor por facilitarnos a comprensión do proceso industrial con visitas á súa fábrica, pola provisión de datos experimentais e polo diálogo permanente.

Finalmente, reservo a miña maior gratitude para quen estea lendo isto e sinta que merecía unha mención explícita nos agradecementos.

Contents

List of Publications vii

List of Figures viii

List of Tables xii

Abstract xiii

Preface xiv

1 Introduction 1
- 1.1 Forming processes . . . 1
  - 1.1.1 Conventional forming processes . . . 2
  - 1.1.2 Energy-assisted forming processes . . . 5
- 1.2 Electric upsetting . . . 7
- 1.3 Motivation . . . 7
- 1.4 Objectives . . . 11
- 1.5 Methodology . . . 11
- 1.6 Thesis outline . . . 13

2 Preliminary tools 14
- 2.1 Elements of Continuum Mechanics . . . 14
- 2.2 Cylindrical symmetry: notation and operators . . . 17

3 Thermo-electrical-mechanical modelling of DC electric upsetting 21
- 3.1 Mechanical model . . . 22
  - 3.1.1 Finite elasticity . . . 23
  - 3.1.2 Elasto-viscoplasticity . . . 25
  - 3.1.3 Boundary conditions . . . 30
  - 3.1.4 Statement of the elasto-viscoplasticity problem . . . 32
- 3.2 Electrical model . . . 35
  - 3.2.1 Direct current model . . . 35
  - 3.2.2 Lagrangian formulation . . . 38
- 3.3 Thermal model . . . 40

3.3.1 Transient heat transfer model . . . 40
3.3.2 Lagrangian formulation . . . 41
3.4 Axisymmetric thermo-electrical-mechanical model . . . 42
3.5 Lagrangian approach in a new reference configuration . . . 44

4 Thermo-electromagnetic-mechanical modelling of AC electric upsetting 48
4.1 Electromagnetic model . . . 49
4.1.1 Eddy current model . . . 49
4.1.2 Lagrangian formulation . . . 53
4.1.3 Eddy current model with power as data . . . 54
4.2 Thermal model . . . 55
4.3 Axisymmetric thermo-electromagnetic-mechanical model . . . 56

5 Numerical methods and results 59
5.1 Time discretisation . . . 60
5.2 Results and discussion . . . 61
5.2.1 Validation tests . . . 61
5.2.1.1 Test 1. Electromagnetic model with analytical solution . . . 62
5.2.1.2 Test 2. Elastic mechanical model with analytical solution . . . 63
5.2.1.3 Test 3. Elastic mechanical model under complex contact constraints . . . 65
5.2.1.4 Test 4. Elasto-viscoplastic mechanical model with prescribed temperature . . . 67
5.2.1.5 Test 5. Thermo-electrical model with known displacement . . . 75
5.2.1.6 Test 6. Thermo-electromagnetic model with known displacement 78
5.2.1.7 Test 7. Fully coupled thermo-electrical-mechanical model . . . 85
5.2.2 Electric upsetting . . . 89
5.2.2.1 In-die electric upsetting . . . 89
5.2.2.2 Free electric upsetting . . . 91

6 Conclusions and further work 101

A Function spaces 103

Nomenclature 105

Bibliography 109

Copyright and permissions 116

Resumo 117

List of Publications

From this PhD thesis, contributions have been made in the form of scientific research papers published in JCR-ranked journals. The following two articles have been partially reproduced in this thesis report:

- M. Benítez*†, A. Bermúdez*‡, P. Fontán§, I. Martínez*‡, P. Salgado*‡ (2024). *A Lagrangian approach for solving an axisymmetric thermo-electromagnetic problem. Application to time-varying geometry processes.* Advances in Computational Mathematics, 50, 45. Electronic ISSN: 1572-9044, Print ISSN: 1019-7168. DOI: 10.1007/s10444-024-10121-y

  Journal rankings: Impact Factor (JCR): 2.1 (2024), Quartile (JCR): Q1 (57/343) (Mathematics, Applied).

  Author's contribution: development of the mathematical model, implementation of the numerical simulations and writing of the article.

  This publication is partially reproduced in Chapter 4 and Chapter 5.

- M. Benítez*†, A. Bermúdez*‡, P. Fontán§, I. Martínez*‡, P. Salgado*‡ (2025). *A pure-Lagrangian finite element approach for solving thermo-electrical-mechanical models. Application to electric upsetting.* Finite Elements in Analysis and Design, 251, 104433. Electronic ISSN: 1872-6925, Print ISSN: 0168-874X. DOI: 10.1016/j.finel.2025.104433

  Journal rankings (last available data): Impact Factor (JCR): 3.5 (2024), Quartile (JCR): Q1 (10/343) (Mathematics, Applied).

  Author's contribution: development of the mathematical model, implementation of the numerical simulations and writing of the article.

  This publication is partially reproduced in Chapter 3 and Chapter 5.

*Centro de Investigación e Tecnoloxía Matemática de Galicia (CITMAga), Campus Vida, Santiago de Compostela E-15782, Spain
†Departamento de Matemáticas, Universidade da Coruña, Elviña s/n, A Coruña E-15071, Spain
‡Departamento de Matemática Aplicada, Universidade de Santiago de Compostela, Campus Vida, Santiago de Compostela E-15782, Spain
§REPSOL Technology Lab, Autovía de Extremadura s/n, Móstoles, Madrid E-28935, Spain

List of Figures

1.1 Rolling. . . . 2
1.2 Forging processes. . . . 3
1.3 Extrusion and drawing processes. . . . 3
1.4 Ironing. . . . 4
1.5 Bending. . . . 4
1.6 Spinning. . . . 5
1.7 Stretching and deep drawing processes. . . . 5
1.8 Electromagnetic metal forming. . . . 6
1.9 Electric upsetting processes. . . . 8
1.10 Schemes of electric upsetting processes. . . . 9
1.11 Final shape and position of an axle shaft. . . . 10
1.12 Coupling schematic. . . . 10

2.1 Motion and material description of spatial fields. . . . 15
2.2 Example of a 3D cylindrical domain and its corresponding meridional section for an electric upsetting process. . . . 18

3.1 Typical stress-strain curves for elasto-viscoplastic materials, where rate-dependent effects become clear. In contrast, a purely elastic response would follow the dashed line. . . . 26
3.2 Multiplicative decomposition of the deformation gradient. . . . 27
3.3 Boundaries of the mechanical domain. . . . 30
3.4 Boundaries of the electrical domain. . . . 37
3.5 Boundaries of the thermal domain. . . . 40
3.6 Configurations and motions referred to Ω, $\Omega(\tau)$ and $\Omega(t)$. . . . 45

4.1 Boundaries of the electromagnetic domain. In general, either current or voltage is imposed on $\Gamma^1_{\mathbf{J}}(t)$. . . . 52

5.1 Domain for validation tests. . . . 62
5.2 Test 1: comparison of analytical and numerical solutions for $\mathrm{Re}(\tilde{\mathcal{H}}_\theta)$ (left) and $\mathrm{Im}(\tilde{\mathcal{H}}_\theta)$ (right). . . . 63

5.3 Test 1: computed $H_h^{1,-1}$ error for $\tilde{\mathcal{H}}_\theta$ (left) and complex error for V_3 (right), versus h^{-1}, in log-log scale. 64
5.4 Test 2: comparison of analytical and numerical solutions for $\widehat{u}_r^{max}$ (left) and $\widehat{\zeta}_m$ (right). 65
5.5 Test 2: maximum radial displacement (blue dots) and minimum determinant of the deformation gradient (red dots) at each time instant, with respect to the current reference configuration, starting at time τ_i and limited by the different background colours. The cumulative $\widehat{u}_r^{max}$ and $\det(\mathbf{F})^{min}$ are also shown in blue and red solid lines, respectively. 66
5.6 Test 3: displacement magnitude in proprietary pure-Lagrangian code (left) and Marc code (right) at $t = 8.6$ s, with both obstacles sketched in black lines. 67
5.7 Test 3: displacement magnitude in proprietary pure-Lagrangian code (left) and Marc code (right) at $t = 20$ s, with both obstacles sketched in black lines. 67
5.8 Young's modulus (left) and Poisson's ratio (right) vs. temperature. 68
5.9 Test 4: modulus of the resultant force applied on $\widehat{\Gamma}_3$. 69
5.10 Test 4: computed $l^\infty(L_h^2)$ (left) and $l^\infty(H_h^1)$ (right) errors in displacement, plastic deformation gradient, and deformation resistance are plotted against the number of time steps on a log-log scale, using a fixed spatial mesh of size $h = 0.0025$. . . 70
5.11 Test 4: computed $l^\infty(L_h^2)$ (left) and $l^\infty(H_h^1)$ (right) errors for displacement, plastic deformation gradient, and deformation resistance, plotted against $1/h$ on a log-log scale, for a fixed number of time steps $N = 100$. 71
5.12 Test 4: deformation resistance, s (top), and norm of the plastic deformation gradient, $|\mathbf{F}^p|$ (bottom), in the final deformed configuration. Note that the reference configuration is also outlined. 72
5.13 Test 4: maximum values attained for $\widehat{u}_r$ (left) and $\widehat{\epsilon^p}$ (right) obtained using the proprietary pure-Lagrangian code, Ansys, and Marc, for varying number of time steps. 73
5.14 Test 4: maximum stabilised values attained for $\widehat{u}_r$ (left) and $\widehat{\epsilon^p}$ (right) in our pure-Lagrangian code, Ansys, and Marc over the simulation time. 74
5.15 Material properties. 76
5.16 Test 5: computed $l^\infty(L_h^2)$ (left) and $l^\infty(H_h^1)$ (right) errors for temperature (top) and voltage (bottom), versus the number of time steps, in log-log scale, for a fixed spatial mesh of size $h = 0.00125$. 77
5.17 Test 5: computed $l^\infty(L_h^2)$ (left) and $l^\infty(H_h^1)$ (right) errors for temperature (top) and voltage (bottom), versus $1/h$, in log-log scale, for $N = 20$. 78
5.18 Test 6: $|\tilde{H}_\theta|$ at $t = 2$ s. Eulerian formulation (top) versus Lagrangian formulation (bottom). 80
5.19 Test 6: $|\tilde{H}_\theta|$ at $t = 20$ s. Eulerian formulation (top) versus Lagrangian formulation (bottom). 80
5.20 Test 6: $|\mathbf{J}|$ at $t = 2$ s. Eulerian formulation (top) versus Lagrangian formulation (bottom). 81

5.21 Test 6: $|\mathbf{J}|$ at $t = 20$ s. Eulerian formulation (top) versus Lagrangian formulation (bottom). 81
5.22 Test 6: comparison of the potential drop between the electrical ports vs. time. . 82
5.23 Test 6: Θ at $t = 2$ s. Eulerian formulation (top) versus Lagrangian formulation (bottom). 82
5.24 Test 6: Θ at $t = 20$ s. Eulerian formulation (top) versus Lagrangian formulation (bottom). 83
5.25 Test 6: computed $l^\infty(L^2_h)$ (left) and $l^\infty(H^1_h)$ (right) errors for temperature (top) and $\tilde{H}_\theta$ (bottom), versus the number of time steps, in log-log scale, for a fixed spatial mesh of size $h = 0.00125$. 84
5.26 Test 6: computed $l^\infty(L^2_h)$ (left) and $l^\infty(H^1_h)$ (right) errors for temperature (top) and $\tilde{H}_\theta$ (bottom), versus $1/h$, in log-log scale, for $N = 20$. 85
5.27 Test 7: normal displacement prescribed on $\widehat{\Gamma}_3$. 86
5.28 Test 7: temperature and deformed domain (the reference domain is outlined in grey) at $t = 85\,\mathrm{s}$, computed using the proposed pure-Lagrangian method (top), Ansys (middle), and Marc (bottom). 87
5.29 Test 7: temperature and deformed domain (the reference domain is outlined in grey) at $t = 95\,\mathrm{s}$, computed using the proposed pure-Lagrangian method (top), Ansys (middle) and Marc (bottom). 87
5.30 Test 7: temperature and deformed domain (the reference domain is outlined in grey) at $t = 100\,\mathrm{s}$, computed using the proposed pure-Lagrangian method (top), Ansys (middle) and Marc (bottom). 88
5.31 Test 7: time evolution of the modulus of the current density, the temperature, and the accumulated inelastic strain at $(r_m, z_m) = (0\,\mathrm{m}, 0.125\,\mathrm{m})$, and maximum radial displacement. 88
5.32 Test 7: Frobenius norm of the plastic deformation gradient and deformed mesh at $t = 100\,\mathrm{s}$, computed with the proposed pure-Lagrangian method. The reference domain is outlined in grey. Significant mesh distortion is observed in the most deformed region (zoomed view on the right), whereas the initial mesh is nearly uniform, with an element size comparable to that of the blue region. 89
5.33 In-die electric upsetting: initial geometry and boundary conditions. 90
5.34 In-die electric upsetting: modulus of the resultant force applied on $\widehat{\Gamma}_5$ (left) and electric potential prescribed on $\widehat{\Gamma}_3$ (right). 90
5.35 In-die electric upsetting: modulus of the current density and deformed domain (the reference domain is outlined in grey) at $t = 46\,\mathrm{s}$, $t = 48\,\mathrm{s}$, $t = 54\,\mathrm{s}$, $t = 63\,\mathrm{s}$. 92
5.36 In-die electric upsetting: temperature and deformed domain (the reference domain is outlined in grey) at $t = 46\,\mathrm{s}$, computed using the proposed pure-Lagrangian method (top), Ansys (middle) and Marc (bottom). 93
5.37 In-die electric upsetting: temperature and deformed domain (the reference domain is outlined in grey) at $t = 48\,\mathrm{s}$, computed using the proposed pure-Lagrangian method (top), Ansys (middle) and Marc (bottom). 93

5.38 In-die electric upsetting: temperature and deformed domain (the reference domain is outlined in grey) at $t = 54\,\mathrm{s}$, computed using the proposed pure-Lagrangian method (top), Ansys (middle) and Marc (bottom). 94
5.39 In-die electric upsetting: temperature and deformed domain (the reference domain is outlined in grey) at $t = 63\,\mathrm{s}$, computed using the proposed pure-Lagrangian method (top), Ansys (middle) and Marc (bottom). 94
5.40 Free electric upsetting: initial geometry and boundaries. 95
5.41 Free electric upsetting: modulus of the resultant force applied on $\widehat{\Gamma}_5$ (left) and active power supplied through $\widehat{\Gamma}_3$ (right). 95
5.42 Free electric upsetting: $\tilde{\mathcal{H}}_\theta$ and deformed domain (the reference domain is outlined in gray) at $t = 1$ s for $f \approx 0$ Hz (top), $f = 50$ Hz (middle) and $f = 100$ Hz (bottom). 96
5.43 Free electric upsetting: temperature and deformed domain (the reference domain is outlined in gray) at $t = 30$ s for $f \approx 0$ Hz (top), $f = 50$ Hz (middle) and $f = 100$ Hz (bottom). 97
5.44 Free electric upsetting: temperature and deformed domain (the reference domain is outlined in gray) at $t = 62$ s for $f \approx 0$ Hz (top), $f = 50$ Hz (middle) and $f = 100$ Hz (bottom). 97
5.45 Free electric upsetting: temperature and deformed domain (the reference domain is outlined in gray) at $t = 66$ s for $f \approx 0$ Hz (top), $f = 50$ Hz (middle) and $f = 100$ Hz (bottom). 98
5.46 Free electric upsetting: $|\mathbf{F}^p|$ and deformed domain (the reference domain is outlined in gray) at $t = 66$ s for $f \approx 0$ Hz (top), $f = 50$ Hz (middle) and $f = 100$ Hz (bottom). 99
5.47 Free electric upsetting: $\tilde{\mathcal{H}}_\theta$ and deformed domain (the reference domain is outlined in gray) at $t = 66$ s for $f \approx 0$ Hz (top), $f = 50$ Hz (middle) and $f = 100$ Hz (bottom). 99
5.48 Free electric upsetting: time evolution of $|I|$ for different frequencies. 100
5.49 Free electric upsetting: time evolution of $|V|$ for different frequencies. 100

A.1 Esquemas dos procesos de electro-recalcado. 119
A.2 Esquemas do acoplamento entre modelos. 120

List of Tables

2.1 Notation for the Eulerian and Lagrangian descriptions. Gradient and divergence operators are denoted in bold when applied to vector and tensor fields, respectively. 17

5.1 Parameters used in the Anand model. 68
5.2 Number of time steps, total computational time, and average duration per time step required by the proprietary pure-Lagrangian code, Ansys, and Marc to achieve a stable solution. 74
5.3 Test 7: errors computed from the curves in Figure 5.31. 89

Abstract

Forming processes are fundamental in modern industry, as they enable the permanent deformation of a workpiece into a desired geometry while preserving cohesion and mass. Compared with casting or machining, forming offers advantages such as low material waste, short production times, precise final shapes, and improved mechanical properties. Nevertheless, it also demands high forces, costly equipment, and faces limitations with complex geometries.

Conventional bulk and sheet forming techniques, which primarily rely on mechanical contact, are widely used but remain challenged by high cost, energy consumption, and environmental impact. To address demands for lighter components, higher precision, and greater sustainability, energy-assisted forming methods have been developed. These include electromagnetic forming, which employs Lorentz forces; ultrasonic-assisted forming, which reduces friction and resistance through vibrations; and electrically assisted forming, which lowers deformation resistance by Joule heating.

This thesis focuses on a particular electrically assisted method known as electric upsetting, whereby the diameter at the end of a metal bar is locally enlarged. The process may occur freely –producing an onion-shaped preform– or within a closed die, and it is of significant relevance in the automotive and aerospace sectors. Electric upsetting involves strongly coupled multiphysics phenomena –thermal, electrical, electromagnetic, and mechanical– governed by factors such as current source, bar geometry, and applied force.

Numerical simulation becomes essential in this context, although most previous studies have been limited to direct current and simplified models, with little attention given to alternating current or closed-die conditions. The main objective of this thesis is the development of suitable mathematical models for electric upsetting under both direct and alternating current excitations, capturing the coupled thermal, electrical/electromagnetic, and mechanical effects. The approach incorporates large deformation theory, viscoplastic constitutive laws, and detailed contact modelling within a fully Lagrangian framework.

The mathematical models, implemented in an own-developed Python/FEniCS finite element code and validated against commercial solvers, provide a robust computational framework for the simulation and optimisation of electric upsetting, highlighting its industrial relevance and potential advantages over conventional forming processes.

Preface

This thesis originates from a collaboration between the Research Group in Mathematical Engineering (mat+i) and the company CIE Galfor, developed over the last decade through several research projects and contracts established between this company and ITMATI (nowadays integrated in CITMAga).

CIE Galfor is a company belonging to the multinational group CIE Automotive. Its industrial plant, located in San Cibrao das Viñas (Ourense), specialises in the manufacturing of forged steel components for the automotive industry. The main products include crankshafts, front axles, axle shafts, drive shafts, suspension arms, knuckles, and stub axles. The company uses a variety of forging techniques in its production processes, with a particular focus on stamping, electric upsetting, and extrusion.

The research developed in this thesis was specifically motivated by two projects funded by the CDTI (Centre for the Development of Technology and Innovation) and formalised through agreements between CIE Galfor and ITMATI. Both projects, identified as *ELECPAL* (2017-2018) and *ELECPAL II* (2020-2023), were entitled *Investigación en procesos de electro-recalcado libre para la optimización de la forja en caliente de palieres de automoción.* These projects were focused on the analysis and optimisation of electric upsetting processes for the manufacturing of automotive components and marked the starting point for the work presented here.

Chapter 1

Introduction

The history of metal forming goes back several millennia and has evolved with human civilisation to become indispensable in today's society. The main types of forming processes and their characteristics are described below, with particular emphasis on electric upsetting, which is the central focus of this thesis. In fact, the electric upsetting process used in the manufacture of automotive parts was the problem that motivated the modelling tools and numerical methods developed in the thesis.

1.1 Forming processes

The objective of a metal forming process is the deformation of a workpiece to a desired geometric shape through plastic strains, i.e., the final preform is retained once the applied stresses are removed. The mass and cohesion of the workpiece remain unchanged after this process.

Metal forming has many advantages when compared to other manufacturing processes such as casting or machining, including: material efficiency (little loss of raw materials), short production times, accurate final shapes or overall improved mechanical properties. On the other hand, several disadvantages are associated to forming processes: requirement for significant loads, high equipment cost or production of intricate geometries due to limited formability of metals.

Despite forming processes are usually complex and many types of stresses are involved there, it is common to classify them according to the effective stress state in the deformation zone [48]. Therefore, forming processes can be dominated by compressive, tensile, combined tensile and compressive, bending or shearing stresses. From a more practical point of view, forming processes can be carried out to deform massive pieces such as rods, slabs or billets (the so-called *bulk forming*) or metal sheets which have a particularly thin dimension (*sheet forming*). In addition, different variants of forming processes are considered depending on the temperature of the metal piece. More precisely, a distinction is made between *cold forming*, which occurs at room temperature; *warm forming*, taking place between room and recrystallisation temperatures; and *hot forming*, when the process is performed above recrystallisation temperature.

As stated in [41], there are more than 250 different metal forming processes in industry and new ones are being developed every year. In what follows, some of the most common metal

forming processes are introduced.

1.1.1 Conventional forming processes

In the classical sense, conventional forming techniques involve a combination of thermal and mechanical phenomena to deform workpieces into a desired shape. Some examples of these techniques are presented in this section.

Regarding bulk forming, a first example is the process of *rolling* (see Figure 1.1), used to reduce the thickness of a metal part by passing it through a pair of rollers rotating in opposite directions, usually maintaining the width of the piece at the end. Metal sheets, strips and plates are obtained from this process.

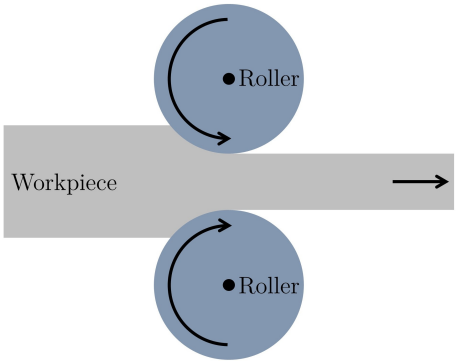

Figure 1.1: Rolling.

The use of power hammers, presses and dies to shape metals through the application of localised compressive forces is called *forging*. Beyond the variants attending to the metal temperature, this process is mainly classified as *open-die forging* (also *upsetting*, see Figure 1.2a), if the compression takes place between two usually flat dies, or as *impression die forging* (see Figure 1.2b), when the metal is adapted to a more complex die shape. Among the many applications of forging are the manufacturing of components for aerospace, automotive or power generation industries.

Another conventional forming process is *extrusion*, which takes place when the cross-section of a metal block is reduced by forcing it through a die opening (see Figure 1.3a). It is widely used for providing products to different sectors, as window frames, railings, hollow pipes or busbars. *Drawing* (see Figure 1.3b) is very similar to extrusion with the difference that the solid metal is pulled through the die instead of pushed. This is the most common method to produce wires of different sizes.

The process of *ironing* (see Figure 1.4) is useful for reducing the wall thickness of a workpiece and to create sheet-like products. It is used in production of lightweight components, such as casings or cans.

In addition to the bulk forming processes mentioned above, there are many different techniques to conduct metal sheet forming. Note that the main purpose of sheet forming is the deformation of relatively thin flat workpieces but a change of thickness is generally not intended.

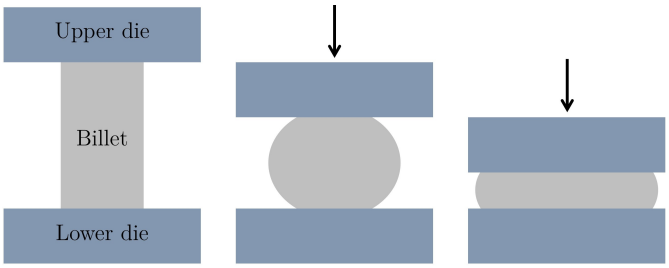

(a) Open-die forging.

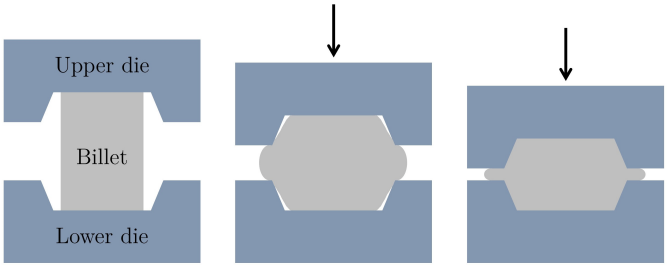

(b) Impression die forging.

Figure 1.2: Forging processes.

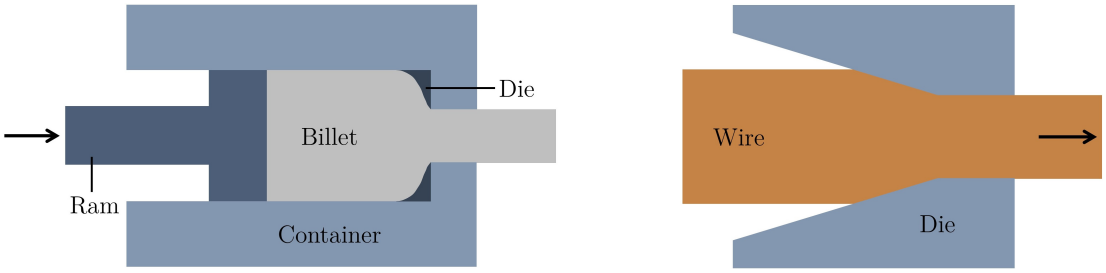

(a) Extrusion. (b) Drawing.

Figure 1.3: Extrusion and drawing processes.

A typical metal sheet forming process is *bending* (see Figure 1.5), involving the deformation of a ductile workpiece to a curved shape. In die bending, the metal sheet is usually placed over a die, which has the final desired curved geometry, and the piece is deformed by a downward force applied with a punch. If there is no contact between the deformed surface and a die the process is called free bending. Moreover, rotary tools can also be used for sheet bending. Many variants of this process are widely used in industry, where curved components are often required.

In the *spinning* forming process (see Figure 1.6) deformed axially symmetric pieces are obtained, based on the application of localised forces to a workpiece rotating at high velocity on a lathe and being deformed against a mandrel by a roller, which also moves. It is used for axisymmetric components, including gas tanks, nose cones or cooking utensils.

Two similar metal sheet forming processes are *stretching* and *deep drawing*. As sketched in Figure 1.7a, on the first process shaped dies are used to deform a workpiece clamped at its

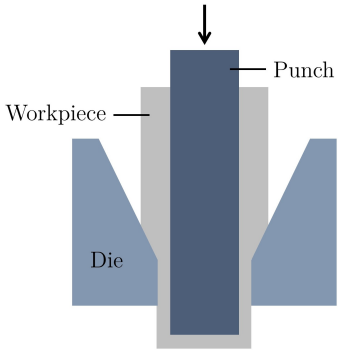

Figure 1.4: Ironing.

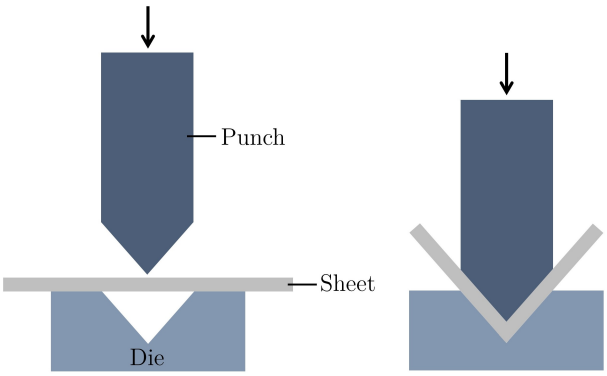

Figure 1.5: Bending.

ends. This results in a stretching force on the clamps and a thickness reduction on the piece. In deep drawing (see Figure 1.7b) the clamps also exist, but a controlled material flow into the die is allowed as the punch force is applied, and therefore the initial thickness can be retained. In the same line as deep drawing, a more recent and advanced process called *incremental sheet forming* can avoid the need of dies. The incremental action of a controllable punch that applies localised stresses is able to transform a flat sheet into its desired shape. The flexibility of this process makes it particularly suitable for producing parts with complex shapes, but it is slower than deep drawing or stretching.

The processes mentioned so far are capable of deforming a workpiece to a desired shape by means of solid contact with tools such as dies, presses or punches. Nevertheless, sheet metal forming can also be achieved by using pressure gradients produced on certain material media. An example of the former is *hydroforming* [9], where a high-pressurised hydraulic fluid is used to press the workpiece into a die with the desired shape, which can be quite complex. As a general idea, one of the variants of hydroforming can be seen as a deep drawing process where the punch is replaced by a high-pressurised fluid which is injected into the cavity and can deform the metal sheet against the die. Moreover, instead of an injection of high-pressurised fluid, the energy from controlled detonations of adequate explosive charges can be transmitted through shock waves (usually in water) to deform the workpiece against a die with the desired shape. This

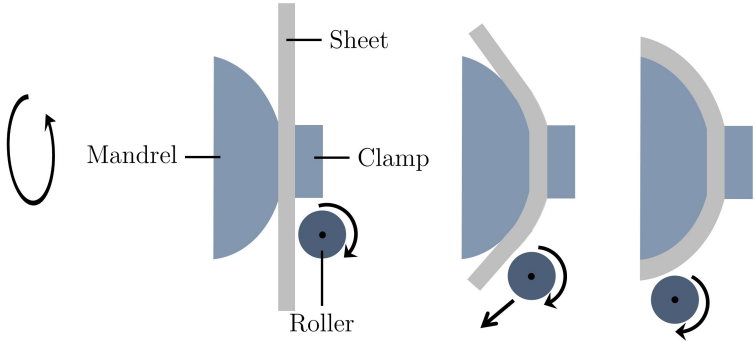

Figure 1.6: Spinning.

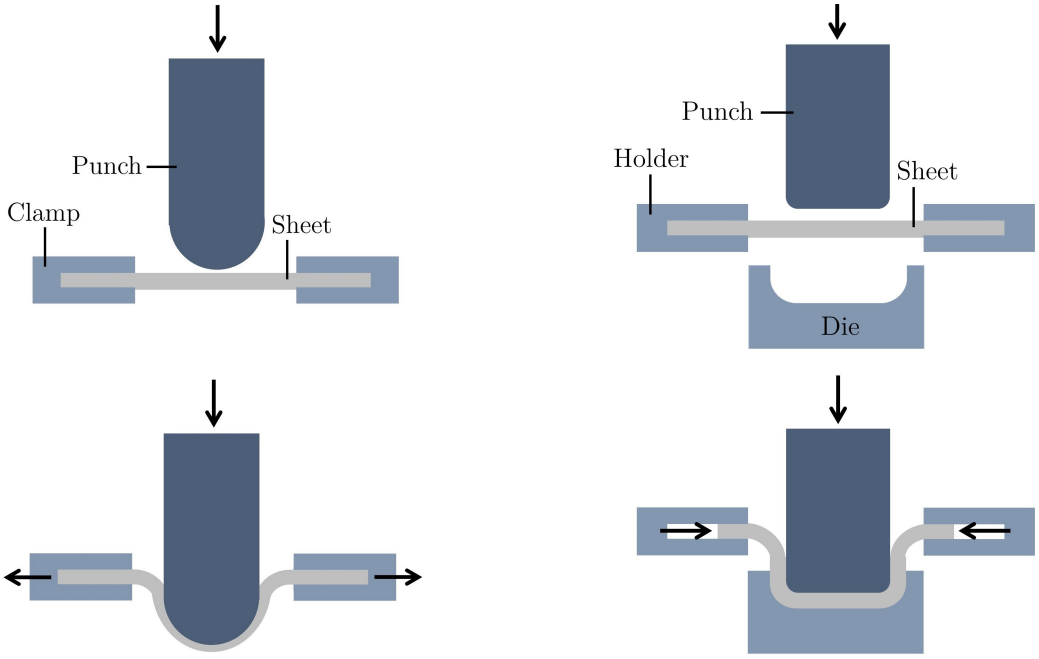

(a) Stretching. (b) Deep drawing.

Figure 1.7: Stretching and deep drawing processes.

process is the so-called *explosive forming*, which has been used for large and complex pieces in the aerospace industry during the Space Age or in exclusive architectural designs where conventional techniques are not adequate. A detailed description of explosive forming and its applications can be found in [58].

1.1.2 Energy-assisted forming processes

As can be seen from the above examples, the number and typology of forming processes encountered in industrial applications is enormous. Although conventional forming techniques are still widely used, they have inherent drawbacks such as high costs, limited forming capabilities or significant carbon emissions, and the optimisation of existing methods is not sufficient to meet

some of the new requirements in today's world. New demands from the manufacturing industries must be progressively addressed, including high performance, lightweight pieces, more precise designs and environmental sustainability. In this context, *energy-assisted forming processes* are emerging, which consist in the integration of new energy sources in the forming environment, with proven successful results to enhance formability and material properties, reduce forming resistance, prevent forming defects or improve the surface quality of final products.

According to [51], energy-assisted forming techniques are classified depending on the energy source used in the process. Among these, we can highlight *Electromagnetic Metal Forming* (EMF) processes, where an electrically conductive workpiece is deformed in response to the Lorentz force caused by the electromagnetic field generated by a transient electrical current passing through a nearby coil. More precisely, the workpiece is placed close to a coil carrying a high-intensity current pulse, as a result of the discharge of a high-voltage capacitor bank. This transient current creates a rapidly oscillating magnetic field around it and, due to electromagnetic induction, a new current arises in the metallic piece. This induced current also creates an electromagnetic field around the workpiece which, according to Lenz's law, is opposite to the original magnetic field. As a consequence of this interaction, Lorentz forces are created and the workpiece is deformed at high velocity against a desired shape, typically with a duration of tens of microseconds. This contactless deformation process is widely used in industry for forming of lightweight materials, as aluminium or magnesium, specially in cylindrical tubes or flat sheets. A sketch of electromagnetic metal forming is depicted in Figure 1.8. A detailed overview of EMF technology and its applications can be found in [33].

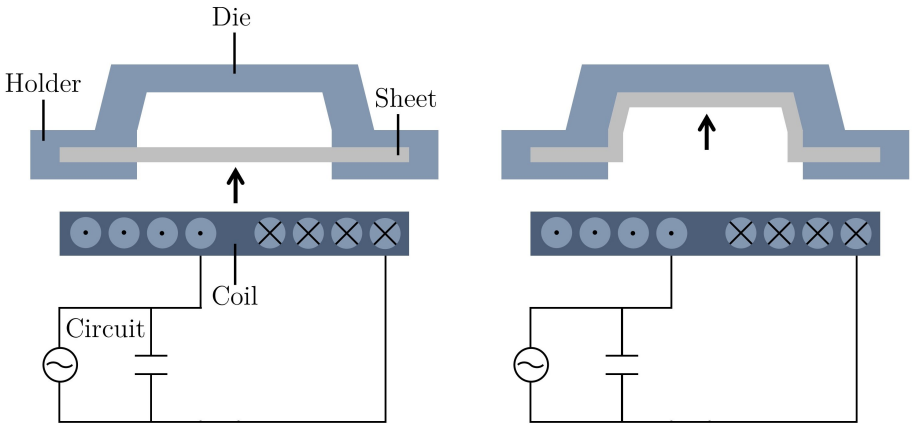

Figure 1.8: Electromagnetic metal forming.

On the other hand, ultrasounds are also used to enhance forming processes in the so-called *Ultrasonic Vibration Assisted Forming* (UVAF). With this technology, an ultrasonic frequency vibration is applied on the forming tool during the forming process and transmitted to the workpiece, reducing the friction and the resistance to deformation. A complete review of UVAF processes can be found in [70].

Another energy-aided technology, characterised by the use of electrical current to achieve permanent deformations in metals, is *Electrically Assisted Forming* (EAF). In this type of pro-

cess, electrical current flows through the material, causing the workpiece to heat up due to Joule effect, thereby reducing the force required to achieve the desired deformation. The direct introduction of current into the workpiece in EAF processes is a significant advantage in terms of efficiency compared to other common hot forming technologies, as the heat loss is reduced. In this sense, EAF eliminates the need for additional heating devices and thermal insulation, resulting in simpler and more flexible equipment.

One particular EAF process is *electric upsetting*, which will be the main subject of this thesis. This technology has gained great industrial interest in recent years, for instance in the manufacture of parts in the automotive and aeronautical sectors [31].

1.2 Electric upsetting

Electric upsetting is an EAF method able to create a local enlarged diameter at one end of a metal bar. In this process, a bar at room temperature is placed in a horizontal upsetting machine and clamped by gripper jaws. A high-amperage, low-voltage electrical current passes through the bar via contact between one of its ends and the gripper jaws. This causes the bar end to heat up and acquire a plastic behaviour. When it reaches enough temperature, the bar is pushed against the anvil with the help of a force applied by a pusher located at the opposite end. As a consequence, the diameter at the hot end is enlarged, leading to the formation of a preform called *onion*. Figure 1.9a provides a global view of the experimental setup, while Figure 1.9b details the evolution of the onion preform during the process. Note that this variant of the process, in which the onion preform is created after growing without a strict limit, is the so-called *free electric upsetting*. A sketch of this process, including the main elements involved, is shown in Figure 1.10a.

In subsequent stages of the free electric upsetting process, the piece can be forged without further heating to get the final desired shape. This is the case, for example, in the manufacture of axle shafts for automotive applications (see Figure 1.11a), which are crucial parts of the vehicle transmission system, as sketched in Figure 1.11b. In that case, after the main free electric upsetting process, the onion preform undergoes an impression die forging stage to get the desired *plate* shape at one of the ends of the piece.

It is also of industrial interest to limit the diameter growth at the hot end of the bar by enclosing it within a closed volume (see Figure 1.9c). This technique, known as *in-die electric upsetting*, is illustrated in Figure 1.10b and is used to manufacture the pinion part of axle shafts, as opposed to the plate shown in Figure 1.11a.

1.3 Motivation

Electric upsetting usually involves complex physical phenomena, so its industrial control and optimisation has typically relied on practical experience. This kind of process is sensitive to several parameters, including the source of electrical current, the upsetting force or the material, dimensions and initial temperature of the bar. In this context, numerical simulation can offer valuable insights into the process, by evaluating numerous potential actions and configurations

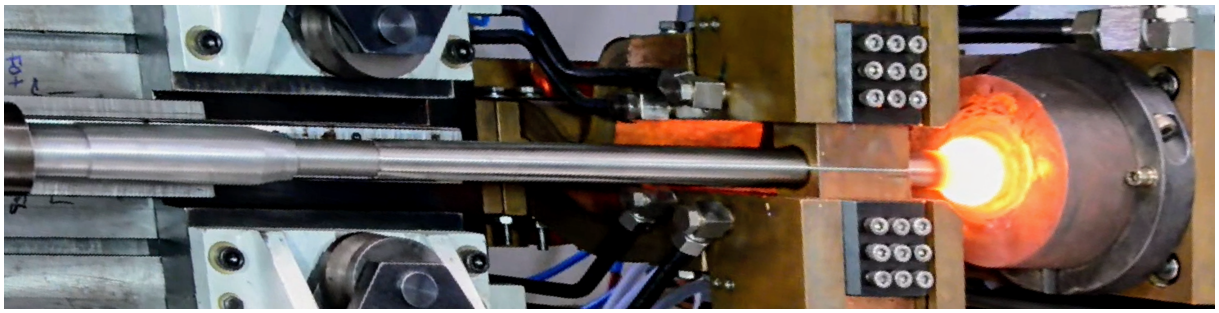

(a) Free electric upsetting process. Reproduced from ETA Technology YouTube channel with the permission of ETA Technology.

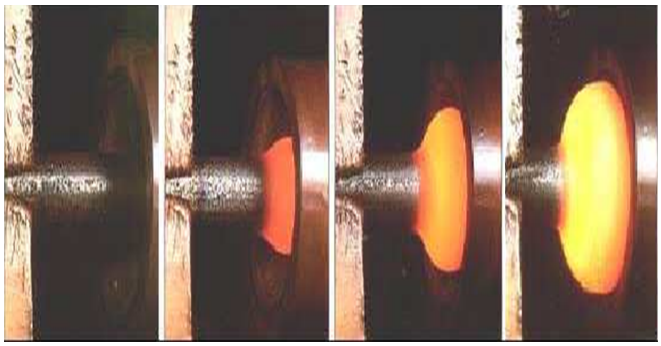

(b) Thickening of the diameter at one end of a steel bar undergoing free electric upsetting.

(c) In-die closed volume. Reproduced from CEMSA International catalogue with the permission of CEMSA International.

Figure 1.9: Electric upsetting processes.

that would be expensive and time-consuming to test on-site. Different publications can be found in the literature concerning the numerical simulation of free electric upsetting processes. In particular, the influence of the process variables on the temperature is analysed in [65], possible defects on the final preform are addressed in [60, 67], and the optimisation of different variables is considered in [66, 73]. On the other hand, as far as we know, the only approach to in-die electric upsetting processes is found in [3]. The common denominator of the previous works is the numerical simulation with DC power sources in commercial software. To the author's knowledge, there are no studies addressing modelling and simulation for AC power sources. It is also worth noting that the current research was motivated by the collaboration with the Spanish company CIE Galfor which uses electric upsetting in the manufacture of automotive parts such as axle shafts. The collaboration was developed within the framework of a project funded by the Centre for the Development of Technology and Innovation (CDTI) and formalised through an agreement between the company and CITMAga.

In electric upsetting, deformation and heating occur simultaneously. It is crucial to control both the upsetting force and the electrical input signal to achieve the desired shape and quality of the final product. In principle, electric upsetting can be performed using either direct current (DC) or alternating current (AC), depending on the case. Despite other operating benefits, the use of AC may be limited, as it can result in slow and non-uniform heating if the skin effect

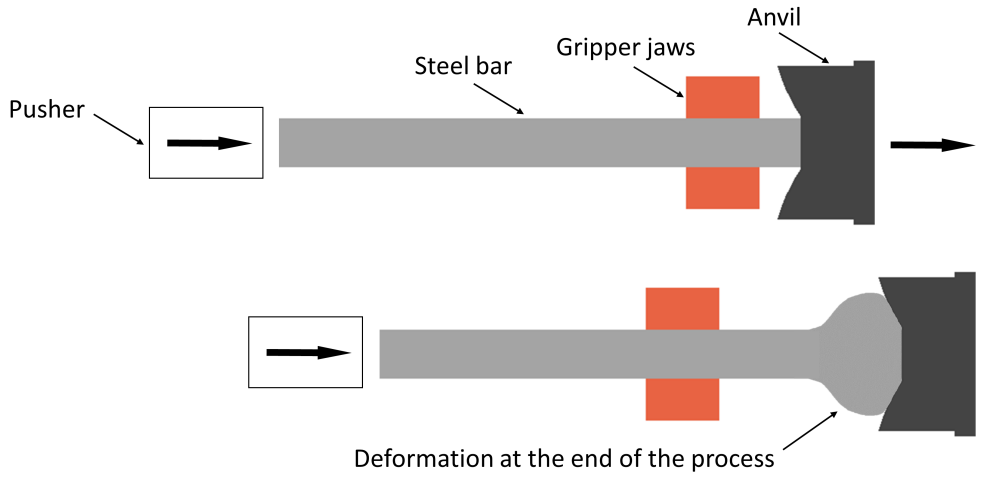

(a) Free electric upsetting.

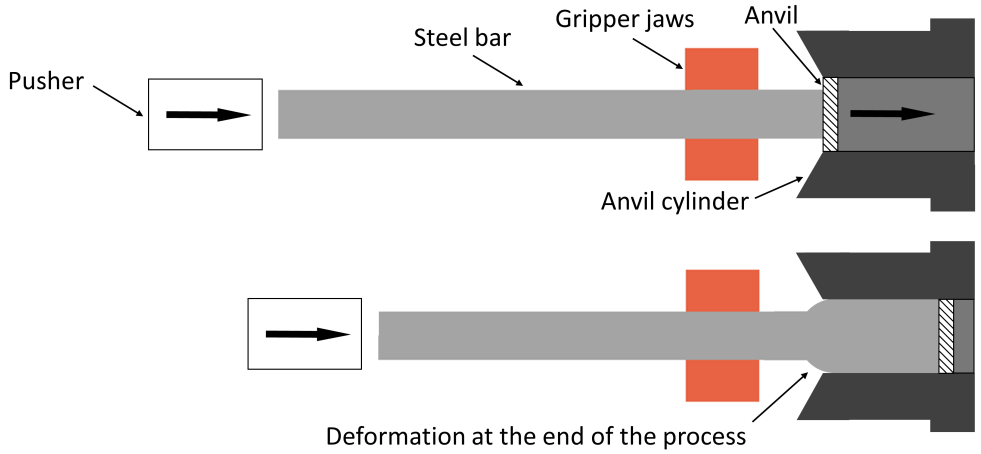

(b) In-die electric upsetting.

Figure 1.10: Schemes of electric upsetting processes.

is pronounced in the bar. If direct current sources are considered, magnetic phenomena are not present in the problem and the mathematical modelling is limited to the electrical part. However, if the industrial process is powered by alternating current, non-linear electromagnetic models are generally required.

The full simulation involves coupled thermal, electrical or electromagnetic, and mechanical phenomena, with the coupling influenced by various factors. Firstly, the deformation of the metal bar alters the computational domain for all models. Additionally, the electric, magnetic, and mechanical properties of the material are temperature-dependent, creating a coupling with the thermal model. Moreover, the heat source in the thermal model is derived from the Joule effect, which is associated with the power dissipated due to the electrical current flow through the bar, as computed by the electromagnetic model. Additionally, in AC current, the magnetic permeability is highly non-linear and depends on both the temperature and the magnitude of

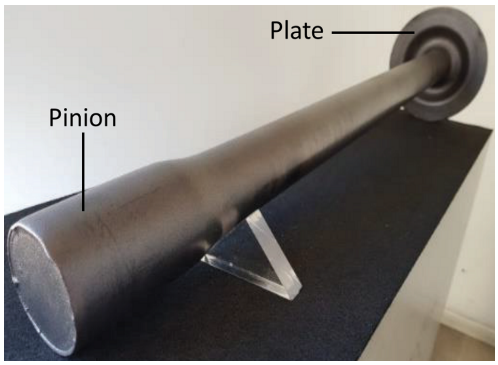

(a) Axle shaft ends: pinion and plate.

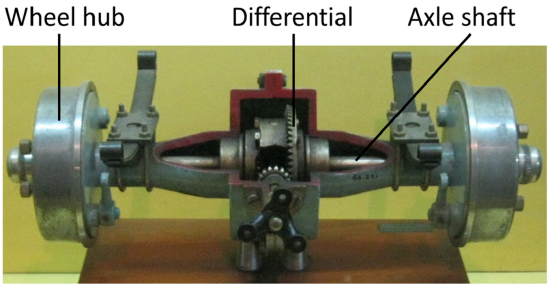

(b) Demonstration model of a motor car rear axle. Adapted from the original by Amanjosan2008, CC BY-SA 4.0.

Figure 1.11: Final shape and position of an axle shaft.

the magnetic field. The coupling schemes for DC (electric) and AC (electromagnetic) models are illustrated in Figure 1.12.

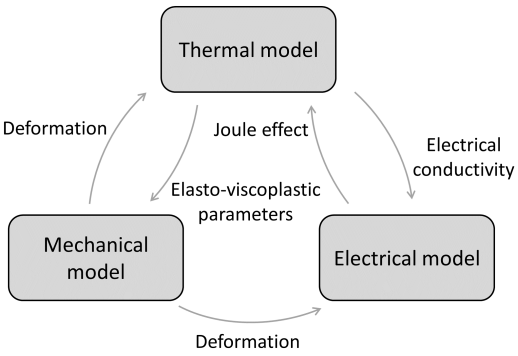

(a) Coupling with electrical model.

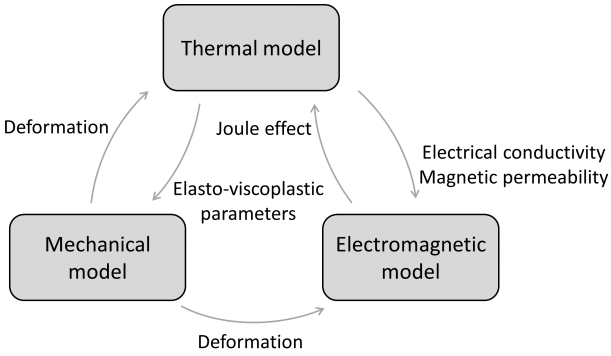

(b) Coupling with electromagnetic model.

Figure 1.12: Coupling schematic.

Regarding the mechanical aspect, the magnitude of displacements and deformations observed in practice renders infinitesimal strain theory invalid for electric upsetting modelling. Instead, finite strain theory, which includes a multiplicative decomposition of the deformation gradient into elastic and viscoplastic parts, should be considered. The literature often employs highly complex models for viscoplastic behaviour, necessitating several additional parameters to complete the mechanical model. Another critical component of the modelling is the contact between the bar and the surrounding elements, namely the anvil and the gripper jaws, which are essential for achieving the desired final shape. Adequate techniques must be developed to model and simulate these phenomena, encompassing not only the mechanical aspects but also the thermal and electrical contact.

Computing approximations to the solutions of this fully coupled problem presents significant challenges that require the development of reliable and accurate numerical methods. This thesis contributes to the development of multiphysics coupling models and numerical simulations of EAF processes, with a specific focus on electric upsetting. Numerical solutions for electric

upsetting problems are often derived from commercial codes, as in [3, 60, 65, 67], where the mathematical and numerical models are not presented in detail. In this work, the objective is to carefully introduce coupled mathematical models for electric upsetting and achieve their numerical solution through a suitable implementation in an own-developed Python-FEniCS code.

1.4 Objectives

The aim of this thesis is the mathematical modelling and numerical simulation of coupled formulations with application to electric upsetting processes. More specifically, the main objectives are:

- Mathematical modelling of the industrial problem of electric upsetting both in DC and AC current regimes.
- Multiphysics modelling of the coupled thermal, electrical or electromagnetic, and mechanical phenomena.
- Development of efficient and competitive numerical tools in our own code to address the numerical simulation of the coupled problem with large deformations and thermo-electromagnetic-mechanical contact.
- Model validation and application to the simulation of electric upsetting processes.

1.5 Methodology

In order to achieve the above objectives, it was necessary to develop a suitable methodology capable of meeting the different challenges involved in the problem under study.

As a first step, a literature review was carried out on different aspects of mathematical modelling and advanced numerical techniques related to the problem. Topics covered include thermo-mechanical and low frequency electromagnetic models, Lagrangian coordinates, viscoplastic mechanical models, and appropriate numerical techniques for addressing contact problems.

The developed model is a strongly coupled thermo-electromagnetic-mechanical one, where the main physical phenomena governing the problem have been considered for both DC and AC current sources and tailored for axisymmetric geometries. A unified pure-Lagrangian approach has been proposed for solving the three fully coupled models: thermal, electrical (or electromagnetic), and mechanical. To better discuss the relevance of our efforts towards devising these formulations, we briefly review here the development of characteristics-based methods, which are extensively used for solving convection-diffusion problems dominated by convection (see the review paper [35]). These methods are based on time discretisation of the time derivative along characteristic curves. When they are referred to a fixed domain (respectively, to a time dependent domain) they are called pure-Lagrangian methods (respectively, semi-Lagrangian methods). When combined with finite element methods, they are often called Lagrange-Galerkin

methods. Classical methods of characteristics, formulated in Eulerian coordinates, have been mathematically analysed and applied to different problems with time independent domains by several authors (e.g., [32], [64], [72], [69], [27], [34] and [10]). Higher-order schemes for time discretisation along characteristic curves enhance time accuracy (see [69], [27] and [10]).

In solid mechanics, numerical models are typically based on a Lagrangian formulation, contrasting with the Eulerian approach commonly used for fluid mechanics, thermo-electrical, or electromagnetic problems. Traditional challenges of the Eulerian description include the treatment of convective terms and the modelling and tracking of free surfaces, which are eliminated in the Lagrangian framework. Pure-Lagrangian methods offer additional advantages, such as a time-independent and predefined computational domain, higher accuracy in regions with strong gradients or solution discontinuities, and the absence of error terms involving the time step in the denominator, which are common in semi-Lagrangian methods. However, due to significant distortion of the moving mesh, remeshing and reinitialisation may be periodically required. Methods derived from this Lagrangian framework belong to the class of characteristics-based methods.

Recent contributions in literature include the development of Lagrange-Galerkin methods to solve convection-diffusion equations with time dependent domains, first for scalar linear problems (see [11], [12], [13]) and then for nonlinear vector ones (see [14], [15], [16]). Most of these methods are linear and all of them are obtained by introducing a change of variable from the current configuration to a reference configuration (known) and employ high-order time discretisations. Unified formulations to state pure-Lagrangian and semi-Lagrangian methods have been proposed for both scalar and vector convection-diffusion problems in [13], [14] and [16].

Sequential multiphysics algorithms that use a Lagrangian approach for mechanical problems and an Eulerian approach for thermo-electromagnetic problems are commonly employed in electro-mechanical simulations (see, for instance, [1]), where solutions are combined using staggered methods. A fully coupled Lagrangian approach for medical EAF problems was introduced in [59]. We have extended this framework by incorporating high-order Runge-Kutta schemes and an elasto-viscoplastic model for large deformations, based on the ideas in [75], rather than using backward Euler integration and the elastoplastic model considered in [59]. Additionally, we have addressed contact conditions and axisymmetric formulations relevant to electric upsetting processes. For a work focused on electromagnetic forming that employs a Lagrangian approach using a least-action variational principle, see [74]. Recent progress has been made in [38] to consider Lagrangian formulations for solving thermo-electrical-mechanical problems using direct current sources and assuming small deformations.

Moreover, electro-mechanical simulations have been explored in various contexts, including electro-visco-hyperelastic beams [37], dielectric elastomers [39], growing materials [52], polymer-based magneto-electric-elastic composites [55], and semiconductor materials [57].

The aforementioned pure-Lagrangian formulations have been implemented in a custom-developed code using the FEniCS library to solve partial differential equations via the finite element method, selecting appropriate discrete spaces for the unknowns of the problem. Various tests were conducted to validate the implemented models, either against known analytical solutions or by comparison with simulations in commercial software. Once the implementation

was sufficiently validated, the numerical simulation of electric upsetting processes was finally undertaken.

1.6 Thesis outline

In Chapter 2, the fundamentals of Continuum Mechanics are revisited, as this theoretical framework underpins the mathematical models presented in the subsequent chapters. Moreover, this chapter also outlines key definitions and notations for axisymmetric settings, since electric upsetting processes are often suitable to simplify 3D formulations to cylindrically symmetric cases.

In Chapter 3, DC sources and the associated electrical model are examined. A comprehensive description of the fully coupled thermo-electrical-mechanical model is provided, with particular emphasis on the mechanical aspect due to its complexity. This includes a detailed introduction to finite strain theory and the multiplicative decomposition of deformations into elastic and viscoplastic parts, as well as thorough descriptions of the viscoplastic constitutive law and mechanical contact with obstacles. Starting from the natural 3D Eulerian description, appropriate developments are made to achieve a final axisymmetric pure-Lagrangian formulation, which is used for simulation purposes.

In Chapter 4, AC sources are introduced, complicating the electromagnetic model primarily due to the non-linearities associated with the complex ferromagnetic behavior of materials. To address the differing time scales of the three models, a time-harmonic eddy current model is used for the electromagnetic part to avoid excessively small time steps. Additionally, it is assumed that currents and potential drops at certain electrical ports are known and included in the model as boundary conditions. The fully coupled thermo-electromagnetic-mechanical problem is then formulated within a pure-Lagrangian axisymmetric framework.

The fully coupled mathematical models developed in Chapters 3 and 4 are implemented in a proprietary code built using Python-FEniCS. The problem is discretised using the finite element method for the spatial component and high-order Runge-Kutta schemes for time integration. Chapter 5 presents the main numerical results obtained with this code, including real case studies and validation examples against robust commercial simulation software such as Ansys® and Marc®. Finally, Chapter 6 discusses final remarks and future tasks.

Chapter 2

Preliminary tools

In this chapter, we revisit the fundamentals of Continuum Mechanics, adopting the notation proposed by Gurtin [42]. These foundational tools are essential for the mathematical models developed in Chapters 3 and 4, which encompass Eulerian and Lagrangian formulations. Furthermore, the characteristics of the electric upsetting processes examined in this work are particularly suited to restrict 3D formulations to problems with cylindrical symmetry. Consequently, this chapter also includes the key definitions and notations relevant to axisymmetric settings.

2.1 Elements of Continuum Mechanics

Let Ω be a bounded domain in $\mathbb{R}^3$ with Lipschitz boundary Γ. Let $\mathsf{X} : \overline{\Omega} \times \mathbb{R} \to \mathbb{R}^3$ be a *motion* in the sense of Gurtin. In particular, $\mathsf{X} \in C^3(\overline{\Omega} \times \mathbb{R})$ and, for each fixed $t \in \mathbb{R}$, $\mathsf{X}(\cdot, t)$ is a one-to-one function satisfying

$$\det \mathbf{F} > 0, \qquad \text{in } \overline{\Omega} \times \mathbb{R}, \tag{2.1}$$

being $\mathbf{F}(\cdot, t) = \mathbf{Grad}\, \mathsf{X}(\cdot, t)$ the *deformation gradient tensor*. Notice that $\overline{\Omega}(t) := \mathsf{X}(\overline{\Omega}, t)$ is a closed region for all t. In practice, a bounded time interval is considered for the motion, namely, $[0, T]$.

For the material point $\mathsf{p} \in \Omega$, its *position* at time t is given by $\mathsf{x} = \mathsf{X}(\mathsf{p}, t)$ and its *velocity* in the material configuration is given by the time derivative of the motion, that is $\dot{\mathsf{X}}(\mathsf{p}, t)$.

Let us introduce the *trajectory* of the motion

$$\mathcal{T} := \{(\mathsf{x}, t) : \mathsf{x} \in \overline{\Omega}(t),\ t \in [0, T]\}. \tag{2.2}$$

We remark that fields defined in $\mathcal{T}$ (respectively, in $\overline{\Omega} \times [0, T]$) are called *spatial fields* (respectively, *material fields*). If ϕ is a spatial field, we define its *material description* ϕ_m by (see Figure 2.1)

$$\phi_m(\mathsf{p}, t) := \phi(\mathsf{X}(\mathsf{p}, t), t). \tag{2.3}$$

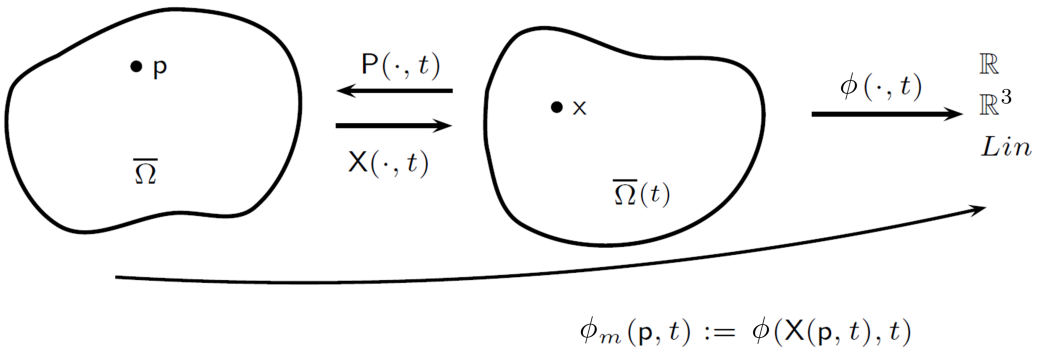

Figure 2.1: Motion and material description of spatial fields.

The spatial description of the velocity is $\mathbf{v}(\mathsf{x},t) = \dot{\mathsf{X}}(\mathsf{P}(\mathsf{x},t),t)$, being $\mathsf{P} : \mathcal{T} \to \overline{\Omega}$ the so-called *reference map* of the motion, that is the inverse of the one-to-one mapping $\mathsf{X}(\cdot,t)$, defined by

$$\mathsf{p} = \mathsf{P}(\mathsf{x},t) \Leftrightarrow \mathsf{x} = \mathsf{X}(\mathsf{p},t). \tag{2.4}$$

Thus, $\mathsf{p} = \mathsf{P}(\mathsf{x},t)$ is the position in the reference configuration of the material point that occupies the location x at time t. Following the same principles, we can define the material *acceleration*, $\ddot{\mathsf{X}}(\mathsf{p},t)$, and the spatial description of the acceleration, $\mathbf{a}(\mathsf{x},t) = \ddot{\mathsf{X}}(\mathsf{P}(\mathsf{x},t),t)$.

From the spatial velocity, $\mathbf{v}$, we introduce the *velocity gradient tensor*, $\mathbf{L}(\mathsf{x},t)$, defined by

$$\mathbf{L}(\mathsf{x},t) = \mathbf{grad}\,\mathbf{v}(\mathsf{x},t),$$

which is also known as *strain rate*. The symmetric and skew parts of $\mathbf{L}$ are denoted by $\mathbf{D}$ and $\mathbf{W}$, respectively. Specifically,

$$\begin{aligned}\mathbf{D}(\mathsf{x},t) =& \frac{1}{2}\left(\mathbf{L}(\mathsf{x},t) + \mathbf{L}^t(\mathsf{x},t)\right),\\ \mathbf{W}(\mathsf{x},t) =& \frac{1}{2}\left(\mathbf{L}(\mathsf{x},t) - \mathbf{L}^t(\mathsf{x},t)\right).\end{aligned}$$

It can be shown (see [42]) that the velocity gradient written in Lagrangian configuration, $\mathbf{L}_m(\mathsf{p},t)$, satisfies the relationship

$$\mathbf{L}_m(\mathsf{p},t) = \dot{\mathbf{F}}(\mathsf{p},t)\,\mathbf{F}^{-1}(\mathsf{p},t). \tag{2.5}$$

The symmetric and skew parts of $\mathbf{L}_m(\mathsf{p},t)$ are called *stretching tensor* and *spin tensor*, respectively.

If Φ is a smooth material field, we denote by $\mathrm{Grad}\,\Phi$ (respectively, by $\mathrm{Div}\,\Phi$) the gradient (respectively, the divergence) with respect to the first argument (p), and by $\dot{\Phi}$ the partial derivative with respect to the second argument (time). Similarly, if ψ is a smooth spatial field, we denote by $\mathrm{grad}\,\psi$ (respectively, by $\mathrm{div}\,\psi$) the gradient (respectively, the divergence) with respect to the first argument (x), and by ψ' the partial derivative with respect to the second argument (time). Gradient and divergence operators are denoted in bold when applied to vector and tensor fields,

respectively. Moreover, in the particular case where $\mathbf{\Phi}$ (or $\boldsymbol{\psi}$) is a smooth material (or spatial) vector field, the differential curl operator is denoted by $\mathbf{Curl}\,\mathbf{\Phi}$ (or $\mathbf{curl}\,\boldsymbol{\psi}$, respectively).

Note that, for smooth spatial fields $\phi(\mathsf{x},t)$ (scalar), $\boldsymbol{\vartheta}(\mathsf{x},t)$ (vector) and $\mathbf{\Psi}(\mathsf{x},t)$ (tensor), the above differential operators in spatial and material descriptions are related as follows:

$$\operatorname{grad}\phi(\mathsf{x},t) = \mathbf{F}^{-t}(\mathsf{p},t)\operatorname{Grad}\phi_m(\mathsf{p},t)\big|_{\mathsf{p}=\mathsf{P}(\mathsf{x},t)}\,, \tag{2.6}$$

$$\mathbf{curl}\,\boldsymbol{\vartheta}(\mathsf{x},t) = \left.\frac{\mathbf{F}(\mathsf{p},t)\,\mathbf{Curl}\left(\mathbf{F}^{t}(\mathsf{p},t)\,\boldsymbol{\vartheta}_m(\mathsf{p},t)\right)}{\det\mathbf{F}(\mathsf{p},t)}\right|_{\mathsf{p}=\mathsf{P}(\mathsf{x},t)}, \tag{2.7}$$

$$\operatorname{div}\left(\mathrm{A}(\mathsf{x},t)\operatorname{grad}\phi(\mathsf{x},t)\right) = \left.\frac{\operatorname{Div}\left(\det\mathbf{F}(\mathsf{p},t)\,\mathrm{A}_m(\mathsf{p},t)\,(\mathbf{F}^{t}\,\mathbf{F})^{-t}(\mathsf{p},t)\operatorname{Grad}\phi_m(\mathsf{p},t)\right)}{\det\mathbf{F}(\mathsf{p},t)}\right|_{\mathsf{p}=\mathsf{P}(\mathsf{x},t)}, \tag{2.8}$$

$$\mathbf{div}\,\mathbf{\Psi}(\mathsf{x},t) = \left.\frac{\mathbf{Div}\left(\det\mathbf{F}(\mathsf{p},t)\,\mathbf{\Psi}_m(\mathsf{p},t)\,\mathbf{F}^{-t}(\mathsf{p},t)\right)}{\det\mathbf{F}(\mathsf{p},t)}\right|_{\mathsf{p}=\mathsf{P}(\mathsf{x},t)}, \tag{2.9}$$

where $\mathrm{A}(\mathsf{x},t)$ is a smooth scalar field. Proofs of these identities are based on the chain rule, and further details can be found in Section 3.9 of [56].

On the other hand, if ψ is a smooth spatial field, $\dot{\psi}$ denotes the *material time derivative* with respect to time, that is,

$$\dot{\psi}(\mathsf{x},t) = \frac{\partial}{\partial t}\left(\psi(\mathsf{X}(\mathsf{p},t),t)\right)\Big|_{\mathsf{p}=\mathsf{P}(\mathsf{x},t)}, \quad \forall(\mathsf{x},t)\in\mathcal{T}. \tag{2.10}$$

In particular, for a smooth scalar spatial field $\phi(\mathsf{x},t)$, the material time derivative is given by

$$\dot{\phi}(\mathsf{x},t) = \frac{\partial\phi}{\partial t}(\mathsf{x},t) + \mathbf{v}(\mathsf{x},t)\cdot\operatorname{grad}\phi(\mathsf{x},t), \quad \forall(\mathsf{x},t)\in\mathcal{T}. \tag{2.11}$$

Similarly, if $\boldsymbol{\vartheta}(\mathsf{x},t)$ is a smooth vector spatial field, its material time derivative is

$$\dot{\boldsymbol{\vartheta}}(\mathsf{x},t) = \frac{\partial\boldsymbol{\vartheta}}{\partial t}(\mathsf{x},t) + \mathbf{grad}\,\boldsymbol{\vartheta}(\mathsf{x},t)\,\mathbf{v}(\mathsf{x},t), \quad \forall(\mathsf{x},t)\in\mathcal{T}. \tag{2.12}$$

Let $\mathbf{u}(\mathsf{p},t)$ denote the *material displacement* of point p at time t, that is,

$$\mathbf{u}(\mathsf{p},t) = \mathsf{X}(\mathsf{p},t) - \mathsf{p}, \quad \forall(\mathsf{p},t)\in\overline{\Omega}\times[0,T]. \tag{2.13}$$

Consequently, the deformation gradient, $\mathbf{F}(\mathsf{p},t)$, is given by

$$\mathbf{F}(\mathsf{p},t) = \mathbf{Grad}\,\mathsf{X}(\mathsf{p},t) = \mathbf{I} + \mathbf{Grad}\,\mathbf{u}(\mathsf{p},t), \quad \forall(\mathsf{p},t)\in\overline{\Omega}\times[0,T]. \tag{2.14}$$

Note that the material description of the velocity, $\mathbf{v}_m(\mathsf{p},t)$, is related to the material displacement through

$$\mathbf{v}_m(\mathsf{p},t) = \dot{\mathsf{X}}(\mathsf{p},t) = \dot{\mathbf{u}}(\mathsf{p},t), \quad \forall(\mathsf{p},t)\in\overline{\Omega}\times[0,T]. \tag{2.15}$$

Similarly, the material description of the acceleration, $\mathbf{a}_m(\mathsf{p},t)$, is given by

$$\mathbf{a}_m(\mathsf{p},t) = \dot{\mathbf{v}}_m(\mathsf{p},t) = \ddot{\mathsf{X}}(\mathsf{p},t) = \ddot{\mathbf{u}}(\mathsf{p},t), \quad \forall(\mathsf{p},t)\in\overline{\Omega}\times[0,T]. \tag{2.16}$$

When transforming boundary conditions between spatial and material configurations, the outward unit normal vector to the boundary of the current configuration $\Omega(t)$ at a point x, denoted $\mathbf{n}_{\mathsf{x}}(\mathsf{x},t)$, can be expressed in terms of the outward unit normal vector to the boundary of the reference configuration Ω at the corresponding point p, denoted $\mathbf{n}_{\mathsf{p}}(\mathsf{p})$, as follows:

$$\mathbf{n}_{\mathsf{x}}(\mathsf{x},t) = \left.\frac{\mathbf{F}^{-t}(\mathsf{p},t)\,\mathbf{n}_{\mathsf{p}}(\mathsf{p})}{|\mathbf{F}^{-t}(\mathsf{p},t)\,\mathbf{n}_{\mathsf{p}}(\mathsf{p})|}\right|_{\mathsf{p}=\mathsf{P}(\mathsf{x},t)}. \tag{2.17}$$

This relation is particularly useful for transforming integrals defined over the current domain $\Omega(t)$ (or surface $\Gamma(t)$) into integrals over the reference domain Ω (or reference surface Γ). To this end, the following identities introduced in [42] are helpful. Let $\phi(\mathsf{x},t)$ and $\boldsymbol{\vartheta}(\mathsf{x},t)$ denote smooth scalar and vector spatial fields, respectively. Then

$$\int_{\Gamma(t)} \phi(\mathsf{x},t)\,\mathrm{d}A_{\mathsf{x}} = \int_{\Gamma} \phi_m(\mathsf{p},t)\det\mathbf{F}(\mathsf{p},t)|\mathbf{F}^{-t}(\mathsf{p},t)\mathbf{n}_{\mathsf{p}}(\mathsf{p})|\,\mathrm{d}A_{\mathsf{p}}, \tag{2.18}$$

$$\int_{\Omega(t)} \phi(\mathsf{x},t)\,\mathrm{d}V_{\mathsf{x}} = \int_{\Omega} \phi_m(\mathsf{p},t)\det\mathbf{F}(\mathsf{p},t)\,\mathrm{d}V_{\mathsf{p}}, \tag{2.19}$$

$$\int_{\Gamma(t)} \boldsymbol{\vartheta}(\mathsf{x},t)\cdot\mathbf{n}_{\mathsf{x}}(\mathsf{x},t)\,\mathrm{d}A_{\mathsf{x}} = \int_{\Gamma} \boldsymbol{\vartheta}_m(\mathsf{p},t)\cdot\det\mathbf{F}(\mathsf{p},t)\mathbf{F}^{-t}(\mathsf{p},t)\mathbf{n}_{\mathsf{p}}(\mathsf{p})\,\mathrm{d}A_{\mathsf{p}}. \tag{2.20}$$

A summary of the notation used for the Eulerian (spatial) and Lagrangian (material) descriptions can be found in Table 2.1.

Element	**Eulerian**	**Lagrangian**
Domain	$\Omega(t)$	Ω
Domain boundary	$\Gamma(t)$	Γ
Normal unit vector	$\mathbf{n}_{\mathsf{x}}$	$\mathbf{n}_{\mathsf{p}}$
Tangent unit vector	$\boldsymbol{\tau}_{\mathsf{x}}$	$\boldsymbol{\tau}_{\mathsf{p}}$
Differential line element	$\mathrm{d}l_{\mathsf{x}}$	$\mathrm{d}l_{\mathsf{p}}$
Differential surface element	$\mathrm{d}A_{\mathsf{x}}$	$\mathrm{d}A_{\mathsf{p}}$
Differential volume element	$\mathrm{d}V_{\mathsf{x}}$	$\mathrm{d}V_{\mathsf{p}}$
Magnitude	$L(\mathsf{x},t)$	$L_m(\mathsf{p},t)$
Divergence operator	div	Div
Gradient operator	grad	Grad
Curl operator	**curl**	**Curl**

Table 2.1: Notation for the Eulerian and Lagrangian descriptions. Gradient and divergence operators are denoted in bold when applied to vector and tensor fields, respectively.

2.2 Cylindrical symmetry: notation and operators

In certain cases, real forming devices can be reasonably approximated as axisymmetric. This assumption is valid for many electric upsetting processes, including those examined in this

work. In this section, we consider a three-dimensional case exhibiting cylindrical symmetry, and introduce the main definitions and notations associated with axisymmetric configurations.

Let us assume that the reference domain $\Omega \subset \mathbb{R}^3$ can be obtained by rotating a bounded domain $\widehat{\Omega} \subset \mathbb{R}^2$, with boundary $\partial\widehat{\Omega} = \widehat{\Gamma}_{\mathrm{D}} \cup \widehat{\Gamma}$, around the axis of symmetry:

$$\Omega := \{(r_m, \theta_m, z_m) : \theta_m \in [0, 2\pi), (r_m, z_m) \in \widehat{\Omega}\}, \tag{2.21}$$

and

$$\Gamma := \partial\Omega = \{(r_m, \theta_m, z_m) : \theta_m \in [0, 2\pi), (r_m, z_m) \in \widehat{\Gamma}\}. \tag{2.22}$$

Notice that $\widehat{\Gamma}_{\mathrm{D}}$ is defined by

$$\widehat{\Gamma}_{\mathrm{D}} := \{(r_m, z_m) \in \partial\widehat{\Omega} : r_m = 0\}. \tag{2.23}$$

In fact, all the boundaries of the models in Chapters 3 and 4 are generated by rotating their corresponding parts of $\widehat{\Gamma}$ around the axis of symmetry and denoted by adding a hat. An example of a typical electric upsetting setup, where the original 3D domain can be reduced to an axisymmetric configuration, is illustrated in Figure 2.2.

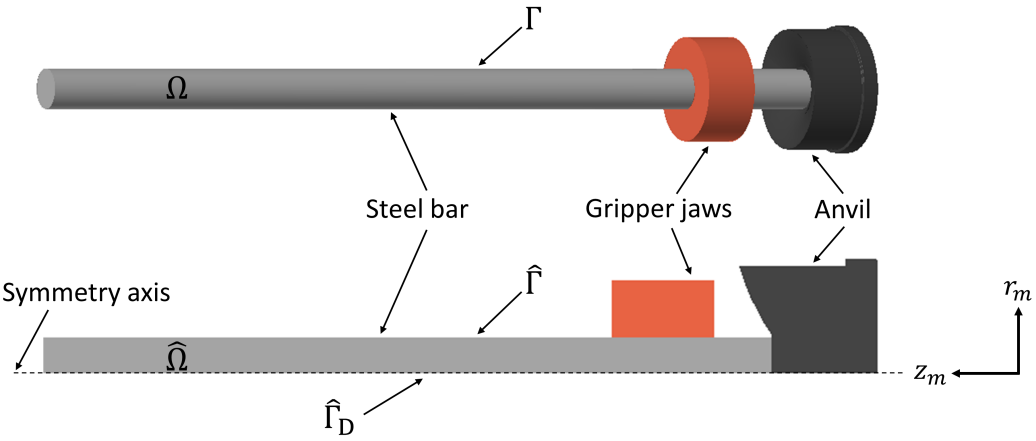

Figure 2.2: Example of a 3D cylindrical domain and its corresponding meridional section for an electric upsetting process.

We will assume that all the fields appearing in the problem present cylindrical symmetry. They will be specified with a hat. More precisely, if ϕ_m is a material scalar field independent of the azimuthal coordinate, then $\widehat{\phi}_m$ will denote its description in $\widehat{\Omega}$. That is,

$$\phi_m(\mathsf{p}, t) := \widehat{\phi}_m(\widehat{\mathsf{p}}, t), \tag{2.24}$$

where $\widehat{\mathsf{p}} := (r_m, z_m) \in \widehat{\Omega}$ denotes radial and axial coordinates of the material point $\mathsf{p} \in \Omega$.

A material vector field with cylindrical symmetry, $\boldsymbol{\vartheta}_m(\mathsf{p}, t)$, is defined by its coordinates in the basis $\{\mathbf{e}_r, \mathbf{e}_\theta, \mathbf{e}_z\}$ as

$$\boldsymbol{\vartheta}_m(\mathsf{p}, t) := \widehat{\vartheta}_r(\widehat{\mathsf{p}}, t)\mathbf{e}_r + \widehat{\vartheta}_z(\widehat{\mathsf{p}}, t)\mathbf{e}_z. \tag{2.25}$$

The vector of its coordinates is denoted with a hat:

$$\widehat{\boldsymbol{\vartheta}}_m(\widehat{\mathsf{p}},t) := \begin{pmatrix} \widehat{\vartheta}_r(\widehat{\mathsf{p}},t) \\ \\ \widehat{\vartheta}_z(\widehat{\mathsf{p}},t) \end{pmatrix}. \tag{2.26}$$

Let $\boldsymbol{\Psi}_m(\mathsf{p},t)$ be a material tensor field with cylindrical symmetry. This means that its components do not explicitly depend on the azimuthal coordinate and they remain unchanged under a rotation about the z axis. The most general form of such a tensor is

$$\begin{aligned}\boldsymbol{\Psi}_m(\mathsf{p},t) :=& \widehat{\Psi}_{rr}(\widehat{\mathsf{p}},t)\mathbf{e}_r\otimes\mathbf{e}_r + \widehat{\Psi}_{rz}(\widehat{\mathsf{p}},t)\mathbf{e}_r\otimes\mathbf{e}_z + \widehat{\Psi}_{\theta\theta}(\widehat{\mathsf{p}},t)\mathbf{e}_\theta\otimes\mathbf{e}_\theta \\ &+ \widehat{\Psi}_{zr}(\widehat{\mathsf{p}},t)\mathbf{e}_z\otimes\mathbf{e}_r + \widehat{\Psi}_{zz}(\widehat{\mathsf{p}},t)\mathbf{e}_z\otimes\mathbf{e}_z,\end{aligned} \tag{2.27}$$

for $\widehat{\mathsf{p}} := (r_m, z_m) \in \widehat{\Omega}$. Moreover, let us introduce the material tensor field $\widehat{\boldsymbol{\Psi}}_m(\widehat{\mathsf{p}},t)$ defined by its coordinates in the basis $\{\widehat{\mathbf{e}}_r, \widehat{\mathbf{e}}_z\}$ as follows:

$$\widehat{\boldsymbol{\Psi}}_m(\widehat{\mathsf{p}},t) := \begin{pmatrix} \widehat{\Psi}_{rr}(\widehat{\mathsf{p}},t) & \widehat{\Psi}_{rz}(\widehat{\mathsf{p}},t) \\ \\ \widehat{\Psi}_{zr}(\widehat{\mathsf{p}},t) & \widehat{\Psi}_{zz}(\widehat{\mathsf{p}},t) \end{pmatrix},\ \widehat{\mathsf{p}} := (r_m, z_m) \in \widehat{\Omega}. \tag{2.28}$$

Note that similar relations can be defined for spatial fields with cylindrical symmetry.

Therefore, if $\widehat{\mathbf{u}}(\widehat{\mathsf{p}},t)$ is the displacement field of point $\widehat{\mathsf{p}}$ at time t, the position of $\widehat{\mathsf{p}}$ in the current configuration (i.e., in the Eulerian configuration) is $\widehat{\mathsf{x}} = (r,z) \in \widehat{\Omega}(t)$ with components

$$r = r_m + \widehat{u}_r(\widehat{\mathsf{p}},t), \tag{2.29}$$

$$z = z_m + \widehat{u}_z(\widehat{\mathsf{p}},t). \tag{2.30}$$

For a problem with cylindrical symmetry, the deformation gradient $\mathbf{F}(\mathsf{p},t)$ has the form,

$$\mathbf{F}(\mathsf{p},t) = \mathbf{I_3} + \mathbf{Grad}\,\mathbf{u}(\mathsf{p},t) = \begin{pmatrix} 1+\dfrac{\partial\widehat{u}_r(\widehat{\mathsf{p}},t)}{\partial r_m} & 0 & \dfrac{\partial\widehat{u}_r(\widehat{\mathsf{p}},t)}{\partial z_m} \\ 0 & 1+\dfrac{\widehat{u}_r(\widehat{\mathsf{p}},t)}{r_m} & 0 \\ \dfrac{\partial\widehat{u}_z(\widehat{\mathsf{p}},t)}{\partial r_m} & 0 & 1+\dfrac{\partial\widehat{u}_z(\widehat{\mathsf{p}},t)}{\partial z_m} \end{pmatrix}.$$

We now introduce the material differential operator $\widehat{\mathrm{Grad}}$ which, when applied to a scalar material field with cylindrical symmetry, $\widehat{\phi}_m(\widehat{\mathsf{p}},t)$, is defined as

$$\widehat{\mathrm{Grad}}\,\widehat{\phi}_m(\widehat{\mathsf{p}},t) := \begin{pmatrix} \dfrac{\partial\widehat{\phi}_m(\widehat{\mathsf{p}},t)}{\partial r_m} \\ \\ \dfrac{\partial\widehat{\phi}_m(\widehat{\mathsf{p}},t)}{\partial z_m} \end{pmatrix}, \tag{2.31}$$

and, when applied to a vector field with cylindrical symmetry, $\widehat{\boldsymbol{\vartheta}}_m(\widehat{\mathsf{p}},t)$, provides

$$\widehat{\mathbf{Grad}}\,\widehat{\boldsymbol{\vartheta}}_m(\widehat{\mathsf{p}},t) := \begin{pmatrix} \dfrac{\partial\widehat{\vartheta}_r(\widehat{\mathsf{p}},t)}{\partial r_m} & \dfrac{\partial\widehat{\vartheta}_r(\widehat{\mathsf{p}},t)}{\partial z_m} \\ \\ \dfrac{\partial\widehat{\vartheta}_z(\widehat{\mathsf{p}},t)}{\partial r_m} & \dfrac{\partial\widehat{\vartheta}_z(\widehat{\mathsf{p}},t)}{\partial z_m} \end{pmatrix}. \tag{2.32}$$

The previous definition naturally leads to the introduction of the deformation gradient tensor in axisymmetric form, $\widehat{\mathbf{F}}(\widehat{\mathsf{p}},t)$, defined by

$$\widehat{\mathbf{F}}(\widehat{\mathsf{p}},t) := \mathbf{I_2} + \widehat{\mathbf{Grad}}\,\widehat{\mathbf{u}}(\widehat{\mathsf{p}},t) = \begin{pmatrix} 1+\dfrac{\partial \widehat{u}_r(\widehat{\mathsf{p}},t)}{\partial r_m} & \dfrac{\partial \widehat{u}_r(\widehat{\mathsf{p}},t)}{\partial z_m} \\ \dfrac{\partial \widehat{u}_z(\widehat{\mathsf{p}},t)}{\partial r_m} & 1+\dfrac{\partial \widehat{u}_z(\widehat{\mathsf{p}},t)}{\partial z_m} \end{pmatrix}, \tag{2.33}$$

which verifies the relation

$$\det \mathbf{F}(\mathsf{p},t) = \left(1+\frac{\widehat{u}_r(\widehat{\mathsf{p}},t)}{r_m}\right) \det \widehat{\mathbf{F}}(\widehat{\mathsf{p}},t). \tag{2.34}$$

Chapter 3

Thermo-electrical-mechanical modelling of DC electric upsetting

The aim of this chapter is to describe the coupled mechanical, electrical and thermal models required for the numerical simulation of electric upsetting processes using DC electrical sources. First, the geometric setting considered throughout the chapter is introduced.

The experimental setup for real electric upsetting primarily consists of a metal bar to be deformed supported on an anvil. The bar is held by gripper jaws through which current is passed, causing the Joule effect that heats the end of the bar (see Figure 2.2). The computational domain considered in this work includes only the workpiece to be deformed. The relevant neighbouring elements, namely the anvil and the gripper jaws, are accounted for in the mathematical modelling through appropriate boundary conditions. More precisely, electrical sources are considered on the part of the boundary associated with the gripper jaws, and suitable contact conditions are imposed on those parts of the boundary where the deformed bar reaches the anvil position, which is assumed to be a non-deformable geometric object.

Given the cylindrical nature of the metal bars used in the electric upsetting processes discussed in this work, as well as the characteristics of the electrical sources and the applied forces, the 3D computational domain can be simplified to an axisymmetric setting. Therefore, we will start from the 3D strong Eulerian formulation and take the necessary steps to achieve the final axisymmetric Lagrangian weak formulation of the problem.

To compute the power dissipated in the bar, the temperature, and the deformation, it is necessary to solve coupled mechanical, electrical, and thermal models. Recall that the coupling between the three models is due to several factors. On one hand, the Joule effect caused by the electrical current flow acts as a heat source for the thermal model, and conversely, the electrical

This chapter partially reproduces contents from the following publication:

- M. Benítez, A. Bermúdez, P. Fontán, I. Martínez, P. Salgado (2025). *A pure-Lagrangian finite element approach for solving thermo-electrical-mechanical models. Application to electric upsetting.* Finite Elements in Analysis and Design, 251, 104433. Electronic ISSN: 1872-6925, Print ISSN: 0168-874X. DOI: 10.1016/j.finel.2025.104433

conductivity is temperature-dependent. Moreover, the mechanical material parameters are also temperature-dependent and the computational domain for the three models changes due to mechanical deformations.

In Section 3.1, the mechanical model is described in detail. We first introduce the equation of motion, suitable constitutive laws, and some useful definitions in the context of finite elasticity. Subsequently, combined elastic and viscoplastic effects are considered through the multiplicative decomposition of the deformation gradient. The detailed development of the elasto-viscoplastic model leads us to the introduction of the Anand constitutive law which is suitable for describing this type of behaviour. We also focus on boundary conditions, including Dirichlet, Neumann, and unilateral contact which requires detailed treatment. Once all the elements are assembled, the weak Lagrangian formulation of the 3D problem is presented.

In Section 3.2, we introduce the electrical model under DC considerations. The so-called direct current model is obtained from Maxwell's equations and formulated in terms of the electric potential. Additionally, Dirichlet and Neumann boundary conditions are considered, with the option to provide the total power supplied to the system as data. Finally, the 3D Lagrangian weak formulation is described.

The thermal model is described in Section 3.3, beginning with the energy conservation equation in the Eulerian configuration. Suitable Dirichlet and Robin boundary conditions are considered, along with the heat source term due to the Joule effect, which is computed from the electrical model. The final step is the description of the 3D Lagrangian weak formulation.

Section 3.4 focuses on the coupled thermo-electrical-mechanical model under the assumption of cylindrical symmetry. This assumption is appropriate for representing the typical domains of electric upsetting processes and helps us to reduce computational effort. The notation introduced in Chapter 2 is used here.

Finally, for the sake of completeness, Section 3.5 includes some formal computations regarding the Lagrangian approach in a new reference configuration. These issues may be relevant when the deformations are very large, necessitating a change in the reference domain during the process.

3.1 Mechanical model

The metal bar is deformed by a combination of thermo-electrical heating and the subsequent upsetting process when a certain force is applied, typically resulting in large deformations. There are two main types of deformation in electric upsetting processes: elastic and viscoplastic. Elastic deformations are reversible; when a body subjected to external forces undergoes this type of deformation, it can return to its original shape once the forces are removed. Viscoplastic deformations, on the other hand, are permanent and associated with plastic behaviour, and they also depend on the rate at which the loads are applied.

Due to the characteristics of electric upsetting, where large displacements and deformations are common, the infinitesimal strain theory is no longer valid, necessitating the use of a finite strain model. A finite elasticity model is introduced below and then coupled with the viscoplastic component of the deformations.

3.1.1 Finite elasticity

Let us consider a reference configuration $\Omega \subset \mathbb{R}^3$ subjected to a system of forces during a motion

$$\mathsf{X} : \Omega \times [0,T] \to \mathbb{R}^3,$$

such that the current (spatial) configuration at time t is given by $\Omega(t) = \mathsf{X}(\Omega, t)$. The system of forces acting on the body consists of

- a *body force density* $\mathbf{b}(\cdot,t) : \overline{\Omega}(t) \times [0,T] \to \mathbb{R}^3$, representing forces per unit volume exerted by the environment, and
- a *surface force density* $\mathbf{s}(\mathbf{n}_\mathsf{x}, \mathsf{x}, t)$, acting across any oriented surface $\mathcal{S} \subset \overline{\Omega}(t)$, where $\mathbf{n}_\mathsf{x}$ is the unit normal to the surface at $\mathsf{x} \in \mathcal{S}$.

Recall that, according to *Cauchy's hypothesis*, for each unit normal $\mathbf{n}_\mathsf{x}$, there exists a traction vector $\mathbf{s}(\mathbf{n}_\mathsf{x}, \mathsf{x}, t)$ that represents the force per unit area exerted across the surface $\mathcal{S}$ at point x and time t, by the material on one side of $\mathcal{S}$ onto the material on the other side.

Assuming the balance of linear and angular momentum laws, *Cauchy's Theorem* establishes the existence of a symmetric tensor field, the so-called *Cauchy stress tensor*, $\mathbf{T}(\mathsf{x},t) : \overline{\Omega}(t) \times [0,T] \longrightarrow Lin$, verifying the following equation of motion in Eulerian coordinates at every time t and every point $\mathsf{x} \in \Omega(t)$,

$$\rho(\mathsf{x},t)\,\frac{\partial \mathbf{v}}{\partial t}(\mathsf{x},t) + \rho(\mathsf{x},t)\,\mathbf{grad}\,\mathbf{v}(\mathsf{x},t)\,\mathbf{v}(\mathsf{x},t) = \mathbf{div}\,\mathbf{T}(\mathsf{x},t) + \mathbf{b}(\mathsf{x},t), \tag{3.1}$$

where we recall that $\mathbf{v}(\cdot,t) : \overline{\Omega}(t) \times [0,T] \longrightarrow \mathbb{R}^3$ is the velocity field and $\rho(\cdot,t) : \overline{\Omega}(t) \times [0,T] \longrightarrow \mathbb{R}$ is the mass density. Moreover,

$$\mathbf{s}(\mathbf{n}_\mathsf{x}, \mathsf{x}, t) = \mathbf{T}(\mathsf{x},t)\,\mathbf{n}_\mathsf{x}(\mathsf{x},t). \tag{3.2}$$

To express the motion equation in Lagrangian coordinates, let us recall the mass conservation principle which states that

$$\rho_m(\mathsf{p},t)\,\det \mathbf{F}(\mathsf{p},t) = \rho_0(\mathsf{p}), \tag{3.3}$$

being $\rho_0(\mathsf{p})$ the mass density in the reference configuration.

Using the mass conservation (3.3), the relation (2.16), and the identities (2.12) and (2.9), particularised for $\boldsymbol{\vartheta}(\mathsf{x},t) = \mathbf{v}(\mathsf{x},t)$ and $\boldsymbol{\Psi}(\mathsf{x},t) = \mathbf{T}(\mathsf{x},t)$, respectively, the motion equation (3.1) in Lagrangian coordinates reads as follows:

$$\rho_0(\mathsf{p})\,\ddot{\mathbf{u}}(\mathsf{p},t) = \mathbf{Div}\left(\det(\mathbf{F}(\mathsf{p},t))\,\mathbf{T}_m(\mathsf{p},t)\,\mathbf{F}^{-t}(\mathsf{p},t)\right) + \det(\mathbf{F}(\mathsf{p},t))\,\mathbf{b}_m(\mathsf{p},t). \tag{3.4}$$

From the *deformation gradient*, $\mathbf{F}(\mathsf{p},t)$, we introduce the *right Cauchy-Green strain tensor*, $\mathbf{C}(\mathsf{p},t)$, and the *left Cauchy-Greeen strain tensor*, $\mathbf{B}(\mathsf{p},t)$, as

$$\mathbf{C}(\mathsf{p},t) = \mathbf{F}^t(\mathsf{p},t)\,\mathbf{F}(\mathsf{p},t), \tag{3.5}$$

$$\mathbf{B}(\mathsf{p},t) = \mathbf{F}(\mathsf{p},t)\,\mathbf{F}^t(\mathsf{p},t). \tag{3.6}$$

Additionally, from the *Polar Decomposition Theorem*, $\mathbf{F}(\mathsf{p},t)$ can be factorised as

$$\mathbf{F}(\mathsf{p},t) = \mathbf{R}(\mathsf{p},t)\,\mathbf{U}(\mathsf{p},t) = \mathbf{V}(\mathsf{p},t)\,\mathbf{R}(\mathsf{p},t), \tag{3.7}$$

where $\mathbf{R}$ is a rotation tensor field (i.e., orthogonal with determinant equal to 1), and $\mathbf{U}$ and $\mathbf{V}$ are symmetric positive definite tensor fields called *right stretch tensor* and *left stretch tensor*, respectively:

$$\mathbf{U}(\mathsf{p},t) = \mathbf{C}^{1/2}(\mathsf{p},t) = \left(\mathbf{F}^t(\mathsf{p},t)\,\mathbf{F}(\mathsf{p},t)\right)^{1/2}, \tag{3.8}$$

$$\mathbf{V}(\mathsf{p},t) = \mathbf{B}^{1/2}(\mathsf{p},t) = \left(\mathbf{F}(\mathsf{p},t)\,\mathbf{F}^t(\mathsf{p},t)\right)^{1/2}. \tag{3.9}$$

A constitutive law is needed for the elastic part of the mechanical model, relating the stresses applied to the domain with the subsequent strains produced. Some common strain tensors in the literature include the *Green–Lagrange (or Green–Saint-Venant) strain tensor*, $\mathbf{G}$, given by

$$\begin{aligned}\mathbf{G}(\mathsf{p},t) &= \frac{1}{2}\left(\mathbf{C}(\mathsf{p},t) - \mathbf{I}\right) = \frac{1}{2}\left(\mathbf{F}^t(\mathsf{p},t)\,\mathbf{F}(\mathsf{p},t) - \mathbf{I}\right)\\ &= \frac{1}{2}\left(\mathbf{Grad}\,\mathbf{u}(\mathsf{p},t) + (\mathbf{Grad}\,\mathbf{u}(\mathsf{p},t))^t + (\mathbf{Grad}\,\mathbf{u}(\mathsf{p},t))^t\;\mathbf{Grad}\,\mathbf{u}(\mathsf{p},t)\right),\end{aligned} \tag{3.10}$$

which has a linear part named *infinitesimal strain tensor*:

$$\boldsymbol{\varepsilon}(\mathsf{p},t) = \frac{1}{2}\left(\mathbf{Grad}\,\mathbf{u}(\mathsf{p},t) + (\mathbf{Grad}\,\mathbf{u}(\mathsf{p},t))^t\right). \tag{3.11}$$

We also introduce the *right Hencky strain tensor*, $\mathbf{H_R}$, defined as

$$\mathbf{H_R}(\mathsf{p},t) = \ln \mathbf{U}(\mathsf{p},t) = \frac{1}{2}\ln \mathbf{C}(\mathsf{p},t), \tag{3.12}$$

and the *left Hencky strain tensor*, $\mathbf{H_L}$, given by

$$\mathbf{H_L}(\mathsf{p},t) = \ln \mathbf{V}(\mathsf{p},t) = \frac{1}{2}\ln \mathbf{B}(\mathsf{p},t). \tag{3.13}$$

Related to the Cauchy stress tensor via $\mathbf{F}$ there are also several stress tensors, classical in Continuum Mechanics. Among them, we recall the *first Piola–Kirchhoff stress tensor*,

$$\mathbf{S}(\mathsf{p},t) = \det(\mathbf{F}(\mathsf{p},t))\,\mathbf{T}_m(\mathsf{p},t)\,\mathbf{F}^{-t}(\mathsf{p},t), \tag{3.14}$$

the *second Piola–Kirchhoff stress tensor*,

$$\boldsymbol{\Sigma}(\mathsf{p},t) = \det(\mathbf{F}(\mathsf{p},t))\,\mathbf{F}^{-1}(\mathsf{p},t)\,\mathbf{T}_m(\mathsf{p},t)\,\mathbf{F}^{-t}(\mathsf{p},t), \tag{3.15}$$

and the *Kirchhoff stress tensor*, $\mathbf{K}$,

$$\mathbf{K}(\mathsf{p},t) = \det(\mathbf{F}(\mathsf{p},t))\,\mathbf{T}_m(\mathsf{p},t). \tag{3.16}$$

There is a large variety of possible definitions for the stress and strain tensors, but only certain combinations of them are valid according to the second law of thermodynamics (see [21]

for further details). These are the so-called *work-conjugate stress–strain pairs*, among which the combinations $(\boldsymbol{\Sigma}, \mathbf{G})$ or $(\mathbf{K}, \mathbf{H_L})$ are included.

The constitutive law relating the stress tensor and its conjugate strain tensor can be obtained as a generalisation of the Hooke's law, originally formulated for infinitesimal isotropic elasticity, by replacing the Cauchy stress tensor and the infinitesimal strain tensor with the corresponding work-conjugate stress–strain pair. In particular, by using the pair $(\mathbf{K}, \mathbf{H_L})$, the *Hencky elasticity model* is obtained:

$$\mathbf{K}(\mathsf{p}, t) = 2\mu_{\mathrm{M}}(\mathsf{p}, t)\mathbf{H_L}(\mathsf{p}, t) + \lambda_{\mathrm{M}}(\mathsf{p}, t)\mathrm{tr}\left(\mathbf{H_L}(\mathsf{p}, t)\right)\mathbf{I}, \tag{3.17}$$

where λ_{M} and μ_{M} are the Lamé parameters for the considered material which, in the present study, are assumed to be temperature-dependent.

Similarly, by using the conjugate pair $(\boldsymbol{\Sigma}, \mathbf{G})$ the *Saint-Venant–Kirchhoff elasticity model* can be established

$$\boldsymbol{\Sigma}(\mathsf{p}, t) = 2\mu_{\mathrm{M}}(\mathsf{p}, t)\mathbf{G}(\mathsf{p}, t) + \lambda_{\mathrm{M}}(\mathsf{p}, t)\mathrm{tr}\left(\mathbf{G}(\mathsf{p}, t)\right)\mathbf{I}. \tag{3.18}$$

3.1.2 Elasto-viscoplasticity

Once the electric upsetting process is complete, the workpiece remains permanently deformed. This key phenomenon is related to the inelastic part of the deformations, which must be accurately modelled to obtain realistic results. In addition to the permanent nature of these deformations, it is observed that the strain state of the body exhibits a strong dependence on time, both on the rate at which the load is applied and on the time scale under consideration. These effects must be captured by a suitable *viscoplasticity* model which accounts for rate-dependent plastic behaviour. A typical stress-strain response for elasto-viscoplastic materials is illustrated in Figure 3.1, where the influence of strain rate can clearly be seen. Accordingly, the finite elasticity model introduced in the previous section will now be extended to include a contribution from viscoplastic strains.

As mentioned in [30], the interest in large-strain elastoplastic formulations dates back to the late 1950s with the first scientific publications on the subject appearing in the 1970s. Early formulations were primarily based on straightforward extensions of classical infinitesimal theories, often implemented in a somewhat crude manner. As a result, several theoretical and practical issues arose, such as the appearance of dissipative effects even during purely elastic processes, oscillatory stress responses under monotonic loading, and other undesirable features from a theoretical standpoint. Although these so-called hypoelastic-based models remain widely used in various applications, hyperelastic-based models began to emerge in the late 1980s as a means of addressing the aforementioned drawbacks. By combining hyperelastic formulations for reversible behaviour (see Section 3.1.1) with the multiplicative decomposition of the deformation gradient, these models provide a more consistent and physically sound framework. This hyperelastic-based multiplicative approach, extensively reviewed in [71], has gained significant traction over the past few decades and is now implemented in many commercial finite element codes for large-deformation analysis. It is worth noting that the general mathematical structure of elasto-viscoplastic models closely resembles that of elastoplastic ones, differing mainly in the

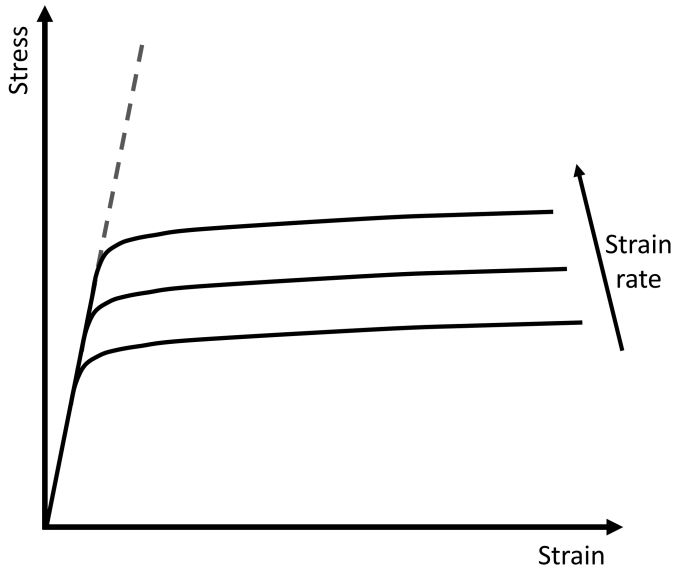

Figure 3.1: Typical stress-strain curves for elasto-viscoplastic materials, where rate-dependent effects become clear. In contrast, a purely elastic response would follow the dashed line.

physical assumptions made to account for rate-dependent effects. These viscoplastic behaviours are described through appropriate constitutive laws tailored to capture time-dependent material responses.

In the context of elasto-viscoplasticity, the fundamental assumption is the multiplicative Kröner decomposition of the deformation gradient tensor, originally introduced by Lee and Liu [49, 50]. This decomposition expresses the total deformation gradient as the product of an elastic part and a viscoplastic part:

$$\mathbf{F}(\mathsf{p},t) = \mathbf{F}^e(\mathsf{p},t)\,\mathbf{F}^p(\mathsf{p},t), \tag{3.19}$$

where $\mathbf{F}^e$ and $\mathbf{F}^p$ are called, respectively, the *elastic* and *plastic deformation gradients*.

This multiplicative decomposition is a natural extension of the classical additive strain split used in infinitesimal plasticity. From a micromechanical perspective, it reflects the notion that only elastic deformations contribute to the stress state within the material. In this framework, the total deformation is interpreted as a sequential process: first, a viscoplastic deformation, $\mathbf{F}^p$, which brings the material to a local stress-free intermediate configuration; second, an elastic deformation, $\mathbf{F}^e$, which maps this intermediate configuration to the current deformed state and generates stress.

This conceptual framework is schematically illustrated in Figure 3.2. It is important to emphasise that, in general, there does not exist a motion map $\mathsf{X}^p(\mathsf{p},t)$ such that

$$\mathbf{F}^p(\mathsf{p},t) = \mathbf{Grad}\,\mathsf{X}^p(\mathsf{p},t), \tag{3.20}$$

so $\mathbf{F}^p$ cannot always be interpreted as the gradient of a physically feasible deformation.

Analogously to the polar decomposition of $\mathbf{F}$ in (3.7), the elastic and plastic deformation

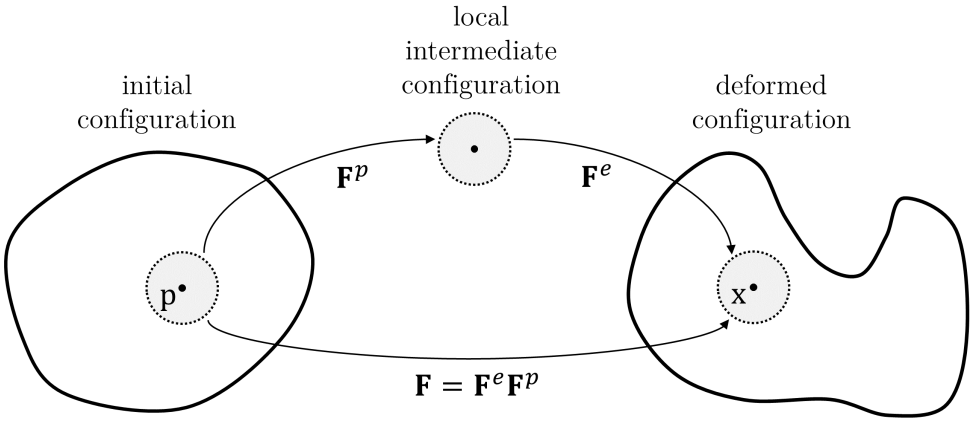

Figure 3.2: Multiplicative decomposition of the deformation gradient.

gradients, $\mathbf{F}^e$ and $\mathbf{F}^p$, also admit polar decompositions of the form

$$\mathbf{F}^e(\mathsf{p},t) = \mathbf{R}^e(\mathsf{p},t)\,\mathbf{U}^e(\mathsf{p},t) = \mathbf{V}^e(\mathsf{p},t)\,\mathbf{R}^e(\mathsf{p},t), \tag{3.21}$$

$$\mathbf{F}^p(\mathsf{p},t) = \mathbf{R}^p(\mathsf{p},t)\,\mathbf{U}^p(\mathsf{p},t) = \mathbf{V}^p(\mathsf{p},t)\,\mathbf{R}^p(\mathsf{p},t), \tag{3.22}$$

where $\mathbf{R}^e$ and $\mathbf{R}^p$ are rotation tensors and $\mathbf{U}^e$, $\mathbf{V}^e$, $\mathbf{U}^p$, $\mathbf{V}^p$ are symmetric positive-definite tensors associated with the elastic and plastic deformations, respectively.

In addition, one can define the *elastic* and *plastic velocity gradients*, denoted by $\mathbf{L}^e$ and $\mathbf{L}^p$, respectively, as material tensor fields given by

$$\mathbf{L}^e(\mathsf{p},t) = \dot{\mathbf{F}}^e(\mathsf{p},t)\;(\mathbf{F}^e(\mathsf{p},t))^{-1}, \tag{3.23}$$

$$\mathbf{L}^p(\mathsf{p},t) = \dot{\mathbf{F}}^p(\mathsf{p},t)\;(\mathbf{F}^p(\mathsf{p},t))^{-1}. \tag{3.24}$$

If the identities (2.5), (3.19), (3.23) and (3.24) are taken into account it can be shown that

$$\mathbf{L}_m(\mathsf{p},t) = \mathbf{L}^e(\mathsf{p},t) + \mathbf{F}^e(\mathsf{p},t)\,\mathbf{L}^p(\mathsf{p},t)\;(\mathbf{F}^e(\mathsf{p},t))^{-1}. \tag{3.25}$$

Following classical notation, we introduce the symmetric and skew-symmetric parts of $\mathbf{L}^e$ and $\mathbf{L}^p$, respectively, given by

- $\mathbf{D}^e$ and $\mathbf{D}^p$: the *rate of deformation* tensors (symmetric parts),
- $\mathbf{W}^e$ and $\mathbf{W}^p$, the *spin* tensors (skew-symmetric parts),

such that

$$\mathbf{L}^e = \mathbf{D}^e + \mathbf{W}^e,\;\; \mathbf{L}^p = \mathbf{D}^p + \mathbf{W}^p.$$

From this point forward, we consider the Hencky model (3.17) as the constitutive law for the elastic behaviour. Since only the elastic strains contribute to stress generation, the constitutive relation is expressed as

$$\mathbf{K}(\mathsf{p},t) = 2\mu_{\mathrm{M}}(\mathsf{p},t)\mathbf{H}^{\mathbf{e}}_{\mathbf{L}}(\mathsf{p},t) + \lambda_{\mathrm{M}}(\mathsf{p},t)\mathrm{tr}\left(\mathbf{H}^{\mathbf{e}}_{\mathbf{L}}(\mathsf{p},t)\right)\mathbf{I}, \tag{3.26}$$

where $\mathbf{H}^{\mathbf{e}}_{\mathbf{L}}$ is the elastic part of the left Hencky strain tensor, given by

$$\mathbf{H}^{\mathbf{e}}_{\mathbf{L}}(\mathsf{p},t) = \ln \mathbf{V}^e(\mathsf{p},t) = \frac{1}{2}\ln\left(\mathbf{F}^e(\mathsf{p},t)\,\mathbf{F}^{e,t}(\mathsf{p},t)\right). \tag{3.27}$$

Regarding the viscoplastic contribution, we introduce the *spatially rotated plastic stretching tensor*, $\tilde{\mathbf{D}}^p$, which is built from $\mathbf{D}^p$ and $\mathbf{R}^e$ as

$$\tilde{\mathbf{D}}^p(\mathsf{p},t) = \mathbf{R}^e(\mathsf{p},t)\,\mathbf{D}^p(\mathsf{p},t)\,\mathbf{R}^{e,t}(\mathsf{p},t). \tag{3.28}$$

Under assumptions of isotropic elasto-viscoplasticity, it can be shown (see [43] for a detailed proof) that

$$\mathbf{W}^p(\mathsf{p},t) = \mathbf{0}. \tag{3.29}$$

Then $\mathbf{L}^p$ is symmetric and verifies $\mathbf{L}^p = \mathbf{D}^p$. By considering this result in (3.24) and (3.28), we obtain

$$\mathbf{D}^p(\mathsf{p},t) = (\ln\,\mathbf{F}^p(\mathsf{p},t))^{\cdot} = \dot{\mathbf{F}}^p(\mathsf{p},t)\,(\mathbf{F}^p(\mathsf{p},t))^{-1} = \mathbf{R}^{e,t}(\mathsf{p},t)\,\tilde{\mathbf{D}}^p(\mathsf{p},t)\,\mathbf{R}^e(\mathsf{p},t), \tag{3.30}$$

where $\tilde{\mathbf{D}}^p$ takes the form

$$\tilde{\mathbf{D}}^p(\mathsf{p},t) = \mathbf{G}\left(\mathbf{K}(\mathsf{p},t), \dot{\epsilon}^p(\mathsf{p},t)\right) = \frac{3}{2}\frac{\mathbf{K}^d}{q\left(\mathbf{K}^d\right)}\dot{\epsilon}^p, \tag{3.31}$$

being $\mathbf{K}^d$ the deviatoric tensor of $\mathbf{K}$,

$$\mathbf{K}^d(\mathsf{p},t) = \mathbf{K}(\mathsf{p},t) - \frac{1}{3}\,\mathrm{tr}(\mathbf{K}(\mathsf{p},t))\,\mathbf{I}, \tag{3.32}$$

and q defined by

$$q\left(\mathbf{K}^d\right) = \sqrt{\frac{3}{2}\mathbf{K}^d : \mathbf{K}^d}. \tag{3.33}$$

In metal forming applications, it is crucial to preserve as much of the initial workpiece volume as possible once the deformation process is complete. It is well known that changes in volume during deformation are governed by the value of $\det \mathbf{F}$. Since viscoplastic deformations typically dominate over elastic ones in such processes, only minor volume changes are expected and these are solely attributable to elastic strains. In other words, based on the preceding equations, the following lemma can be established: at every point p and time t, viscoplastic deformations do not contribute to volume changes.

Lemma 3.1. *Assuming null initial deformation, i.e.,* $\mathbf{F}^p(\mathsf{p},0) = \mathbf{I}\ \forall \mathsf{p}$, *then*

$$\det \mathbf{F}^p(\mathsf{p},t) = 1\ \forall \mathsf{p},\ \forall t. \tag{3.34}$$

Proof. By integrating (3.30), we deduce

$$\mathbf{F}^p(\mathsf{p},t) = \exp\left(\int_0^t \mathbf{R}^{e,t}(\mathsf{p},s)\,\mathbf{G}\left(\mathbf{K}(\mathsf{p},s), \dot{\epsilon}^p(\mathsf{p},s)\right)\,\mathbf{R}^e(\mathsf{p},s)\,\mathrm{d}s\right). \tag{3.35}$$

Since for a given smooth tensor field $\mathbf{A}$ we have that $\det(\exp(\mathbf{A})) = \exp(\mathrm{tr}(\mathbf{A}))$, then

$$\det \mathbf{F}^p(\mathsf{p},t) = \exp\left(\mathrm{tr}\left(\int_0^t \mathbf{R}^{e,t}(\mathsf{p},s)\,\mathbf{G}\left(\mathbf{K}(\mathsf{p},s),\dot{\epsilon}^p(\mathsf{p},s)\right)\,\mathbf{R}^e(\mathsf{p},s)\,\mathrm{d}s\right)\right) \tag{3.36}$$

$$= \exp\left(\int_0^t \mathrm{tr}\left(\mathbf{R}^{e,t}(\mathsf{p},s)\,\mathbf{G}\left(\mathbf{K}(\mathsf{p},s),\dot{\epsilon}^p(\mathsf{p},s)\right)\,\mathbf{R}^e(\mathsf{p},s)\right)\mathrm{d}s\right) \tag{3.37}$$

$$= \exp\left(\int_0^t \mathrm{tr}\left(\mathbf{G}\left(\mathbf{K}(\mathsf{p},s),\dot{\epsilon}^p(\mathsf{p},s)\right)\right)\mathrm{d}s\right) = 1, \tag{3.38}$$

where we have used (3.31) and the facts that the trace is a linear mapping and $\mathbf{K}^d$ is a deviatoric tensor. □

Once the previous relations have been established, a rate-dependent constitutive law is required to complete the modelling of the viscoplastic response, specifically to describe the inelastic strain rate $\dot{\epsilon}^p$. To this end, we adopt the Anand model [4, 5], a unified viscoplasticity framework that captures both creep and plasticity through a set of two coupled differential equations. These equations relate the inelastic strain rate to the flow resistance in materials undergoing large, isotropic viscoplastic deformations with relatively small elastic strains. Originally developed to model the high-temperature rate-dependent deformation of metals (see [44], for instance) the Anand model has become the standard viscoplasticity model in the analysis of solder joints [28, 29, 36]. Notably, this model does not require an explicit yield surface or a loading/unloading condition. It also introduces a single internal state variable that effectively characterises the evolution of material resistance and captures the essential mechanisms of plastic deformation from both physical and experimental standpoints.

Therefore, the following constitutive equation is proposed for $\dot{\epsilon}^p$,

$$\dot{\epsilon}^p(\mathsf{p},t) = f\left(q(\mathbf{K}^d(\mathsf{p},t)), s(\mathsf{p},t), \Theta_m(\mathsf{p},t)\right), \tag{3.39}$$

with another constitutive equation for s, called *hardening equation*, given by

$$\dot{s}(\mathsf{p},t) = g\left(\dot{\epsilon}^p(\mathsf{p},t), s(\mathsf{p},t), \Theta_m(\mathsf{p},t)\right). \tag{3.40}$$

As set out in [68], we adopt the following functional forms for f and g:

$$f(q(\mathbf{K}^d), s, \Theta_m) = A\exp\left(-\frac{Q}{R\,\Theta_m}\right)\left[\sinh\left(\xi\frac{q(\mathbf{K}^d)}{s}\right)\right]^{\frac{1}{m}}, \tag{3.41}$$

$$g(\dot{\epsilon}^p, s, \Theta_m) = \left\{h_0\left|1 - \frac{s}{s^*(\dot{\epsilon}^p,\Theta_m)}\right|^a \mathrm{sign}\left(1 - \frac{s}{s^*(\dot{\epsilon}^p,\Theta_m)}\right)\right\}\dot{\epsilon}^p, \tag{3.42}$$

where s^* describes the saturation value of s associated with a couple of given temperature and strain-rate. It is given by

$$s^*(\dot{\epsilon}^p,\Theta_m) = \widetilde{s}\left[\frac{\dot{\epsilon}^p}{A}\exp\left(\frac{Q}{R\,\Theta_m}\right)\right]^n, \tag{3.43}$$

where R is the universal constant for ideal gases and A, Q, ξ, m, h_0, a, $\tilde{s}$ and n are constant parameters of the Anand model, specific for each material. More precisely:

- A is a pre-exponential factor,
- Q is the activation energy,
- ξ is the stress multiplier,
- m is the strain rate sensitivity of stress,
- h_0 represents the hardening/softening constant,
- a is the strain rate sensitivity of hardening/softening,
- $\tilde{s}$ is associated with the saturation of the deformation resistance,
- n quantifies the strain rate sensitivity of this saturation value.

3.1.3 Boundary conditions

As mentioned above, in the electric upsetting process the bar is pushed from one end and fixed at the opposite end. Additionally, the deformation is restricted by a rigid obstacle. Therefore, if the mechanical model is considered in a 3D Eulerian domain, $\Omega(t)$, its boundary is decomposed into three disjoint parts: a Dirichlet boundary, $\Gamma_{\mathrm{DM}}(t)$, a Neumann boundary, $\Gamma_{\mathrm{NM}}(t)$, and a contact boundary, $\Gamma_{\mathrm{CM}}(t)$, so that $\partial\Omega(t) = \Gamma_{\mathrm{DM}}(t) \cup \Gamma_{\mathrm{NM}}(t) \cup \Gamma_{\mathrm{CM}}(t)$. The displacement is specified on $\Gamma_{\mathrm{DM}}(t)$, while a Neumann-like boundary condition is prescribed on $\Gamma_{\mathrm{NM}}(t)$. $\Gamma_{\mathrm{CM}}(t)$ refers to the boundary that may come into contact with the obstacle. A sketch of the mechanical domain and its corresponding boundaries is shown in Figure 3.3.

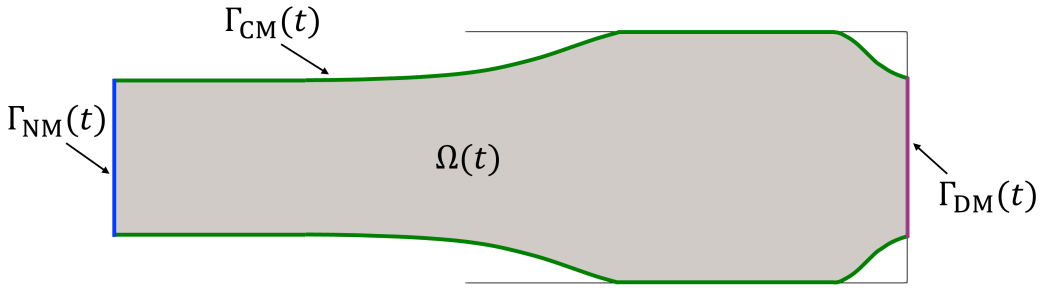

Figure 3.3: Boundaries of the mechanical domain.

The Dirichlet boundary condition is naturally written in the Lagrangian configuration as

$$\mathbf{u}(\mathsf{p}, t) = \mathbf{u}^{\mathrm{DM}}(\mathsf{p}, t) \quad \text{on } \Gamma_{\mathrm{DM}} \times (0, T], \tag{3.44}$$

where $\mathbf{u}^{\mathrm{DM}}(\cdot, t) : \Gamma_{\mathrm{DM}}(t) \longrightarrow \mathbb{R}^3$ is the imposed displacement field on the Dirichlet boundary.

The Neumann boundary condition follows from (3.2) and is given by

$$\mathbf{T}(\mathsf{x}, t)\, \mathbf{n}_{\mathsf{x}}(\mathsf{x}, t) = \mathbf{h}(\mathsf{x}, t) \quad \text{on } \Gamma_{\mathrm{NM}}(t) \times (0, T], \tag{3.45}$$

where $\mathbf{h}(\cdot, t) : \Gamma_{\mathrm{NM}}(t) \longrightarrow \mathbb{R}^3$ is a known surface force field.

Regarding the mechanical contact, a *frictionless unilateral contact* boundary condition is considered. Specifically, part of the mechanical boundary comes into contact with a rigid (non-deformable) obstacle, which reacts to this contact with a force opposite to that exerted by the metal bar over the obstacle. In a mathematical sense, if the rigid obstacle occupies a region C, then

$$\mathsf{x} \notin \mathsf{C} \quad \text{on } \Gamma_{\mathrm{CM}}(t) \times (0,T], \tag{3.46}$$

$$\mathbf{T}(\mathsf{x},t)\,\mathbf{n}_{\mathsf{x}}(\mathsf{x},t) = -\zeta(\mathsf{x},t)\,\mathbf{n}_{\mathsf{x}}(\mathsf{x},t) \quad \text{on } \Gamma_{\mathrm{CM}}(t) \times (0,T], \tag{3.47}$$

$$\zeta(\mathsf{x},t) \geq 0 \quad \text{on } \Gamma_{\mathrm{CM}}(t) \times (0,T], \tag{3.48}$$

$$\zeta(\mathsf{x},t) = 0 \text{ if } \mathsf{x} \notin \partial\mathsf{C} \quad \text{on } \Gamma_{\mathrm{CM}}(t) \times (0,T], \tag{3.49}$$

where $\zeta : \Gamma_{\mathrm{CM}}(t) \times [0,T] \longrightarrow \mathbb{R}$ is the Lagrange multiplier associated with mechanical contact.

To express the mechanical model in Lagrangian configuration, it is mandatory to transform the boundary conditions (3.45)-(3.49) from the Eulerian configuration in which they are naturally written. By evaluating them at a point $\mathsf{x} = \mathsf{X}(\mathsf{p},t)$ and using (2.17), it can be shown that these boundary conditions, when expressed in Lagrangian coordinates, can be rewritten as

$$\mathbf{T}_m(\mathsf{p},t)\,\mathbf{F}^{-t}(\mathsf{p},t)\,\mathbf{n}_{\mathsf{p}}(\mathsf{p}) = |\mathbf{F}^{-t}(\mathsf{p},t)\,\mathbf{n}_{\mathsf{p}}(\mathsf{p})|\,\mathbf{h}_m(\mathsf{p},t) \quad \text{on } \Gamma_{\mathrm{NM}} \times (0,T], \tag{3.50}$$

$$\mathsf{X}(\mathsf{p},t) \notin \mathsf{C} \quad \text{on } \Gamma_{\mathrm{CM}} \times (0,T], \tag{3.51}$$

$$\mathbf{T}_m(\mathsf{p},t)\,\mathbf{F}^{-t}(\mathsf{p},t)\,\mathbf{n}_{\mathsf{p}}(\mathsf{p}) = -\zeta_m(\mathsf{p},t)\,\mathbf{F}^{-t}(\mathsf{p},t)\,\mathbf{n}_{\mathsf{p}}(\mathsf{p}) \quad \text{on } \Gamma_{\mathrm{CM}} \times (0,T], \tag{3.52}$$

$$\zeta_m(\mathsf{p},t) \geq 0 \quad \text{on } \Gamma_{\mathrm{CM}} \times (0,T], \tag{3.53}$$

$$\zeta_m(\mathsf{p},t) = 0 \text{ if } \mathsf{p} \notin \partial\mathsf{C} \quad \text{on } \Gamma_{\mathrm{CM}} \times (0,T]. \tag{3.54}$$

Before proceeding with the complete formulation of the elasto-viscoplastic problem, it is pertinent to go deeper into the mechanical contact boundary conditions. The condition in (3.51) means that any kinematically admissible motion cannot penetrate the obstacle, which covers a certain area in the 3D space defined by an inequality of the form $M(\mathsf{p}) < 0$, where M is a known function for each obstacle. For instance, if the obstacle is the unit sphere, $M(\mathsf{p}) = M(r_m) = r_m - 1$, indicating that the obstacle covers the volume defined by the inequality $r_m - 1 < 0$.

Therefore, kinematically admissible motions must satisfy

$$M(\mathsf{X}(\mathsf{p},t)) \geq 0 \quad \text{in } \Omega \times (0,T]. \tag{3.55}$$

If the function M is introduced to rewrite the unilateral contact, the boundary conditions (3.50)-(3.54) are expressed as follows,

$$\mathbf{T}_m(\mathsf{p},t)\,\mathbf{F}^{-t}(\mathsf{p},t)\,\mathbf{n}_{\mathsf{p}}(\mathsf{p}) = |\mathbf{F}^{-t}(\mathsf{p},t)\,\mathbf{n}_{\mathsf{p}}(\mathsf{p})|\,\mathbf{h}_m(\mathsf{p},t) \quad \text{on } \Gamma_{\mathrm{NM}} \times (0,T], \tag{3.56}$$

$$\mathbf{T}_m(\mathsf{p},t)\,\mathbf{F}^{-t}(\mathsf{p},t)\,\mathbf{n}_{\mathsf{p}}(\mathsf{p}) = -\zeta_m(\mathsf{p},t)\,\mathbf{F}^{-t}(\mathsf{p},t)\,\mathbf{n}_{\mathsf{p}}(\mathsf{p}) \quad \text{on } \Gamma_{\mathrm{CM}} \times (0,T], \tag{3.57}$$

$$\zeta_m(\mathsf{p},t) \geq 0 \quad \text{on } \Gamma_{\mathrm{CM}} \times (0,T], \tag{3.58}$$

$$M(\mathsf{X}(\mathsf{p},t)) \geq 0 \quad \text{on } \Gamma_{\mathrm{CM}} \times (0,T], \tag{3.59}$$

$$\zeta_m(\mathsf{p},t)\,M(\mathsf{X}(\mathsf{p},t)) = 0 \quad \text{on } \Gamma_{\mathrm{CM}} \times (0,T]. \tag{3.60}$$

3.1.4 Statement of the elasto-viscoplasticity problem

At this stage, taking into account the motion equation (3.4), the multiplicative decomposition in (3.19), the elastic (3.26) and viscoplastic (3.39)-(3.43) constitutive laws, the boundary conditions (3.44) and (3.56)-(3.60), along with the relevant definitions from Chapter 2, the strong Lagrangian formulation for the elasto-viscoplastic mechanical model is established:

Lagrangian mechanical problem (LMP). *Find a vector field (displacement)* $\mathbf{u} : \overline{\Omega}\times[0,T] \longrightarrow \mathbb{R}^3$*, a tensor field (plastic deformation gradient)* $\mathbf{F}^p : \overline{\Omega}\times[0,T] \longrightarrow Lin$*, a scalar field (deformation resistance)* $s : \overline{\Omega}\times[0,T] \longrightarrow \mathbb{R}$ *and a scalar field (contact multiplier)* $\zeta_m : \Gamma_{\rm CM}\times[0,T] \longrightarrow \mathbb{R}$ *satisfying*

$$\rho_0\,\ddot{\mathbf{u}} = \mathbf{Div}\left(\mathbf{K}\,(\mathbf{I}+\mathbf{Grad}\,\mathbf{u})^{-t}\right) + \det(\mathbf{I}+\mathbf{Grad}\,\mathbf{u})\,\mathbf{b}_m, \tag{3.61}$$

$$\mathbf{K} = 2\check{\mu}_{\rm M}(\Theta_m)\mathbf{H}^e_{\mathbf{L}} + \check{\lambda}_{\rm M}(\Theta_m)\mathrm{tr}\,(\mathbf{H}^e_{\mathbf{L}})\,\mathbf{I}, \tag{3.62}$$

$$\mathbf{H}^e_{\mathbf{L}} = \frac{1}{2}\ln\left((\mathbf{I}+\mathbf{Grad}\,\mathbf{u})(\mathbf{F}^p)^{-1}(\mathbf{F}^p)^{-t}(\mathbf{I}+\mathbf{Grad}\,\mathbf{u})^t\right), \tag{3.63}$$

$$\dot{\mathbf{F}}^p\,(\mathbf{F}^p)^{-1} = \mathbf{R}^{e,t}\left(\frac{3}{2}\frac{\mathbf{K}^d}{q\,(\mathbf{K}^d)}\dot{\epsilon}^p\right)\mathbf{R}^e, \tag{3.64}$$

$$\mathbf{R}^e = \left[(\mathbf{I}+\mathbf{Grad}\,\mathbf{u})\,(\mathbf{F}^p)^{-1}\,(\mathbf{F}^p)^{-t}\,(\mathbf{I}+\mathbf{Grad}\,\mathbf{u})^t\right]^{-1/2}(\mathbf{I}+\mathbf{Grad}\,\mathbf{u})\,(\mathbf{F}^p)^{-1}, \tag{3.65}$$

$$\dot{\epsilon}^p = A\exp\left(-\frac{Q}{R\,\Theta_m}\right)\left[\sinh\left(\xi\frac{q(\mathbf{K}^d)}{s}\right)\right]^{\frac{1}{m}}, \tag{3.66}$$

$$\dot{s} = \left\{h_0\left|1-\frac{s}{s^*}\right|^a \mathrm{sign}\left(1-\frac{s}{s^*}\right)\right\}\dot{\epsilon}^p, \tag{3.67}$$

$$s^* = \widetilde{s}\left[\frac{\dot{\epsilon}^p}{A}\exp\left(\frac{Q}{R\,\Theta_m}\right)\right]^n, \tag{3.68}$$

in $\Omega\times(0,T]$, where $\check{\mu}_M : \mathbb{R} \longrightarrow \mathbb{R}$ and $\check{\lambda}_M : \mathbb{R} \longrightarrow \mathbb{R}$ are functions of temperature, and subject to the boundary conditions

$$\mathbf{u}(\mathsf{p},t) = \mathbf{u}^{\rm DM}(\mathsf{p},t) \quad \text{on } \Gamma_{\rm DM}\times(0,T], \tag{3.69}$$

$$\mathbf{K}(\mathsf{p},t)\,\mathbf{F}^{-t}(\mathsf{p},t)\,\mathbf{n}_{\mathsf{p}}(\mathsf{p}) = \det(\mathbf{F}(\mathsf{p},t))\,|\mathbf{F}^{-t}(\mathsf{p},t)\,\mathbf{n}_{\mathsf{p}}(\mathsf{p})|\,\mathbf{h}_m(\mathsf{p},t) \quad \text{on } \Gamma_{\rm NM}\times(0,T], \tag{3.70}$$

$$\mathbf{K}(\mathsf{p},t)\,\mathbf{F}^{-t}(\mathsf{p},t)\,\mathbf{n}_{\mathsf{p}}(\mathsf{p}) = -\zeta_m(\mathsf{p},t)\det(\mathbf{F}(\mathsf{p},t))\,\mathbf{F}^{-t}(\mathsf{p},t)\,\mathbf{n}_{\mathsf{p}}(\mathsf{p}) \quad \text{on } \Gamma_{\rm CM}\times(0,T], \tag{3.71}$$

$$\zeta_m(\mathsf{p},t) \geq 0 \quad \text{on } \Gamma_{\rm CM}\times(0,T], \tag{3.72}$$

$$M(\mathsf{X}(\mathsf{p},t)) \geq 0 \quad \text{on } \Gamma_{\rm CM}\times(0,T], \tag{3.73}$$

$$\zeta_m(\mathsf{p},t)\,M(\mathsf{X}(\mathsf{p},t)) = 0 \quad \text{on } \Gamma_{\rm CM}\times(0,T], \tag{3.74}$$

and the initial conditions

$$\mathbf{u}(\mathsf{p},0) = \mathbf{u}^0(\mathsf{p}) \quad \text{in } \overline{\Omega}, \tag{3.75}$$

$$\dot{\mathbf{u}}(\mathsf{p},0) = \mathbf{v}^0_m(\mathsf{p}) \quad \text{in } \overline{\Omega}, \tag{3.76}$$

$$s(\mathsf{p},0) = s^0(\mathsf{p}) \quad \text{in } \overline{\Omega}, \tag{3.77}$$

$$\mathbf{F}^p(\mathsf{p},0) = \mathbf{I} \quad \text{in } \overline{\Omega}, \tag{3.78}$$

where $\mathbf{u}^0 : \overline{\Omega} \longrightarrow \mathbb{R}^3$, $\mathbf{v}_m^0 : \overline{\Omega} \longrightarrow \mathbb{R}^3$ and $s^0 : \overline{\Omega} \longrightarrow \mathbb{R}$ are the known initial fields.

To derive the weak formulation of the mechanical model and facilitate its subsequent implementation, it is useful to reduce the set of conditions (3.72)-(3.74) to a single equation. This can be achieved by leveraging the properties of *Nonlinear Complementarity Problem* (NCP) functions, which are functions ϕ_{NCP} that satisfy the following condition:

$$\phi_{NCP}(a,b) = 0 \iff a \geq 0,\ b \geq 0,\ a \cdot b = 0. \tag{3.79}$$

Well-known examples of NCP functions are

$$\phi_{min}(a,b) = \min(a,b), \tag{3.80}$$

$$\phi_{FB}(a,b) = \sqrt{a^2+b^2} - (a+b), \tag{3.81}$$

$$\phi_{BM}^{\delta}(a,b) = a - (a-\delta b)^+, \tag{3.82}$$

where δ is an adjustable parameter and x^+ denotes the positive part of x. Further examples and remarkable mathematical properties of NCP functions can be found in [40].

Therefore, conditions (3.72)-(3.74) can be simply rewritten as

$$\phi_{NCP}\left(\zeta_m(\mathsf{p},t), M\left(\mathsf{X}(\mathsf{p},t)\right)\right) = 0 \quad \text{on } \Gamma_{\text{CM}} \times (0,T]. \tag{3.83}$$

The weak formulation of the above problem **(LMP)** is derived from formal computations assuming appropriate regularity of the involved fields. For that purpose, we multiply (3.61) by a suitable test function $\mathbf{z}$, integrate in Ω, and apply the standard Green's formula along with the boundary conditions (3.70) and (3.71). Similarly, let us multiply (3.64), (3.67) and the complementarity condition (3.83) by adequate test functions $\mathbf{Q}$, w, and μ, respectively, and integrate them in Ω. As a result, we obtain the following weak formulation for **(LMP)**:

Lagrangian weak mechanical problem. *Given the initial conditions* (3.75)-(3.78), *find a vector field* $\mathbf{u} : \overline{\Omega} \times [0,T] \longrightarrow \mathbb{R}^3$ *verifying* (3.69), *a tensor field* $\mathbf{F}^p : \overline{\Omega} \times [0,T] \longrightarrow Lin$, *a scalar field* $s : \overline{\Omega} \times [0,T] \longrightarrow \mathbb{R}$, *and a scalar field* $\zeta_m : \Gamma_{\text{CM}} \times [0,T] \longrightarrow \mathbb{R}$, *satisfying*

$$\begin{aligned}
&\int_\Omega \rho_0\, \ddot{\mathbf{u}} \cdot \mathbf{z}\, \mathrm{d}V_{\mathsf{p}} + \int_\Omega \left(\mathbf{K}\,\mathbf{F}^{-t}\right) : \mathbf{Grad}\,\mathbf{z}\, \mathrm{d}V_{\mathsf{p}} + \int_{\Gamma_{\text{CM}}} \zeta_m \det\mathbf{F}\left(\mathbf{F}^{-t}\mathbf{n}_{\mathsf{p}}\right)\cdot \mathbf{z}\, \mathrm{d}A_{\mathsf{p}} \\
&= \int_{\Gamma_{\text{NM}}} \det\mathbf{F}\,|\mathbf{F}^{-t}\mathbf{n}_{\mathsf{p}}|\,\mathbf{h}_m \cdot \mathbf{z}\, \mathrm{d}A_{\mathsf{p}} + \int_\Omega \det\mathbf{F}\,\mathbf{b}_m \cdot \mathbf{z}\, \mathrm{d}V_{\mathsf{p}}, \quad \forall \mathbf{z} \text{ with } \mathbf{z}|_{\Gamma_{\text{DM}}} = \mathbf{0}, \\
&\int_{\Gamma_{\text{CM}}} \phi_{NCP}\left(\zeta_m, M\left(\mathsf{X}(\mathsf{p},t)\right)\right)\mu\, \mathrm{d}A_{\mathsf{p}} = 0, \quad \forall \mu, \\
&\int_\Omega \dot{\mathbf{F}}^p \left(\mathbf{F}^p\right)^{-1} : \mathbf{Q}\, \mathrm{d}V_{\mathsf{p}} = \int_\Omega \mathbf{R}^{e,t}\left(\frac{3}{2}\frac{\mathbf{K}^d}{q\left(\mathbf{K}^d\right)}\dot{\epsilon}^p\right)\mathbf{R}^e : \mathbf{Q}\, \mathrm{d}V_{\mathsf{p}}, \quad \forall \mathbf{Q}, \\
&\int_\Omega \dot{s}\, w\, \mathrm{d}V_{\mathsf{p}} = \int_\Omega \left\{h_0 \left|1 - \frac{s}{s^*}\right|^a \operatorname{sign}\left(1 - \frac{s}{s^*}\right)\right\}\dot{\epsilon}^p\, w\, \mathrm{d}V_{\mathsf{p}}, \quad \forall w,
\end{aligned}$$

where $\mathbf{K}$ is related to the unknowns of the problem through (3.62) and (3.63), $\mathbf{R}^e$ through (3.65) and s^* and $\dot{\epsilon}^p$ via (3.66) and (3.68), respectively.

Remark 3.1. *The mechanical problem considered so far includes the possibility of prescribing a known surface traction vector as a Neumann boundary condition. However, in many practical applications, the total force applied over the boundary is known instead of the surface traction vector. This is the case in some of the numerical examples presented in this thesis. Under this assumption, a spatially uniform resultant force,* $\mathbf{P}(t)$*, is prescribed along time on the boundary* $\Gamma_{\mathrm{NM}}(t)$ *while the surface traction vector,* $\mathbf{h}(\mathsf{x}, t)$*, becomes an additional unknown to be determined. Based on these assumptions, we now outline the necessary modifications to the formulation of the mechanical model.*

The total resulting force applied on $\Gamma_{\mathrm{NM}}(t)$*,* $\mathbf{P}(t)$*, is given by*

$$\mathbf{P}(t) = \int_{\Gamma_{\mathrm{NM}}(t)} \mathbf{h}(\mathsf{x}, t)\, \mathrm{d}A_{\mathsf{x}},$$

where $\mathbf{h}(\mathsf{x}, t)$ *is the (unknown) surface traction vector distribution over the Neumann boundary at time* t*. If* $\mathbf{h}(\mathsf{x}, t)$ *corresponds to a surface traction vector with spatially uniform magnitude, it can be written as*

$$\mathbf{h}(\mathsf{x}, t) = h(t)\, \mathbf{m}(\mathsf{x}, t),$$

where $h(t)$ *is a scalar function representing the magnitude at time* t*, and* $\mathbf{m}(\mathsf{x}, t)$ *denotes a unit vector at point* x *on the boundary* $\Gamma_{\mathrm{NM}}(t)$*.*

In some cases, the direction of the applied force remains fixed in the spatial frame, regardless of the deformation experienced by the body. In other words, the force direction is not updated to follow the evolving configuration of the body. This defines what is known as a non-follower force. Under this assumption, the vector field $\mathbf{m}(\mathsf{x}, t)$ *is replaced by a constant unit vector* $\mathbf{m}^0$*, prescribed uniformly in both space and time, i.e.,* $\forall \mathsf{x} \in \Gamma_{\mathrm{NM}}(t),\ \forall t \in [0, T]$*. Accordingly, the resultant force becomes*

$$\mathbf{P}(t) = h(t)\, \mathbf{m}^0 \int_{\Gamma_{\mathrm{NM}}(t)} \mathrm{d}A_{\mathsf{x}} = h(t)\, \mathbf{m}^0\, \mathrm{area}(\Gamma_{\mathrm{NM}}(t)).$$

If the area of the Neumann boundary is computed in the Lagrangian configuration,

$$\mathbf{P}(t) = h(t)\, \mathbf{m}^0 \int_{\Gamma_{\mathrm{NM}}} \det \mathbf{F}(\mathsf{p}, t)\, |\mathbf{F}^{-t}(\mathsf{p}, t)\, \mathbf{n}_{\mathsf{p}}(\mathsf{p})|\, \mathrm{d}A_{\mathsf{p}},$$

where $\mathbf{n}_{\mathsf{p}}$ *denotes the unit normal vector in the Lagrangian configuration.*

It is important to note that the known quantity is now the resultant force $\mathbf{P}(t)$*, while the scalar traction magnitude* $h(t)$ *must be determined from the relation above. Taking the scalar product of this equation with a constant vector* $\mathbf{w} \in \mathbb{R}^3$ *yields*

$$\mathbf{P}(t) \cdot \mathbf{w} = \int_{\Gamma_{\mathrm{NM}}} \det \mathbf{F}(\mathsf{p}, t)\, |\mathbf{F}^{-t}(\mathsf{p}, t)\, \mathbf{n}_{\mathsf{p}}(\mathsf{p})|\, h(t)\, \mathbf{m}^0 \cdot \mathbf{w}\, \mathrm{d}A_{\mathsf{p}}, \quad \forall \mathbf{w} \in \mathbb{R}^3.$$

For $\mathbf{w} = \mathbf{m}^0$*, we can obtain* $h(t)$ *from* $\mathbf{P}(t)$*:*

$$h(t) = \frac{\mathbf{P}(t) \cdot \mathbf{m}^0}{\int_{\Gamma_{\mathrm{NM}}} \det \mathbf{F}(\mathsf{p}, t)\, |\mathbf{F}^{-t}(\mathsf{p}, t)\, \mathbf{n}_{\mathsf{p}}(\mathsf{p})|\, \mathrm{d}A_{\mathsf{p}}}.$$

As a consequence, the Lagrangian weak formulation of the mechanical problem introduced in Section 3.1.4 becomes

Lagrangian weak mechanical problem with resultant force as data. *Given the initial conditions (3.75)-(3.78), find a vector field* $\mathbf{u} : \overline{\Omega} \times [0,T] \longrightarrow \mathbb{R}^3$ *verifying (3.69), a tensor field* $\mathbf{F}^p : \overline{\Omega} \times [0,T] \longrightarrow Lin$, *a scalar field* $s : \overline{\Omega} \times [0,T] \longrightarrow \mathbb{R}$, *and a scalar field* $\zeta_m : \Gamma_{\mathrm{CM}} \times [0,T] \longrightarrow \mathbb{R}$, *satisfying*

$$\begin{aligned}
\int_\Omega \rho_0\, \ddot{\mathbf{u}} \cdot \mathbf{z}\, \mathrm{d}V_{\mathsf{p}} + \int_\Omega \left(\mathbf{K}\, \mathbf{F}^{-t}\right) : \mathbf{Grad}\, \mathbf{z}\, \mathrm{d}V_{\mathsf{p}} + \int_{\Gamma_{\mathrm{CM}}} \zeta_m \det \mathbf{F}\, \left(\mathbf{F}^{-t}\mathbf{n}_{\mathsf{p}}\right) \cdot \mathbf{z}\, \mathrm{d}A_{\mathsf{p}} \\
- \frac{\mathbf{P}\cdot\mathbf{m}^0}{\int_{\Gamma_{\mathrm{NM}}} \det \mathbf{F}\, |\mathbf{F}^{-t}\, \mathbf{n}_{\mathsf{p}}|\, \mathrm{d}A_{\mathsf{p}}} \int_{\Gamma_{\mathrm{NM}}} \det \mathbf{F}\, |\mathbf{F}^{-t}\mathbf{n}_{\mathsf{p}}|\, \mathbf{m}^0 \cdot \mathbf{z}\, \mathrm{d}A_{\mathsf{p}} \\
= \int_\Omega \det \mathbf{F}\, \mathbf{b}_m \cdot \mathbf{z}\, \mathrm{d}V_{\mathsf{p}}, \quad \forall \mathbf{z} \text{ with } \mathbf{z}|_{\Gamma_{\mathrm{DM}}} = \mathbf{0}, \\
\int_{\Gamma_{\mathrm{CM}}} \phi_{NCP}\left(\zeta_m, M\left(\mathsf{X}(\mathsf{p},t)\right)\right) \mu\, \mathrm{d}A_{\mathsf{p}} = 0, \quad \forall \mu, \\
\int_\Omega \dot{\mathbf{F}}^p \left(\mathbf{F}^p\right)^{-1} : \mathbf{Q}\, \mathrm{d}V_{\mathsf{p}} = \int_\Omega \mathbf{R}^{e,t} \left(\frac{3}{2}\frac{\mathbf{K}^d}{q\left(\mathbf{K}^d\right)}\dot{\epsilon}^p\right) \mathbf{R}^e : \mathbf{Q}\, \mathrm{d}V_{\mathsf{p}}, \quad \forall \mathbf{Q}, \\
\int_\Omega \dot{s}\, w\, \mathrm{d}V_{\mathsf{p}} = \int_\Omega \left\{h_0 \left|1 - \frac{s}{s^*}\right|^a sign\left(1 - \frac{s}{s^*}\right)\right\} \dot{\epsilon}^p\, w\, \mathrm{d}V_{\mathsf{p}}, \quad \forall w,
\end{aligned}$$

where $\mathbf{K}$ *is related to the unknowns of the problem through (3.62) and (3.63),* $\mathbf{R}^e$ *through (3.65) and* s^* *and* $\dot{\epsilon}^p$ *via (3.66) and (3.68), respectively.*

3.2 Electrical model

The computational domain evolves based on the deformations calculated from the mechanical model introduced earlier, which, in turn, influences both the thermal and electrical models. In this section, we assume that the electrical source driving the electric upsetting process is a direct current (DC), i.e., time-independent. Accordingly, we introduce a suitable model to describe the resulting electrical phenomena.

3.2.1 Direct current model

The direct current model will be obtained from Maxwell's equations, which describe the propagation of electromagnetic fields. These equations can be summarised as follows:

$$\mathrm{div}\, \mathbf{D}(\mathsf{x},t) = \rho_{\mathrm{V}}(\mathsf{x},t), \quad \text{(Gauss' law for electric field)} \tag{3.84}$$

$$\mathrm{div}\, \mathbf{B}(\mathsf{x},t) = 0, \quad \text{(Gauss' law for magnetic field)} \tag{3.85}$$

$$\frac{\partial \mathbf{D}(\mathsf{x},t)}{\partial t} - \mathbf{curl}\, \mathbf{H}(\mathsf{x},t) = -\mathbf{J}(\mathsf{x},t), \quad \text{(Ampère's law)} \tag{3.86}$$

$$\frac{\partial \mathbf{B}(\mathsf{x},t)}{\partial t} + \mathbf{curl}\, \mathbf{E}(\mathsf{x},t) = \mathbf{0}, \quad \text{(Faraday's law)} \tag{3.87}$$

where it should be noted that all the fields are, in general, space and time dependent. In the preceding equations, $\mathbf{D}$ denotes the electric displacement field, $\mathbf{B}$ the magnetic induction field, $\mathbf{H}$ the magnetic field and $\mathbf{E}$ the electric field. Furthermore, ρ_{V} represents the electric charge density, and $\mathbf{J}$ represents the current density.

This system is complemented by the following constitutive laws, which incorporate the material properties of the medium:

$$\mathbf{D}(\mathsf{x},t) = \varepsilon(\mathsf{x},t)\mathbf{E}(\mathsf{x},t), \tag{3.88}$$

$$\mathbf{B}(\mathsf{x},t) = \mu(\mathsf{x},t)\mathbf{H}(\mathsf{x},t), \tag{3.89}$$

$$\mathbf{J}(\mathsf{x},t) = \sigma(\mathsf{x},t)\mathbf{E}(\mathsf{x},t), \quad \text{(Ohm's law)} \tag{3.90}$$

where, under the assumption of isotropic media, the electric permittivity ε, magnetic permeability μ, and electrical conductivity σ are scalar fields. These constitutive laws are generally nonlinear and may depend on additional variables, such as temperature, or in the case of μ, on the magnitude of the magnetic field.

In the specific case of direct current (DC) sources, the fields become time-independent, and Maxwell's equations decouple into separate equations for the electric and magnetic fields:

$$\operatorname{div}\mathbf{D}(\mathsf{x}) = \rho_{\mathrm{V}}(\mathsf{x}), \tag{3.91}$$

$$\operatorname{div}\mathbf{B}(\mathsf{x}) = 0, \tag{3.92}$$

$$\mathbf{curl}\,\mathbf{H}(\mathsf{x}) = \mathbf{J}(\mathsf{x}), \tag{3.93}$$

$$\mathbf{curl}\,\mathbf{E}(\mathsf{x}) = \mathbf{0}, \tag{3.94}$$

supplemented by the the constitutive laws (3.88)-(3.90).

In this context, since the electric and magnetic fields can be computed independently, the current density $\mathbf{J}$ can be determined from a simplified model. This is particularly useful, as the current distribution serves as the primary source of heating through the Joule effect. Therefore, a key objective of the classical DC model is to compute $\mathbf{J}$ within the conducting regions in order to provide the heat source term for the thermal model. Applying the divergence operator to Ampère's law and using Ohm's law yields:

$$\operatorname{div}\left(\sigma(\mathsf{x})\,\mathbf{E}(\mathsf{x})\right) = 0, \tag{3.95}$$

which is valid only within the conducting regions, such as the metal bar in our computational domain.

In addition, Faraday's law implies the existence of an electric potential, $\mathrm{V}(\mathsf{x})$, such that

$$\mathbf{E}(\mathsf{x}) = -\operatorname{grad}\mathrm{V}(\mathsf{x}). \tag{3.96}$$

Finally, by replacing (3.96) in (3.95), we get

$$-\operatorname{div}\left(\sigma(\mathsf{x})\operatorname{grad}\mathrm{V}(\mathsf{x})\right) = 0. \tag{3.97}$$

This constitutes the classical DC current model, which is completed by imposing appropriate boundary conditions on the conducting domain to account for the electrical sources. However,

in electric upsetting processes, the domain evolves over time, in contrast to the classical steady-state DC model where the geometry is fixed. Therefore, from this point onward, we will consider time-dependent fields to account for the coupling with mechanical deformation. Specifically, we adopt a three-dimensional Eulerian description of the electrical domain, denoted by $\Omega(t)$, and introduce the following equation governing the time-dependent electric scalar potential $\mathrm{V}(\mathsf{x}, t)$:

$$-\operatorname{div}\left(\check{\sigma}(\Theta(\mathsf{x}, t))\operatorname{grad}\mathrm{V}(\mathsf{x}, t)\right) = 0 \quad \text{in } \Omega(t) \times [0, T], \tag{3.98}$$

where $\check{\sigma} : \mathbb{R} \longrightarrow \mathbb{R}$ is the electrical conductivity as a function of temperature, $\Theta : \overline{\Omega}(t) \times [0, T] \longrightarrow \mathbb{R}$, which is computed by solving the thermal model introduced below in Section 3.3.

The boundary of $\Omega(t)$ is decomposed into two disjoint parts: a Dirichlet part, $\Gamma_{\mathrm{DE}}(t)$, where the potential is imposed, and a Neumann boundary, $\Gamma_{\mathrm{NE}}(t)$, where the normal component of the current density is imposed. More precisely, $\partial\Omega(t) = \Gamma_{\mathrm{DE}}(t) \cup \Gamma_{\mathrm{NE}}(t)$ (see Figure 3.4) and we consider

$$\mathrm{V}(\mathsf{x}, t) = \mathrm{V}^{\mathrm{DE}}(\mathsf{x}, t) \quad \text{on } \Gamma_{\mathrm{DE}}(t) \times (0, T], \tag{3.99}$$

where $\mathrm{V}^{\mathrm{DE}}(\cdot, t) : \Gamma_{\mathrm{DE}}(t) \longrightarrow \mathbb{R}$ is the known electric potential, and

$$-\check{\sigma}(\Theta(\mathsf{x}, t)\operatorname{grad}\mathrm{V}(\mathsf{x}, t) \cdot \mathbf{n}_{\mathsf{x}}(\mathsf{x}, t) = \mathbf{J}(\mathsf{x}, t) \cdot \mathbf{n}_{\mathsf{x}}(\mathsf{x}, t) = g(\mathsf{x}, t) \quad \text{on } \Gamma_{\mathrm{NE}}(t) \times (0, T]. \tag{3.100}$$

Here, g denotes a prescribed Neumann-type boundary data on $\Gamma_{\mathrm{NE}}(t)$, which is zero everywhere except on the portion of the boundary in contact with the gripper jaws, through which the electric current is applied. In practice, when g is provided as part of the industrial process specifications, it is typically approximated as the total applied current divided by the area of the input section. Additionally, it is important to ensure that a Dirichlet boundary condition is imposed on a portion of the boundary to guarantee the uniqueness of the electric potential solution.

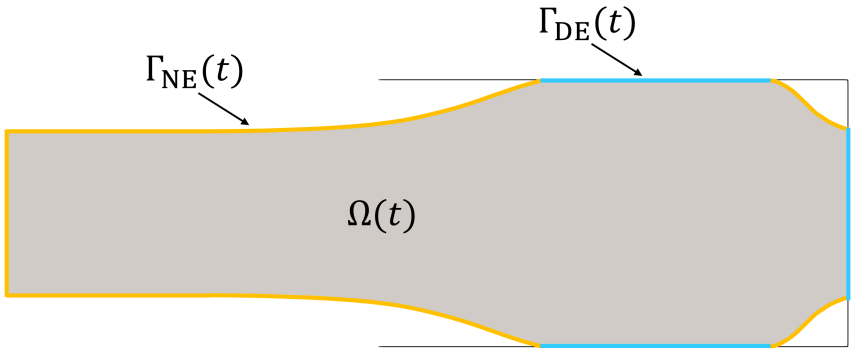

Figure 3.4: Boundaries of the electrical domain.

Hence, the strong 3D Eulerian formulation of the electrical model is established:

Eulerian electrical problem (EEP). *Find an electric potential* $\mathrm{V} : \overline{\Omega}(t) \times [0,T] \longrightarrow \mathbb{R}$ *satisfying*

$$-\operatorname{div}\left(\check{\sigma}(\Theta)\operatorname{grad}\mathrm{V}(\mathsf{x},t)\right) = 0 \quad \text{in } \Omega(t)\times[0,T], \tag{3.101}$$

$$\mathrm{V}(\mathsf{x},t) = \mathrm{V}^{\mathrm{DE}}(\mathsf{x},t) \quad \text{on } \Gamma_{\mathrm{DE}}(t)\times[0,T], \tag{3.102}$$

$$-\check{\sigma}(\Theta)\operatorname{grad}\mathrm{V}(\mathsf{x},t)\cdot\mathbf{n}_{\mathsf{x}}(\mathsf{x},t) = g(\mathsf{x},t) \quad \text{on } \Gamma_{\mathrm{NE}}(t)\times[0,T]. \tag{3.103}$$

3.2.2 Lagrangian formulation

To express the Eulerian electrical model in Lagrangian coordinates, we apply identity (2.8), with the choice $\mathrm{A}(\mathsf{x},t) = \check{\sigma}(\Theta(\mathsf{x},t))$ and $\phi(\mathsf{x},t) = \mathrm{V}(\mathsf{x},t)$. Additionally, identities (2.6) and (2.17) are employed to transform the Neumann boundary condition. As a result, the Lagrangian formulation of the electrical problem is stated as follows:

Lagrangian electrical problem (LEP). *Find an electric potential* $\mathrm{V}_m : \overline{\Omega}\times[0,T] \longrightarrow \mathbb{R}$ *satisfying*

$$\operatorname{Div}\left(\det\mathbf{F}(\mathsf{p},t)\,\mathbf{F}^{-1}(\mathsf{p},t)\,\check{\sigma}(\Theta_m)\,\mathbf{F}^{-t}(\mathsf{p},t)\operatorname{Grad}\mathrm{V}_m(\mathsf{p},t)\right) = 0 \quad \text{in } \Omega\times[0,T], \tag{3.104}$$

$$\mathrm{V}_m(\mathsf{p},t) = \mathrm{V}_m^{\mathrm{DE}}(\mathsf{p},t) \quad \text{on } \Gamma_{\mathrm{DE}}\times[0,T], \tag{3.105}$$

$$-\check{\sigma}(\Theta_m)\mathbf{F}^{-t}(\mathsf{p},t)\operatorname{Grad}\mathrm{V}_m(\mathsf{p},t)\cdot\frac{\mathbf{F}^{-t}(\mathsf{p},t)\,\mathbf{n}_{\mathsf{p}}(\mathsf{p})}{|\mathbf{F}^{-t}(\mathsf{p},t)\,\mathbf{n}_{\mathsf{p}}(\mathsf{p})|} = g_m(\mathsf{p},t) \quad \text{on } \Gamma_{\mathrm{NE}}\times[0,T]. \tag{3.106}$$

By multiplying equation (3.104) by a suitable test function and applying a Green's formula, the Lagrangian weak formulation of the electrical problem is obtained:

Lagrangian weak electrical problem. *Find an electric potential* $\mathrm{V}_m : \overline{\Omega}\times[0,T] \longrightarrow \mathbb{R}$, *with* $\mathrm{V}_m = \mathrm{V}_m^{\mathrm{DE}}$ *on* $\Gamma_{\mathrm{DE}}\times[0,T]$, *satisfying*

$$\int_\Omega \check{\sigma}(\Theta_m)\,\mathbf{F}^{-t}\operatorname{Grad}\mathrm{V}_m\cdot\mathbf{F}^{-t}\operatorname{Grad}\mathrm{W}\det\mathbf{F}\,\mathrm{d}V_{\mathsf{p}} = -\int_{\Gamma_{\mathrm{NE}}}|\mathbf{F}^{-\mathrm{t}}\,\mathbf{n}_{\mathsf{p}}|\,g_m\mathrm{W}\det\mathbf{F}\,\mathrm{d}A_{\mathsf{p}},\ \forall\mathrm{W}\text{ with }\mathrm{W}|_{\Gamma_{\mathrm{DE}}}=0.$$

Remark 3.2. *The boundary conditions considered so far for the electrical model allow us to impose the electric potential or the normal component of the current density on a portion of the boundary. However, from an industrial perspective, the total power supplied to the electrical system is often the quantity that is known or controlled. In order to derive a formulation of the electrical problem in terms of the total power, we will assume that the current enters and leaves the domain perpendicularly to the electrical ports. For the sake of simplicity, let us assume that the current enters the domain through* $\Gamma_1(t)$ *(the gripper jaws) and leaves it perpendicularly to* $\Gamma_0(t)$ *(the anvil). Elsewhere on the boundary, the electrical current is tangential. These conditions can be written as*

$$\mathbf{J}(\mathsf{x},t)\times\mathbf{n}(\mathsf{x},t) = -\check{\sigma}(\Theta)\operatorname{grad}\mathrm{V}(\mathsf{x},t)\times\mathbf{n}(\mathsf{x},t) = \mathbf{0} \quad \text{on } \Gamma_0(t)\cup\Gamma_1(t)\times[0,T], \tag{3.107}$$

$$\mathbf{J}(\mathsf{x},t)\cdot\mathbf{n}(\mathsf{x},t) = -\check{\sigma}(\Theta)\operatorname{grad}\mathrm{V}(\mathsf{x},t)\cdot\mathbf{n}(\mathsf{x},t) = 0 \quad \text{on } \partial\Omega(t)\setminus(\Gamma_0(t)\cup\Gamma_1(t))\times[0,T]. \tag{3.108}$$

From condition (3.107)*, since boundaries* $\Gamma_0(t)$ *and* $\Gamma_1(t)$ *are assumed to be connected, we deduce that*

$$\mathrm{V}(\mathsf{x},t) = \mathrm{V}_i(t) \quad \text{on } \Gamma_i(t)\times[0,T],\ i=0,1, \tag{3.109}$$

where $V_i(t)$, $i=0,1$, *only depend on time. To ensure the uniqueness of the solution, we choose* $V_0(t)=0$ *and impose a Dirichlet condition on* $\Gamma_0(t)$.

On the other hand, let us consider the input net current intensity, $I_1(t)$*, through* $\Gamma_1(t)$*, which is defined by*

$$I_1(t) = \int_{\Gamma_1(t)} \check{\sigma}(\Theta)\,\mathrm{grad}\,\mathrm{V}(\mathsf{x},t)\cdot\mathbf{n}_{\mathsf{x}}(\mathsf{x},t)\,\mathrm{d}A_{\mathsf{x}}. \tag{3.110}$$

Notice that $V_1(t)$ *is spatially constant on* $\Gamma_1(t)$*, but its value is unknown. To determine* $I_1(t)$ *and* $V_1(t)$ *on this boundary, we will assume that the total supplied power is given. More precisely, in a three-dimensional Eulerian configuration, the total power,* $P_{DC}(t)$*, supplied to a DC system is given by*

$$P_{DC}(t) = \int_{\Omega(t)} \mathbf{J}(\mathsf{x},t)\cdot\mathbf{E}(\mathsf{x},t)\,\mathrm{d}V_{\mathsf{x}} = \int_{\Omega(t)} \check{\sigma}(\Theta)\,\mathrm{grad}\,\mathrm{V}(\mathsf{x},t)\cdot\mathrm{grad}\,\mathrm{V}(\mathsf{x},t)\,\mathrm{d}V_{\mathsf{x}}, \tag{3.111}$$

where relations (3.90) *and* (3.96) *were considered. By using a Green's formula,*

$$P_{DC}(t) = -\int_{\Omega(t)} \mathrm{div}(\check{\sigma}(\Theta)\,\mathrm{grad}\,\mathrm{V}(\mathsf{x},t))\,\mathrm{V}(\mathsf{x},t)\,\mathrm{d}V_{\mathsf{x}} + \int_{\partial\Omega(t)} \check{\sigma}(\Theta)\,\mathrm{grad}\,\mathrm{V}(\mathsf{x},t)\cdot\mathbf{n}_{\mathsf{x}}(\mathsf{x},t)\mathrm{V}(\mathsf{x},t)\,\mathrm{d}A_{\mathsf{x}}. \tag{3.112}$$

In (3.112)*, the volume integral is null due to* (3.97) *and the surface integral is only non-null on* $\Gamma_1(t)$ *because of* (3.108) *and* (3.109) *with* $\mathrm{V}|_{\Gamma_0(t)}=0$*. Therefore, since* $\mathrm{V}|_{\Gamma_1(t)}=V_1(t)$ *is spatially constant, we have*

$$P_{DC}(t) = V_1(t)I_1(t). \tag{3.113}$$

If we consider a slightly modified version of the Lagrangian weak formulation in Section 3.2.2 with $I_1(t)$ *as a new unknown, include* (3.113) *by multiplying it by a constant test function* (β)*, and ensure that condition* (3.107) *is fulfilled on* $\Gamma_1(t)$*, we finally get the Lagrangian weak formulation with the total supplied power as data.*

Lagrangian weak electrical problem with power as data. *Given the total active power supplied to the system,* $P_{DC}:\Gamma_1\times[0,T]\longrightarrow\mathbb{R}$*, find an electric potential* $\mathrm{V}_m:\overline{\Omega}\times[0,T]\longrightarrow\mathbb{R}$*, with* $\mathrm{V}_m=0$ *on* $\Gamma_0\times[0,T]$ *and* $\mathrm{V}_m=const.$ *on* $\Gamma_1\times[0,T]$*, and* $I_1:\Gamma_1\times[0,T]\longrightarrow\mathbb{R}$ *satisfying*

$$\int_{\Omega} \check{\sigma}(\Theta_m)\,\mathbf{F}^{-t}\,\mathrm{Grad}\,\mathrm{V}_m\cdot\mathbf{F}^{-t}\,\mathrm{Grad}\,\mathrm{W}\,\det\mathbf{F}\,\mathrm{d}V_{\mathsf{p}} - I_1\,\mathrm{W}|_{\Gamma_1}=0,\ \forall \mathrm{W}\text{ with }\mathrm{W}|_{\Gamma_0}=0,\ \mathrm{W}|_{\Gamma_1}=\text{const.},$$

$$I_1\,\mathrm{V}_m|_{\Gamma_1}\,\beta = P_{DC}\,\beta,\ \forall\beta.$$

Note that the time dependence of the power data has been retained, as it may vary throughout the process. In many practical cases, it is intended to represent a piecewise constant function of time.

3.3 Thermal model

The electric current flowing through the conductive metal bar leads to power dissipation due to the Joule effect, which is a heat source in the thermal model. Based on the electrical model described earlier, the current density within the conducting region can be determined to evaluate the corresponding heat source in the thermal analysis.

In this section, we present the thermal model used to compute the temperature distribution in the workpiece. To this end, we follow an approach analogous to that of the electrical model, beginning with the Eulerian form of the energy conservation equation and ultimately deriving a formulation expressed in the reference (Lagrangian) configuration.

3.3.1 Transient heat transfer model

Let us consider a thermal domain $\Omega(t)$ with boundary $\Gamma(t)$ which is decomposed into a part $\Gamma_{\mathrm{DT}}(t)$, where the temperature is known, and a part $\Gamma_{\mathrm{RT}}(t)$, where a convection-radiation boundary condition is imposed. Thus, $\partial\Omega(t) = \Gamma_{\mathrm{DT}}(t) \cup \Gamma_{\mathrm{RT}}(t)$; see Figure 3.5.

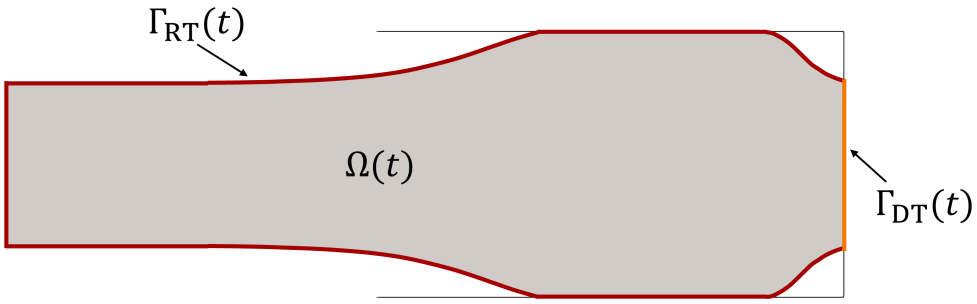

Figure 3.5: Boundaries of the thermal domain.

The evolution of the temperature, $\Theta(\mathsf{x}, t)$, is governed by the initial-boundary value problem derived from the principle of energy conservation in the domain $\Omega(t) \times (0, T]$:

$$\rho \check{c}_p(\Theta(\mathsf{x},t)) \left(\frac{\partial \Theta(\mathsf{x},t)}{\partial t} + \mathbf{v}(\mathsf{x},t) \cdot \operatorname{grad} \Theta(\mathsf{x},t) \right) - \operatorname{div}(\check{k}(\Theta(\mathsf{x},t)) \operatorname{grad} \Theta(\mathsf{x},t)) = P(\mathsf{x},t), \quad (3.114)$$

where $\check{c}_p : \mathbb{R} \longrightarrow \mathbb{R}$ and $\check{k} : \mathbb{R} \longrightarrow \mathbb{R}$ are functions of temperature and denote the specific heat and thermal conductivity, respectively; $\mathbf{v} : \overline{\Omega}(t) \times [0, T] \longrightarrow \mathbb{R}^3$ is the velocity field, computed from the mechanical model described in Section 3.1; $P : \overline{\Omega}(t) \times [0, T] \longrightarrow \mathbb{R}$ is the heat source associated to the Joule effect, computed from the electrical model in Section 3.2. In addition, we suppose that the temperature at initial time, $\Theta^0 : \overline{\Omega}(0) \longrightarrow \mathbb{R}$, is given.

The temperature field is assumed to be known on $\Gamma_{\mathrm{DT}}(t)$, so the associated Dirichlet boundary condition reads

$$\Theta(\mathsf{x}, t) = \Theta^{\mathrm{DT}}(\mathsf{x}, t) \quad \text{on } \Gamma_{\mathrm{DT}}(t) \times (0, T], \quad (3.115)$$

where $\Theta^{\mathrm{DT}}(\cdot, t) : \Gamma_{\mathrm{DT}}(t) \longrightarrow \mathbb{R}$ is the temperature on the Dirichlet boundary.

On the other hand, the convection-radiation boundary condition prescribed on $\Gamma_{\mathrm{RT}}(t)$ is

$$\begin{aligned}\check{k}(\Theta(\mathsf{x},t))\,\mathrm{grad}\,\Theta(\mathsf{x},t)\cdot\mathbf{n}_{\mathsf{x}}(\mathsf{x},t) = h(\mathsf{x},t)[\Theta^{\mathrm{C}}(\mathsf{x},t)-\Theta(\mathsf{x},t)]\\ +\sigma_{SB}\epsilon(\mathsf{x},t)[(\Theta^{\mathrm{R}}(\mathsf{x},t))^4-(\Theta(\mathsf{x},t))^4] \quad \text{on } \Gamma_{\mathrm{RT}}(t)\times(0,T],\end{aligned} \tag{3.116}$$

where $h(\cdot,t):\Gamma_{\mathrm{RT}}(t)\longrightarrow\mathbb{R}$ is the heat transfer coefficient; $\sigma_{SB}=5.67\times10^{-8}\,\mathrm{Wm^{-2}K^{-4}}$ is the Stefan-Boltzmann constant; $\epsilon(\cdot,t):\Gamma_{\mathrm{RT}}(t)\longrightarrow\mathbb{R}$ denotes the emissivity; $\Theta^{\mathrm{C}}(\cdot,t):\Gamma_{\mathrm{RT}}(t)\longrightarrow\mathbb{R}$ is the convection temperature and $\Theta^{\mathrm{R}}(\mathsf{x},t):\Gamma_{\mathrm{RT}}(t)\longrightarrow\mathbb{R}$ is the radiation temperature.

The thermal source term associated with the Joule effect, $P(\mathsf{x},t)$, is defined as

$$P(\mathsf{x},t)=\mathbf{J}(\mathsf{x},t)\cdot\mathbf{E}(\mathsf{x},t), \tag{3.117}$$

which, by applying equations (3.90) and (3.96), can be expressed in terms of the electric potential, V, as

$$P(\mathsf{x},t)=\check{\sigma}(\Theta)\,|\mathrm{grad}\mathrm{V}(\mathsf{x},t)|^2. \tag{3.118}$$

Therefore, the three-dimensional strong form of the thermal model is established in the Eulerian configuration as follows:

Eulerian thermal problem with DC sources (ETPDC). *Find a temperature field* $\Theta:\overline{\Omega}(t)\times[0,T]\longrightarrow\mathbb{R}$ *satisfying*

$$\begin{aligned}\rho(\mathsf{x},t)\,\check{c}_p(\Theta)\left(\frac{\partial\Theta(\mathsf{x},t)}{\partial t}+\mathbf{v}(\mathsf{x},t)\cdot\mathrm{grad}\,\Theta(\mathsf{x},t)\right)-\mathrm{div}(\check{k}(\Theta)\,\mathrm{grad}\,\Theta(\mathsf{x},t))\\ =\check{\sigma}(\Theta)\,|\mathrm{grad}\mathrm{V}(\mathsf{x},t)|^2 \quad \text{in } \Omega(t)\times(0,T],\end{aligned} \tag{3.119}$$

$$\Theta(\mathsf{x},t)=\Theta^{\mathrm{DT}}(\mathsf{x},t) \quad \text{on } \Gamma_{\mathrm{DT}}(t)\times(0,T], \tag{3.120}$$

$$\begin{aligned}\check{k}(\Theta)\,\mathrm{grad}\,\Theta(\mathsf{x},t)\cdot\mathbf{n}_{\mathsf{x}}(\mathsf{x},t)=\sigma_{SB}\,\epsilon(\mathsf{x},t)[(\Theta^{\mathrm{R}}(\mathsf{x},t))^4-(\Theta(\mathsf{x},t))^4]\\ +h(\mathsf{x},t)[\Theta^{\mathrm{C}}(\mathsf{x},t)-\Theta(\mathsf{x},t)] \quad \text{on } \Gamma_{\mathrm{RT}}(t)\times(0,T],\end{aligned} \tag{3.121}$$

$$\Theta(\mathsf{x},0)=\Theta^0(\mathsf{x}), \quad \text{in } \overline{\Omega}(0). \tag{3.122}$$

3.3.2 Lagrangian formulation

The previously derived Eulerian thermal model can be transformed into Lagrangian coordinates in a manner similar to that used for the electrical problem. This transformation involves the application of identity (2.8), particularised for $\mathrm{A}(\mathsf{x},t)=\check{k}(\Theta(\mathsf{x},t))$ and $\phi(\mathsf{x},t)=\Theta(\mathsf{x},t)$. The material time derivative is introduced via identity (2.11), also particularised for $\phi(\mathsf{x},t)=\Theta(\mathsf{x},t)$. Additionally, identities (2.6) and (2.17), together with the mass conservation principle (3.3), are required.

As a result, the three-dimensional strong form of the thermal problem is obtained in the Lagrangian configuration:

Lagrangian thermal problem with DC sources (LTPDC). *Find a temperature field* $\Theta_m : \overline{\Omega} \times [0,T] \longrightarrow \mathbb{R}$ *satisfying*

$$\rho_0(\mathsf{p})\,\check{c}_p(\Theta_m)\,\dot{\Theta}_m(\mathsf{p},t) - \mathrm{Div}\left(\det\mathbf{F}(\mathsf{p},t)\,\mathbf{F}^{-1}(\mathsf{p},t)\,\check{k}(\Theta_m)\,\mathbf{F}^{-t}(\mathsf{p},t)\,\mathrm{Grad}\,\Theta_m(\mathsf{p},t)\right)$$
$$= \det\mathbf{F}(\mathsf{p},t)\,\check{\sigma}(\Theta_m)\,\left|\mathbf{F}^{-t}(\mathsf{p},t)\,\mathrm{Grad}\mathrm{V}_m(\mathsf{p},t)\right|^2 \quad \text{in } \Omega\times(0,T], \tag{3.123}$$

$$\Theta_m(\mathsf{p},t) = \Theta_m^{\mathrm{DT}}(\mathsf{p},t) \quad \text{on } \Gamma_{\mathrm{DT}}\times(0,T], \tag{3.124}$$

$$\check{k}(\Theta_m)\,\mathbf{F}^{-t}(\mathsf{p},t)\,\mathrm{Grad}\,\Theta_m(\mathsf{p},t)\cdot\frac{\mathbf{F}^{-t}(\mathsf{p},t)\,\mathbf{n}_{\mathsf{p}}(\mathsf{p})}{|\mathbf{F}^{-t}(\mathsf{p},t)\,\mathbf{n}_{\mathsf{p}}(\mathsf{p})|} = \sigma_{SB}\,\epsilon_m(\mathsf{p},t)[(\Theta_m^{\mathrm{R}}(\mathsf{p},t))^4 - (\Theta_m(\mathsf{p},t))^4]$$
$$+h_m(\mathsf{p},t)(\Theta_m^{\mathrm{C}}(\mathsf{p},t) - \Theta_m(\mathsf{p},t)) \quad \text{on } \Gamma_{\mathrm{RT}}\times(0,T], \tag{3.125}$$

$$\Theta_m(\mathsf{p},0) = \Theta^0(\mathsf{p}) \quad \text{in } \overline{\Omega}. \tag{3.126}$$

The Lagrangian weak formulation of the previous problem can be obtained through standard techniques:

Lagrangian weak thermal problem with DC sources. *Find a temperature field* $\Theta_m : \overline{\Omega}\times[0,T]\longrightarrow\mathbb{R}$, *with* $\Theta_m = \Theta_m^{\mathrm{DT}}$ *on* $\Gamma_{\mathrm{DT}}\times(0,T]$ *and* $\Theta_m(\mathsf{p},0) = \Theta^0(\mathsf{p})$ *in* $\overline{\Omega}$ *such that*

$$\int_\Omega \rho_0\,\check{c}_p(\Theta_m)\,\dot{\Theta}_m\psi\,\mathrm{d}V_{\mathsf{p}} + \int_\Omega \check{k}(\Theta_m)\,\mathbf{F}^{-t}\,\mathrm{Grad}\,\Theta_m\cdot\mathbf{F}^{-t}\,\mathrm{Grad}\,\psi\,\det\mathbf{F}\,\mathrm{d}V_{\mathsf{p}}$$
$$-\int_{\Gamma_{\mathrm{RT}}}\left[h_m(\Theta_m^{\mathrm{C}}-\Theta_m) + \sigma_{SB}\epsilon_m\left((\Theta_m^{\mathrm{R}})^4 - \Theta_m^4\right)\right]|\mathbf{F}^{-\mathrm{t}}\mathbf{n}_{\mathsf{p}}|\psi\,\det\mathbf{F}\,\mathrm{d}A_{\mathsf{p}}$$
$$= \int_\Omega \det\mathbf{F}\,\check{\sigma}(\Theta_m)\,|\mathbf{F}^{-t}\,\mathrm{Grad}\,\mathrm{V}_m|^2\,\psi\,\mathrm{d}V_{\mathsf{p}}, \quad \forall\psi \text{ with } \psi|_{\Gamma_{\mathrm{DT}}} = 0.$$

3.4 Axisymmetric thermo-electrical-mechanical model

The electric upsetting problem exhibits axial symmetry with respect to the z-axis, which allows the three-dimensional weak formulation to be reduced to an axisymmetric case. In this setting, it is assumed that all fields are independent of the azimuthal variable θ, and the problem can be solved over a meridional section $\widehat{\Omega}$. The full three-dimensional domain Ω is then recovered by revolving $\widehat{\Omega}$ around the axis of symmetry.

As a consequence, the boundary of the axisymmetric domain, $\partial\widehat{\Omega}$, in the mechanical model splits as

$$\partial\widehat{\Omega} = \widehat{\Gamma}_{\mathrm{DM}}\cup\widehat{\Gamma}_{\mathrm{NM}}\cup\widehat{\Gamma}_{\mathrm{CM}}\cup\widehat{\Gamma}_{\mathrm{D}},$$

where $\widehat{\Gamma}_{\mathrm{D}}$ corresponds to the portion of the boundary lying on the symmetry axis, on which a symmetry condition, specifically, zero normal displacement, is imposed. Moreover, the fields involved in the mechanical model adopt the axisymmetric representations introduced in equations (2.24)–(2.28), and the notations and definitions from Section 2.2 are considered. Consequently, the axisymmetric Lagrangian formulation of the mechanical model is established:

Lagrangian weak mechanical problem with cylindrical symmetry. *Find a vector field* $\widehat{\mathbf{u}} : \overline{\widehat{\Omega}} \times [0,T] \longrightarrow \mathbb{R}^2$*, with zero normal component on* $\widehat{\Gamma}_{\mathrm{D}}$ *and verifying* (3.69)*, a tensor field* $\widehat{\mathbf{F}^p} : \overline{\widehat{\Omega}} \times [0,T] \longrightarrow Lin$*, and scalar fields* $\widehat{s} : \overline{\widehat{\Omega}} \times [0,T] \longrightarrow \mathbb{R}$ *and* $\widehat{\zeta}_m : \widehat{\Gamma}_{\mathrm{CM}} \times [0,T] \longrightarrow \mathbb{R}$ *satisfying*

$$\int_{\widehat{\Omega}} \rho_0 \, \ddot{\widehat{\mathbf{u}}} \cdot \widehat{\mathbf{z}} \, r_m \, \mathrm{d}r_m \mathrm{d}z_m + \int_{\widehat{\Omega}} \left(\widehat{\mathbf{K}} \, \widehat{\mathbf{F}}^{-t} \right) : \widehat{\mathbf{Grad}} \, \widehat{\mathbf{z}} \, r_m \, \mathrm{d}r_m \mathrm{d}z_m + \int_{\widehat{\Omega}} \frac{\widehat{K}_{\theta\theta} \widehat{z}_r}{r_m + \widehat{u}_r} \, r_m \, \mathrm{d}r_m \mathrm{d}z_m$$
$$+ \int_{\widehat{\Gamma}_{\mathrm{CM}}} \widehat{\zeta}_m \left(1 + \frac{\widehat{u}_r}{r_m} \right) \det \widehat{\mathbf{F}} \left(\widehat{\mathbf{F}}^{-t} \widehat{\mathbf{n}}_{\mathsf{p}} \right) \cdot \widehat{\mathbf{z}} \, r_m \, \mathrm{d}\widehat{l}_p = \int_{\widehat{\Gamma}_{\mathrm{NM}}} \left(1 + \frac{\widehat{u}_r}{r_m} \right) \det \widehat{\mathbf{F}} \left| \widehat{\mathbf{F}}^{-t} \widehat{\mathbf{n}}_{\mathsf{p}} \right| \widehat{\mathbf{h}}_m \cdot \widehat{\mathbf{z}} \, r_m \, \mathrm{d}\widehat{l}_p$$
$$+ \int_{\widehat{\Omega}} \left(1 + \frac{\widehat{u}_r}{r_m} \right) \det \widehat{\mathbf{F}} \, \widehat{\mathbf{b}}_m \cdot \widehat{\mathbf{z}} \, r_m \, \mathrm{d}r_m \mathrm{d}z_m, \quad \forall \widehat{\mathbf{z}} \text{ with zero normal component on } \widehat{\Gamma}_{\mathrm{D}} \text{ and } \widehat{\mathbf{z}}|_{\widehat{\Gamma}_{\mathrm{DM}}} = \mathbf{0},$$

$$\int_{\widehat{\Gamma}_{\mathrm{CM}}} \widehat{\phi}_{NCP} \left(\widehat{\zeta}_m, \widehat{M} \left(\widehat{\mathsf{X}}(\widehat{\mathsf{p}}, t) \right) \right) \widehat{\mu} \, r_m \, \mathrm{d}\widehat{l}_p = 0, \quad \forall \widehat{\mu},$$

$$\int_{\widehat{\Omega}} \dot{\mathbf{F}}^p (\mathbf{F}^p)^{-1} : \mathbf{Q} \, r_m \, \mathrm{d}r_m \mathrm{d}z_m = \int_{\widehat{\Omega}} \mathbf{R}^{e,t} \left(\frac{3}{2} \frac{\mathbf{K}^d}{q\,(\mathbf{K}^d)} \dot{\widehat{\epsilon^p}} \right) \mathbf{R}^e : \mathbf{Q} \, r_m \, \mathrm{d}r_m \mathrm{d}z_m, \quad \forall \mathbf{Q},$$

$$\int_{\widehat{\Omega}} \dot{\widehat{s}} \, \widehat{w} \, r_m \, \mathrm{d}r_m \mathrm{d}z_m = \int_{\widehat{\Omega}} \left\{ h_0 \left| 1 - \frac{\widehat{s}}{\widehat{s^*}} \right|^a \mathrm{sign} \left(1 - \frac{\widehat{s}}{\widehat{s^*}} \right) \right\} \dot{\widehat{\epsilon^p}} \, \widehat{w} \, r_m \, \mathrm{d}r_m \mathrm{d}z_m, \quad \forall \widehat{w},$$

subject to the Dirichlet boundary and initial conditions

$$\widehat{\mathbf{u}}(\widehat{\mathsf{p}}, t) = \widehat{\mathbf{u}}^{\mathrm{DM}}(\widehat{\mathsf{p}}, t) \quad \text{on } \widehat{\Gamma}_{\mathrm{DM}} \times (0,T] \tag{3.127}$$
$$\widehat{u}_r(\widehat{\mathsf{p}}, t) = 0 \quad \text{on } \widehat{\Gamma}_{\mathrm{D}} \times (0,T] \tag{3.128}$$
$$\widehat{\mathbf{u}}(\widehat{\mathsf{p}}, 0) = \widehat{\mathbf{u}}^0(\widehat{\mathsf{p}}) \quad \text{in } \overline{\widehat{\Omega}}, \tag{3.129}$$
$$\dot{\widehat{\mathbf{u}}}(\widehat{\mathsf{p}}, 0) = \widehat{\mathbf{v}}^0_m(\widehat{\mathsf{p}}) \quad \text{in } \overline{\widehat{\Omega}}, \tag{3.130}$$
$$\widehat{s}(\widehat{\mathsf{p}}, 0) = \widehat{s}^0(\widehat{\mathsf{p}}) \quad \text{in } \overline{\widehat{\Omega}}, \tag{3.131}$$
$$\mathbf{F}^p(\widehat{\mathsf{p}}, 0) = \mathbf{I} \quad \text{in } \overline{\widehat{\Omega}}, \tag{3.132}$$

and where

$$\mathbf{K} = 2\check{\mu}_{\mathrm{M}}(\widehat{\Theta}_m) \mathbf{H}^e_{\mathbf{L}} + \check{\lambda}_{\mathrm{M}}(\widehat{\Theta}_m) \mathrm{tr}\,(\mathbf{H}^e_{\mathbf{L}})\, \mathbf{I}, \tag{3.133}$$
$$\mathbf{H}^e_{\mathbf{L}} = \frac{1}{2} \ln \left(\mathbf{F}\,(\mathbf{F}^p)^{-1}\,(\mathbf{F}^p)^{-t}\,\mathbf{F}^t \right), \tag{3.134}$$
$$\mathbf{R}^e = \left[\mathbf{F}\,(\mathbf{F}^p)^{-1}\,(\mathbf{F}^p)^{-t}\,\mathbf{F}^t \right]^{-1/2} \mathbf{F}\,(\mathbf{F}^p)^{-1}, \tag{3.135}$$
$$\dot{\widehat{\epsilon^p}} = A \exp \left(-\frac{Q}{R\,\widehat{\Theta}_m} \right) \left[\sinh \left(\xi \frac{q(\mathbf{K}^d)}{\widehat{s}} \right) \right]^{\frac{1}{m}}, \tag{3.136}$$
$$\widehat{s^*} = \widetilde{s} \left[\frac{\dot{\widehat{\epsilon^p}}}{A} \exp \left(\frac{Q}{R\,\widehat{\Theta}_m} \right) \right]^n, \tag{3.137}$$

in $\overline{\widehat{\Omega}} \times [0,T]$.

Similarly, the boundaries of the electric domain, Γ_{DE} and Γ_{NE}, are obtained by rotating their corresponding parts of $\widehat{\Gamma}$ around the axis of symmetry. These parts are denoted by $\widehat{\Gamma}_{\mathrm{DE}}$ and $\widehat{\Gamma}_{\mathrm{NE}}$, respectively. On the symmetry axis, the normal component of the current density is zero. Thus, the following axisymmetric Lagrangian weak formulation is derived for the electrical problem:

Lagrangian weak electrical problem with cylindrical symmetry. *Find an electric potential* $\widehat{\mathrm{V}}_m : \overline{\widehat{\Omega}} \times [0,T] \longrightarrow \mathbb{R}$, *with* $\widehat{\mathrm{V}}_m = \widehat{\mathrm{V}}_m^{\mathrm{DE}}$ *on* $\widehat{\Gamma}_{\mathrm{DE}} \times [0,T]$, *satisfying*

$$\begin{aligned}&\int_{\widehat{\Omega}} \check{\sigma}(\widehat{\Theta}_m)\, \widehat{\mathbf{F}}^{-t}\, \widehat{\mathrm{Grad}}\, \widehat{\mathrm{V}}_m \cdot \widehat{\mathbf{F}}^{-t}\, \widehat{\mathrm{Grad}}\, \widehat{\mathrm{W}} \left(1+\frac{\widehat{u}_r}{r_m}\right) \det \widehat{\mathbf{F}}\, r_m\, \mathrm{d}r_m \mathrm{d}z_m \\ &= -\int_{\widehat{\Gamma}_{\mathrm{NE}}} \left|\widehat{\mathbf{F}}^{-t}\widehat{\mathbf{n}}_{\mathsf{p}}\right| \widehat{g}_m \widehat{\mathrm{W}} \left(1+\frac{\widehat{u}_r}{r_m}\right) \det \widehat{\mathbf{F}}\, r_m\, \mathrm{d}\widehat{l}_{\mathsf{p}}, \quad \forall \widehat{\mathrm{W}} \text{ with } \widehat{\mathrm{W}}|_{\widehat{\Gamma}_{\mathrm{DE}}} = 0.\end{aligned}$$

Finally, concerning the thermal model, Γ_{DT} and Γ_{RT} are obtained by rotating their corresponding parts of $\widehat{\Gamma}$ around the axis of symmetry. These parts are denoted by $\widehat{\Gamma}_{\mathrm{DT}}$ and $\widehat{\Gamma}_{\mathrm{RT}}$, respectively. On the symmetry axis, the normal component of the heat flux is zero. This leads to obtain the axisymmetric Lagrangian weak formulation for the thermal problem:

Lagrangian weak thermal problem with cylindrical symmetry. *Find a temperature field* $\widehat{\Theta}_m : \overline{\widehat{\Omega}} \times [0,T] \longrightarrow \mathbb{R}$, *with* $\widehat{\Theta}_m = \widehat{\Theta}_m^{\mathrm{DT}}$ *on* $\widehat{\Gamma}_{\mathrm{DT}} \times (0,T]$ *and* $\widehat{\Theta}_m(\mathsf{p},0) = \widehat{\Theta}^0(\mathsf{p})$ *in* $\overline{\widehat{\Omega}}$, *such that*

$$\begin{aligned}&\int_{\widehat{\Omega}} \widehat{\rho}_0\, \check{c}_p(\widehat{\Theta}_m)\, \dot{\widehat{\Theta}}_m \widehat{\psi}\, r_m\, \mathrm{d}r_m \mathrm{d}z_m + \int_{\widehat{\Omega}} \check{k}(\widehat{\Theta}_m)\, \widehat{\mathbf{F}}^{-t}\, \widehat{\mathrm{Grad}}\, \widehat{\Theta}_m \cdot \widehat{\mathbf{F}}^{-t}\, \widehat{\mathrm{Grad}}\, \widehat{\psi} \left(1+\frac{\widehat{u}_r}{r_m}\right) \det \widehat{\mathbf{F}}\, r_m\, \mathrm{d}r_m \mathrm{d}z_m \\ &\quad - \int_{\widehat{\Gamma}_{\mathrm{RT}}} \left[\widehat{h}_m(\widehat{\Theta}_m^{\mathrm{C}} - \widehat{\Theta}_m) + \sigma_{SB}\widehat{\epsilon}_m \left((\widehat{\Theta}_m^{\mathrm{R}})^4 - \widehat{\Theta}_m^4\right)\right] \left|\widehat{\mathbf{F}}^{-t}\widehat{\mathbf{n}}_{\mathsf{p}}\right| \widehat{\psi} \left(1+\frac{\widehat{u}_r}{r_m}\right) \det \widehat{\mathbf{F}}\, r_m\, \mathrm{d}\widehat{l}_{\mathsf{p}} \\ &\quad = \int_{\widehat{\Omega}} \check{\sigma}(\widehat{\Theta}_m) \left|\widehat{\mathbf{F}}^{-t}\widehat{\mathrm{Grad}}\widehat{\mathrm{V}}_m\right|^2 \widehat{\psi} \left(1+\frac{\widehat{u}_r}{r_m}\right) \det \widehat{\mathbf{F}}\, r_m\, \mathrm{d}r_m \mathrm{d}z_m, \quad \forall \widehat{\psi} \text{ with } \widehat{\psi}|_{\widehat{\Gamma}_{\mathrm{DT}}} = 0.\end{aligned}$$

3.5 Lagrangian approach in a new reference configuration

One of the main motivations for modelling the electric upsetting problem using pure-Lagrangian methods is to avoid the need to update the computational domain at each instant, which is inherent to Eulerian methods. In pure-Lagrangian formulations, a reference configuration is fixed and all equations are referred to it, so that the same domain is always considered and the deformation gradient accounts for its deformation.

However, in cases where the deformations are large, the reference domain may become too distorted, and obtaining sufficiently accurate solutions may be particularly difficult due to numerical issues. Therefore, in these situations, it would be recommended to consider a new reference domain, transfer the information from the previous one, and continue solving the problem. This process typically involves reinitialisation steps before attaining the final deformed state, and often necessitates remeshing of the discretised domain.

Below, the primary challenges associated with the reinitialisation process are examined from a Lagrangian perspective. Issues involving the reference domain influence not only the mechanical model but also the thermal and electrical models, owing to their full coupling.

Up to now, we had considered a domain, Ω, in a reference configuration at $t = 0$ and its motion, $\mathsf{X}(\cdot, t)$, until a configuration at time t, $\Omega(t)$. Moreover, we had introduced the reference map of the motion, $\mathsf{P}(\cdot, t)$, which is the inverse of the application $\mathsf{X}(\cdot, t)$, taking spatial points from $\Omega(t)$ to material points in Ω.

A new configuration is now introduced at time $\tau \in [0, T]$, such that, by definition, we have $\Omega(\tau) = \mathsf{X}(\Omega, \tau)$. In addition, the relative motion with respect to $\Omega(\tau)$, $\mathsf{X}_\tau : \Omega(\tau) \times [0, T] \to \mathbb{R}^3$, is given by

$$\mathsf{X}_\tau(\mathsf{y}, t) := \mathsf{X}(\mathsf{P}(\mathsf{y}, \tau), t), \qquad \forall\, (\mathsf{y}, t) \in \Omega(\tau) \times [0, T]. \tag{3.138}$$

Note that the material points in Ω are denoted by p, the spatial points in $\Omega(t)$ by x and the points in $\Omega(\tau)$ by y. A schematic view of the relations between the different motions and configurations is depicted in Figure 3.6.

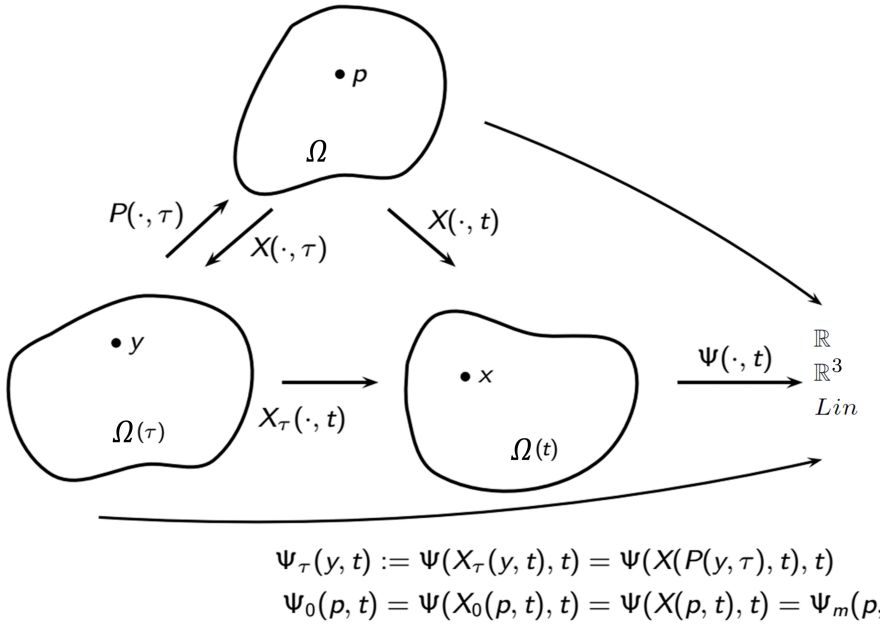

Figure 3.6: Configurations and motions referred to Ω, $\Omega(\tau)$ and $\Omega(t)$.

In order to reach a spatial point x in $\Omega(t)$ starting from a material point p in Ω there are two possibilities: going directly or passing through $\Omega(\tau)$. From a mathematical point of view, this equivalence can be established as

$$\mathsf{X}(\mathsf{p}, t) = \mathsf{X}_\tau(\mathsf{X}(\mathsf{p}, \tau), t), \tag{3.139}$$

so we have the following composition

$$\mathsf{X}(\cdot, t) = \mathsf{X}_\tau(\cdot, t) \circ \mathsf{X}(\cdot, \tau). \tag{3.140}$$

If the deformation gradient with respect to $\Omega(\tau)$, $\mathbf{F}_\tau(\mathsf{y},t) := \mathbf{Grad}_\mathsf{y}\,\mathsf{X}_\tau(\mathsf{y},t)$ is introduced, the chain rule gives the following relation

$$\mathbf{F}(\mathsf{p},t) = \mathbf{F}_\tau(\mathsf{X}(\mathsf{p},\tau),t)\,\mathbf{F}(\mathsf{p},\tau). \tag{3.141}$$

The general idea behind reinitialisation can be seen in (3.141). Firstly, the deformation gradient $\mathbf{F}(\mathsf{p},\tau)$ is obtained until time τ, when the reinitialisation takes place; then, the computation of the deformation is performed with respect to the new reference configuration, $\Omega(\tau)$, via $\mathbf{F}_\tau(\mathsf{X}(\mathsf{p},\tau),t)$. Note that, with respect to the configuration $\Omega(\tau)$, the domain is not deformed at all when the reinitialisation takes place, i.e., $\mathbf{F}_\tau(\mathsf{y},\tau) = \mathbf{I}$.

The displacement field $\mathbf{u}_\tau(\mathsf{y},t)$ with respect to configuration $\Omega(\tau)$ is defined as

$$\mathbf{u}_\tau(\mathsf{y},t) := \mathsf{X}_\tau(\mathsf{y},t) - \mathsf{y}, \tag{3.142}$$

and then we have

$$\mathbf{F}_\tau(\mathsf{y},t) = \mathbf{Grad}_\mathsf{y}\,\mathsf{X}_\tau(\mathsf{y},t) = \mathbf{I} + \mathbf{Grad}_\mathsf{y}\,\mathbf{u}_\tau(\mathsf{y},t). \tag{3.143}$$

From the previous definitions, the following additive rule for displacements can be derived,

$$\mathbf{u}(\mathsf{p},t) = \mathbf{u}(\mathsf{p},\tau) + \mathbf{u}_\tau(\mathsf{y},t). \tag{3.144}$$

This identity shows that the displacement needed to go from the reference configuration, Ω, to the current configuration, $\Omega(t)$, is the sum of the accumulated displacements required to go from Ω to $\Omega(\tau)$ and then from $\Omega(\tau)$ to $\Omega(t)$. Regarding the reinitialisation process, it is important to note that the displacement field satisfies $\mathbf{u}_\tau(\mathsf{y},\tau) = \mathbf{0}$, thereby facilitating computations based on the new reference configuration.

Once the configuration $\Omega(\tau)$ is established, the primary objective is to formulate the governing equations for this new configuration. It should be noted that classical elasticity models are conventionally defined for the original reference configuration, which usually is a *natural state*, i.e., there are no residual stresses or deformations. Notice that the configuration $\Omega(\tau)$ is not a natural state because stresses and strains have been generated before τ.

Focusing on the Hencky elasticity model, we have the constitutive law (3.26) with respect to the configuration Ω, written as

$$\mathbf{K}(\mathsf{p},t) = 2\mu_\mathrm{M}\mathbf{H}^e_\mathbf{L}(\mathsf{p},t) + \lambda_\mathrm{M}\mathrm{tr}\left(\mathbf{H}^e_\mathbf{L}(\mathsf{p},t)\right)\mathbf{I}. \tag{3.145}$$

The elastic left Hencky tensor and the Kirchhoff tensor for configuration $\Omega(\tau)$ are, by definition

$$(\mathbf{H}^e_\mathbf{L})_\tau(\mathsf{y},t) := \mathbf{H}^e_\mathbf{L}(\mathsf{P}(\mathsf{y},\tau),t), \tag{3.146}$$

$$\mathbf{K}_\tau(\mathsf{y},t) := \mathbf{K}(\mathsf{P}(\mathsf{y},\tau),t). \tag{3.147}$$

Since the reinitialisation process also affects the viscoplastic part of the deformations, it is appropriate to consider a decomposition for $\mathbf{F}^p$ in the form (3.141). Thus, the constitutive law with respect to configuration $\Omega(\tau)$ is

$$\mathbf{K}_\tau(\mathsf{y},t) = 2\mu_\mathrm{M}(\mathbf{H}^e_\mathbf{L})_\tau(\mathsf{y},t) + \lambda_\mathrm{M}\mathrm{tr}\left((\mathbf{H}^e_\mathbf{L})_\tau(\mathsf{y},t)\right)\mathbf{I}, \tag{3.148}$$

with

$$(\mathbf{H}^e_{\mathbf{L}})_\tau(\mathsf{y},t) = \frac{1}{2}\left[\mathbf{F}_\tau(\mathsf{y},t)\,\mathbf{F}(\mathsf{P}(\mathsf{y},\tau),\tau)\,(\mathbf{F}^p)^{-1}(\mathsf{P}(\mathsf{y},\tau),\tau)\,(\mathbf{F}^p_\tau)^{-1}(\mathsf{y},t)\right.$$
$$\left.(\mathbf{F}^p_\tau)^{-t}(\mathsf{y},t)\,(\mathbf{F}^p)^{-t}(\mathsf{P}(\mathsf{y},\tau),\tau)\,\mathbf{F}^t(\mathsf{P}(\mathsf{y},\tau),\tau)\,(\mathbf{F}_\tau)^t(\mathsf{y},t)\right]. \tag{3.149}$$

Note that, in addition to the constitutive law, all the equations involving $\mathbf{F}$ in any way should be properly transformed to include the reinitialisation effects. For instance, it can be shown that the equation for the time evolution of $\mathbf{F}^p$ in (3.30) should be rewritten as

$$\dot{\mathbf{F}}^p_\tau(\mathsf{y},t)\,(\mathbf{F}^p_\tau)^{-1}(\mathsf{y},t) = \mathbf{R}^{e,t}(\mathsf{p},\tau)\,\mathbf{R}^{e,t}_\tau(\mathsf{y},t)\,\mathbf{G}(\mathbf{K}(\mathsf{p},t),\dot{\epsilon}^p(\mathsf{p},t))\,\mathbf{R}^e_\tau(\mathsf{y},t)\,\mathbf{R}^e(\mathsf{p},\tau)\big|_{\mathsf{p}=\mathsf{P}(\mathsf{y},\tau)}. \tag{3.150}$$

Besides making all the necessary changes in the formulation for the three coupled models, the unknowns should also be reinitialised appropriately.

Chapter 4

Thermo-electromagnetic-mechanical modelling of AC electric upsetting

When AC electrical sources are considered in electric upsetting processes, the electrical model introduced in Chapter 3 is not adequate to describe the new emerging electromagnetic phenomena. In this chapter, a detailed description of a more complex electromagnetic model is provided.

Let us recall that the general considerations in Chapter 3 concerning the characteristics of the computational domain are still valid. In fact, the features of the problem make it suitable for an axisymmetric formulation, which only includes the metal bar in the computational domain. The neighbouring elements, as the anvil and the gripper jaws, are taken into account through the boundary conditions of the model.

In addition to the Joule effect, the mechanical deformation of the domain, the temperature-dependent electrical conductivity, and the elasto-viscoplastic properties, the coupling between the mechanical, electromagnetic, and thermal models is also influenced by the magnetic permeability present in the electromagnetic model. This material property, which relates the magnetic field and the magnetic induction, is highly non-linearly dependent on the magnitude of the magnetic field and on the temperature.

Contrary to the electrical model, which is completely changed, the formulations of the mechanical and thermal models described in Chapter 3 remain essentially the same when AC sources are considered instead of DC ones. The main exception is the heat source of the thermal model, the expression of which is modified to be computed from the electromagnetic model as detailed in the present chapter.

In Section 4.1, we present the three-dimensional Eulerian formulation of the electromagnetic

This chapter partially reproduces contents from the following publication:

- M. Benítez, A. Bermúdez, P. Fontán, I. Martínez, P. Salgado (2024). *A Lagrangian approach for solving an axisymmetric thermo-electromagnetic problem. Application to time-varying geometry processes*. Advances in Computational Mathematics, 50, 45. Electronic ISSN: 1572-9044, Print ISSN: 1019-7168. DOI: 10.1007/s10444-024-10121-y

model, which is based on an eddy current approximation in the time-harmonic regime. Assuming cylindrical symmetry, the model is restricted to conductive regions and reformulated in terms of the magnetic field. A subsequent transformation from Eulerian to Lagrangian coordinates leads to the final axisymmetric Lagrangian weak formulation. Additionally, in Section 4.2, the thermal model is addressed, where the heat source term resulting from the Joule effect is recalculated to account for alternating current (AC) conditions.

4.1 Electromagnetic model

This section details the computation of the electromagnetic field within the workpiece during electric upsetting. The alternating current (AC) sources are defined by specifying voltages and currents along selected boundary segments. By incorporating cylindrical symmetry into the electromagnetic model, the formulation enables the restriction of the problem to the conducting regions, achieved through the application of appropriate boundary conditions.

4.1.1 Eddy current model

Let us assume that the conducting domain $\Omega(t)$ is cylindrically symmetric, namely

$$\Omega(t) := \left\{ (r, \theta, z) : \ \theta \in [0, 2\pi), \ (r, z) \in \widehat{\Omega}(t) \right\},$$

for some bounded subset $\widehat{\Omega}(t) \subset \mathbb{R}^2$. Let $\mathbf{n}_{\mathsf{x}}(\mathsf{x}, t) = \widehat{n}_r(\widehat{\mathsf{x}}, t)\mathbf{e}_r + \widehat{n}_z(\widehat{\mathsf{x}}, t)\mathbf{e}_z$ be the outward unit normal vector to $\partial\Omega(t)$. We restrict our attention to a simply connected set $\Omega(t)$ that intersects the axis $r = 0$ in a set of positive one-dimensional measure, so that $\widehat{\Omega}(t)$ is also simply connected.

Let us further assume that the physical properties, more specifically, the electrical conductivity, σ, and the magnetic permeability, μ, are independent of θ, i.e.,

$$\sigma(\mathsf{x}, t) := \widehat{\sigma}(\widehat{\mathsf{x}}, t), \quad \mu(\mathsf{x}, t) := \widehat{\mu}(\widehat{\mathsf{x}}, t),$$

and the AC sources are such that the current density in the conducting part is of the form

$$\mathbf{J}(\mathsf{x}, t) := \widehat{J}_r(\widehat{\mathsf{x}}, t)\mathbf{e}_r + \widehat{J}_z(\widehat{\mathsf{x}}, t)\mathbf{e}_z \quad \text{in } \Omega(t).$$

Under these assumptions, an eddy current model can be defined within the conducting domain, denoted by $\Omega(t)$, by applying suitable boundary conditions. The *eddy current model* represents a simplified form of Maxwell's equations (3.84)-(3.87), derived by neglecting the electric displacement term in Ampère's law. For a detailed discussion on the parameter ranges in which this approximation holds, we refer the reader to [25]. This simplification is generally valid for low-frequency electrical applications, such as those encountered in electric upsetting processes.

The eddy current model consists of the following system of partial differential equations:

$$\operatorname{div} \mathbf{B}(\mathsf{x}, t) = 0, \tag{4.1}$$

$$\mathbf{curl}\, \mathbf{H}(\mathsf{x}, t) = \mathbf{J}(\mathsf{x}, t), \tag{4.2}$$

$$\frac{\partial \mathbf{B}(\mathsf{x}, t)}{\partial t} + \mathbf{curl}\, \mathbf{E}(\mathsf{x}, t) = \mathbf{0}, \tag{4.3}$$

together with the constitutive laws

$$\mathbf{B}(\mathsf{x},t) = \mu(\mathsf{x},t)\mathbf{H}(\mathsf{x},t), \tag{4.4}$$

$$\mathbf{J}(\mathsf{x},t) = \sigma(\mathsf{x},t)\mathbf{E}(\mathsf{x},t), \tag{4.5}$$

where σ is usually temperature-dependent and μ generally depends on the temperature and the modulus of the magnetic field for nonlinear materials. Later, this model will be completed with appropriate current sources.

Furthermore, note that if the current sources are alternating and the materials have linear magnetic behaviour, a time-harmonic approximation is often a suitable solution to avoid working with time-scales which are very different for thermal, mechanical, and electromagnetic phenomena; see, for instance, [17, 22]. However, even considering materials with nonlinear magnetic behaviour, as in the electric upsetting problem, this time-harmonic approximation is frequently used to avoid long transient simulations, which would be needed to reach a steady state in a genuine transient electromagnetic model. We refer the reader to [61] for further details in the complex representation of the ferromagnetic behaviour in nonlinear time-harmonic problems.

Thus, under the time-harmonic approximation, each field is assumed to be of the form

$$\mathbf{G}(\mathsf{x},t) = \mathrm{Re}(\mathrm{e}^{i\omega t}\hat{\mathbf{G}}(\mathsf{x})), \tag{4.6}$$

where $\hat{\mathbf{G}}$ is a complex field called complex amplitude or *phasor* and ω is the angular frequency (in rad/s), related to the frequency, f (in Hz), by $\omega = 2\pi f$.

In the case of a fixed domain, the complex phasors are time-independent. However, in the present scenario, a reasoning similar to that used in the DC case is applied: since the domain $\Omega(t)$ evolves due to mechanical deformation, it is necessary to account for the time dependence in all complex amplitudes. Therefore, under the time-harmonic approximation, we consider the following eddy current model, which is restricted to the time-dependent domain $\Omega(t)$:

$$i\omega\mathbf{B}(\mathsf{x},t) + \mathbf{curl}\,\mathbf{E}(\mathsf{x},t) = \mathbf{0}, \tag{4.7}$$

$$\mathbf{curl}\,\mathbf{H}(\mathsf{x},t) = \mathbf{J}(\mathsf{x},t), \tag{4.8}$$

$$\mathrm{div}\,\mathbf{B}(\mathsf{x},t) = 0, \tag{4.9}$$

$$\mathbf{B}(\mathsf{x},t) = \check{\mu}(|\mathbf{H}(\mathsf{x},t)|, \Theta(\mathsf{x},t))\mathbf{H}(\mathsf{x},t), \tag{4.10}$$

$$\mathbf{J}(\mathsf{x},t) = \check{\sigma}(\Theta(\mathsf{x},t))\mathbf{E}(\mathsf{x},t), \tag{4.11}$$

where $\mathbf{B}$, $\mathbf{H}$, $\mathbf{E}$, and $\mathbf{J}$ are the complex amplitudes associated with the magnetic induction, the magnetic field, the electric field, and the current density, respectively (notice that we have dropped the hats for simplicity). Moreover, $\check{\mu} : \mathbb{R}\times\mathbb{R} \longrightarrow \mathbb{R}$ and $\check{\sigma} : \mathbb{R} \longrightarrow \mathbb{R}$ are, respectively, the magnetic permeability and the electrical conductivity as functions of the temperature, $\Theta : \overline{\Omega}(t)\times[0,T] \longrightarrow \mathbb{R}$, which is computed by solving the thermal model.

Next, we follow similar arguments as those developed in [19] to describe the problem in a bounded conducting domain under axisymmetric assumptions. Assuming that none of the components of the fields depend on θ, we can look for a solution of the previous equations

satisfying

$$\begin{aligned}\mathbf{E}(\mathsf{x},t) &:= \widehat{E}_r(\widehat{\mathsf{x}},t)\mathbf{e}_r + \widehat{E}_z(\widehat{\mathsf{x}},t)\mathbf{e}_z \quad \text{in } \Omega(t),\\ \mathbf{H}(\mathsf{x},t) &:= \widehat{H}_\theta(\widehat{\mathsf{x}},t)\mathbf{e}_\theta \quad \text{in } \Omega(t).\end{aligned}$$

Consequently, the following boundary condition can be imposed on the whole boundary of the conducting domain:

$$\check{\mu}(|\mathbf{H}|,\Theta)\,\mathbf{H}(\mathsf{x},t)\cdot\mathbf{n}_{\mathsf{x}}(\mathsf{x},t) = 0 \quad \text{on } \partial\Omega(t). \tag{4.12}$$

This property will enable us to set boundary conditions on $\partial\Omega(t)$ that impose currents and/or potential drops on electrical ports. Indeed, let us assume that the boundary of $\Omega(t)$ splits as follows:

$$\partial\Omega(t) := \Gamma_{\mathrm{N}}(t)\cup\Gamma_{\mathbf{J}}(t)\cup\Gamma_{\mathbf{E}}(t),$$

where $\Gamma_{\mathbf{J}}(t)$ and $\Gamma_{\mathbf{E}}(t)$ are the parts of the boundary connected to an electrical source with known currents or potential drops, while $\Gamma_{\mathrm{N}}(t)$ is the isolated part, i.e., there is no current flux through this boundary. In eddy current models with electrical ports, it is usual to assume that currents enter and exit the domain perpendicularly, and, consequently, we will set

$$\mathbf{E}(\mathsf{x},t)\times\mathbf{n}_{\mathsf{x}}(\mathsf{x},t) = \mathbf{0} \quad \text{on } \Gamma_{\mathbf{J}}(t)\cup\Gamma_{\mathbf{E}}(t), \tag{4.13}$$

while the isolation condition means

$$\mathbf{J}(\mathsf{x},t)\cdot\mathbf{n}_{\mathsf{x}}(\mathsf{x},t) = \mathbf{curl}\,\mathbf{H}(\mathsf{x},t)\cdot\mathbf{n}_{\mathsf{x}}(\mathsf{x},t) = 0 \quad \text{on } \Gamma_{\mathrm{N}}(t). \tag{4.14}$$

From condition (4.12) we can deduce that there exists a sufficiently smooth function $\mathrm{U}(t)$ defined in $\Omega(t)$ up to a constant, such that $\mathrm{U}|_{\partial\Omega(t)}$ is a surface potential of the tangential component of $\mathbf{E}$, namely, $\mathbf{E}\times\mathbf{n}_{\mathsf{x}} = -\operatorname{grad}\mathrm{U}\times\mathbf{n}_{\mathsf{x}}$ on $\partial\Omega(t)$. On the other hand, equation (4.13) implies that U must remain constant on each connected component of $\Gamma_{\mathbf{J}}(t)\cup\Gamma_{\mathbf{E}}(t)$ to be called a port. We assume that the entire set $\Gamma_{\mathbf{E}}(t)$ is a single port, and denote the individual ports within $\Gamma_{\mathbf{J}}(t)$ as $\Gamma^k_{\mathbf{J}}(t)$, where k indexes the ports. By setting $\mathrm{U}=0$ on $\Gamma_{\mathbf{E}}(t)$, the complex quantity $\mathrm{U}_k := \mathrm{U}|_{\Gamma^k_{\mathbf{J}}(t)} - \mathrm{U}|_{\Gamma_{\mathbf{E}}(t)}$ represents the potential drop between $\Gamma^k_{\mathbf{J}}(t)$ and $\Gamma_{\mathbf{E}}(t)$; consequently, $\mathrm{U}_k := \mathrm{U}|_{\Gamma^k_{\mathbf{J}}(t)}$.

Based on the previous discussion, we assume that for each surface $\Gamma^k_{\mathbf{J}}(t)$, one of the following quantities is known:

- potential drop (or voltage) $\mathrm{U}_k(t) := \mathrm{U}|_{\Gamma^k_{\mathbf{J}}(t)}$,
- current intensity, $I_k(t)$, through $\Gamma^k_{\mathbf{J}}(t)$, i.e.,

$$\int_{\Gamma^k_{\mathbf{J}}(t)}\mathbf{J}(\mathsf{x},t)\cdot\mathbf{n}_{\mathsf{x}}(\mathsf{x},t)\,\mathrm{d}A_{\mathsf{x}} = \int_{\Gamma^k_{\mathbf{J}}(t)}\mathbf{curl}\,\mathbf{H}(\mathsf{x},t)\cdot\mathbf{n}_{\mathsf{x}}(\mathsf{x},t)\,\mathrm{d}A_{\mathsf{x}} = I_k(t).$$

To obtain a weak formulation of this problem, let us multiply Faraday's equation (4.7) defined in $\Omega(t)$ by a smooth test vector field $\mathbf{G}(\mathrm{x},t)$ such that $\mathbf{curl}\,\mathbf{G}\cdot\mathbf{n}_{\mathrm{x}}=0$ on $\Gamma_{\mathrm{N}}(t)$. From Ampère's and Ohm's laws and using a Green's formula, we obtain

$$\begin{aligned}
0 &= \int_{\Omega(t)} i\omega\mathbf{B}\cdot\bar{\mathbf{G}}\,\mathrm{d}V_{\mathrm{x}} + \int_{\Omega(t)} \mathbf{curl}\,\mathbf{E}\cdot\bar{\mathbf{G}}\,\mathrm{d}V_{\mathrm{x}} \\
&= \int_{\Omega(t)} i\omega\check{\mu}(|\mathbf{H}|,\Theta)\mathbf{H}\cdot\bar{\mathbf{G}}\,\mathrm{d}V_{\mathrm{x}} + \int_{\Omega(t)} \mathbf{E}\cdot\mathbf{curl}\,\bar{\mathbf{G}}\,\mathrm{d}V_{\mathrm{x}} - \int_{\partial\Omega(t)} \mathbf{E}\times\mathbf{n}_{\mathrm{x}}\cdot\bar{\mathbf{G}}\,\mathrm{d}A_{\mathrm{x}} \\
&= \int_{\Omega(t)} i\omega\check{\mu}(|\mathbf{H}|,\Theta)\mathbf{H}\cdot\bar{\mathbf{G}}\,\mathrm{d}V_{\mathrm{x}} + \int_{\Omega(t)} \frac{1}{\check{\sigma}(\Theta)}\mathbf{curl}\,\mathbf{H}\cdot\mathbf{curl}\,\bar{\mathbf{G}}\,\mathrm{d}V_{\mathrm{x}} + \int_{\partial\Omega(t)} \bar{\mathbf{G}}\times\mathrm{grad}\,\mathrm{U}\cdot\mathbf{n}_{\mathrm{x}}\,\mathrm{d}A_{\mathrm{x}},
\end{aligned}$$

and using the appropriate Green's formulas,

$$\begin{aligned}
\int_{\Omega(t)} i\omega\check{\mu}(|\mathbf{H}|,\Theta)\mathbf{H}\cdot\bar{\mathbf{G}}\,\mathrm{d}V_{\mathrm{x}} + \int_{\Omega(t)} \frac{1}{\check{\sigma}(|\mathbf{H}|,\Theta)}\mathbf{curl}\,\mathbf{H}\cdot\mathbf{curl}\,\bar{\mathbf{G}}\,\mathrm{d}V_{\mathrm{x}} &= -\int_{\Omega(t)} \mathrm{grad}\,\mathrm{U}\cdot\mathbf{curl}\,\bar{\mathbf{G}}\,\mathrm{d}V_{\mathrm{x}} \\
&= -\int_{\partial\Omega(t)} \mathrm{U}\,\mathbf{curl}\,\bar{\mathbf{G}}\cdot\mathbf{n}_{\mathrm{x}}\,\mathrm{d}A_{\mathrm{x}} \\
&= -\int_{\Gamma_{\mathbf{J}}(t)} \mathrm{U}\,\mathbf{curl}\,\bar{\mathbf{G}}\cdot\mathbf{n}_{\mathrm{x}}\,\mathrm{d}A_{\mathrm{x}},
\end{aligned}$$

where in the last equality we have used that $\mathrm{U}=0$ on $\Gamma_{\mathbf{E}}(t)$ and $\mathbf{curl}\,\mathbf{G}\cdot\mathbf{n}_{\mathrm{x}}=0$ on $\Gamma_{\mathrm{N}}(t)$.

We distinguish between ports in $\Gamma_{\mathbf{J}}(t)$ where the currents are known and those where the voltages are specified. More precisely, the set of N indices corresponding to the ports of $\Gamma_{\mathbf{J}}(t)$ is divided into two disjoint sets N_{V} and N_{I}, where

- For $k\in N_{\mathrm{V}}$, voltage $V_k(t)\in\mathbb{C}$ is given.
- For $k\in N_{\mathrm{I}}$, current $I_k(t)\in\mathbb{C}$ is given.

The different parts of the electromagnetic boundary for a typical electric upsetting configuration are shown in Figure 4.1.

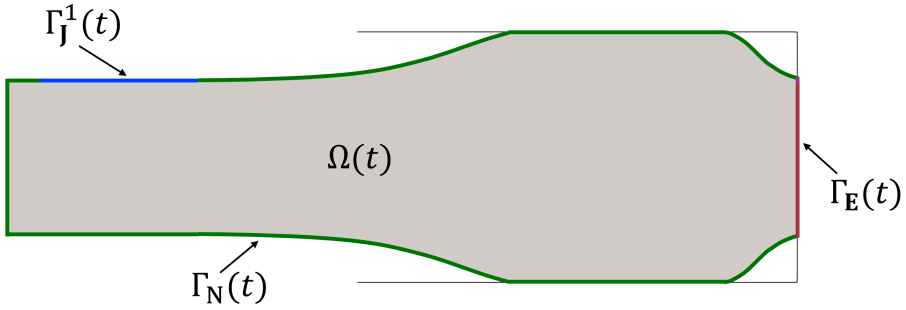

Figure 4.1: Boundaries of the electromagnetic domain. In general, either current or voltage is imposed on $\Gamma_{\mathbf{J}}^1(t)$.

Thus, taking into account the previous relations, the weak formulation of the electromagnetic problem can be established:

Eulerian weak electromagnetic problem. *Given the currents* $I_k : \Gamma_{\mathbf{J}}^k(t) \times [0,T] \longrightarrow \mathbb{C}$ *for* $k \in N_{\mathrm{I}}$ *and the voltages* $\mathrm{V}_k : \Gamma_{\mathbf{J}}^k(t) \times [0,T] \longrightarrow \mathbb{C}$ *for* $k \in N_{\mathrm{V}}$*, find complex fields* $\mathbf{H} : \overline{\Omega}(t) \times [0,T] \longrightarrow \mathbb{C}^3$*,* $\lambda : \Gamma_{\mathrm{N}}(t) \times [0,T] \longrightarrow \mathbb{C}$*, and* $\mathrm{V}_k : \Gamma_{\mathbf{J}}^k(t) \times [0,T] \longrightarrow \mathbb{C}$ *for* $k \in N_{\mathrm{I}}$*, such that,*

$$\int_{\Omega(t)} i\omega\breve{\mu}(|\mathbf{H}|,\Theta)\,\mathbf{H}\cdot\overline{\mathbf{G}}\,\mathrm{d}V_{\mathsf{x}} + \int_{\Omega(t)} \frac{1}{\breve{\sigma}(\Theta)}\mathbf{curl}\,\mathbf{H}\cdot\mathbf{curl}\,\overline{\mathbf{G}}\,\mathrm{d}V_{\mathsf{x}} + \int_{\Gamma_{\mathrm{N}}(t)} \lambda\,\mathbf{curl}\,\overline{\mathbf{G}}\cdot\mathbf{n}_{\mathsf{x}}\,\mathrm{d}A_{\mathsf{x}}$$
$$+ \sum_{k\in N_{\mathrm{I}}} \int_{\Gamma_{\mathbf{J}}^k(t)} \mathrm{V}_k\,\mathbf{curl}\,\overline{\mathbf{G}}\cdot\mathbf{n}_{\mathsf{x}}\,\mathrm{d}A_{\mathsf{x}} = -\sum_{k\in N_{\mathrm{V}}} \int_{\Gamma_{\mathbf{J}}^k(t)} \mathrm{V}_k\,\mathbf{curl}\,\overline{\mathbf{G}}\cdot\mathbf{n}_{\mathsf{x}}\,\mathrm{d}A_{\mathsf{x}}, \quad \forall\mathbf{G},$$
$$\int_{\Gamma_{\mathbf{J}}^k(t)} \mathbf{curl}\,\mathbf{H}\cdot\mathbf{n}_{\mathsf{x}}\,\mathrm{d}A_{\mathsf{x}} = \mathrm{I}_k, \quad \forall k \in N_{\mathrm{I}},$$
$$\int_{\Gamma_{\mathrm{N}}(t)} \overline{\eta}\,\mathbf{curl}\,\mathbf{H}\cdot\mathbf{n}_{\mathsf{x}}\,\mathrm{d}A_{\mathsf{x}} = 0, \quad \forall\eta.$$

Function λ, defined on $\Gamma_{\mathrm{N}}(t)$, is the Lagrange multiplier associated with the constraint of null current flux through the isolated boundaries.

Remark 4.1. *To highlight the mixed nature of the weak formulation, the equations imposing the currents through* $\Gamma_{\mathbf{J}}^k(t)$*,* $k \in N_I$*, could be equivalently written as*

$$\sum_{k\in N_{\mathrm{I}}} \int_{\Gamma_{\mathbf{J}}^k(t)} \overline{\mathrm{W}}_k\,\mathbf{curl}\,\mathbf{H}\cdot\mathbf{n}_{\mathsf{x}}\,\mathrm{d}A_{\mathsf{x}} = \sum_{k\in N_{\mathrm{I}}} \overline{\mathrm{W}}_k\,\mathrm{I}_k, \quad \forall \mathrm{W}_k,\ k \in N_{\mathrm{I}},$$

where $W_k \in \mathbb{C}$ *is the spatially constant test function associated to* V_k*,* $k \in N_I$*. The mixed formulation of the axisymmetric problem has been implemented in the code for numerical purposes, following an approach analogous to that used for Problem 4 in [19]. Note that the variables* V_k*,* $k \in N_{\mathrm{I}}$*, are the Lagrange multipliers associated with the constraints that enforce the prescribed currents at the corresponding electrical ports.*

Note that, in general situations, for 3D domains it is not possible to restrict the model to only conducting parts. In that case, a useful approach consists in using a magnetic field in the conducting parts and a scalar potential in the dielectric ones; see, for instance, [26] for a reference work by using these unknowns, applied later to the case of electrical ports as in the present work, both in harmonic and transient regime (see, respectively [20, 24]).

4.1.2 Lagrangian formulation

From the weak formulation in Eulerian coordinates presented above, the weak formulation in Lagrangian coordinates can be obtained. We make use of the identity (2.7) for $\boldsymbol{\vartheta}(\mathsf{x},t) = \mathbf{H}(\mathsf{x},t)$ to transform the curl operator. This property leads us to introduce a new field $\boldsymbol{\mathcal{H}}(\mathsf{p},t)$ which is related to the material description of the unknown $\mathbf{H}$, $\mathbf{H}_m(\mathsf{p},t)$, as follows:

$$\boldsymbol{\mathcal{H}}(\mathsf{p},t) = \mathbf{F}^t(\mathsf{p},t)\,\mathbf{H}_m(\mathsf{p},t). \tag{4.15}$$

In a similar way, a new function $\boldsymbol{\mathcal{G}}(\mathsf{p},t)$ associated with the test function $\mathbf{G}$ will be introduced, satisfying a similar relation to (4.15).

By using (2.7), (2.19), (2.20) and (4.15), we obtain a 3D weak formulation in Lagrangian coordinates:

Lagrangian weak electromagnetic problem. *Given the currents* $I_k : \Gamma_{\mathbf{J}}^k \times [0,T] \longrightarrow \mathbb{C}$ *for* $k \in N_{\mathrm{I}}$ *and the voltages* $\mathrm{V}_k : \Gamma_{\mathbf{J}}^k \times [0,T] \longrightarrow \mathbb{C}$ *for* $k \in N_{\mathrm{V}}$, *find complex fields* $\boldsymbol{\mathcal{H}} : \overline{\Omega} \times [0,T] \longrightarrow \mathbb{C}^3$, $\lambda : \Gamma_{\mathrm{N}} \times [0,T] \longrightarrow \mathbb{C}$ *and* $\mathrm{V}_k : \Gamma_{\mathbf{J}}^k \times [0,T] \longrightarrow \mathbb{C}$ *for* $k \in N_{\mathrm{I}}$, *such that*

$$\int_\Omega i\omega\check{\mu}(|\mathbf{F}^{-t}\boldsymbol{\mathcal{H}}|,\Theta_m)\mathbf{F}^{-t}\boldsymbol{\mathcal{H}}\cdot\mathbf{F}^{-t}\overline{\boldsymbol{\mathcal{G}}}\,\mathrm{det}\mathbf{F}\,\mathrm{d}V_{\mathsf{p}} + \int_\Omega \frac{1}{\check{\sigma}(\Theta_m)\,\mathrm{det}\mathbf{F}}\mathbf{F}\,\mathbf{Curl}\,\boldsymbol{\mathcal{H}}\cdot\mathbf{F}\,\mathbf{Curl}\,\overline{\boldsymbol{\mathcal{G}}}\,\mathrm{d}V_{\mathsf{p}}$$
$$+\int_{\Gamma_{\mathrm{N}}}\lambda\,\mathbf{Curl}\,\overline{\boldsymbol{\mathcal{G}}}\cdot\mathbf{n}_{\mathsf{p}}\,\mathrm{d}A_{\mathsf{p}} + \sum_{k\in N_{\mathrm{I}}}\int_{\Gamma_{\mathbf{J}}^k}\mathrm{V}_k\,\mathbf{Curl}\,\overline{\boldsymbol{\mathcal{G}}}\cdot\mathbf{n}_{\mathsf{p}}\,\mathrm{d}A_{\mathsf{p}} = -\sum_{k\in N_{\mathrm{V}}}\int_{\Gamma_{\mathbf{J}}^k}\mathrm{V}_k\,\mathbf{Curl}\,\overline{\boldsymbol{\mathcal{G}}}\cdot\mathbf{n}_{\mathsf{p}}\,\mathrm{d}A_{\mathsf{p}},\quad \forall\boldsymbol{\mathcal{G}},$$
$$\int_{\Gamma_{\mathbf{J}}^k}\mathbf{Curl}\,\boldsymbol{\mathcal{H}}\cdot\mathbf{n}_{\mathsf{p}}\,\mathrm{d}A_{\mathsf{p}} = \mathrm{I}_k,\quad \forall k\in N_{\mathrm{I}},$$
$$\int_{\Gamma_{\mathrm{N}}}\overline{\eta}\,\mathbf{Curl}\boldsymbol{\mathcal{H}}\cdot\mathbf{n}_{\mathsf{p}}\,\mathrm{d}A_{\mathsf{p}} = 0,\quad \forall\eta.$$

4.1.3 Eddy current model with power as data

In this chapter, we have considered electrical ports in terms of imposed voltages or currents. However, in industrial facilities, the quantity that is actually monitored in practice is the total active power delivered to the metal bar through the gripper jaws. Assuming that all the current enters the metal bar via the gripper jaws, the total active power in AC operation, $P_{AC}(t)$, is given by (see [18] for details)

$$P_{AC}(t) = \frac{1}{2}\mathrm{Re}\left(\mathrm{V}_1\,\bar{\mathrm{I}}_1\right), \tag{4.16}$$

where V_1 and I_1 are, respectively, the voltage and the current on $\Gamma_{\mathbf{J}}^1$, which is the electrical port associated with the gripper jaws. Note that both V_1 and I_1 now become unknowns of the electromagnetic model, since the given data is $P_{AC}(t)$. Since in this work we are considering single-phase electrical sources, it can be assumed, without loss of generality, that I_1 has a null phase and it is a real number, i.e., $\mathrm{I}_1 = |\mathrm{I}_1|$. Therefore, (4.16) can be rewritten as

$$P_{AC}(t) = \frac{1}{2}\mathrm{Re}\left(\mathrm{V}_1\right)\mathrm{I}_1. \tag{4.17}$$

To use the power $P_{AC}(t)$ as a given data in the weak formulation, we consider the product of (4.17) by a spatially constant test function, $\beta(t)$, and achieve the weak formulation of the Lagrangian electromagnetic problem with the total active power as known data.

Lagrangian weak electromagnetic problem with power as data. *Given the total active power supplied to the system,* $P_{AC} : \Gamma^1_{\mathbf{J}} \times [0,T] \longrightarrow \mathbb{R}$, *find complex fields* $\boldsymbol{\mathcal{H}} : \overline{\Omega} \times [0,T] \longrightarrow \mathbb{C}^3$, $\lambda : \Gamma_{\mathrm{N}} \times [0,T] \longrightarrow \mathbb{C}$, $\mathrm{V}_1 : \Gamma^1_{\mathbf{J}} \times [0,T] \longrightarrow \mathbb{C}$ *and* $\mathrm{I}_1 : \Gamma^1_{\mathbf{J}} \times [0,T] \longrightarrow \mathbb{R}$ *such that*

$$\int_\Omega i\omega\check{\mu}(|\mathbf{F}^{-t}\boldsymbol{\mathcal{H}}|,\Theta_m)\mathbf{F}^{-t}\boldsymbol{\mathcal{H}}\cdot\mathbf{F}^{-t}\overline{\boldsymbol{\mathcal{G}}}\,\det\mathbf{F}\,\mathrm{d}V_{\mathsf{p}} + \int_\Omega \frac{1}{\check{\sigma}(\Theta_m)\,\det\mathbf{F}}\mathbf{F}\,\mathbf{Curl}\,\boldsymbol{\mathcal{H}}\cdot\mathbf{F}\,\mathbf{Curl}\,\overline{\boldsymbol{\mathcal{G}}}\,\mathrm{d}V_{\mathsf{p}}$$
$$+\int_{\Gamma_{\mathrm{N}}}\lambda\,\mathbf{Curl}\,\overline{\boldsymbol{\mathcal{G}}}\cdot\mathbf{n}_{\mathsf{p}}\,\mathrm{d}A_{\mathsf{p}} + \int_{\Gamma^1_{\mathbf{J}}}\mathrm{V}_1\,\mathbf{Curl}\,\overline{\boldsymbol{\mathcal{G}}}\cdot\mathbf{n}_{\mathsf{p}}\,\mathrm{d}A_{\mathsf{p}} = 0, \quad \forall\boldsymbol{\mathcal{G}},$$
$$\int_{\Gamma^1_{\mathbf{J}}}\mathbf{Curl}\,\boldsymbol{\mathcal{H}}\cdot\mathbf{n}_{\mathsf{p}}\,\mathrm{d}A_{\mathsf{p}} = \mathrm{I}_1,$$
$$\int_{\Gamma_{\mathrm{N}}}\overline{\eta}\,\mathbf{Curl}\boldsymbol{\mathcal{H}}\cdot\mathbf{n}_{\mathsf{p}}\,\mathrm{d}A_{\mathsf{p}} = 0, \quad \forall\eta,$$
$$\frac{1}{2}\mathrm{Re}\,(\mathrm{V}_1)\,\mathrm{I}_1\,\beta = P_{AC}\,\beta, \quad \forall\beta.$$

4.2 Thermal model

To properly take into account the Joule effect due to AC sources, the thermal model in Section 3.3 has to be modified. Since the expression for the Joule effect due to AC sources differs from the one associated to DC sources, the thermal heat source has to be changed accordingly to be computed in terms of the magnetic field from the electromagnetic formulation in Section 4.1.

When the usual time-harmonic eddy current model is considered, the AC heat source is computed as the average value of the active power dissipated on a cycle (see [18] for further details), which is time-independent and given by

$$P(\mathsf{x}) = \frac{|\mathbf{J}(\mathsf{x})|^2}{2\check{\sigma}(\Theta)}, \tag{4.18}$$

where $\mathbf{J}(\mathsf{x})$ is the complex amplitude of the current density.

However, in a coupled thermo-electromagnetic-mechanical problem, the complex amplitude $\mathbf{J}(\mathsf{x},t)$ is time-dependent due to the mechanical deformation. By assuming that this amplitude varies over time much more slowly than the frequency of the electrical current, the heat source in the thermal problem can be expressed as

$$P(\mathsf{x},t) = \frac{|\mathbf{J}(\mathsf{x},t)|^2}{2\check{\sigma}(\Theta)}, \tag{4.19}$$

where $\mathbf{J}(\mathsf{x},t)$ is obtained from the solution of the electromagnetic model in terms of the magnetic field (4.8).

The Lagrangian weak formulation for the thermal model with AC heat sources is obtained by slightly modifying the Lagrangian weak formulation for DC sources in Section 3.3.2:

Lagrangian weak thermal problem with AC sources. *Find a temperature field* $\Theta_m : \overline{\Omega} \times [0,T] \longrightarrow \mathbb{R}$, *with* $\Theta_m = \Theta_m^{\mathrm{DT}}$ *on* $\Gamma_{\mathrm{DT}} \times (0,T]$ *and* $\Theta_m(\mathsf{p},0) = \Theta^0(\mathsf{p})$ *in* $\overline{\Omega}$, *such that,*

$$\begin{aligned}\int_\Omega \rho_0\, \check{c}_p(\Theta_m)\, \dot{\Theta}_m \psi \,\mathrm{d}V_{\mathsf{p}} + \int_\Omega \check{k}(\Theta_m)\, \mathbf{F}^{-t}\,\mathrm{Grad}\,\Theta_m \cdot \mathbf{F}^{-t}\,\mathrm{Grad}\,\psi \det\mathbf{F}\,\mathrm{d}V_{\mathsf{p}} \\ - \int_{\Gamma_{\mathrm{RT}}} \left[h_m(\Theta_m^{\mathrm{C}} - \Theta_m) + \sigma_{SB}\epsilon_m\left((\Theta_m^{\mathrm{R}})^4 - \Theta_m^4\right)\right] |\mathbf{F}^{-\mathrm{t}}\mathbf{n}_{\mathsf{p}}| \psi \det\mathbf{F}\,\mathrm{d}A_{\mathsf{p}} \\ = \int_\Omega \frac{|\mathbf{J}_m|^2}{2\check{\sigma}(\Theta_m)}\,\psi \det\mathbf{F}\,\mathrm{d}V_{\mathsf{p}}, \quad \forall \psi \text{ with } \psi|_{\Gamma_{\mathrm{DT}}} = 0.\end{aligned}$$

Finally, note that changing the electrical source from DC to AC also affects the mechanical model, due to the different evolution of the temperature field and, consequently, the mechanical deformation. However, this effect is not explicitly reflected in the mathematical formulation, and we continue to refer to Section 3.1 for the mechanical model.

4.3 Axisymmetric thermo-electromagnetic-mechanical model

In this section, we rewrite the electromagnetic and thermal weak formulations in Sections 4.1 and 4.2 under cylindrical symmetry assumptions.

Let us denote by $\partial\widehat{\Omega}(t)$ the boundary of $\widehat{\Omega}(t)$, which can be decomposed for the electromagnetic Eulerian domain as $\partial\widehat{\Omega}(t) := \widehat{\Gamma}_{\mathrm{D}}(t) \cup \widehat{\Gamma}_{\mathbf{J}}(t) \cup \widehat{\Gamma}_{\mathrm{N}}(t) \cup \widehat{\Gamma}_{\mathbf{E}}(t)$ (recall that $\widehat{\Gamma}_{\mathrm{D}}(t)$ is the part of the boundary corresponding to the axis of symmetry $r = 0$).

We consider a vector test function $\mathbf{G}(\mathsf{x},t) = \widehat{G}_\theta(\widehat{\mathsf{x}},t)\mathbf{e}_\theta$. Notice that

$$\mathbf{curl}\,\mathbf{G}\cdot\mathbf{n}_{\mathsf{x}} = \frac{1}{r}\widehat{\mathbf{grad}}(r\widehat{G}_\theta)\cdot\widehat{\boldsymbol{\tau}}_{\mathsf{x}} = \frac{1}{r}\frac{\partial(r\widehat{G}_\theta)}{\partial\widehat{\boldsymbol{\tau}}_{\mathsf{x}}}. \tag{4.20}$$

Let us assume that $\widehat{\Gamma}_{\mathbf{J}}(t)$ has N connected components such that $\widehat{\Gamma}_{\mathbf{J}}(t) := \bigcup_{k=1}^{N} \widehat{\Gamma}_{\mathbf{J}}^k(t)$. For $k = 1,\dots,N$, we have,

$$\begin{aligned}\int_{\Gamma_{\mathbf{J}}^k(t)} \mathbf{curl}\,\mathbf{H}\cdot\mathbf{n}_{\mathsf{x}}\,\mathrm{d}A_{\mathsf{x}} = I_k &= 2\pi\int_{\widehat{\Gamma}_{\mathbf{J}}^k(t)} \frac{1}{r}\frac{\partial(r\widehat{H}_\theta)}{\partial\widehat{\boldsymbol{\tau}}_{\mathsf{x}}} r\mathrm{d}\widehat{l}_{\mathsf{x}} \\ &= 2\pi\int_{\widehat{\Gamma}_{\mathbf{J}}^k(t)} \frac{\partial(r\widehat{H}_\theta)}{\partial\widehat{\boldsymbol{\tau}}_{\mathsf{x}}}\mathrm{d}\widehat{l}_{\mathsf{x}}.\end{aligned}$$

It is useful to make the change of variable $\tilde{H}_\theta := r\widehat{H}_\theta$ and $\tilde{G}_\theta := r\widehat{G}_\theta$. Following the notation introduced in Section 2.2, we achieve the Eulerian weak formulation written in the meridional section $\widehat{\Omega}(t)$.

Eulerian weak electromagnetic problem with cylindrical symmetry. *Given the currents* $I_k : \widehat{\Gamma}^k_{\mathbf{J}}(t)\times[0,T] \longrightarrow \mathbb{C}$ *for* $k \in N_{\mathrm{I}}$ *and the voltages* $\mathrm{V}_k : \widehat{\Gamma}^k_{\mathbf{J}}(t)\times[0,T] \longrightarrow \mathbb{C}$ *for* $k \in N_{\mathrm{V}}$, *find complex fields* $\tilde{H}_\theta : \widehat{\Omega}(t)\times[0,T] \longrightarrow \mathbb{C}$ *with* $\tilde{H}_\theta = 0$ *on* $\widehat{\Gamma}_{\mathrm{D}}(t)\times[0,T]$, $\lambda : \widehat{\Gamma}_{\mathrm{N}}(t)\times[0,T] \longrightarrow \mathbb{C}$, *and* $\mathrm{V}_k : \widehat{\Gamma}^k_{\mathbf{J}}(t) \times [0,T] \longrightarrow \mathbb{C}$ *for* $k \in N_{\mathrm{I}}$ *such that,*

$$\int_{\widehat{\Omega}(t)} \frac{i\omega\check{\mu}(|\tilde{H}_\theta/r|,\widehat{\Theta})}{r}\tilde{H}_\theta\overline{\tilde{G}_\theta}\,\mathrm{d}r\mathrm{d}z + \int_{\widehat{\Omega}(t)} \frac{1}{\check{\sigma}(\widehat{\Theta})r}\Big(\frac{\partial\tilde{H}_\theta}{\partial z}\frac{\partial\overline{\tilde{G}_\theta}}{\partial z} + \frac{\partial\tilde{H}_\theta}{\partial r}\frac{\partial\overline{\tilde{G}_\theta}}{\partial r}\Big)\,\mathrm{d}r\mathrm{d}z$$
$$+ \int_{\widehat{\Gamma}_{\mathrm{N}}(t)} \lambda\frac{\partial\overline{\tilde{G}_\theta}}{\partial\widehat{\boldsymbol{\tau}}_{\mathsf{x}}}\mathrm{d}\widehat{l}_{\mathsf{x}} + \sum_{k\in N_{\mathrm{I}}}\int_{\widehat{\Gamma}^k_{\mathbf{J}}(t)} \mathrm{V}_k\frac{\partial\overline{\tilde{G}_\theta}}{\partial\widehat{\boldsymbol{\tau}}_{\mathsf{x}}}\mathrm{d}\widehat{l}_{\mathsf{x}} = -\sum_{k\in N_{\mathrm{V}}}\int_{\widehat{\Gamma}^k_{\mathbf{J}}(t)} \mathrm{V}_k\frac{\partial\overline{\tilde{G}_\theta}}{\partial\widehat{\boldsymbol{\tau}}_{\mathsf{x}}}\mathrm{d}\widehat{l}_{\mathsf{x}}, \quad \forall\tilde{G}_\theta \text{ with } \tilde{G}_\theta|_{\widehat{\Gamma}_{\mathrm{D}}(t)} = 0,$$
$$\int_{\widehat{\Gamma}^k_{\mathbf{J}}(t)} \frac{\partial\tilde{H}_\theta}{\partial\widehat{\boldsymbol{\tau}}_{\mathsf{x}}}\mathrm{d}\widehat{l}_{\mathsf{x}} = \frac{\mathrm{I}_k}{2\pi}, \quad \forall k \in N_{\mathrm{I}},$$
$$\int_{\widehat{\Gamma}_{\mathrm{N}}(t)} \overline{\eta}\,\frac{\partial\tilde{H}_\theta}{\partial\widehat{\boldsymbol{\tau}}_{\mathsf{x}}}\mathrm{d}\widehat{l}_{\mathsf{x}} = 0, \quad \forall\eta.$$

By taking into account the cylindrical symmetry, as we did in the Eulerian case, for the Lagrangian formulation we consider

$$\boldsymbol{\mathcal{H}}(\mathsf{p},t) = \widehat{\mathcal{H}}_\theta(\widehat{\mathsf{p}},t)\mathbf{e}_\theta \quad \text{in } \Omega,$$
$$\boldsymbol{\mathcal{G}}(\mathsf{p},t) = \widehat{\mathcal{G}}_\theta(\widehat{\mathsf{p}},t)\mathbf{e}_\theta \quad \text{in } \Omega.$$

Thus, by introducing the change of variable $\tilde{\mathcal{H}}_\theta = r_m\widehat{\mathcal{H}}_\theta$ and $\tilde{\mathcal{G}}_\theta = r_m\widehat{\mathcal{G}}_\theta$, we get the following relations useful to obtain the Lagrangian weak formulation of the electromagnetic problem in the axisymmetric case:

$$\mathbf{F}^{-t}(\mathsf{p},t)\,\boldsymbol{\mathcal{H}}(\mathsf{p},t)\cdot\mathbf{F}^{-t}(\mathsf{p},t)\,\overline{\boldsymbol{\mathcal{G}}}(\mathsf{p},t) = \frac{1}{(r_m+\widehat{u}_r(\widehat{\mathsf{p}},t))^2}\tilde{\mathcal{H}}_\theta(\widehat{\mathsf{p}},t)\,\overline{\tilde{\mathcal{G}}_\theta}(\widehat{\mathsf{p}},t),$$
$$\mathbf{F}(\mathsf{p},t)\,\mathbf{Curl}\,\boldsymbol{\mathcal{H}}(\mathsf{p},t)\cdot\mathbf{F}(\mathsf{p},t)\,\mathbf{Curl}\,\overline{\boldsymbol{\mathcal{G}}}(\mathsf{p},t) = \frac{1}{r_m^2}\widehat{\mathbf{N}}(\widehat{\mathsf{p}},t)\,\widehat{\mathbf{Grad}}\,\tilde{\mathcal{H}}_\theta(\widehat{\mathsf{p}},t)\cdot\widehat{\mathbf{N}}(\widehat{\mathsf{p}},t)\,\widehat{\mathbf{Grad}}\,\overline{\tilde{\mathcal{G}}_\theta}(\widehat{\mathsf{p}},t),$$

being $\widehat{\mathbf{N}}$ the tensor field

$$\widehat{\mathbf{N}}(\widehat{\mathsf{p}},t) = \begin{pmatrix} \dfrac{\partial\widehat{u}_r(\widehat{\mathsf{p}},t)}{\partial z_m} & -1-\dfrac{\partial\widehat{u}_r(\widehat{\mathsf{p}},t)}{\partial r_m} \\ 1+\dfrac{\partial\widehat{u}_z(\widehat{\mathsf{p}},t)}{\partial z_m} & -\dfrac{\partial\widehat{u}_z(\widehat{\mathsf{p}},t)}{\partial r_m} \end{pmatrix}. \tag{4.21}$$

If we follow the notation introduced in Section 2.2, the Lagrangian weak formulation defined in the meridional section $\widehat{\Omega}$ is established:

Lagrangian weak electromagnetic problem with cylindrical symmetry. *Given the currents* $I_k : \widehat{\Gamma}^k_{\mathbf{J}} \times [0,T] \longrightarrow \mathbb{C}$ *for* $k \in N_{\mathrm{I}}$ *and the voltages* $\mathrm{V}_k : \widehat{\Gamma}^k_{\mathbf{J}} \times [0,T] \longrightarrow \mathbb{C}$ *for* $k \in N_{\mathrm{V}}$, *find complex fields* $\tilde{\mathcal{H}}_\theta : \overline{\widehat{\Omega}} \times [0,T] \longrightarrow \mathbb{C}$, *with* $\tilde{\mathcal{H}}_\theta = 0$ *on* $\widehat{\Gamma}_{\mathrm{D}} \times [0,T]$, $\lambda : \widehat{\Gamma}_{\mathrm{N}} \times [0,T] \longrightarrow \mathbb{C}$, *and* $\mathrm{V}_k : \widehat{\Gamma}^k_{\mathbf{J}} \times [0,T] \longrightarrow \mathbb{C}$ *for* $k \in N_{\mathrm{I}}$, *such that,*

$$\int_{\widehat{\Omega}} \frac{i\omega\check{\mu}(|\tilde{\mathcal{H}}_\theta/(r_m+\widehat{u}_r)|,\widehat{\Theta}_m)}{r_m+\widehat{u}_r}\tilde{\mathcal{H}}_\theta\overline{\tilde{\mathcal{G}}_\theta}\,\det\widehat{\mathbf{F}}\,\mathrm{d}r_m\mathrm{d}z_m + \int_{\widehat{\Omega}} \frac{\widehat{\mathbf{N}}\,\widehat{\mathbf{Grad}}\,\tilde{\mathcal{H}}_\theta\cdot\widehat{\mathbf{N}}\,\widehat{\mathbf{Grad}}\,\overline{\tilde{\mathcal{G}}_\theta}}{\check{\sigma}(\widehat{\Theta}_m)\,(r_m+\widehat{u}_r)\det\widehat{\mathbf{F}}}\,\mathrm{d}r_m\mathrm{d}z_m$$
$$+\int_{\widehat{\Gamma}_{\mathrm{N}}}\lambda\frac{\partial\overline{\tilde{\mathcal{G}}_\theta}}{\partial\widehat{\boldsymbol{\tau}}_{\mathsf{p}}}\mathrm{d}\widehat{l}_{\mathsf{p}} + \sum_{k\in N_{\mathrm{I}}}\int_{\widehat{\Gamma}^k_{\mathbf{J}}}\mathrm{V}_k\frac{\partial\overline{\tilde{\mathcal{G}}_\theta}}{\partial\widehat{\boldsymbol{\tau}}_{\mathsf{p}}}\mathrm{d}\widehat{l}_{\mathsf{p}} = -\sum_{k\in N_{\mathrm{V}}}\int_{\widehat{\Gamma}^k_{\mathbf{J}}}\mathrm{V}_k\frac{\partial\overline{\tilde{\mathcal{G}}_\theta}}{\partial\widehat{\boldsymbol{\tau}}_{\mathsf{p}}}\mathrm{d}\widehat{l}_{\mathsf{p}},\quad \forall\tilde{\mathcal{G}}_\theta \text{ with } \tilde{\mathcal{G}}_\theta|_{\widehat{\Gamma}_{\mathrm{D}}}=0,$$
$$\int_{\widehat{\Gamma}^k_{\mathbf{J}}}\frac{\partial\tilde{\mathcal{H}}_\theta}{\partial\widehat{\boldsymbol{\tau}}_{\mathsf{p}}}\mathrm{d}\widehat{l}_{\mathsf{p}} = \frac{\mathrm{I}_k}{2\pi},\quad \forall k\in N_{\mathrm{I}},$$
$$\int_{\widehat{\Gamma}_{\mathrm{N}}}\overline{\eta}\,\frac{\partial\tilde{\mathcal{H}}_\theta}{\partial\widehat{\boldsymbol{\tau}}_{\mathsf{p}}}\mathrm{d}\widehat{l}_{\mathsf{p}} = 0,\quad \forall\eta.$$

Finally, concerning the thermal model, after following very similar steps as those in Section 3.3, the axisymmetric Lagrangian weak formulation for the thermal model with AC heat sources is obtained:

Lagrangian weak thermal problem with AC sources and cylindrical symmetry. *Find a temperature field,* $\widehat{\Theta}_m : \overline{\widehat{\Omega}}\times[0,T] \longrightarrow \mathbb{R}$ *with* $\widehat{\Theta}_m = \widehat{\Theta}^{\mathrm{DT}}_m$ *on* $\widehat{\Gamma}_{\mathrm{DT}}\times(0,T]$ *and* $\widehat{\Theta}_m(\mathsf{p},0) = \widehat{\Theta}^0(\mathsf{p})$ *in* $\overline{\widehat{\Omega}}$, *such that*

$$\int_{\widehat{\Omega}}\widehat{\rho}_0\check{c}_p(\widehat{\Theta}_m)\,\dot{\widehat{\Theta}}_m\,\widehat{\psi}\,r_m\,\mathrm{d}r_m\mathrm{d}z_m$$
$$+\int_{\widehat{\Omega}}\check{k}(\widehat{\Theta}_m)\,\widehat{\mathbf{F}}^{-t}\,\widehat{\mathrm{Grad}}\,\widehat{\Theta}_m\cdot\widehat{\mathbf{F}}^{-t}\,\widehat{\mathrm{Grad}}\,\widehat{\psi}\left(1+\frac{\widehat{u}_r}{r_m}\right)\det\widehat{\mathbf{F}}\,r_m\,\mathrm{d}r_m\mathrm{d}z_m$$
$$-\int_{\widehat{\Gamma}_{\mathrm{RT}}}\left[\widehat{h}_m(\widehat{\Theta}^{\mathrm{C}}_m-\widehat{\Theta}_m)+\sigma_{SB}\widehat{\epsilon}_m\left((\widehat{\Theta}^{\mathrm{R}}_m)^4-\widehat{\Theta}^4_m\right)\right]|\widehat{\mathbf{F}}^{-t}\widehat{\mathbf{n}}_{\mathsf{p}}|\,\widehat{\psi}\left(1+\frac{\widehat{u}_r}{r_m}\right)\det\widehat{\mathbf{F}}\,r_m\,\mathrm{d}\widehat{l}_{\mathsf{p}}$$
$$=\int_{\widehat{\Omega}}\frac{|\widehat{\mathbf{J}}_m|^2}{2\check{\sigma}(\widehat{\Theta}_m)}\widehat{\psi}\left(1+\frac{\widehat{u}_r}{r_m}\right)\det\widehat{\mathbf{F}}\,r_m\,\mathrm{d}r_m\mathrm{d}z_m,\quad\forall\widehat{\psi}\text{ with }\widehat{\psi}|_{\widehat{\Gamma}_{\mathrm{DT}}}=0.$$

Chapter 5

Numerical methods and results

The models presented in Chapters 3 and 4 are discretised in both time and space for numerical resolution and subsequently implemented in a custom-developed computational code. For this purpose, the open-source platform FEniCS [53] is employed, offering a high-level Python interface for solving partial differential equations using the finite element method.

In Section 5.1, a general overview of the time discretisation methods proposed for the numerical solution of the axisymmetric thermal, electrical, electromagnetic, and mechanical models is provided. A combination of high-order Runge–Kutta methods for time integration with finite elements for the spatial discretisation is proposed.

The implementation process has been progressive, starting with simplified versions of the different models and gradually increasing their complexity until the full simulation of electric upsetting processes is addressed. In Section 5.2, in order to validate the implementation of these models in our own code, several tests have been performed. The obtained results are compared with those of robust and proven commercial codes, namely Ansys 2024 R1 and Marc 2020. In some cases, analytical solutions can be obtained, enabling direct comparisons with the results from the proprietary code and allowing us to assess proper implementation. Moreover, convergence analyses in both time and space were carried out in several tests. Once the implementation has been sufficiently validated, the numerical simulation of electric upsetting processes is addressed.

This chapter partially reproduces contents from the following publications:

- M. Benítez, A. Bermúdez, P. Fontán, I. Martínez, P. Salgado (2024). *A Lagrangian approach for solving an axisymmetric thermo-electromagnetic problem. Application to time-varying geometry processes.* Advances in Computational Mathematics, 50, 45. Electronic ISSN: 1572-9044, Print ISSN: 1019-7168. DOI: 10.1007/s10444-024-10121-y

- M. Benítez, A. Bermúdez, P. Fontán, I. Martínez, P. Salgado (2025). *A pure-Lagrangian finite element approach for solving thermo-electrical-mechanical models. Application to electric upsetting.* Finite Elements in Analysis and Design, 251, 104433. Electronic ISSN: 1872-6925, Print ISSN: 0168-874X. DOI: 10.1016/j.finel.2025.104433

5.1 Time discretisation

The space discretisation of the axisymmetric thermal, electrical, electromagnetic and mechanical Lagrangian formulations developed in Chapters 3 and 4 is addressed by using adequate finite element spaces. For this purpose, we suppose a bounded domain with Lipschitz polygonal boundary and consider a suitable family of regular triangulations compatible with the partitions of the boundary, consisting of elements K of diameter $\leq h$. The finite element spaces considered for each of the unknowns will be detailed in Section 5.2 for the different problems addressed.

The space semi-discretised problem constitutes a system of differential-algebraic equations (DAEs) that is solved by using Runge-Kutta schemes. To introduce the fully discretised scheme, we consider a quite general space semi-discretised problem, which has the form

$$\tilde{\mathbf{M}}(\widehat{\mathbf{y}}_d, \widehat{\mathbf{y}}_a)\dot{\widehat{\mathbf{y}}}_d = \tilde{\mathbf{f}}(\widehat{\mathbf{y}}_d, \widehat{\mathbf{y}}_a, t), \tag{5.1a}$$

$$0 = \tilde{\mathbf{g}}(\widehat{\mathbf{y}}_d, \widehat{\mathbf{y}}_a), \tag{5.1b}$$

$$\widehat{\mathbf{y}}_d(\cdot, t) = \overline{\mathbf{y}}_d(\cdot, t), \text{ on } \widehat{\Gamma}_D, \tag{5.1c}$$

$$\widehat{\mathbf{y}}_a(\cdot, t) = \overline{\mathbf{y}}_a(\cdot, t), \text{ on } \widehat{\Gamma}_D, \tag{5.1d}$$

$$\widehat{\mathbf{y}}_d(\cdot, t_0) = \mathbf{y}_d^0, \text{ in } \overline{\widehat{\Omega}}, \tag{5.1e}$$

where $\tilde{\mathbf{M}}$ is a non-singular matrix representing the mass matrix.

We use the notation

$$\widehat{\mathbf{y}} = \begin{bmatrix} \widehat{\mathbf{y}}_d \\ \widehat{\mathbf{y}}_a \end{bmatrix}, \quad \overline{\mathbf{y}} = \begin{bmatrix} \overline{\mathbf{y}}_d \\ \overline{\mathbf{y}}_a \end{bmatrix}, \quad \mathbf{f} = \begin{bmatrix} \tilde{\mathbf{f}} \\ \tilde{\mathbf{g}} \end{bmatrix}, \quad \mathbf{M} = \begin{bmatrix} \tilde{\mathbf{M}} & 0 \\ 0 & 0 \end{bmatrix}, \tag{5.2}$$

to write the problem in a more compact form, namely,

$$\mathbf{M}(\widehat{\mathbf{y}})\dot{\widehat{\mathbf{y}}} = \mathbf{f}(\widehat{\mathbf{y}}, t), \tag{5.3a}$$

$$\widehat{\mathbf{y}}(\cdot, t) = \overline{\mathbf{y}}(\cdot, t), \text{ on } \widehat{\Gamma}_D, \tag{5.3b}$$

$$\widehat{\mathbf{y}}_d(\cdot, t_0) = \mathbf{y}_d^0, \text{ in } \overline{\widehat{\Omega}}. \tag{5.3c}$$

In order to solve these coupled problems, an implicit Runge-Kutta method defined in the PETSc framework will be used. The PETSc library [6, 7, 8] includes a temporal integration module called *time stepping ode solver* [2] allowing for the numerical resolution of ODEs and DAEs by means of different numerical schemes (Runge-Kutta, Rosenbrock-Wanner, BDF).

For the resolution of the type of problem stated in (5.3), the family of schemes called *ARKIMEX* is generally considered, consisting of Runge-Kutta additive methods where it is possible to separate the problem into two parts, one treated implicitly and the other one explicitly. In the case of DAEs, only the implicit strategy involving the use of DIRK methods (Diagonal Implicit Runge-Kutta) is used.

Specifically, in problem (5.3), at each time instant t_n, $\widehat{\mathbf{y}}^{n-1} \approx \widehat{\mathbf{y}}(\cdot, t_{n-1})$ and the following

system of nonlinear equations is solved for each stage $i \in [1, s]$ of the method:

$$\check{\mathbf{f}}(\mathbf{Y}_{n,i}, \dot{\mathbf{Y}}_{n,i}, t_{n-1} + c_i \Delta t) = \mathbf{M}(\mathbf{Y}_{n,i})\dot{\mathbf{Y}}_{n,i} - \mathbf{f}(\mathbf{Y}_{n,i}, t_{n-1} + c_i \Delta t) = 0, \tag{5.4a}$$

$$\mathbf{Z} = \widehat{\mathbf{y}}^{n-1} + \Delta t \sum_{j=1}^{i-1} a_{ij} \dot{\mathbf{Y}}_{n,j}, \tag{5.4b}$$

$$\dot{\mathbf{Y}}_{n,i} = \frac{1}{\Delta t}(\mathbf{Y}_{n,i} - \mathbf{Z}), \tag{5.4c}$$

whose Jacobian matrix can be obtained by applying the chain rule and using (5.4c):

$$\begin{aligned} \frac{\mathrm{d}}{\mathrm{d}\mathbf{Y}_{n,i}}(\check{\mathbf{f}}(\mathbf{Y}_{n,i}, \dot{\mathbf{Y}}_{n,i}(\mathbf{Y}_{n,i}), \cdot)) &= \frac{\partial \check{\mathbf{f}}}{\partial \dot{\mathbf{Y}}_{n,i}}(\mathbf{Y}_{n,i}, \dot{\mathbf{Y}}_{n,i}(\mathbf{Y}_{n,i}), \cdot)\frac{\partial \dot{\mathbf{Y}}_{n,i}}{\partial \mathbf{Y}_{n,i}} + \frac{\partial \check{\mathbf{f}}}{\partial \mathbf{Y}_{n,i}}(\mathbf{Y}_{n,i}, \dot{\mathbf{Y}}_{n,i}(\mathbf{Y}_{n,i}), \cdot) \\ &= \frac{1}{\Delta t}\frac{\partial \check{\mathbf{f}}}{\partial \dot{\mathbf{Y}}_{n,i}}(\mathbf{Y}_{n,i}, \dot{\mathbf{Y}}_{n,i}(\mathbf{Y}_{n,i}), \cdot) + \frac{\partial \check{\mathbf{f}}}{\partial \mathbf{Y}_{n,i}}(\mathbf{Y}_{n,i}, \dot{\mathbf{Y}}_{n,i}(\mathbf{Y}_{n,i}), \cdot) \end{aligned} \tag{5.5}$$

Therefore, in order to solve the problem, two functions have to be defined in the PETSc module:

- $\check{\mathbf{f}}(\mathbf{y}, \dot{\mathbf{y}}, t)$,
- $\frac{\mathrm{d}\check{\mathbf{f}}}{\mathrm{d}\mathbf{y}}(\mathbf{y}, \dot{\mathbf{y}}, t, \Delta t)$.

The module includes strategies for adaptive timestepping based on local error estimates that are also exploited.

Let us note that, since the electromagnetic model involves a complex formulation, the real and imaginary parts of the corresponding equations are considered separately in the numerical resolution in proprietary code.

5.2 Results and discussion

The purpose of the proprietary code developed in Python-FEniCS is the accurate numerical resolution of electric upsetting problems. However, before addressing those real-world cases, it is essential to validate the own-developed code. For that purpose, increasingly difficult tests are performed and the achieved results are compared with commercial software or analytical solutions, when possible. Once the validation stage has been satisfactorily completed, the simulation of the in-die and free electric upsetting processes is addressed.

5.2.1 Validation tests

This section contains a series of validation tests, arranged in order of increasing complexity. All computations are performed under axisymmetric conditions, with the reference configuration defined as a rectangle of radius R and height L, as illustrated in Figure 5.1. The boundaries of this axisymmetric domain, $\widehat{\Omega}$, are denoted as $\widehat{\Gamma}_1$ ($z_m = 0$), $\widehat{\Gamma}_2$ ($r_m = R$), $\widehat{\Gamma}_3$ ($z_m = L$) and $\widehat{\Gamma}_4$ ($r_m = 0$), such that $\partial\widehat{\Omega} = \bigcup_{i=1}^{4} \widehat{\Gamma}_i$. Notice that $\widehat{\Gamma}_4$ coincides with the axis of symmetry.

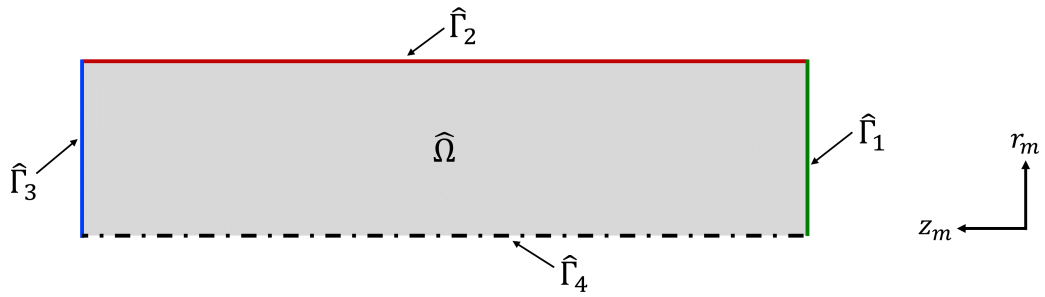

Figure 5.1: Domain for validation tests.

5.2.1.1 Test 1. Electromagnetic model with analytical solution

The implementation of the axisymmetric weak formulation for the electromagnetic model in Section 4.3 is tested for a problem with a known analytical solution. It is assumed that there are no temperature variations or displacements from the reference configuration.

The dimensions of the domain are $R = 0.025$ m and $L = 0.5$ m, and the material has electrical conductivity $\sigma = 2\times10^7\ (\Omega\,\mathrm{m})^{-1}$ and vacuum magnetic permeability $\mu = \mu_0 = 4\pi\times10^{-7}\ \mathrm{H\,m^{-1}}$. A sinusoidal electrical current enters through $\widehat{\Gamma}_3$ and exits through $\widehat{\Gamma}_1$, with angular frequency $\omega = 1000\pi\ \mathrm{rad\,s^{-1}}$ and amplitude $I_3 = 10^3/\sqrt{2}$ A. There is no current flow through $\widehat{\Gamma}_2$. The electric potential reference is set on the port $\widehat{\Gamma}_1$, i.e., $\mathrm{V}_1 = 0$. Moreover, a symmetry condition ($\tilde{\mathcal{H}}_\theta = 0$) is assumed on $\widehat{\Gamma}_4$.

It can be shown (see [18] for further details) that the analytical solution of this problem is

$$\tilde{\mathcal{H}}_\theta(r_m) = r_m \frac{I_3}{2\pi R}\frac{\mathcal{I}_1(\gamma r_m)}{\mathcal{I}_1(\gamma R)}, \tag{5.6}$$

where $\mathcal{I}_1$ is the modified Bessel function of the first kind of order 1 and $\gamma = \sqrt{i\omega\mu\sigma}$. Note that, since the couplings with the other models are absent and the amplitude of the current source is constant, the solution of the electromagnetic model is time-independent.

In Figure 5.2, the analytical solution is compared with the numerical one obtained using proprietary code along the segment $z_m = L/2$, for the real and imaginary parts of $\tilde{\mathcal{H}}_\theta$.

This problem has been solved by using a continuous piecewise-linear finite element discretisation for $\tilde{\mathcal{H}}_\theta$ and piecewise-constant elements along the edges of the boundary $\widehat{\Gamma}_2$ for the Lagrange multiplier λ. We are about to check the spatial convergence behaviour of the solution. For that purpose, errors between the discrete numerical solution and the analytical solution are computed by using quadrature formulas on mesh vertices. In particular, the axisymmetric electromagnetic weak formulation in Section 4.3 encourages the use of the discrete approximation of the norm in space $H^{1,-1}$ (see Appendix A) to compute the error for $\tilde{\mathcal{H}}_\theta$. This error is shown in Figure 5.3-left as a function of h^{-1}, being h the mesh size parameter. First-order accuracy is achieved with the $H_h^{1,-1}$ norm, in accordance with [19], where theoretical and numerical convergence results are provided for this formulation.

Note that the electric potential on $\widehat{\Gamma}_3$ is also a complex unknown of this problem, and its

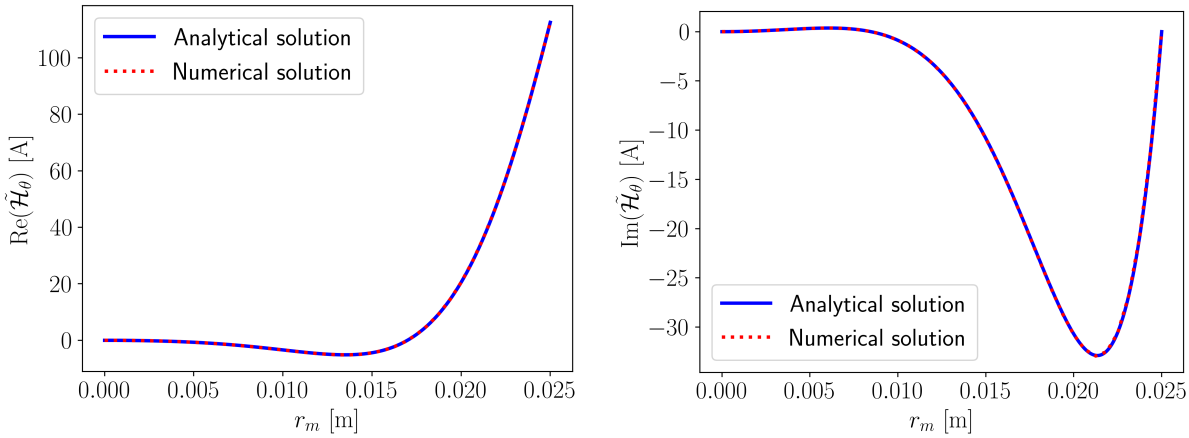

Figure 5.2: Test 1: comparison of analytical and numerical solutions for $\mathrm{Re}(\tilde{\mathcal{H}}_\theta)$ (left) and $\mathrm{Im}(\tilde{\mathcal{H}}_\theta)$ (right).

analytical expression is given by

$$V_3 = \frac{I_3 \gamma L}{2\pi\sigma R} \frac{\mathcal{I}_0(\gamma R)}{\mathcal{I}_1(\gamma R)}, \tag{5.7}$$

where $\mathcal{I}_0$ is the modified Bessel function of the first kind of order 0.

Since V_3 is approximated by a constant complex number on $\widehat{\Gamma}_3$, the difference between the analytical and discrete values is computed using the complex norm $|\cdot|$ for each mesh discretisation. Figure 5.3-right shows this error which illustrates a second-order accuracy. This result is consistent with the findings presented in [23] for a similar mixed formulation.

5.2.1.2 Test 2. Elastic mechanical model with analytical solution

An analytical solution to the mechanical model outlined in Section 3.1 can be derived for a specific case within the hyperelastic strain regime. This scenario assumes that $\mathbf{F}^p = \mathbf{I}$ for all $t \in [0, T]$, effectively neglecting viscoplastic deformations. Specifically, equations (3.61) through (3.63) are considered. The inertial and volume force density terms are omitted from equation (3.61), and this simplification applies to this test case and all subsequent numerical results. Additionally, the initial displacement is assumed to be zero.

A rectangular domain with $R = 0.025$ m and $L = 0.5$ m is considered, with Young's modulus $E = 2 \times 10^{11}$ N m^{-2} and Poisson's coefficient $\nu = 0.2845$. The initial domain is deformed until $T = 100$ s by a resultant force, $\mathbf{P}(t)$, applied on $\widehat{\Gamma}_3$ and given by

$$\mathbf{P}(t) = \pi R^2 E \frac{\ln\left(1 - \frac{ct}{L}\right)}{1 - \frac{ct}{L}} \mathbf{e}_z \quad \text{on } \widehat{\Gamma}_3 \times (0, T], \tag{5.8}$$

where $c = L/(2T) = 0.0025$ m s^{-1} is adjusted so that the cylinder is compressed by half at the end of the time. This is possible because a vertical planar obstacle is placed along $\widehat{\Gamma}_1$ and mechanical contact takes place. Therefore, the mechanical contact on this boundary is modelled by the reaction force in (3.71) and by (3.83), with $\widehat{M}\left(\widehat{\mathsf{X}}(\widehat{\mathsf{p}}, t)\right) = z_m + \widehat{u}_z(\widehat{\mathsf{p}}, t)$ on $\widehat{\Gamma}_1 \times (0, T]$.

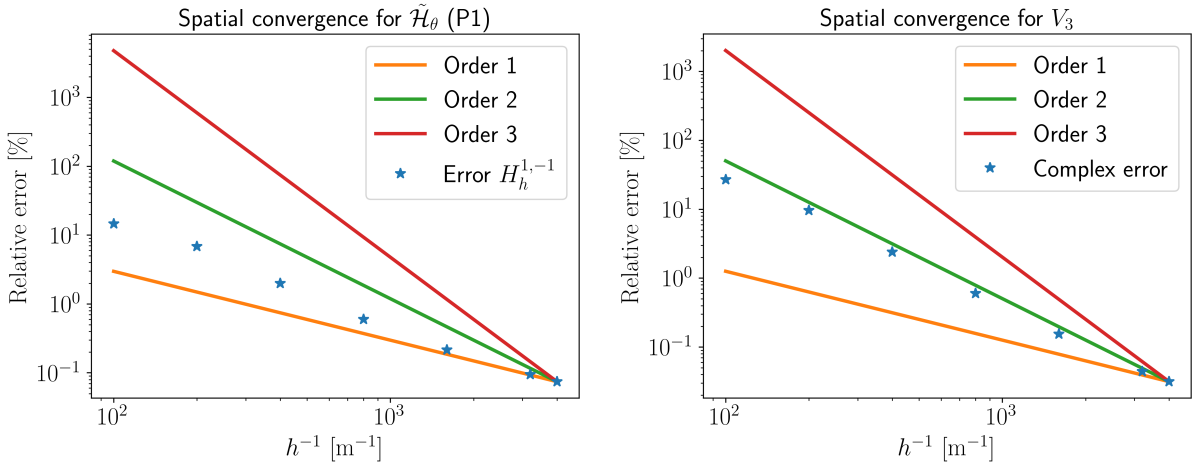

Figure 5.3: Test 1: computed $H_h^{1,-1}$ error for $\tilde{\mathcal{H}}_\theta$ (left) and complex error for V_3 (right), versus h^{-1}, in log-log scale.

Furthermore, to uniquely determine $\widehat{\mathbf{u}}$ and $\widehat{\zeta}_m$ in $\widehat{\Omega}$, the boundary $\widehat{\Gamma}_2$ is assumed to be stress-free, and symmetry conditions are applied on $\widehat{\Gamma}_4$.

The analytical solution of this problem is given by

$$\widehat{u}_r(r_m, t) = \left[\left(1 - \frac{ct}{L}\right)^{-\nu} - 1\right] r_m, \tag{5.9}$$

$$\widehat{u}_z(z_m, t) = -\frac{ct}{L} z_m, \tag{5.10}$$

$$\widehat{\zeta}_m(t) = -E\left(1 - \frac{ct}{L}\right)^{2\nu-1} \ln\left(1 - \frac{ct}{L}\right). \tag{5.11}$$

Figure 5.4 shows a comparison between the analytical and numerical solutions for the maximum radial displacement achieved over time, $\widehat{u}_r^{max}(t)$, and for the evolution of the (constant) Lagrange contact multiplier, $\widehat{\zeta}_m$, on boundary $\widehat{\Gamma}_1$. This problem was solved numerically using a continuous, piecewise-linear finite element discretisation for $\widehat{\mathbf{u}}$ and constant, discontinuous finite elements for $\widehat{\zeta}_m$. Time discretisation was performed via the implicit Euler method with uniform time steps and $N = 100$ steps. All computations were carried out relative to the initial reference configuration, without any field reinitialisation.

To evaluate the robustness of this method –specially under conditions where avoiding severe mesh distortion is critical– the test was repeated with a reinitialisation procedure triggered by a distortion criterion. Specifically, when the determinant of the deformation gradient, $\det \mathbf{F}$, falls below a preset threshold (chosen here as 0.9 for demonstration), the mesh is deemed excessively distorted relative to the reference configuration. At this point, both the involved field variables are reinitialised and, if necessary, remeshing is performed. Subsequent calculations are then conducted with respect to the new reference configuration, which corresponds to the configuration just prior to reinitialisation.

In addition to the reinitialisation techniques, adaptive time step methods are considered.

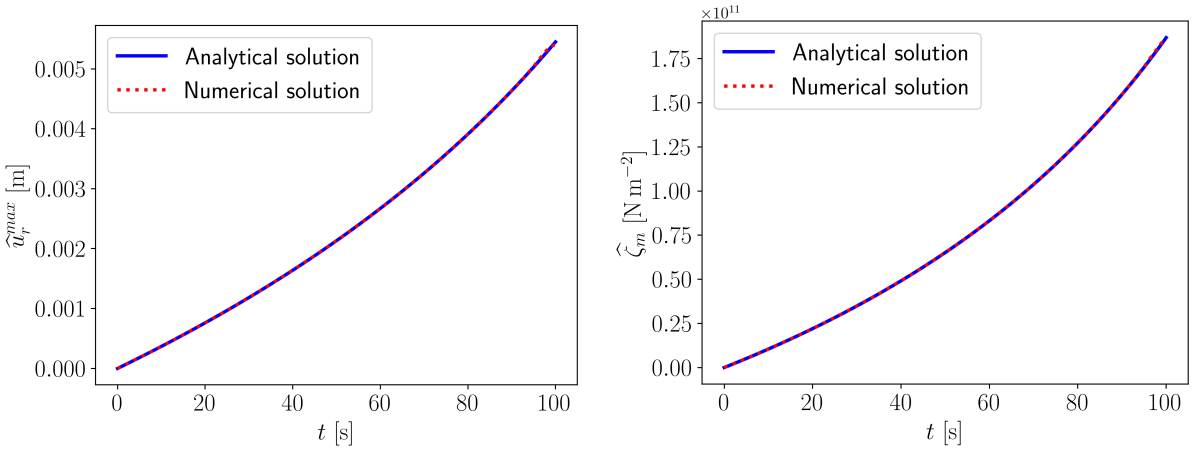

Figure 5.4: Test 2: comparison of analytical and numerical solutions for $\widehat{u}_r^{max}$ (left) and $\widehat{\zeta}_m$ (right).

These methods, provided by PETSc [2], are necessary for complex simulations and also facilitate the restart of calculations after the reinitialisation process, when smaller time steps are recommended.

Figure 5.5 presents the simulation results following reinitialisation, illustrating two metrics relative to the current reference configuration at each time instant: maximum radial displacement, denoted $\widehat{u}_{r,\tau_i}^{\max}$ (blue dots), and minimum of the determinant of the deformation gradient, $\det(\mathbf{F}_{\tau_i})^{\min}$ (red dots).

These quantities are computed with respect to the current reference configuration at each time instant. The initial reference configuration starts at $\tau_0 = 0$ s and, after the first and second reinitialisation processes, the new reference configurations are denoted by τ_1 and τ_2, respectively, being $\tau_1 = 44.24$ s and $\tau_2 = 79.82$ s the instants when the reinitialisation criteria ($\det \mathbf{F}_{\tau_i} < 0.9$) is fulfilled for the first and second time.

Additionally, the cumulative maximum radial displacement (solid blue line) and the total determinant of the deformation gradient (solid red line) are calculated with respect to the original reference configuration, using equations (3.144) and (3.141), respectively. These results align closely with those obtained when no reinitialisation is applied, and they agree with the analytical solution, as expected.

5.2.1.3 Test 3. Elastic mechanical model under complex contact constraints

In Test 2, a vertical planar static obstacle was considered, so contact was already taken into account. However, to validate the implementation of this important feature of the mechanical model, the simulation results from the proprietary code were compared with those from the commercial software Marc, now using more complex obstacles.

The hyperelastic behaviour and equations (3.61)-(3.63) are still applied in an axisymmetric domain with $R = 0.05$ m and $L = 0.05$ m, with Young's modulus $E = 2 \times 10^{11}$ N m^{-2} and Poisson's coefficient $\nu = 0.2845$. The total simulation time for this test is $T = 20$ s and the

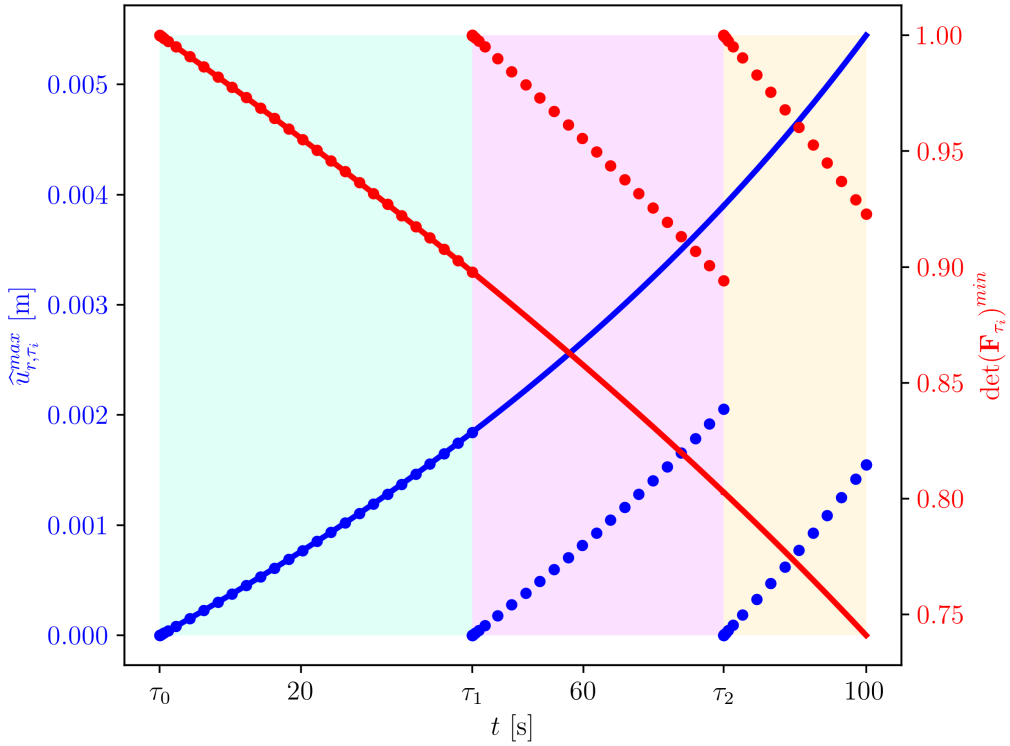

Figure 5.5: Test 2: maximum radial displacement (blue dots) and minimum determinant of the deformation gradient (red dots) at each time instant, with respect to the current reference configuration, starting at time τ_i and limited by the different background colours. The cumulative $\widehat{u}_r^{max}$ and $\det(\mathbf{F})^{min}$ are also shown in blue and red solid lines, respectively.

normal component of the displacement is prescribed on $\widehat{\Gamma}_3$, as

$$\widehat{u}_z(r_m, L, t) = -0.001t \quad \text{on } \widehat{\Gamma}_3 \times (0, T]. \tag{5.12}$$

This test includes two different obstacles: a static circular obstacle and a moving horizontal one. The circular obstacle has a radius of 0.0125 m, its centre is located at $z_m = -0.02$ m along $\widehat{\Gamma}_4$. It is subject to contact with the boundary $\widehat{\Gamma}_1$. Meanwhile, a planar horizontal obstacle, initially located at $r_m = 0.05$ m and in contact with $\widehat{\Gamma}_2$, moves at a constant velocity of 0.0005 $\mathrm{m\,s^{-1}}$ in the negative r_m-direction. Consequently, the reaction forces associated with the mechanical contact in equation (3.71) are considered on both $\widehat{\Gamma}_1$ and $\widehat{\Gamma}_2$, and the obstacles are defined by

$$\widehat{M}\left(\widehat{\mathsf{X}}(\widehat{\mathsf{p}}, t)\right) = (r_m + \widehat{u}_r(\widehat{\mathsf{p}}, t))^2 + (z_m + \widehat{u}_z(\widehat{\mathsf{p}}, t) + 0.02)^2 - (0.0125)^2 \quad \text{on } \widehat{\Gamma}_1 \times (0, T], \tag{5.13}$$

$$\widehat{M}\left(\widehat{\mathsf{X}}(\widehat{\mathsf{p}}, t)\right) = 0.05 - 0.0005t - (r_m + \widehat{u}_r(\widehat{\mathsf{p}}, t)) \quad \text{on } \widehat{\Gamma}_2 \times (0, T]. \tag{5.14}$$

Note that from a 3D perspective, the problem involves a cylinder compressed by an infinitely long surrounding ring and deformed against a spherical obstacle at one of its ends.

The magnitude of the displacement field in the deformed configuration, in the presence of both obstacles at two different time instants, is shown in Figures 5.6 and 5.7. The results demonstrate good agreement between the proprietary and commercial codes. Note that the colour distributions in the two scales are different.

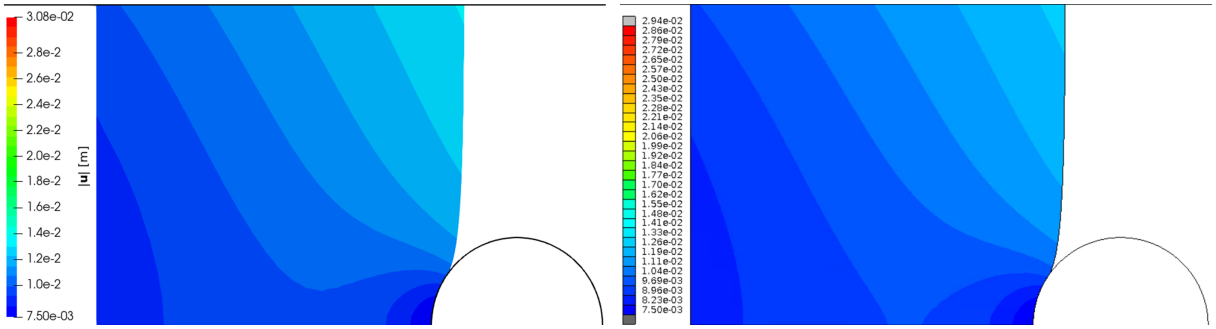

Figure 5.6: Test 3: displacement magnitude in proprietary pure-Lagrangian code (left) and Marc code (right) at $t = 8.6$ s, with both obstacles sketched in black lines.

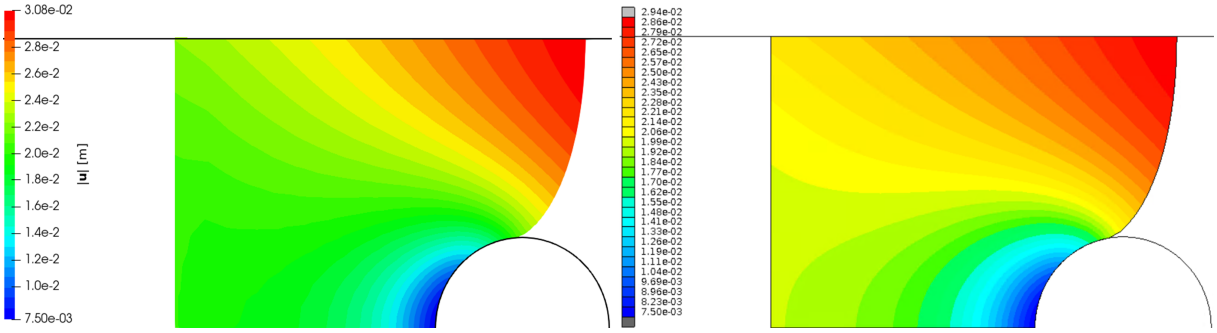

Figure 5.7: Test 3: displacement magnitude in proprietary pure-Lagrangian code (left) and Marc code (right) at $t = 20$ s, with both obstacles sketched in black lines.

5.2.1.4 Test 4. Elasto-viscoplastic mechanical model with prescribed temperature

The mechanical model, accounting for both elastic and viscoplastic deformations, is now considered. Furthermore, to prevent uniform deformations, a non-uniform temperature distribution is assumed to be known throughout the domain at all times.

The axisymmetric rectangular domain extends from $z_m = 0.25$ m to $z_m = 0.375$ m (i.e., $L = 0.125$ m), with $R = 0.025$ m. The simulation lasts up to $T = 100$ s. The known temperature distribution (in K) is given by

$$\Theta_m(\mathsf{p}, t) = -17600 z_m^2 + 8800 z_m + 300. \tag{5.15}$$

The material considered in this study is a typical steel, and the corresponding elastic parameters $\check{E}$ (Young's modulus) and $\check{\nu}$ (Poisson's ratio) are temperature-dependent. More precisely, they

are given by

$$\check{E}(\Theta) = 1.333 \times 10^{11} \sin\left(1.005 \times 10^{-6}\Theta + 0.958\right) + 1.072 \times 10^{11} \sin\left(2.159 \times 10^{-3}\Theta + 0.879\right) + 1.323 \times 10^{10} \sin\left(7.401 \times 10^{-3}\Theta + 1.254\right), \tag{5.16}$$

$$\check{\nu}(\Theta) = \begin{cases} 6.353 \times 10^{-10}\Theta^{2.602} + 0.2828 & \text{if } \Theta \leq 923.15, \\ 0.3158 & \text{if } \Theta > 923.15, \end{cases} \tag{5.17}$$

and are graphically represented in Figure 5.8.

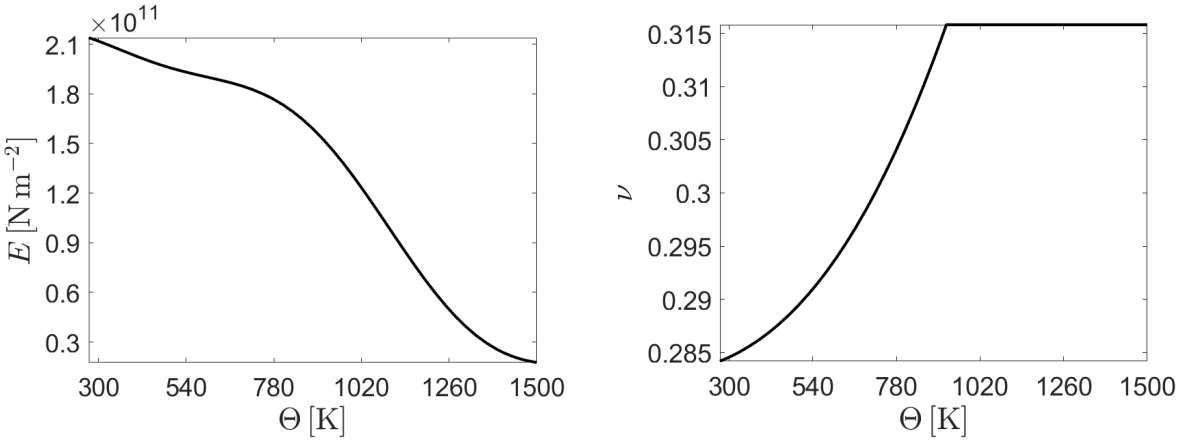

Figure 5.8: Young's modulus (left) and Poisson's ratio (right) vs. temperature.

The parameters used in the Anand viscoplastic model are listed in Table 5.1, where the deformation resistance at initial time, s^0, is given.

Parameter	$A\,[\mathrm{s}^{-1}]$	$Q\,[\mathrm{J\,mol}^{-1}]$	ξ	$h_0\,[\mathrm{Pa}]$	$\tilde{s}\,[\mathrm{Pa}]$	m	a	n	$s^0\,[\mathrm{Pa}]$
Value	10^{11}	$2.703 \cdot 10^5$	1.15	$13.29 \cdot 10^8$	$1.476 \cdot 10^8$	0.147	1	0.06869	$0.43 \cdot 10^8$

Table 5.1: Parameters used in the Anand model.

To satisfy symmetry conditions, zero normal displacements are enforced on $\widehat{\Gamma}_1$ and $\widehat{\Gamma}_4$. A null Neumann condition (stress-free) is imposed on $\widehat{\Gamma}_2$, while a non-follower resultant force, represented in Figure 5.9, is applied over time on $\widehat{\Gamma}_3$, namely,

$$\mathbf{P}(t) = \pi(0.025)^2 \times 5.5 \times 10^7 \frac{\ln\left(1 - 0.005t\right)}{1 - 0.005t}\mathbf{e}_z. \tag{5.18}$$

Convergence analysis

Numerical experiments are conducted to assess the rates of convergence of the various fields involved in this problem, both in time and space. For the time discretisation, the second-order ARKIMEX L2 method (SSP2(2,2,2) in [62]) is employed. Regarding the spatial discretisation,

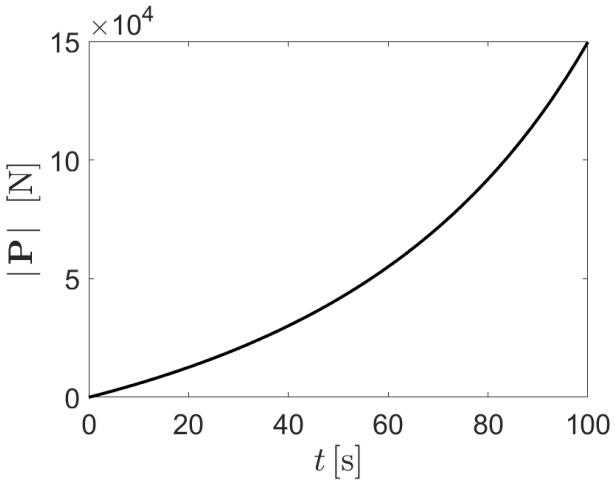

Figure 5.9: Test 4: modulus of the resultant force applied on $\widehat{\Gamma}_3$.

continuous piecewise-linear finite elements are used for each component of the plastic deformation gradient and the deformation resistance, while continuous piecewise-quadratic finite elements are adopted for each displacement component.

To compute the errors between successive discrete numerical approximations and a reference solution, the theoretical L^2 and H^1 norms (see Appendix A) are approximated using quadrature formulas at the mesh vertices. In addition, the maximum norm, l^∞, is considered over time. Thus, if $\mathbf{w}$ denotes the vector of differences between a certain solution and the reference solution for a scalar field at each time instant t_i, $i = 1, \ldots, N$, the computed error norms are given by

$$\|\mathbf{w}\|_{l^\infty(L^2_h(\widehat{\Omega}))} = \max_{i=1}^{N} \|\mathbf{w}_i\|_{L^2_h(\widehat{\Omega})}\,, \tag{5.19}$$

$$\|\mathbf{w}\|_{l^\infty(H^1_h(\widehat{\Omega}))} = \max_{i=1}^{N} \|\mathbf{w}_i\|_{H^1_h(\widehat{\Omega})}\,, \tag{5.20}$$

with natural extensions for vector and tensor fields. From now on, the computed errors are relative –with respect to the reference solution– and expressed as a percentage.

In Figure 5.10 we fix the spatial mesh and show the $l^\infty(L^2_h)$ and $l^\infty(H^1_h)$ errors for displacement, plastic deformation gradient, and deformation resistance, as functions of the number of time steps. A reference solution computed with a finer time step ($N = 3200$) and mesh-size ($h = 0.0025$) is used for comparison. The results demonstrate that the scheme achieves second-order accuracy in time for plastic deformation gradient and deformation resistance, and first-order accuracy in time for displacement.

In Figure 5.11 we represent the computed $l^\infty\left(L^2_h\right)$ and $l^\infty\left(H^1_h\right)$ errors for displacement, plastic deformation gradient, and deformation resistance, as functions of $1/h$, using a fixed small time step, namely, $N = 100$. A reference solution obtained with $N = 100$ and $h = 0.00015625$ has been used for comparison. The results indicate that the scheme achieves second-order accuracy in space for the $l^\infty(L^2_h)$-norm and first-order accuracy in space for the $l^\infty(H^1_h)$-norm.

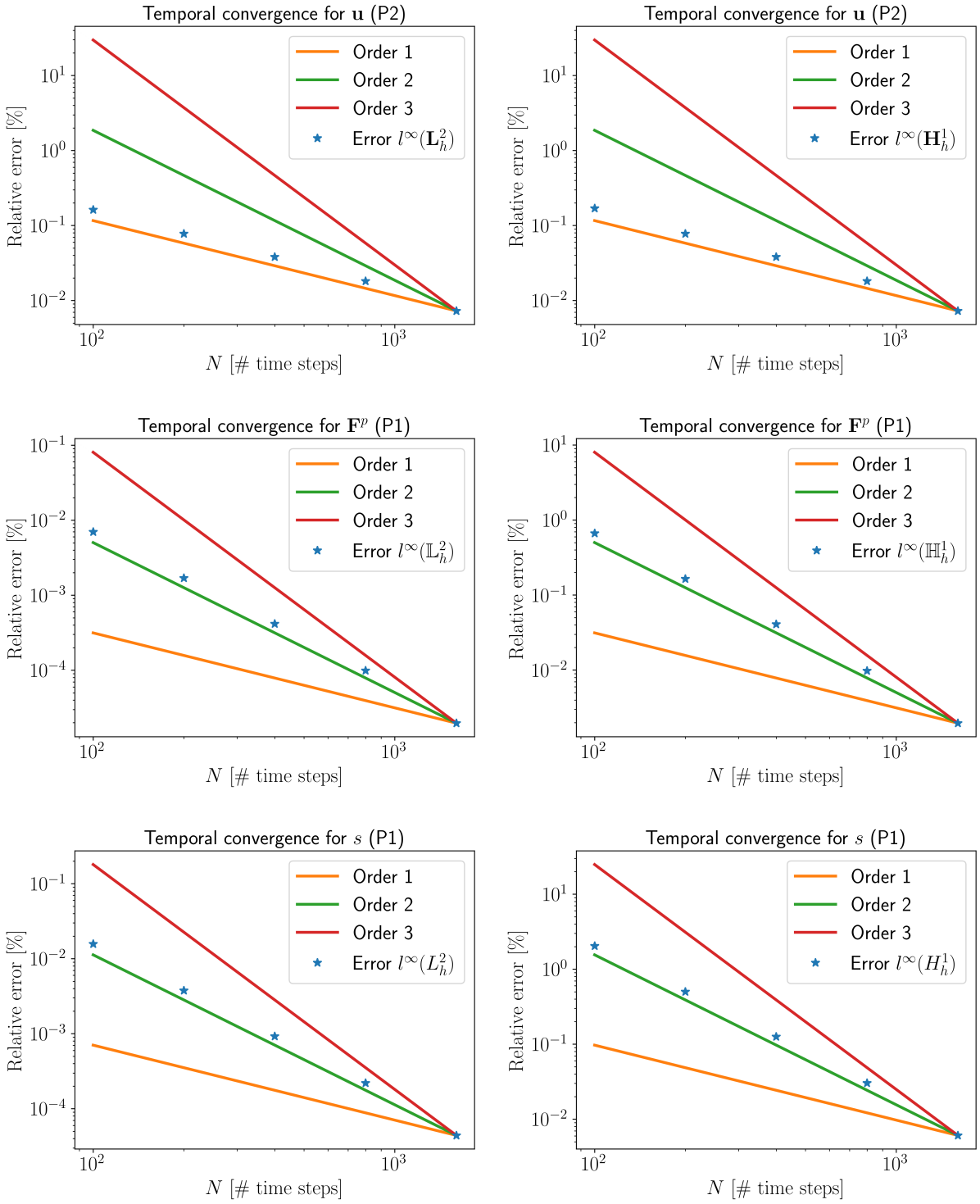

Figure 5.10: Test 4: computed $l^\infty(L^2_h)$ (left) and $l^\infty(H^1_h)$ (right) errors in displacement, plastic deformation gradient, and deformation resistance are plotted against the number of time steps on a log-log scale, using a fixed spatial mesh of size $h = 0.0025$.

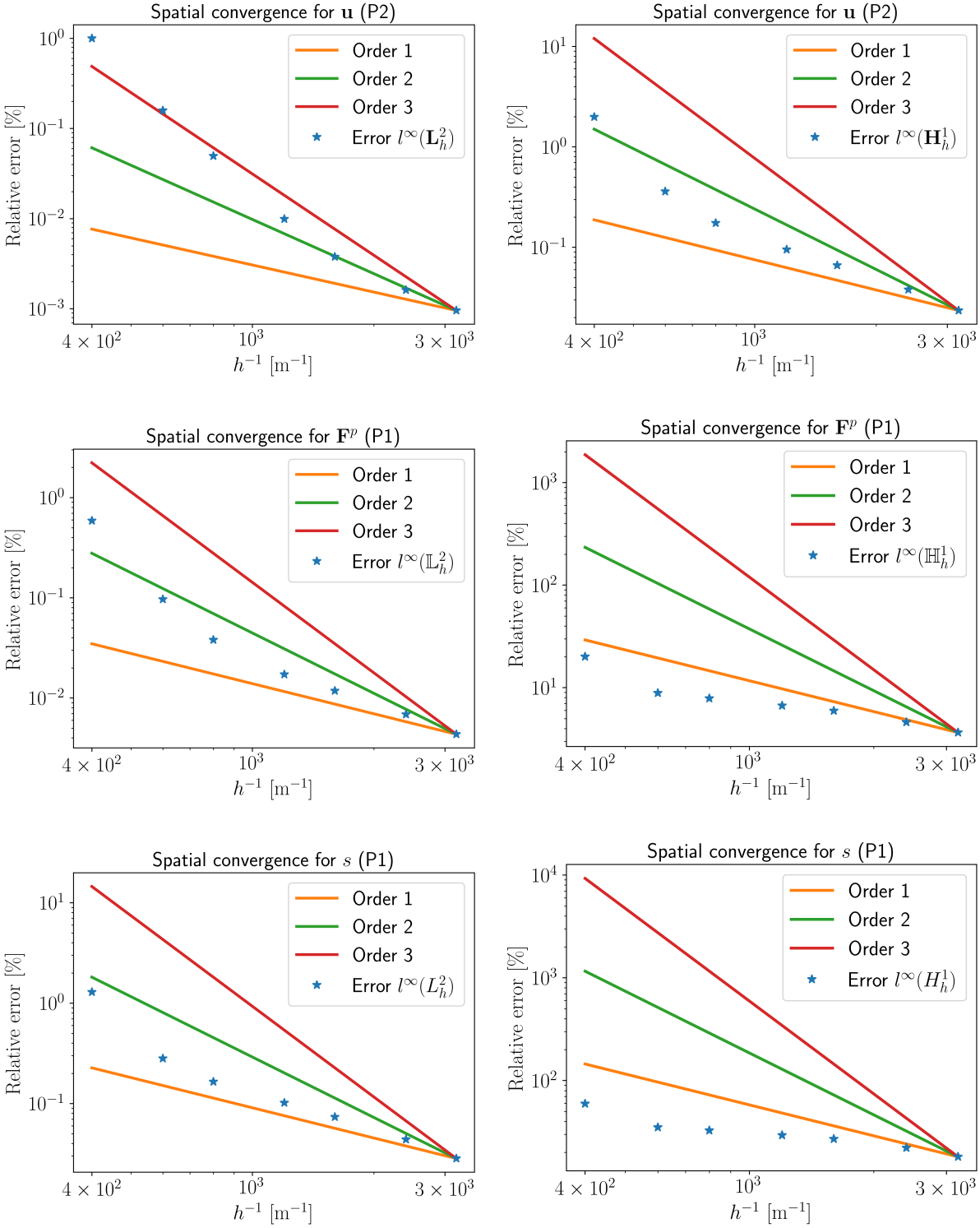

Figure 5.11: Test 4: computed $l^\infty(L^2_h)$ (left) and $l^\infty(H^1_h)$ (right) errors for displacement, plastic deformation gradient, and deformation resistance, plotted against $1/h$ on a log-log scale, for a fixed number of time steps $N = 100$.

Finally, the reference solution for the deformation resistance, s, and the norm of the plastic deformation gradient, $|\mathbf{F}^p|$, are shown in Figure 5.12, in the final deformed configuration.

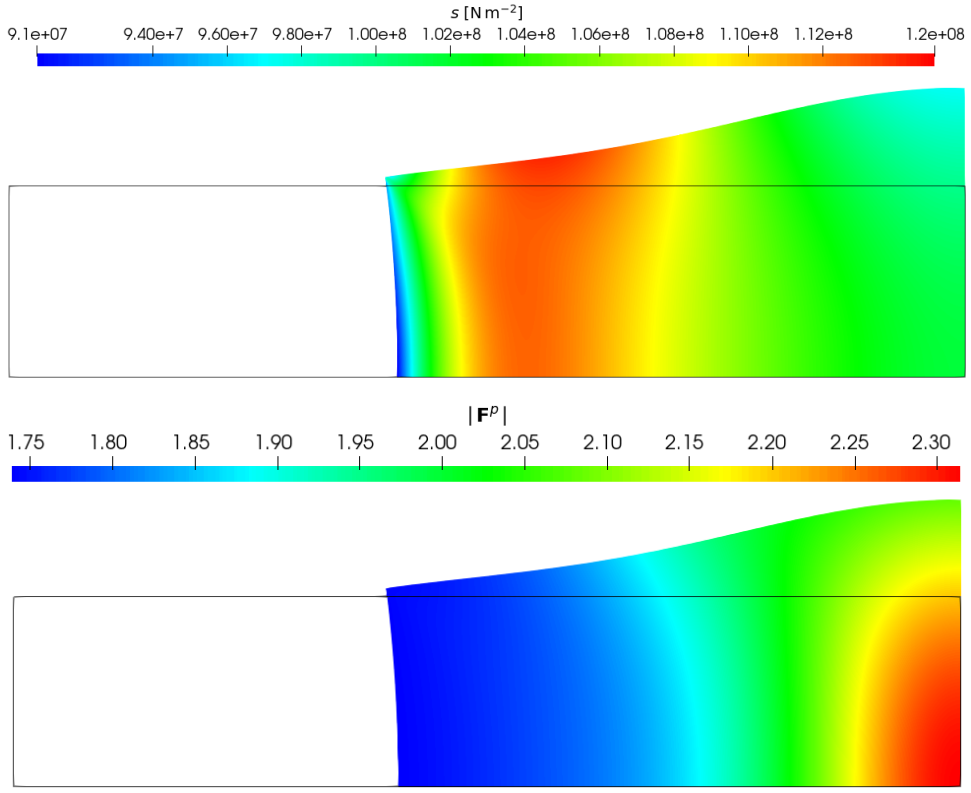

Figure 5.12: Test 4: deformation resistance, s (top), and norm of the plastic deformation gradient, $|\mathbf{F}^p|$ (bottom), in the final deformed configuration. Note that the reference configuration is also outlined.

Analysis of the calculation time

The accuracy of the in-house developed code is compared with that of the commercial simulation packages Ansys and Marc throughout the numerical results presented in this work. This section also compares the temporal discretisation features and total computational time for a specific problem.

For that purpose, the initial version of Test 4, previously used for convergence analysis, is slightly modified. Firstly, despite the modified problem is still symmetric, $\widehat{\Gamma}_1$ is no longer modelled as a symmetry boundary and a different domain is considered, now with $R = 0.025$ m and $L = 0.5$ m (from $z_m = 0$ to $z_m = 0.5$ m). On the other hand, instead of a resultant force, the normal component of the displacement is prescribed on $\widehat{\Gamma}_3$, as

$$\widehat{u}_z(r_m, L, t) = -0.0005t \quad \text{on } \widehat{\Gamma}_3 \times (0, T]. \tag{5.21}$$

Note that, as the solution is symmetric with respect to $z = L/2$, the same normal displace-

ment with opposite direction is applied on $\widehat{\Gamma}_1$, i.e.,

$$\widehat{u}_z(r_m, 0, t) = 0.0005t \quad \text{on } \widehat{\Gamma}_1 \times (0, T]. \tag{5.22}$$

Moreover, the temperature distribution in equation (5.15) is still considered, with a maximum value of 1400 K at $z_m = L/2$ and a minimum value of 300 K at $z_m = 0$ and $z_m = L$.

A very fine spatial discretisation is employed in all three codes, with a mesh size of $h = 6.25 \times 10^{-4}$ m. Starting from an initial number of time steps N in each code, progressively finer time discretisations are applied until the solution stabilises and shows negligible variation. To determine when this point is reached, the maximum values of radial displacement, $\widehat{u}_r$, and inelastic strain, $\widehat{\epsilon^p}$, as defined in equation (3.39), are evaluated. Figure 5.13 presents the maximum values of these quantities for various time discretisations across the three codes. It is worth noting that only the cases with 1000 and 2000 time steps were analysed for our pure-Lagrangian code in FEniCS and for Ansys, as the solutions in both cases were already stable and closely matched. In contrast, the solution obtained with Marc exhibited greater sensitivity to time discretisation; even in the final case considered, it deviated by approximately 5% from the results produced by FEniCS and Ansys.

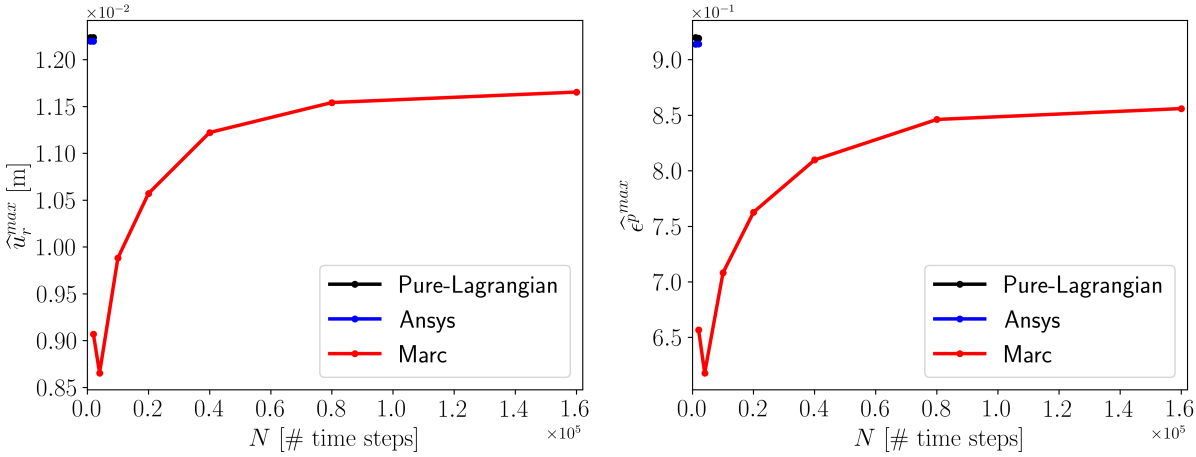

Figure 5.13: Test 4: maximum values attained for $\widehat{u}_r$ (left) and $\widehat{\epsilon^p}$ (right) obtained using the proprietary pure-Lagrangian code, Ansys, and Marc, for varying number of time steps.

Figure 5.14 presents the maximum values of $\widehat{u}_r$ and $\widehat{\epsilon^p}$ over the simulation period ($T = 100$ s). These results correspond to the cases where the solution has effectively converged in each code, specifically the simulations with the highest number of time steps shown in Figure 5.13. It is worth noting that the solutions obtained with our pure-Lagrangian code and Ansys are nearly identical, while the results from Marc consistently differ by approximately 5% throughout the entire simulation.

Moreover, beyond accuracy and convergence, computational efficiency is also a key consideration. Specifically, we examine the time required by each code to reach a solution that is independent of the temporal discretisation, that is, the computational time needed to perform

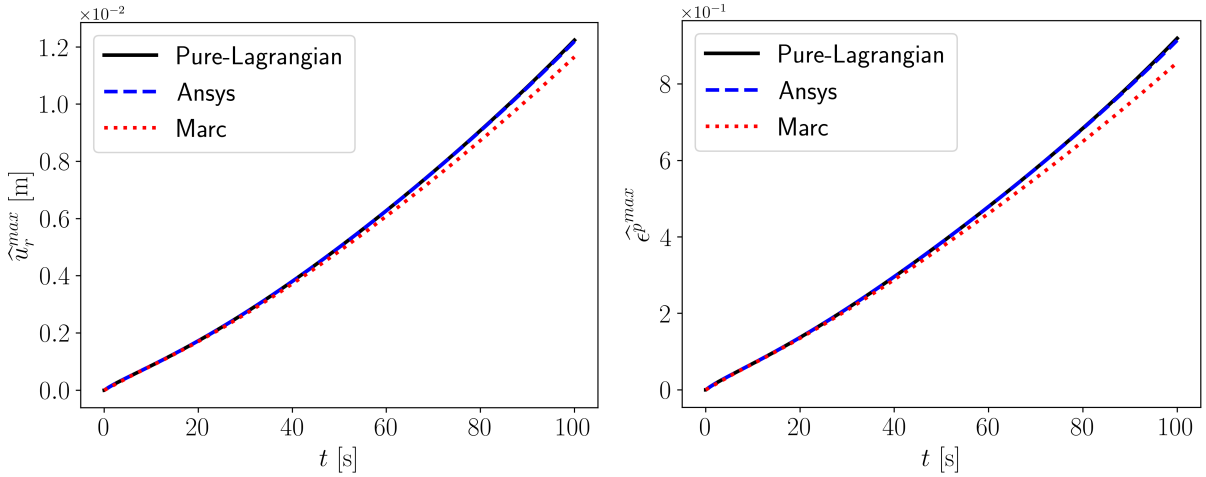

Figure 5.14: Test 4: maximum stabilised values attained for $\widehat{u}_r$ (left) and $\widehat{\epsilon^p}$ (right) in our pure-Lagrangian code, Ansys, and Marc over the simulation time.

the simulation using the highest number of time steps considered in Figure 5.13. These computational times, along with the corresponding number of time steps and the average duration of each time step, are summarised in Table 5.2 for this test. While Marc performs individual time steps more quickly, its total computational time is higher due to the larger number of time steps required to achieve a stable solution. The simulations were performed in a machine that is part of the Mariscal computer cluster hosted at the CESGA. It is equipped with several nodes, each one with 4 processors Intel(R) Xeon(R) Gold 6126 CPU @ 2.60 GHz and 380 GB of RAM. Note that, unlike commercial solvers, our proprietary code does not use parallelisation tools.

Code	**# time steps**	**Total time [s]**	**Time per step [s]**
Pure-Lagrangian	2×10^3	4.8×10^5	240
Ansys	2×10^3	8.7×10^4	43.5
Marc	1.6×10^5	9.8×10^5	6.1

Table 5.2: Number of time steps, total computational time, and average duration per time step required by the proprietary pure-Lagrangian code, Ansys, and Marc to achieve a stable solution.

Let us note that an updated Lagrangian method is used in Ansys to solve the mechanical problem, where the discrete equations are formulated based on the configuration from the previous time step. Additionally, Ansys employs a staggered approach in which a unified code independently solves the electrical, mechanical, and thermal problems. In contrast, the Marc code adopts an Eulerian framework, which involves recalculating the computational domain and reinitialising the motion at each time step. Both strategies require additional computational resources to update and maintain the domain at each time step.

Considering the results obtained in the present test case, it appears that Marc is faster per time step than the other codes; however, the large number of time steps required to reach a

stable solution results in a longer total computational time. By contrast, Ansys and the pure-Lagrangian method converge with significantly fewer time steps, with Ansys demonstrating the shortest overall computation time.

5.2.1.5 Test 5. Thermo-electrical model with known displacement

This example is designed to assess the convergence rates of the scheme proposed in this thesis when applied to a thermo-electrical problem, under the assumption of a known deformation field. The setup aims to replicate the conditions of a typical electric upsetting process.

The electrical direct current model and the transient heat conduction equation are considered within an axisymmetric domain of length $L = 0.165\,\mathrm{m}$ and radius $R = 0.02875\,\mathrm{m}$, subject to appropriate boundary conditions. These models are coupled through Joule heating and temperature-dependent electrical properties. The simulation lasts for $T = 20$ s. A displacement vector field is prescribed, featuring a zero axial component and a radial component $\widehat{u}_r(r_m, z_m)$, given by

$$\widehat{u}_r(r_m, z_m) = \begin{cases} 10^3 r_m \left(-188.2593 z_m + 6.1464\right) z_m^2 & \text{if } z_m \leq 0.02, \\ r_m \left[1.0793 \exp\left(-\left(\dfrac{z_m - 0.0293}{0.03104} \right)^2 \right) + \right. \\ -18.4974 \exp\left(-\left(\dfrac{z_m + 0.03324}{0.01705} \right)^2 \right) + \\ \left. +1.0779 \exp\left(-\left(\dfrac{z_m - 0.4363}{1.263} \right)^2 \right) - 1 \right] & \text{if } z_m > 0.02. \end{cases} \tag{5.23}$$

The physical properties considered in this test are temperature-dependent functions obtained by fitting tables of data corresponding to a typical steel. They are depicted in Figure 5.15. More precisely, for temperature Θ in K,

$$\check{\sigma}(\Theta) = \frac{1}{-4.3306 \times 10^{-13} \left(\Theta - 273.15\right)^2 + 1.0839 \times 10^{-9} \left(\Theta - 273.15\right) + 2.0170 \times 10^{-7}}, \tag{5.24}$$

$$\begin{aligned} \check{k}(\Theta) = {} & -2.7834 \times 10^{-11} \left(\Theta - 273.15\right)^4 + 1.1045 \times 10^{-7} \left(\Theta - 273.15\right)^3 \\ & - 1.3658 \times 10^{-4} \left(\Theta - 273.15\right)^2 + 0.04639 \left(\Theta - 273.15\right) + 34.0140, \end{aligned} \tag{5.25}$$

$$\begin{aligned} \check{c}_p(\Theta) = {} & 660.9 \exp\left(-\left(\frac{\Theta - 996.45}{23.93} \right)^2 \right) + 288.9 \exp\left(-\left(\frac{\Theta - 970.75}{133.5} \right)^2 \right) \\ & + 657.1 \exp\left(-\left(\frac{\Theta - 1181.25}{1497.0} \right)^2 \right). \end{aligned} \tag{5.26}$$

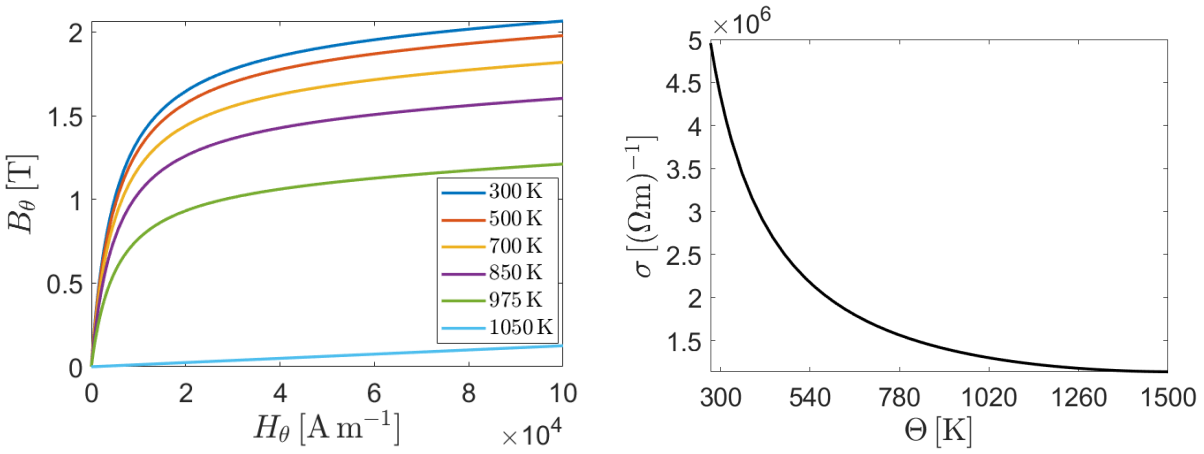

(a) Relationship between H_θ and B_θ at different temperatures (left) and electrical conductivity vs. temperature (right).

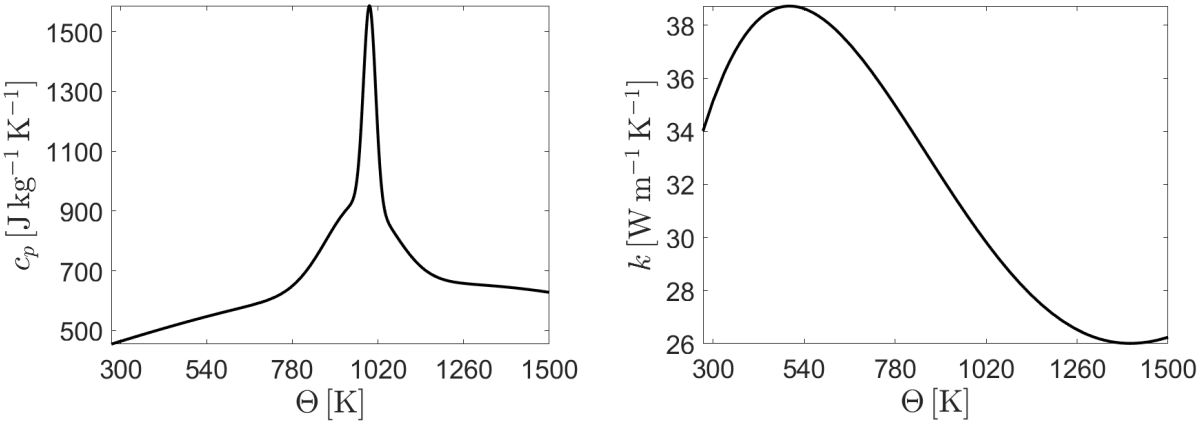

(b) Specific heat (left) and thermal conductivity (right) vs. temperature.

Figure 5.15: Material properties.

A constant mass density $\rho_m = 7799$ kg m^{-3} is assumed. For the thermal model, a zero heat flux condition is imposed on $\widehat{\Gamma}_4$, while convection and radiation boundary conditions are applied on $\widehat{\Gamma}_1$, $\widehat{\Gamma}_2$ and $\widehat{\Gamma}_3$. The heat transfer coefficient is set to $h = 20$ W m^{-2} K^{-1}, with a convection temperature $\widehat{\Theta}^C = 295.15$ K, emissivity $\epsilon = 0.9$, and radiation temperature $\widehat{\Theta}^R = 303.15$ K. The initial temperature is taken as $\widehat{\Theta}^0 = 300$ K.

For the direct current model, we impose a null electric potential on $\widehat{\Gamma}_1$, and a given normal electrical current density on $\widehat{\Gamma}_3$, namely, $\mathbf{J} \cdot \mathbf{n} = -4 \times 10^{10} r_m^2$. Notice that r_m is the radial coordinate and the current travels from $\widehat{\Gamma}_3$ to $\widehat{\Gamma}_1$. On $\widehat{\Gamma}_2$ and $\widehat{\Gamma}_4$, tangential electrical current is considered (natural Neumann boundary conditions).

This problem has been solved by using the second-order ARKIMEX L2 method. For spatial discretisation, continuous piecewise-linear finite elements are employed for both the temperature and the electric potential fields.

In Figure 5.16 we fix the spatial mesh and show $l^\infty(L_h^2)$ and $l^\infty(H_h^1)$ errors for temperature

and voltage as a function of the number of time steps. A reference solution computed with a finer time step ($N = 5120$) and mesh-size ($h = 0.00125$) is used for comparison. We can observe that the scheme shows second-order accuracy in time for temperature and voltage.

In Figure 5.17 we represent the computed $l^\infty\left(L_h^2\right)$ and $l^\infty\left(H_h^1\right)$ errors for temperature and voltage as functions of $1/h$, using a fixed small time step, namely $N = 20$. A reference solution obtained with $N = 20$ and $h = 0.0003125$ has been used for comparison. We can observe that the scheme possesses second-order accuracy in space in the $l^\infty(L_h^2)$-norm, and first-order accuracy in space in the $l^\infty(H_h^1)$-norm. Error estimations for a stationary thermo-electrical model can be found in [54], and the reported spatial convergence order is consistent with the results presented here.

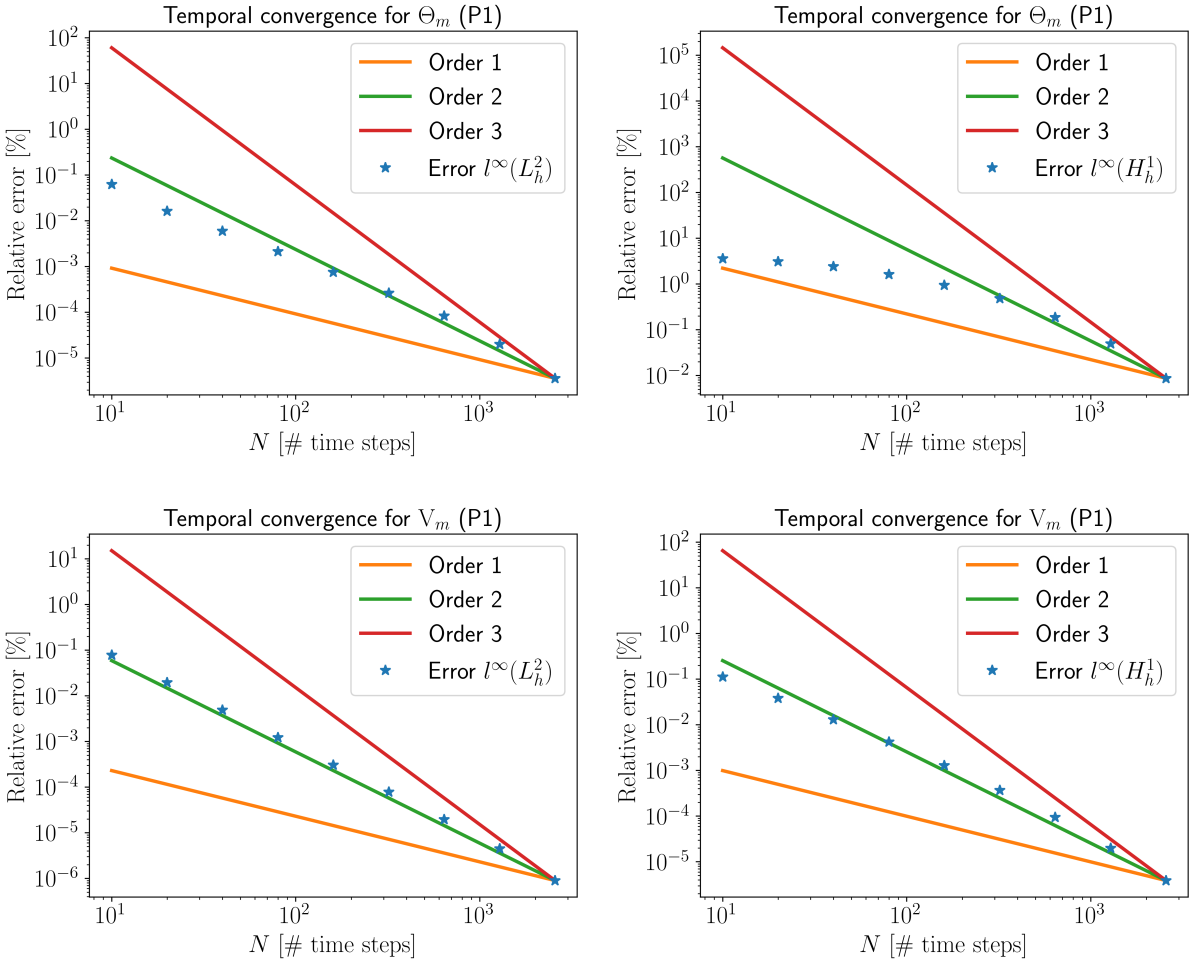

Figure 5.16: Test 5: computed $l^\infty(L_h^2)$ (left) and $l^\infty(H_h^1)$ (right) errors for temperature (top) and voltage (bottom), versus the number of time steps, in log-log scale, for a fixed spatial mesh of size $h = 0.00125$.

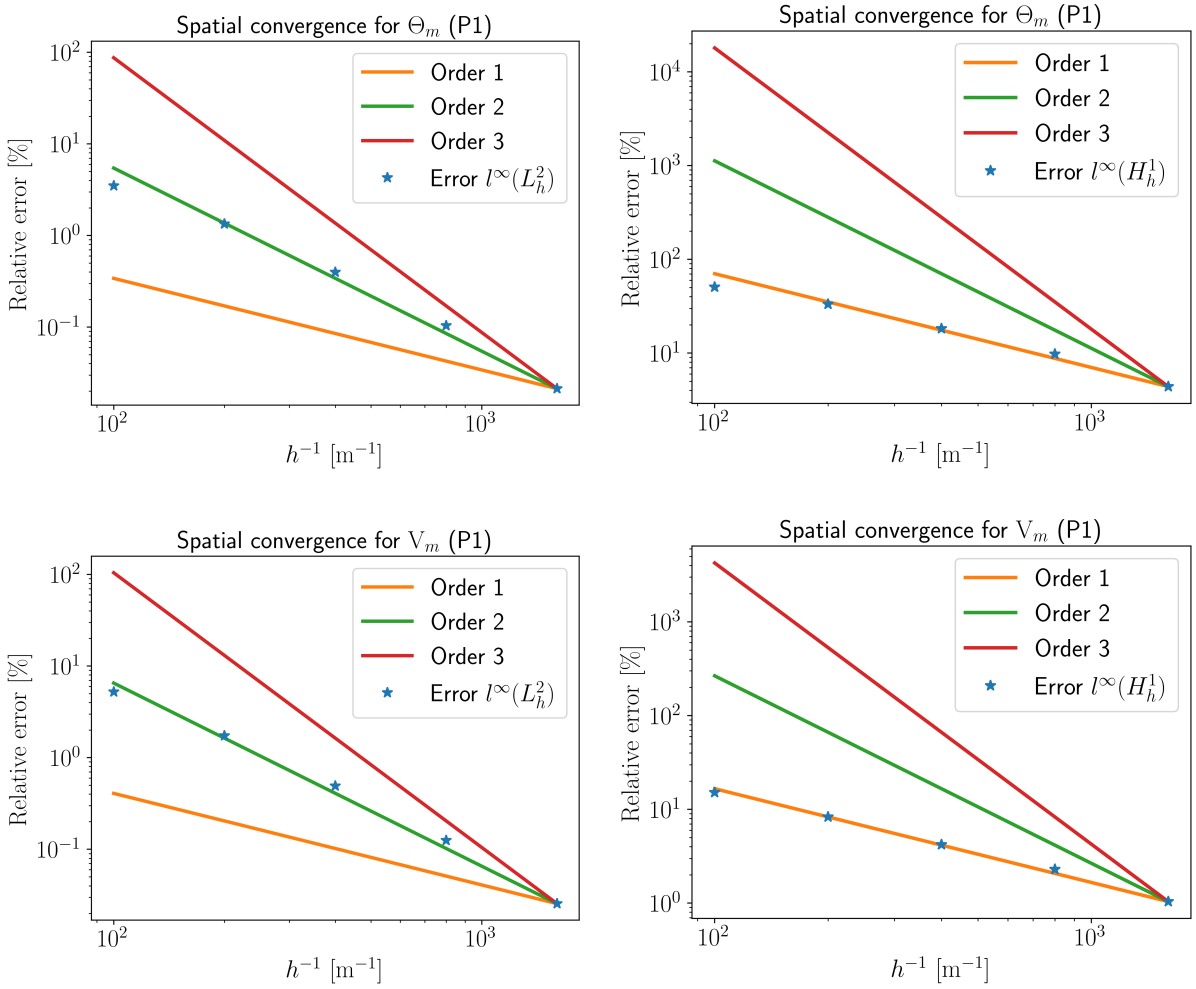

Figure 5.17: Test 5: computed $l^\infty(L_h^2)$ (left) and $l^\infty(H_h^1)$ (right) errors for temperature (top) and voltage (bottom), versus $1/h$, in log-log scale, for $N = 20$.

5.2.1.6 Test 6. Thermo-electromagnetic model with known displacement

A problem similar to that in Test 5 is considered, with the key difference being the replacement of the electrical model by the electromagnetic eddy current model described in Chapter 4. Consequently, an axisymmetric thermo-electromagnetic model is analysed, using the same domain and prescribed displacement field (5.23) as in Test 5.

An alternating current flows through the domain from $\widehat{\Gamma}_3$ to $\widehat{\Gamma}_1$, while the lateral surface $\widehat{\Gamma}_2$ is electrically insulated, meaning that the current flux across it is zero. The input current is applied at $\widehat{\Gamma}_3$, and the ground is set at $\widehat{\Gamma}_1$, following the notation introduced in Chapter 4 with $N_{\mathrm{I}} = \{1\}$ and $N_{\mathrm{V}} = \emptyset$. The current has an amplitude of 35000 A and a frequency of 500 Hz, resulting in a supplied current of $I_1 = 35000e^{i1000\pi t}$. As specified in the model, the current enters and exits the domain normal to the electrical ports.

The thermal properties and electrical conductivity shown in Figure 5.15 are used in this anal-

ysis. In the electromagnetic model, magnetic permeability is also taken into account. Specifically, it is treated as a function of both temperature and the magnetic field magnitude, and is defined using a modified version of the Fröhlich–Kennelly model, as described in [63]. More precisely, $\breve{\mu}$ in terms of the modulus of the magnetic field $|\mathbf{H}|$ and the temperature Θ is given by

$$\breve{\mu}(|\mathbf{H}|, \Theta) = \mu_0 + \frac{f(\Theta)}{a + b|\mathbf{H}|}, \tag{5.27}$$

where $\mu_0 = 4\pi \times 10^{-7}\ \mathrm{H\,m^{-1}}$ is the vacuum permeability, $a = 2532.35\ \mathrm{T^{-1}\,A\,m^{-1}}$ and $b = 0.49\ \mathrm{T^{-1}}$; $f(\Theta)$ is a temperature-dependent factor given by

$$f(\Theta) = \begin{cases} \left(\dfrac{(\Theta^C)^2 - \Theta^2}{(\Theta^C)^2 - (\Theta^0)^2} \right)^{\frac{1}{4}} & \text{if } \Theta < \Theta^C, \\ 0 & \text{if } \Theta \geq \Theta^C, \end{cases} \tag{5.28}$$

where $\Theta^C = 1021.84$ K is the Curie temperature of the material and $\Theta^0 = 296.65$ K is the room temperature. The relationship between H_θ and B_θ is shown in Figure 5.15a-left for different values of temperature. Note that, above the Curie temperature, the magnetic permeability of the material decreases to $\mu = \mu_0$.

The mass density is constant and equal to $\rho_m = 7799\ \mathrm{kg\,m^{-3}}$. Finally, the initial temperature of the cylinder is equal to 293.15 K and there is null convective and radiative heat flux through the boundaries, so $h = 0$ and $\epsilon = 0$.

Time discretisation is performed using the implicit Euler method. For spatial discretisation, both the temperature and the electromagnetic variable $\tilde{H}_\theta$ are approximated using continuous piecewise-linear finite elements. The Lagrange multiplier λ, which enforces boundary conditions on $\widehat{\Gamma}_2$ is discretised using piecewise-constant elements defined along the edges of that boundary.

Comparison of Lagrangian and Eulerian solutions

To validate the code implementation in Lagrangian coordinates, the problem was also solved in Eulerian coordinates using a similar discretisation, and the results were compared. The coupled problem was simulated over a period of $T = 20$ s with results presented for two distinct time points: one when the temperature remains below the Curie threshold, and another when the Curie temperature is reached in certain regions, leading to attenuation of the skin effect. It is important to note that all results related to the Lagrangian formulation have been mapped from the reference configuration –where the problem is originally solved– into the deformed configuration via composition with $\mathsf{P}(\mathsf{x}, t)$, and are shown in the deformed configuration.

Figures 5.18 and 5.19 show the modulus of the field $\tilde{H}_\theta$, in Eulerian and Lagrangian approaches after 2 and 20 seconds, respectively. Similarly, Figures 5.20 and 5.21 show the modulus of the electrical current density at different times. On the other hand, a comparison of the voltage between the electrical ports ($\widehat{\Gamma}_3$ and $\widehat{\Gamma}_1$) is presented in Figure 5.22. Finally, regarding the thermal response, Figures 5.23 and 5.24 show the temperature field at two different time instants. The results demonstrate good agreement between the Eulerian and Lagrangian formulations.

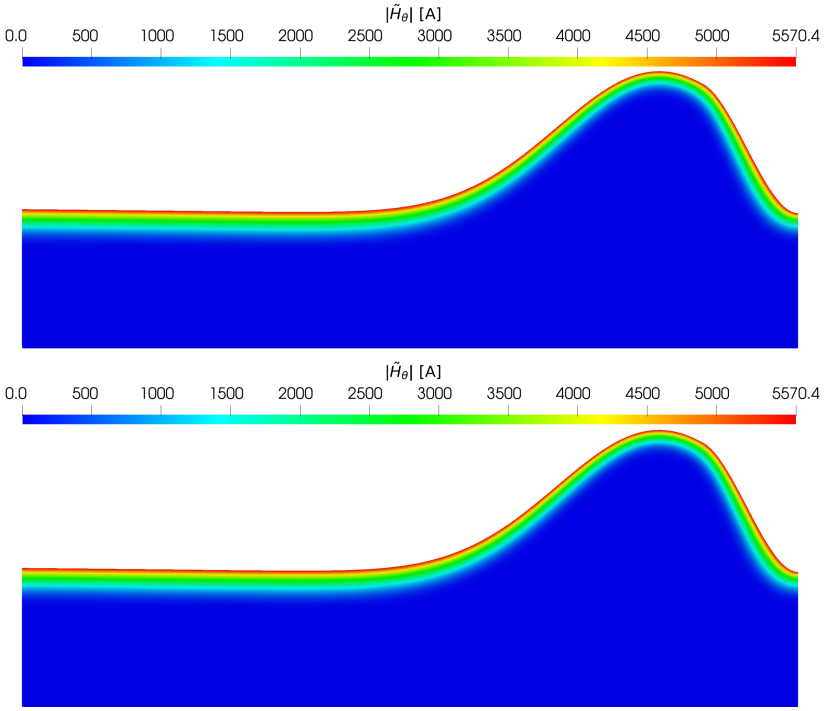

Figure 5.18: Test 6: $|\tilde{H}_\theta|$ at $t = 2$ s. Eulerian formulation (top) versus Lagrangian formulation (bottom).

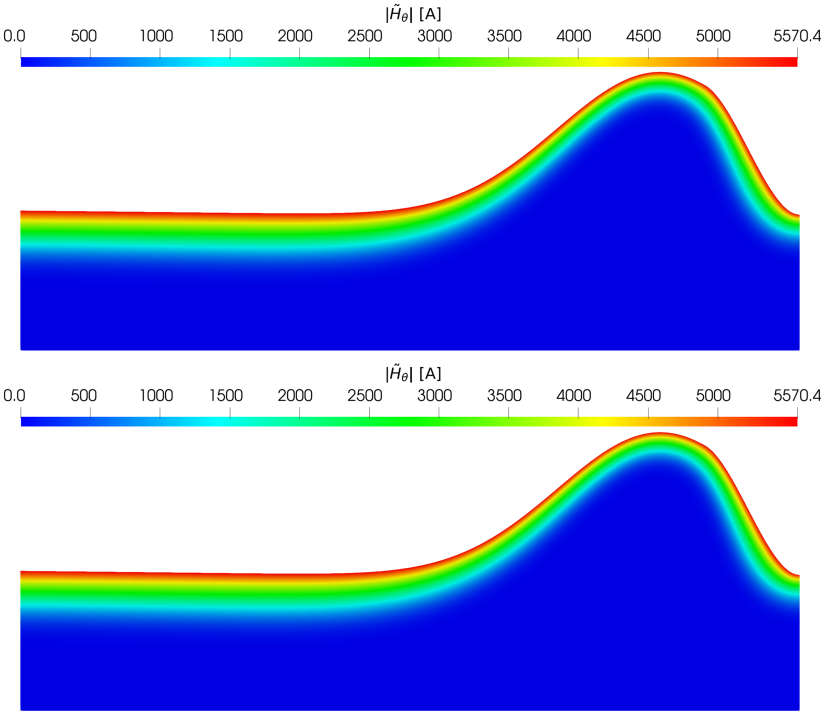

Figure 5.19: Test 6: $|\tilde{H}_\theta|$ at $t = 20$ s. Eulerian formulation (top) versus Lagrangian formulation (bottom).

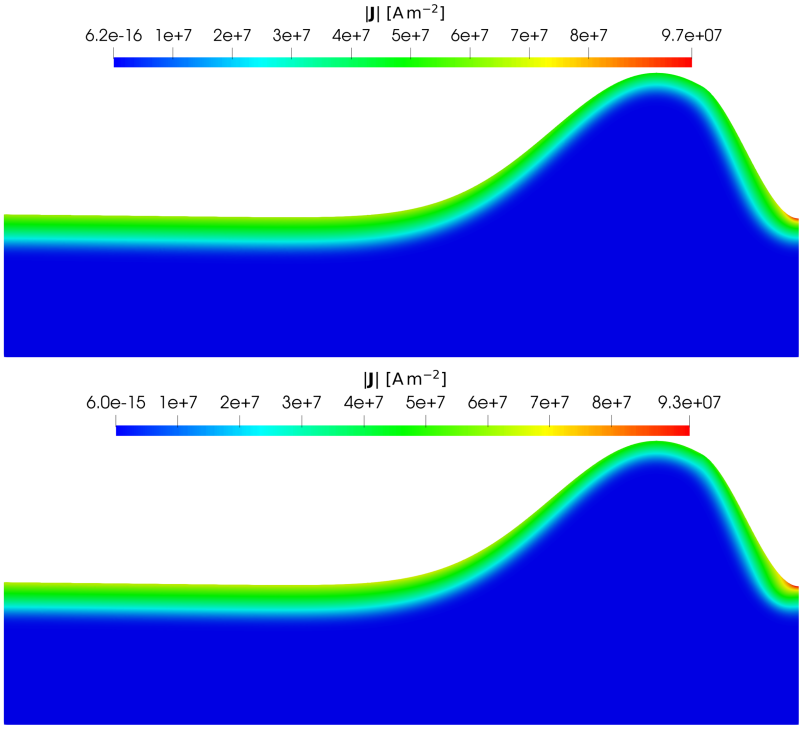

Figure 5.20: Test 6: $|\mathbf{J}|$ at $t = 2$ s. Eulerian formulation (top) versus Lagrangian formulation (bottom).

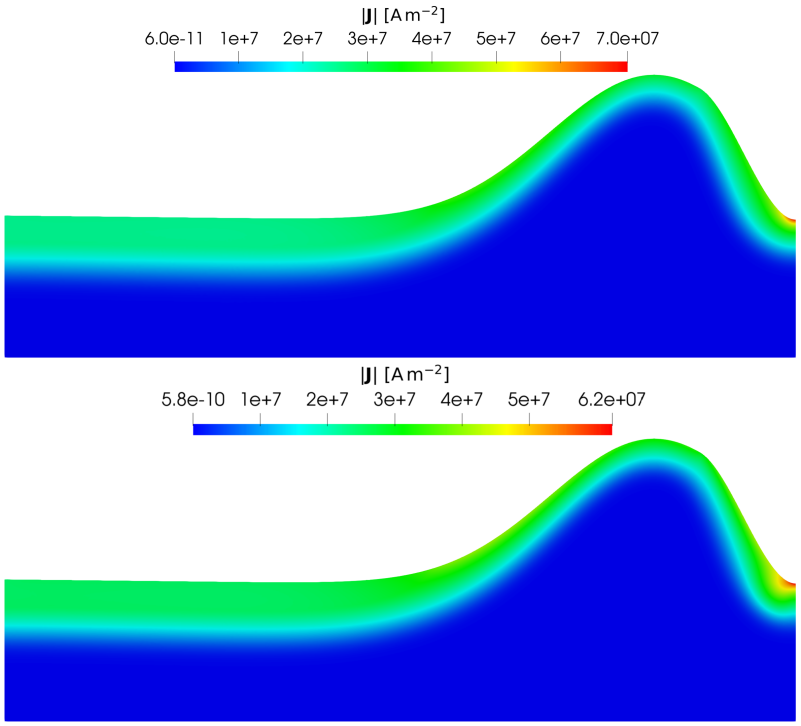

Figure 5.21: Test 6: $|\mathbf{J}|$ at $t = 20$ s. Eulerian formulation (top) versus Lagrangian formulation (bottom).

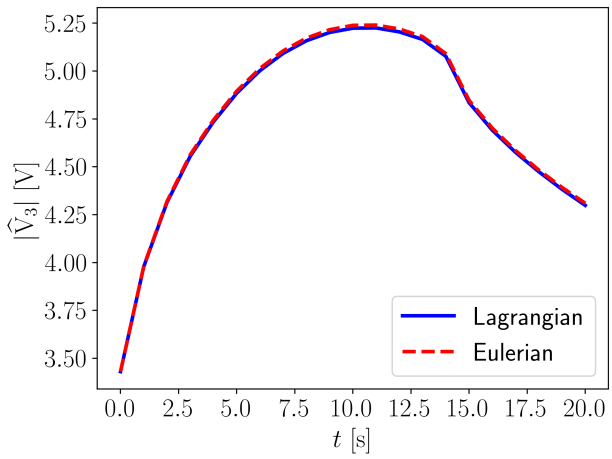

Figure 5.22: Test 6: comparison of the potential drop between the electrical ports vs. time.

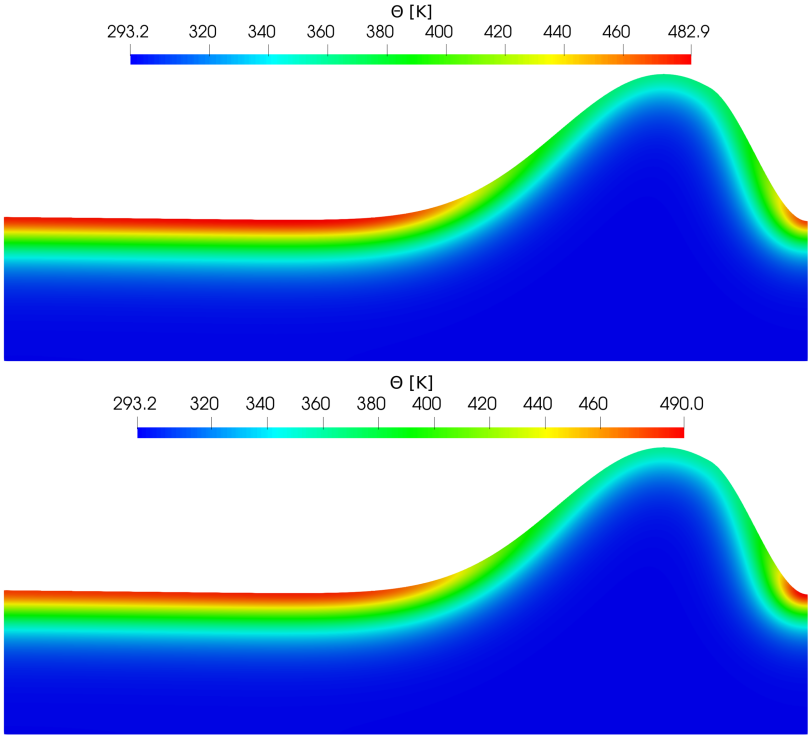

Figure 5.23: Test 6: Θ at $t = 2$ s. Eulerian formulation (top) versus Lagrangian formulation (bottom).

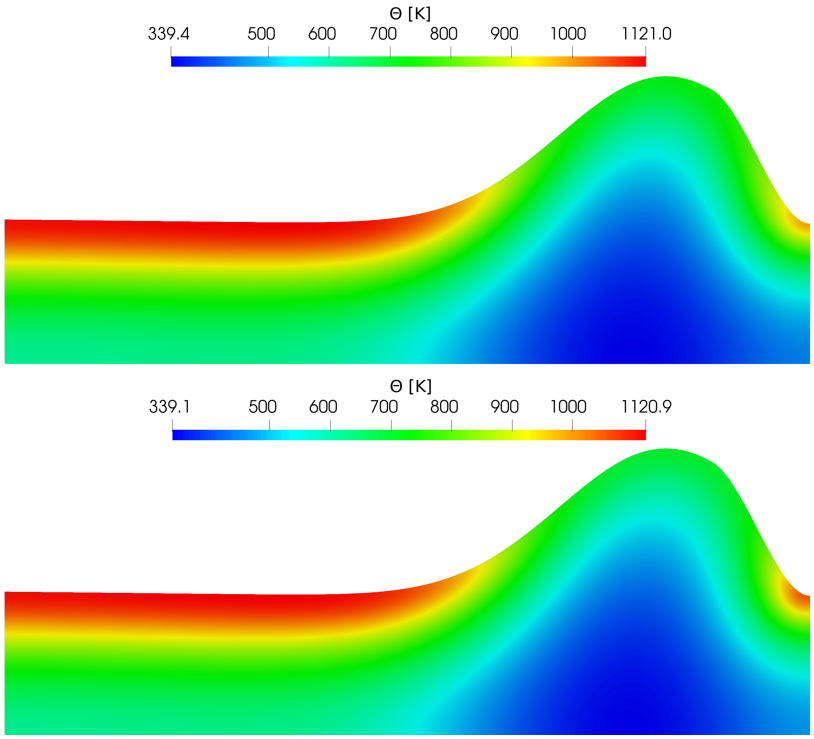

Figure 5.24: Test 6: Θ at $t = 20$ s. Eulerian formulation (top) versus Lagrangian formulation (bottom).

Convergence analysis

Similar to Test 5, the rates of convergence of the involved unknowns are analysed, both in time and space. The backward Euler method was employed for time discretisation, while continuous piecewise-linear finite elements were used for the spatial discretisation of both Θ and $\tilde{H}_\theta$.

In Figure 5.25, the spatial mesh is fixed, and the $l^\infty(L^2_h)$ and $l^\infty(H^1_h)$ errors for the temperature and $\tilde{H}_\theta$ are shown as functions of the number of time steps. A reference solution, computed with a finer time step ($N = 640$) and mesh-size ($h = 0.00125$), is used for comparison. The results indicate that the scheme achieves at least first-order accuracy in time for both Θ and $\tilde{H}_\theta$, as expected from the backward Euler method.

In Figure 5.26, we plot the computed $l^\infty\big(L^2_h\big)$ and $l^\infty\big(H^1_h\big)$ errors for the temperature and $\tilde{H}_\theta$ as functions of $1/h$, using a fixed small time step ($N = 20$). A reference solution obtained with $N = 20$ and $h = 0.0003125$ is used for comparison. The results show that the scheme achieves second-order spatial accuracy in the $l^\infty(L^2_h)$-norm and first-order spatial accuracy in the $l^\infty(H^1_h)$-norm.

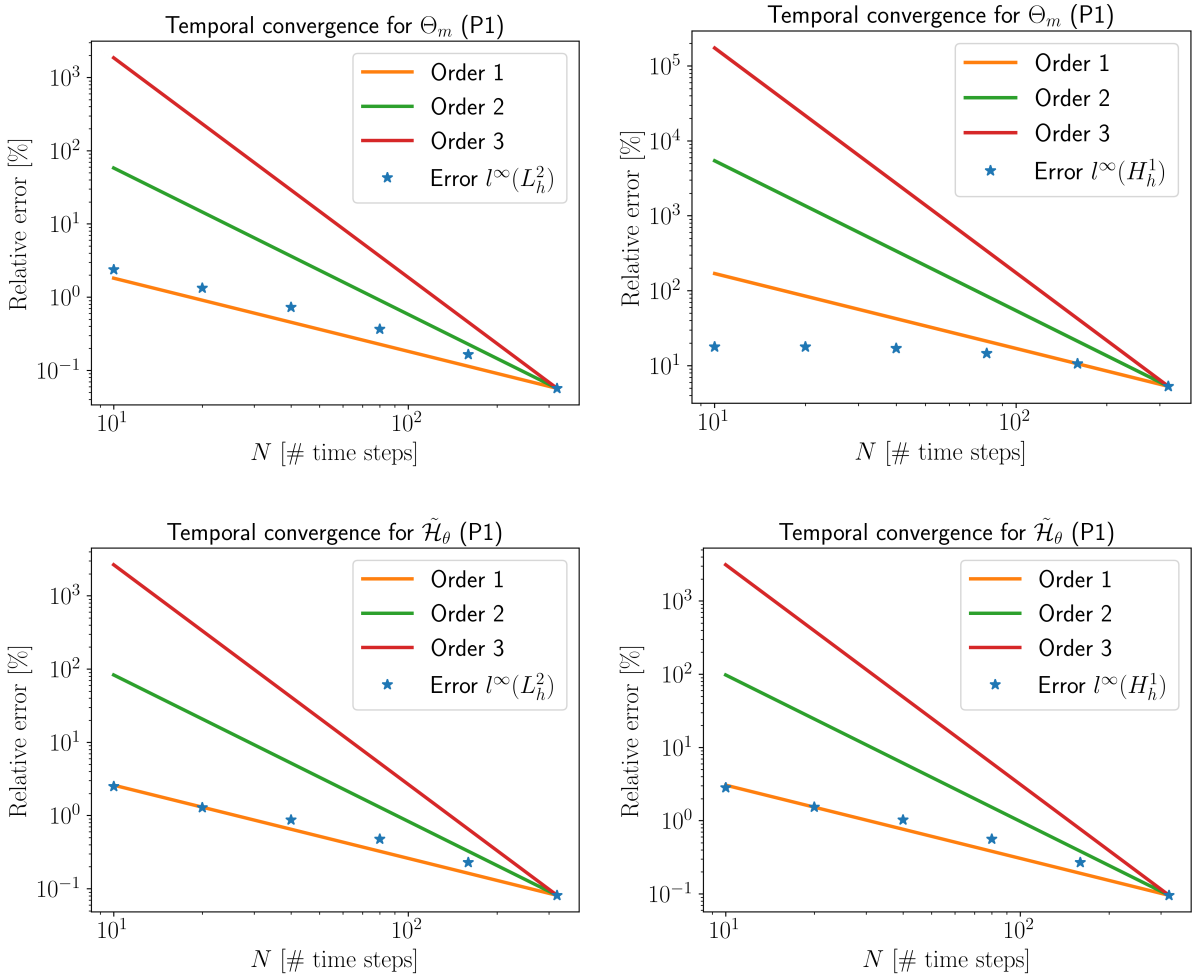

Figure 5.25: Test 6: computed $l^\infty(L_h^2)$ (left) and $l^\infty(H_h^1)$ (right) errors for temperature (top) and $\tilde{H}_\theta$ (bottom), versus the number of time steps, in log-log scale, for a fixed spatial mesh of size $h = 0.00125$.

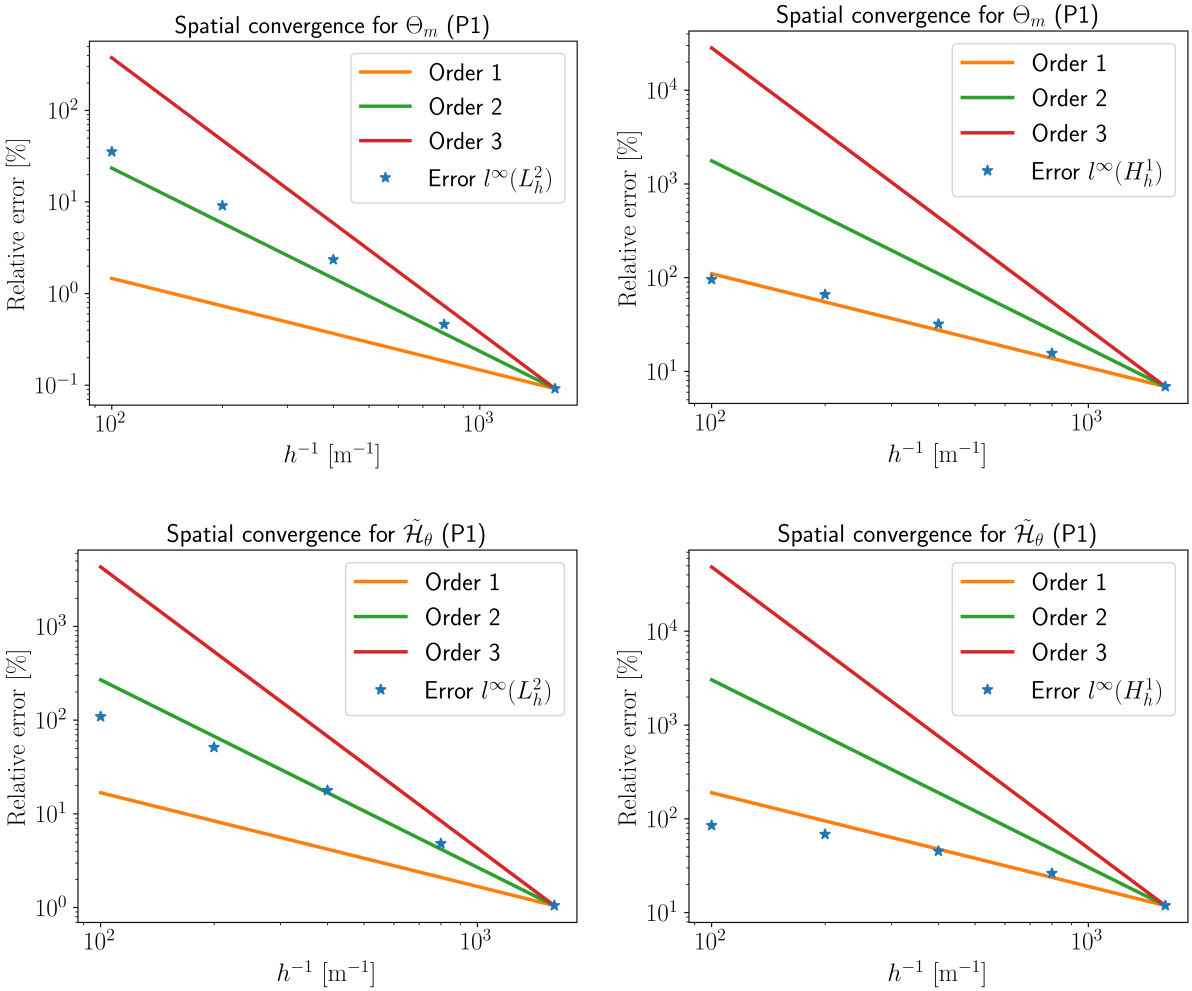

Figure 5.26: Test 6: computed $l^\infty(L^2_h)$ (left) and $l^\infty(H^1_h)$ (right) errors for temperature (top) and $\tilde{H}_\theta$ (bottom), versus $1/h$, in log-log scale, for $N = 20$.

5.2.1.7 Test 7. Fully coupled thermo-electrical-mechanical model

In this example, a fully coupled thermo-electrical-mechanical model is solved in the axisymmetric rectangular domain $\widehat{\Omega} = (0, 0.025) \times (0, 0.25)$, emulating a simplified version of a free electric upsetting process. The time interval is $[t_0, t_f] = [0\,\mathrm{s}, 100\,\mathrm{s}]$. The thermal, electrical and elasto-viscoplastic mechanical properties are those used in previous tests.

A symmetry condition (zero normal displacement) is enforced on $\widehat{\Gamma}_4$ and a force-free condition is assumed on $\widehat{\Gamma}_2$. Mechanical contact is considered on $\widehat{\Gamma}_1$. Moreover, the normal component of the displacement shown in Figure 5.27 is imposed over time on $\widehat{\Gamma}_3$.

Regarding the thermal model, a zero heat flux condition is imposed on the symmetry boundary $\widehat{\Gamma}_4$. At the same time, convection is applied on $\widehat{\Gamma}_2$ and $\widehat{\Gamma}_3$, with a heat transfer coefficient $h = 20\ \mathrm{W\,m^{-2}\,K^{-1}}$ and a convection temperature of $\widehat{\Theta}^C = 300$ K. In addition, a Dirichlet boundary condition with fixed temperature $\widehat{\Theta}^{DT} = 500$ K is prescribed on $\widehat{\Gamma}_1$. The initial

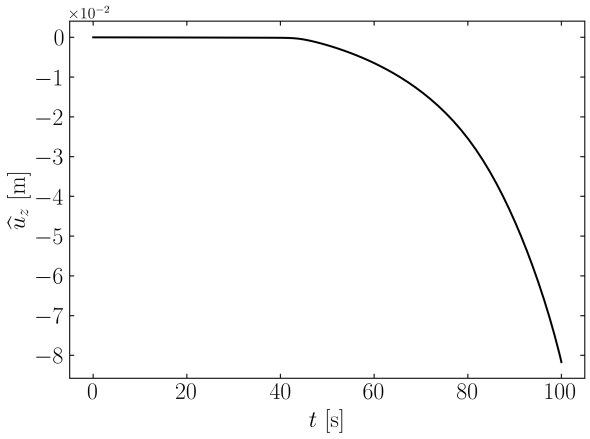

Figure 5.27: Test 7: normal displacement prescribed on $\widehat{\Gamma}_3$.

temperature in the entire domain is set to $\widehat{\Theta}^0 = 273.15$ K.

For the direct current model, a null electric potential is imposed on $\widehat{\Gamma}_1$. In addition, a constant electric potential $\widehat{V}^{DE} = 0.8$ V is fixed on a part of $\widehat{\Gamma}_2$, between $z_m = 0.175\,\mathrm{m}$ and $z_m = 0.2\,\mathrm{m}$. On the remaining boundaries, tangential electrical current is imposed, corresponding to the natural Neumann boundary condition.

Concerning the time discretisation, this problem has been solved using the third order ARKIMEX 3 method. In addition, for space discretisation, we have considered continuous piecewise-linear finite elements for each plastic deformation gradient component F^{p}_{ij}, for the deformation resistance s, the temperature, and the electric potential. In contrast, continuous piecewise quadratic elements are used for each displacement component.

This problem was solved in FEniCS using the pure-Lagrangian method proposed in this thesis, as well as with the commercial software packages Ansys and Marc. Figures 5.28, 5.29, and 5.30 show the temperature distributions on the deformed domain at several time instants, computed with our method and compared with the results obtained using Ansys and Marc. Furthermore, Figure 5.31 presents the evolution of several quantities at the midpoint of the symmetry boundary, $(r_m, z_m) = (0\,\mathrm{m}, 0.125\,\mathrm{m})$, together with the evolution of the maximum radial displacement, demonstrating good agreement among the different solvers. To further quantify this agreement, the following error is computed between the results of the pure-Lagrangian method and those obtained with the commercial software:

$$100\ \frac{1}{N}\sum_{i=1}^{N}\left|\frac{A_i^{\mathrm{Ansys/Marc}} - A_i^{\mathrm{Pure-Lagrangian}}}{A_i^{\mathrm{Ansys/Marc}}}\right|, \tag{5.29}$$

where A refers to the specific magnitude in Figure 5.31 for which the error is computed, the subscript i refers to the simulation time t_i, the superscript denotes the solver, and N is the total number of time instants. Note that linear interpolation is applied to align the time instants across all solvers. Contributions involving divisions by values $A_i^{\mathrm{Ansys/Marc}}$ smaller than 10^{-4} are omitted to avoid distorting the error in ϵ^p and $u_r^{\max}$ during the initial part of the corresponding curves. The resulting errors are summarised in Table 5.3.

To accurately simulate large-strain problems with viscoplastic deformations, the finite element mesh must exhibit sufficient quality and refinement, as element distortion can become very pronounced in highly deformed regions. This is illustrated in Figure 5.32, which shows the Frobenius norm of the plastic deformation gradient at the final time, together with a detailed view of the mesh in the deformed domain.

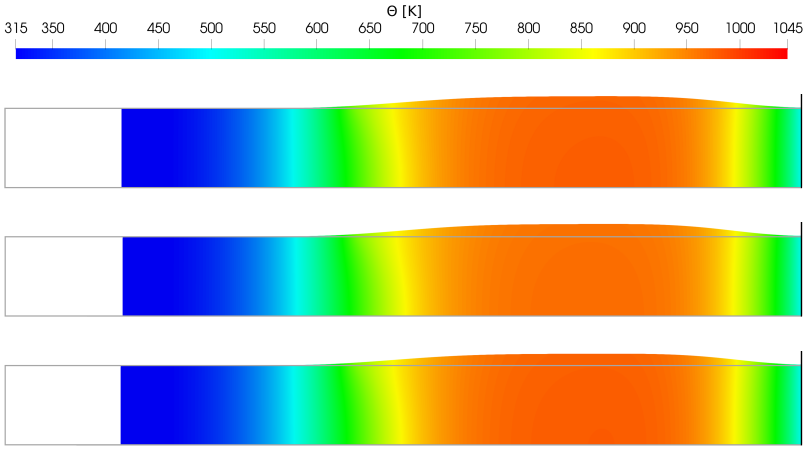

Figure 5.28: Test 7: temperature and deformed domain (the reference domain is outlined in grey) at $t = 85\,\mathrm{s}$, computed using the proposed pure-Lagrangian method (top), Ansys (middle), and Marc (bottom).

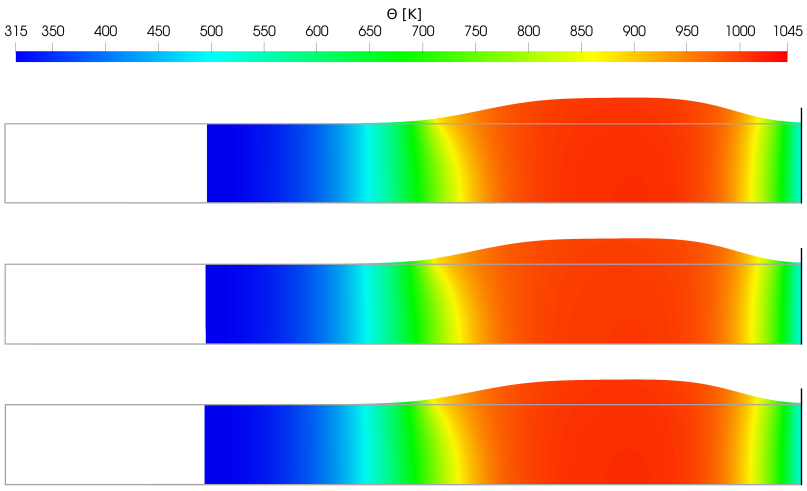

Figure 5.29: Test 7: temperature and deformed domain (the reference domain is outlined in grey) at $t = 95\,\mathrm{s}$, computed using the proposed pure-Lagrangian method (top), Ansys (middle) and Marc (bottom).

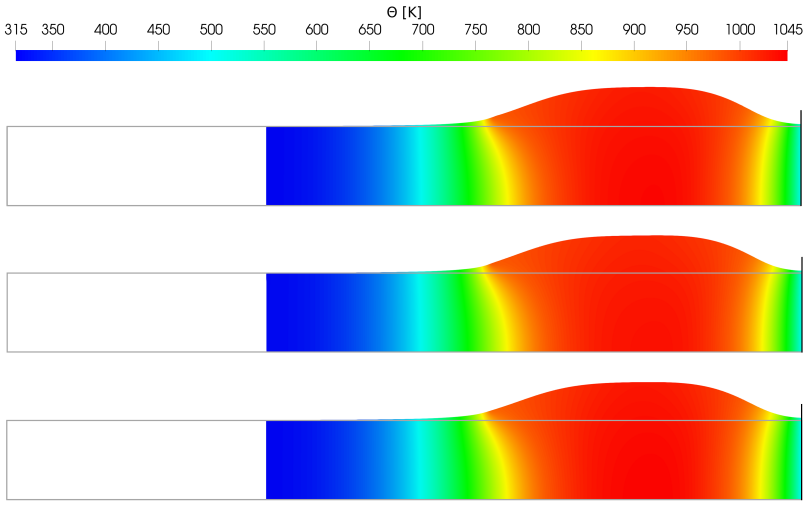

Figure 5.30: Test 7: temperature and deformed domain (the reference domain is outlined in grey) at $t = 100\,\mathrm{s}$, computed using the proposed pure-Lagrangian method (top), Ansys (middle) and Marc (bottom).

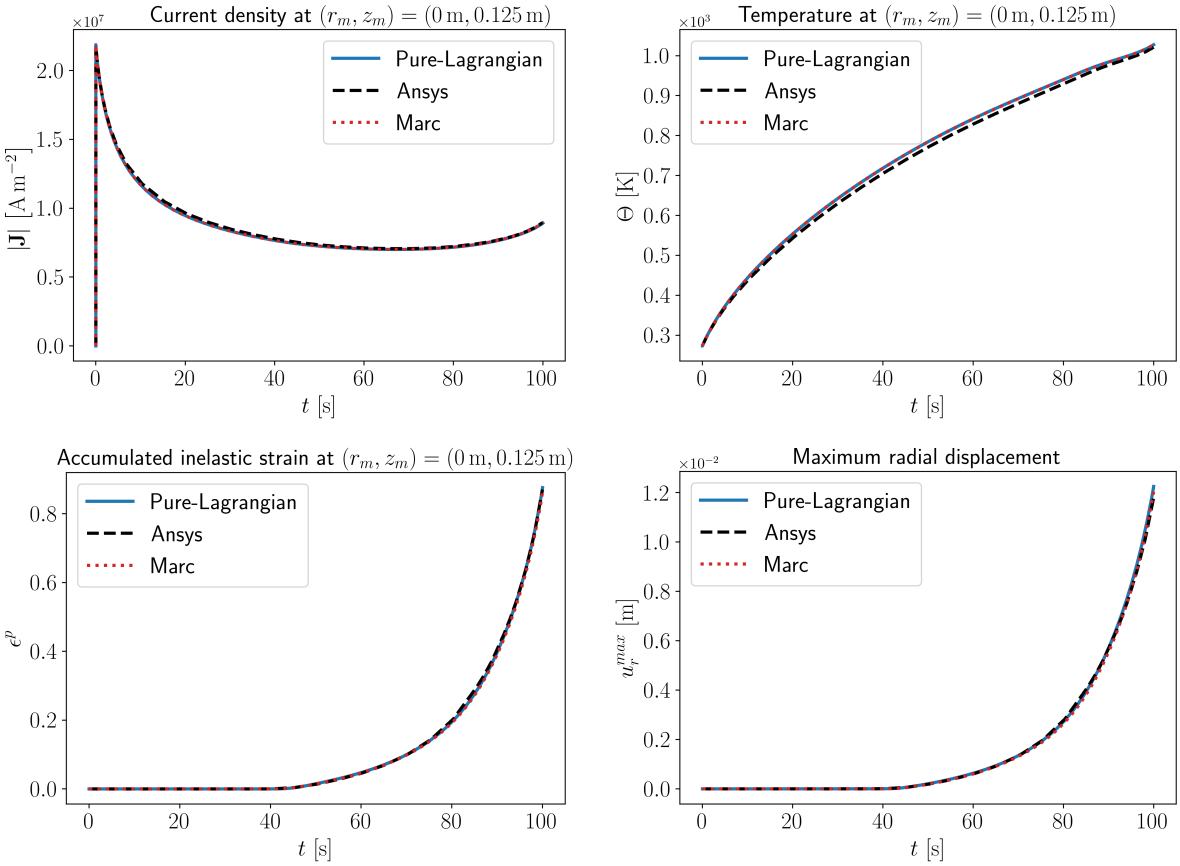

Figure 5.31: Test 7: time evolution of the modulus of the current density, the temperature, and the accumulated inelastic strain at $(r_m, z_m) = (0\,\mathrm{m}, 0.125\,\mathrm{m})$, and maximum radial displacement.

Comparison	Error $\|\mathbf{J}\|$ (%)	Error Θ (%)	Error ϵ^p (%)	Error u_r^{max} (%)
Pure-Lagrangian vs Ansys	1.24	1.48	8.27	2.85
Pure-Lagrangian vs Marc	0.07	0.02	2.00	3.81

Table 5.3: Test 7: errors computed from the curves in Figure 5.31.

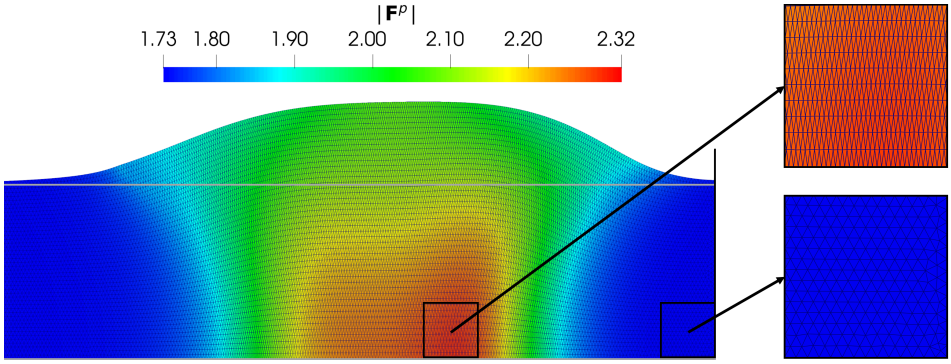

Figure 5.32: Test 7: Frobenius norm of the plastic deformation gradient and deformed mesh at $t = 100\,\mathrm{s}$, computed with the proposed pure-Lagrangian method. The reference domain is outlined in grey. Significant mesh distortion is observed in the most deformed region (zoomed view on the right), whereas the initial mesh is nearly uniform, with an element size comparable to that of the blue region.

5.2.2 Electric upsetting

Once the numerical tools developed to implement the mathematical models in our own code have been thoroughly validated, we can proceed to simulate real electric upsetting processes. In this section, we present fully coupled simulations of both in-die and free electric upsetting of a steel bar, including examples under DC and AC conditions. As part of our collaboration with CIE Galfor, we gained insight into several aspects of their in-plant electric upsetting procedures for specific axle shaft references. Some of these features are incorporated into the simulations below, including the characteristics of the steel bars and the duration of the different stages of the processes. However, other process variables, such as resultant forces or electrical currents, were not available in the form the mathematical model required them. Therefore, reasonable values for those variables are considered to complete the input dataset required for the simulations.

5.2.2.1 In-die electric upsetting

As stated in Chapter 1, the pinion part of axle shafts is formed by means of an in-die electric upsetting process, whose objective is to thicken one end of the steel bar. In this example, we consider a DC current. The process begins with a low-voltage, high-amperage electrical current passing through the bar end, between the electrical contacts of the anvil and the gripper, with a duration of 11 seconds. During the following 23 seconds, the anvil retracts to create space for the bar end to expand. Finally, in the last 29 seconds, the upsetting cylinder pushes on the

opposite end of the bar, causing it to widen and fill the die. Figure 1.10b provides a simplified diagram of the main components involved in the process.

The initial bar dimensions are 44 mm in diameter and 1290 mm in length, while the die diameter is 52.4 mm. The initial geometry and boundary conditions of the coupled problem are illustrated in Figure 5.33, where the dashed line identifies the symmetry boundary $\widehat{\Gamma}_6$. The thermal and electrical properties correspond to those in Figure 5.15, whereas the mechanical properties are given in Figure 5.8 and Table 5.1.

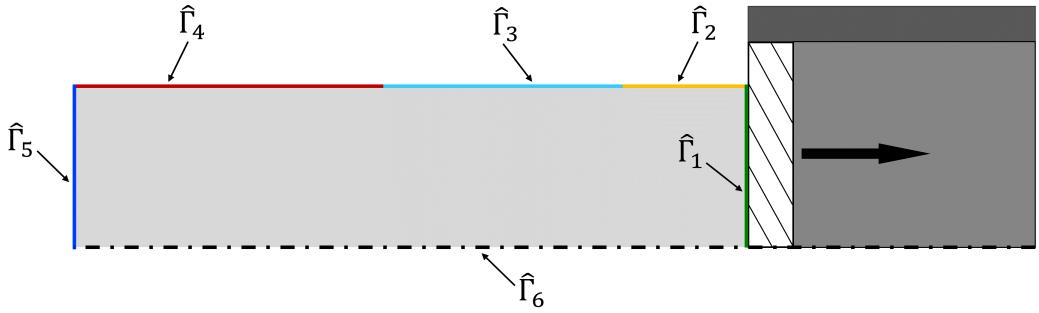

Figure 5.33: In-die electric upsetting: initial geometry and boundary conditions.

A resultant force, depicted in Figure 5.34-left, is applied on $\widehat{\Gamma}_5$, namely,

$$\mathbf{P}(t) = \pi(0.022)^2 \times \begin{cases} -\dfrac{5833035}{34} t\,\mathbf{e}_z & \text{if } t < 34 \text{ s}, \\ 172657836 - \dfrac{10499463}{2} t\,\mathbf{e}_z & \text{if } 34 \text{ s} \le t \le \dfrac{346}{9} \text{ s}, \\ -\dfrac{58330350}{1+\exp\left(\frac{346}{25} - \frac{9}{25}t\right)}\,\mathbf{e}_z & \text{if } t > \dfrac{346}{9} \text{ s}. \end{cases} \tag{5.30}$$

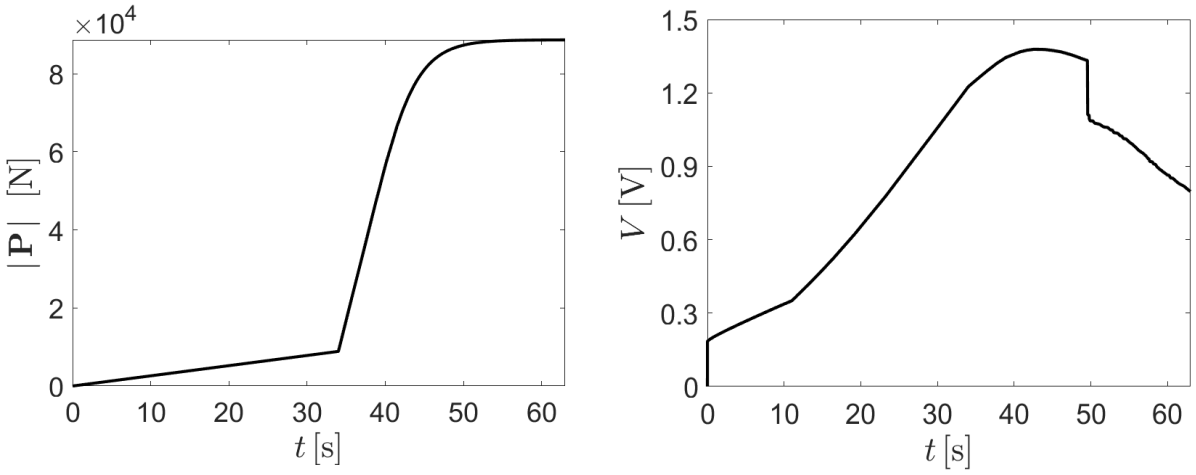

Figure 5.34: In-die electric upsetting: modulus of the resultant force applied on $\widehat{\Gamma}_5$ (left) and electric potential prescribed on $\widehat{\Gamma}_3$ (right).

In addition, a convective–radiative heat flux boundary condition is prescribed on $\bigcup_{i=2}^{5} \widehat{\Gamma}_i$ with

$h = 20\ \mathrm{W\,m^{-2}\,K^{-1}}$, $\Theta^C = 295.15\,\mathrm{K}$, $\Theta^R = 303.15\,\mathrm{K}$, and $\epsilon = 0.9$. The thermal contact between the bar and the anvil, which is excluded from the computational domain, can be modelled under realistic conditions using a convective boundary condition. The magnitude of the heat transfer is controlled by the value of the h coefficient. In this case, an almost perfect contact is considered on $\widehat{\Gamma}_1$, with a high value for the heat transfer coefficient, $h = 10^5\ \mathrm{W\,m^{-2}\,K^{-1}}$, and $\Theta^C = 495.15\,\mathrm{K}$ for the temperature of the anvil.

Regarding the electrical problem, the potential depicted in Figure 5.34-right is applied on $\widehat{\Gamma}_3$. The reference (null) electric potential is imposed on $\widehat{\Gamma}_1$, while a null Neumann condition is applied on the rest of the boundaries. Notably, due to the backward movement of the anvil, the electric potential depicted in Figure 5.34-right is imposed only on a time-dependent part of $\widehat{\Gamma}_3$ with a length matching that of the gripper. Additionally, an obstacle associated with the die-form is considered, which necessitates adjustments to the boundary conditions when the contact takes place. Similarly to the contact heat transfer modelling considered on $\widehat{\Gamma}_1$, we impose a null electric potential and a convective heat flux boundary condition with $h = 10^4\ \mathrm{W\,m^{-2}\,K^{-1}}$, $\Theta^C = 473.15\,\mathrm{K}$, on the part of the boundary that comes into contact with the obstacle.

For the time discretisation of this problem, the third order ARKIMEX 3 method [47] with adaptive time stepping has been used. Concerning the space discretisation, we consider continuous piecewise-linear finite elements for each component of the plastic deformation gradient, while continuous piecewise quadratic elements are used for each displacement component, the deformation resistance, the electric potential and the temperature.

In Figure 5.35, the modulus of the current density obtained in proprietary code is shown across four instantaneous configurations in the deformed domain.

This problem was also solved using the commercial software packages Ansys and Marc, with results that closely match those obtained with our numerical code. The results from Marc, Ansys, and our method are depicted in Figures 5.36-5.39, showing the temperature distribution and the geometry at four different times. It is worth noting that achieving an accurate solution with the Marc code required a smaller time step compared to our method and the Ansys code.

5.2.2.2 Free electric upsetting

The first stage of the process of building the plate shape of the axle shaft consists of a free electric upsetting process, where the diameter of the hot end of a steel bar can grow freely until the onion preform is created.

The simulation procedure is qualitatively similar to that for in-die electric upsetting described in the previous section. In fact, a low-voltage and high-amperage electrical current circulates between the electrical contacts of the anvil and the gripper during the first 19 seconds. Over the next 36 seconds, the anvil retracts to leave space for the onion preform. The actual upsetting process then takes place, with a cylinder pushing the opposite end of the bar to give the desired preform.

The initial bar has a diameter of 57.5 mm and a length of 1330 mm. The different boundaries for the coupled problem are depicted in Figure 5.40 in the reference configuration, where $\widehat{\Gamma}_6$ coincides with the symmetry axis. While the computational domain and the boundaries are

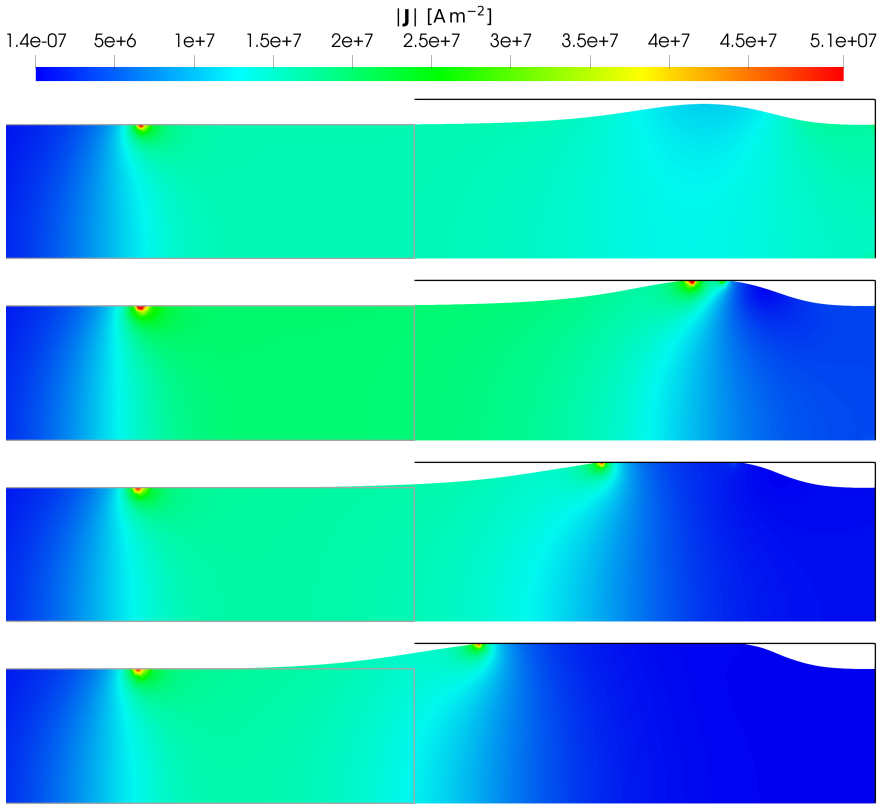

Figure 5.35: In-die electric upsetting: modulus of the current density and deformed domain (the reference domain is outlined in grey) at $t = 46\,\mathrm{s},\ \mathrm{t} = 48\,\mathrm{s},\ \mathrm{t} = 54\,\mathrm{s},\ \mathrm{t} = 63\,\mathrm{s}$.

qualitatively similar to those for the in-die process, the anvil moves as a single block and the hot end thickening is not limited by a horizontal obstacle. Note that the backward movement of the anvil is equivalently represented in the simulation by imposing an opposite but identical movement on the gripper (boundary $\widehat{\Gamma}_3$).

The resultant force (see Figure 5.41-left) applied on $\widehat{\Gamma}_5$ is given by

$$\mathbf{P}(t) = \pi(0.02875)^2 \times \begin{cases} \mathbf{0} & \text{if } t < 55 \text{ s}, \\ 6.16 \times 10^8 - 1.12 \times 10^7 t\, \mathbf{e}_z & \text{if } 55 \text{ s} \leq t \leq 60 \text{ s}, \\ -\dfrac{1.12 \times 10^8}{1 + \exp\left(24 - \frac{2}{5}t\right)}\, \mathbf{e}_z & \text{if } t > 60 \text{ s}. \end{cases} \tag{5.31}$$

In this example, to illustrate the capabilities of the modelling approach presented in Chapter 4, the AC electromagnetic model with prescribed power input is considered. The total active power supplied to the system through $\widehat{\Gamma}_3$ along time (see Figure 5.41-right) is

$$P_{AC}(t) = \begin{cases} 6000.0\, t & \text{if } t < 1 \text{ s}, \\ 581.633\, t + 5418.367 & \text{if } 1 \text{ s} \leq t \leq 50 \text{ s}, \\ 34500.0 & \text{if } t > 50 \text{ s}. \end{cases} \tag{5.32}$$

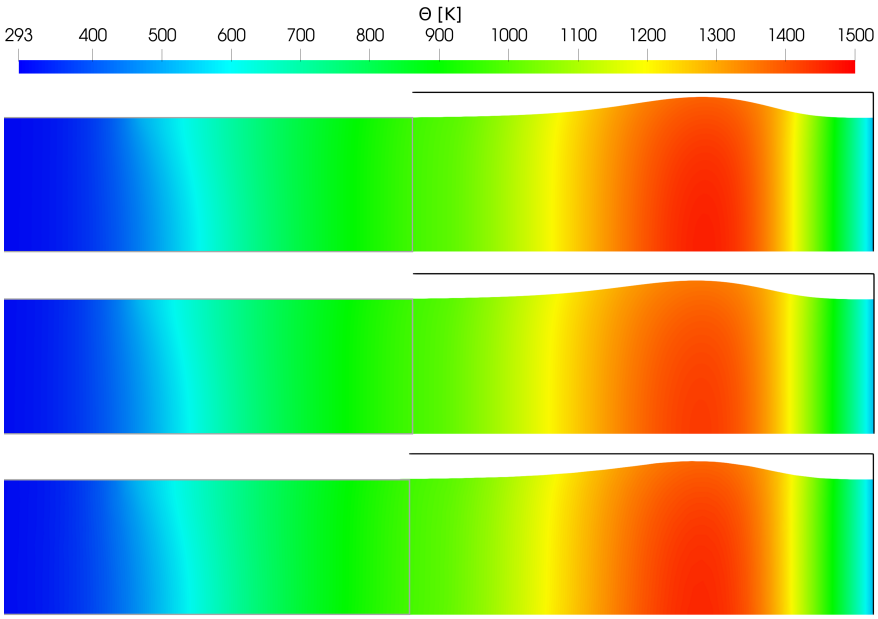

Figure 5.36: In-die electric upsetting: temperature and deformed domain (the reference domain is outlined in grey) at $t = 46\,\mathrm{s}$, computed using the proposed pure-Lagrangian method (top), Ansys (middle) and Marc (bottom).

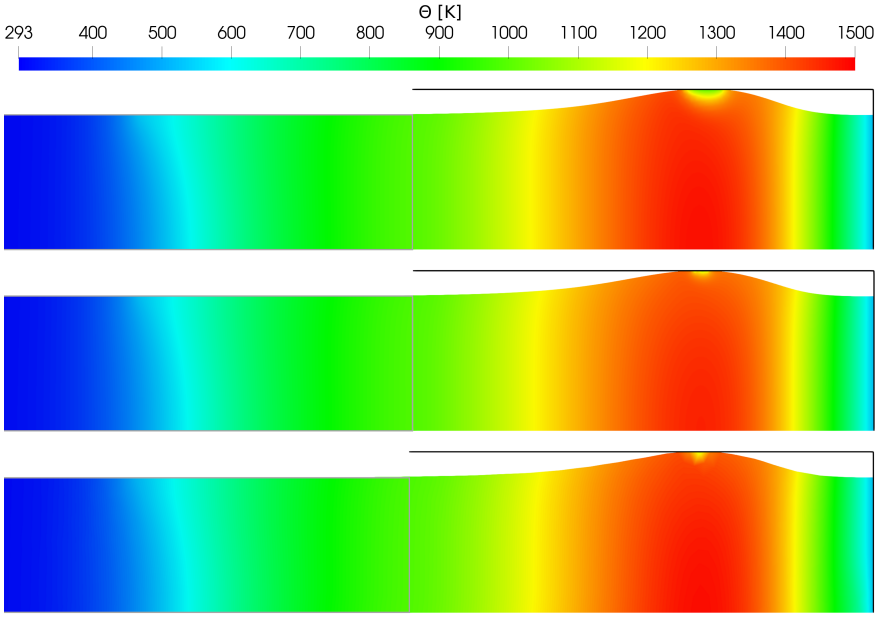

Figure 5.37: In-die electric upsetting: temperature and deformed domain (the reference domain is outlined in grey) at $t = 48\,\mathrm{s}$, computed using the proposed pure-Lagrangian method (top), Ansys (middle) and Marc (bottom).

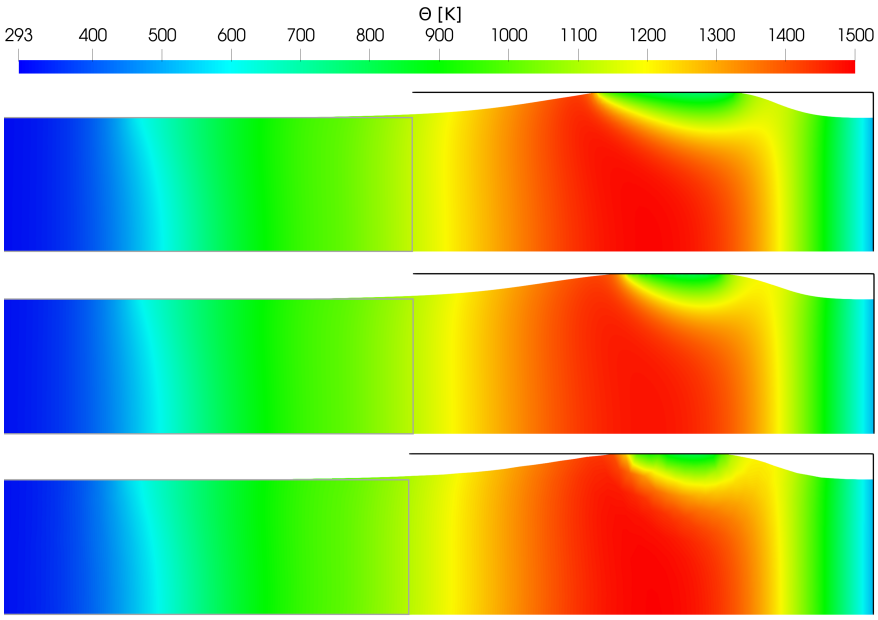

Figure 5.38: In-die electric upsetting: temperature and deformed domain (the reference domain is outlined in grey) at $t = 54\,\mathrm{s}$, computed using the proposed pure-Lagrangian method (top), Ansys (middle) and Marc (bottom).

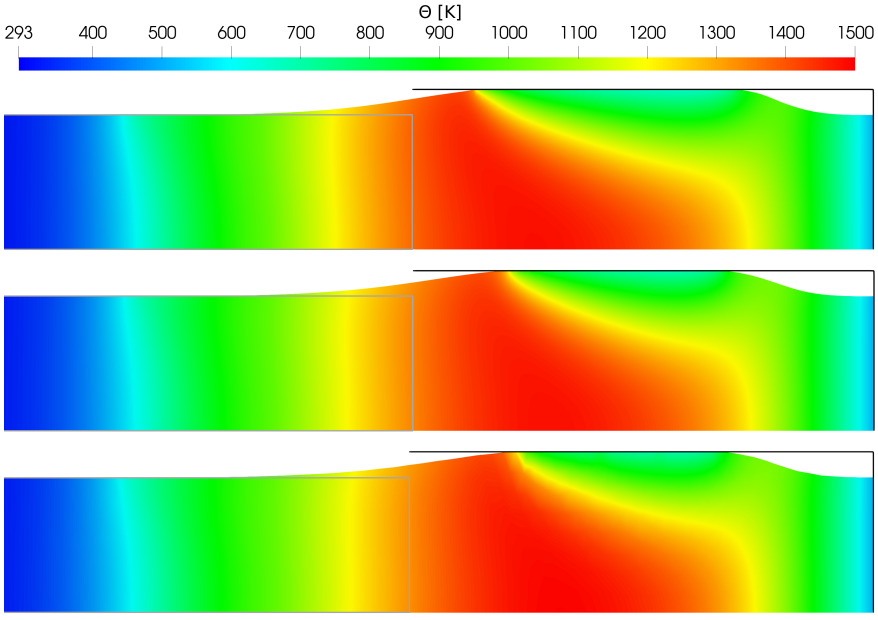

Figure 5.39: In-die electric upsetting: temperature and deformed domain (the reference domain is outlined in grey) at $t = 63\,\mathrm{s}$, computed using the proposed pure-Lagrangian method (top), Ansys (middle) and Marc (bottom).

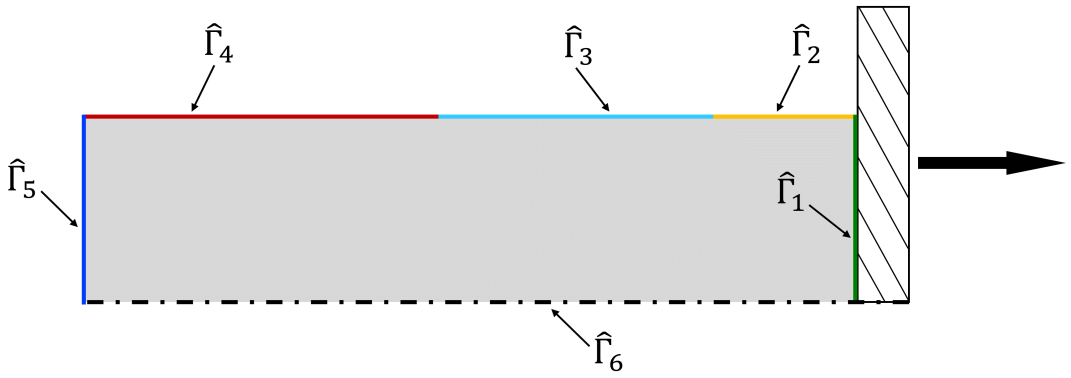

Figure 5.40: Free electric upsetting: initial geometry and boundaries.

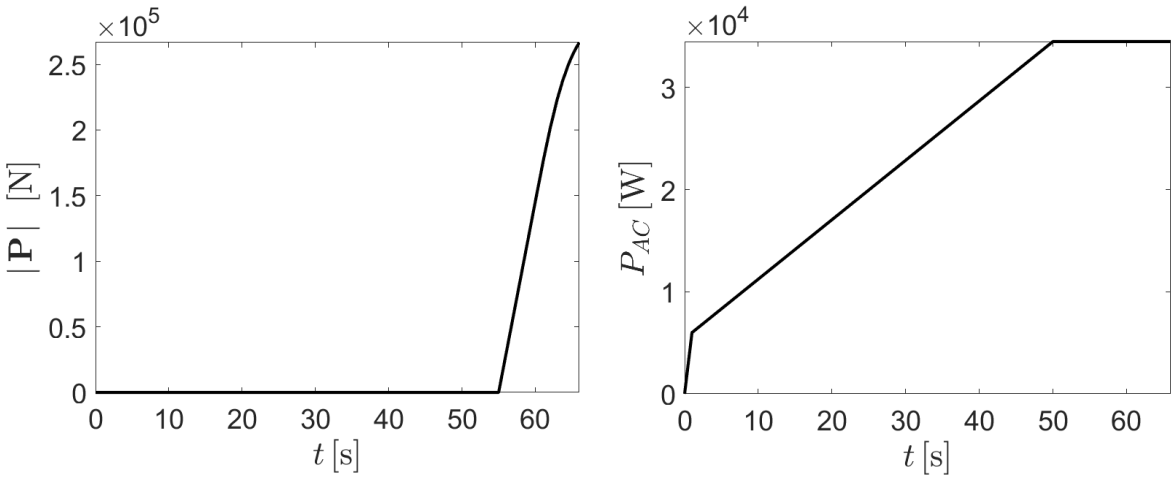

Figure 5.41: Free electric upsetting: modulus of the resultant force applied on $\widehat{\Gamma}_5$ (left) and active power supplied through $\widehat{\Gamma}_3$ (right).

The electric potential is referenced on $\widehat{\Gamma}_1$, while tangential current is imposed on the remaining electromagnetic boundaries. As in the in-die process, when the gripper ($\widehat{\Gamma}_3$) moves back to mimic the anvil displacement, active power is supplied only on a time-dependent portion of that boundary, with a length matching that of the gripper (0.085 m).

In addition, convective–radiative heat flux boundary conditions are prescribed on $\bigcup_{i=2}^{5} \widehat{\Gamma}_i$ with $h = 20\ \mathrm{W\,m^{-2}\,K^{-1}}$, $\Theta^C = 295.15\,\mathrm{K}$, $\Theta^R = 303.15\,\mathrm{K}$, and $\epsilon = 0.9$, whereas a purely convective heat flux condition with $h = 10^5\ \mathrm{W\,m^{-2}\,K^{-1}}$ and $\Theta^C = 850.15\,\mathrm{K}$ is imposed on $\widehat{\Gamma}_1$ to model the contact heat transfer between the bar and the anvil. The mechanical properties are those reported in Figure 5.8 and Table 5.1, while the thermo-electromagnetic properties are given in Figure 5.15.

AC electric upsetting processes are influenced by the skin effect, i.e., the tendency of alternating current to concentrate near the surface of conductors. At low frequencies, the thickness of the *skin* region, where the electromagnetic fields are concentrated, depends on the electrical conductivity, the magnetic permeability of the material, and the current frequency. To assess

the influence of the skin effect on the free electric upsetting process, we examine three cases: $f = 50$ Hz, $f = 100$ Hz, and $f \approx 0$ Hz, the latter representing a near-DC condition in which the skin effect is negligible.

In what follows, we present results for the free electric upsetting problem obtained with our in-house code at different frequencies and time instants in the deformed domain. It is first observed that the skin effect becomes more pronounced at higher frequencies, particularly at lower temperatures before the Curie point is reached. Figure 5.42 shows the distribution of the electromagnetic variable $\tilde{\mathcal{H}}_\theta$ one second after the simulation start for the different frequencies. For visualisation purposes, each case is plotted with an independent scale, highlighting the increasing prominence of the skin effect with frequency.

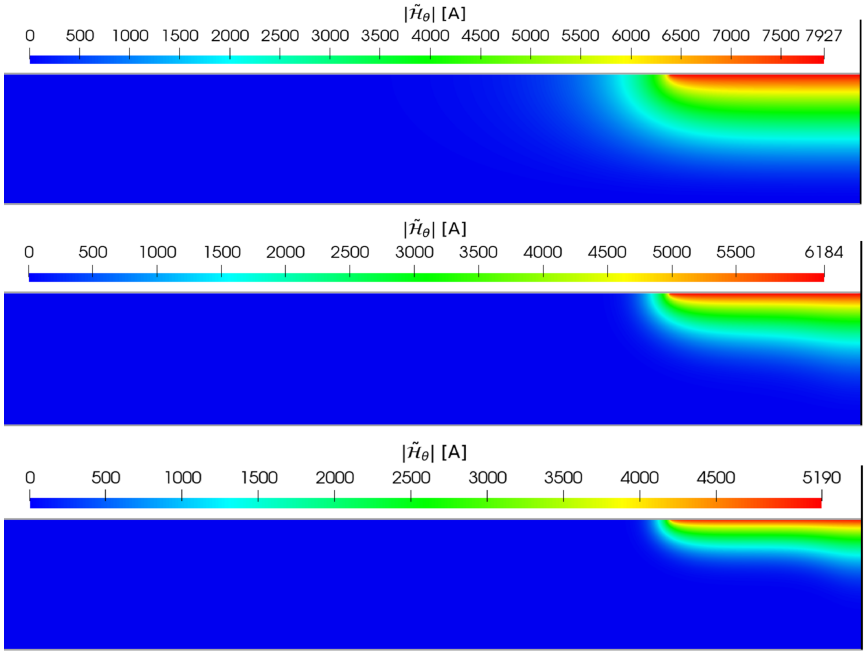

Figure 5.42: Free electric upsetting: $\tilde{\mathcal{H}}_\theta$ and deformed domain (the reference domain is outlined in gray) at $t = 1$ s for $f \approx 0$ Hz (top), $f = 50$ Hz (middle) and $f = 100$ Hz (bottom).

Since the current is concentrated near the surface of the bar, the associated Joule heating is likewise localised in that region. This is illustrated in Figure 5.43, where the temperature distribution is nearly uniform in the near-DC case, but significantly higher near the surface at 50 Hz and, in particular, at 100 Hz. Although the maximum temperature values are similar for the three frequencies at this time instant, the reduced uniformity at higher frequencies hinders heat conduction through the bar.

As expected, once the upsetting force is applied, the deformation is greater at lower frequencies, owing to the more uniform temperature distribution, which also reaches higher values at this stage. The corresponding temperature fields in the deformed configuration are shown in Figure 5.44 at $t = 62$ s and in Figure 5.45 at $t = 66$ s.

Note that the final deformation obtained in the DC case is greater than in the AC cases affected by the skin effect, with the maximum radial displacement reaching nearly twice the

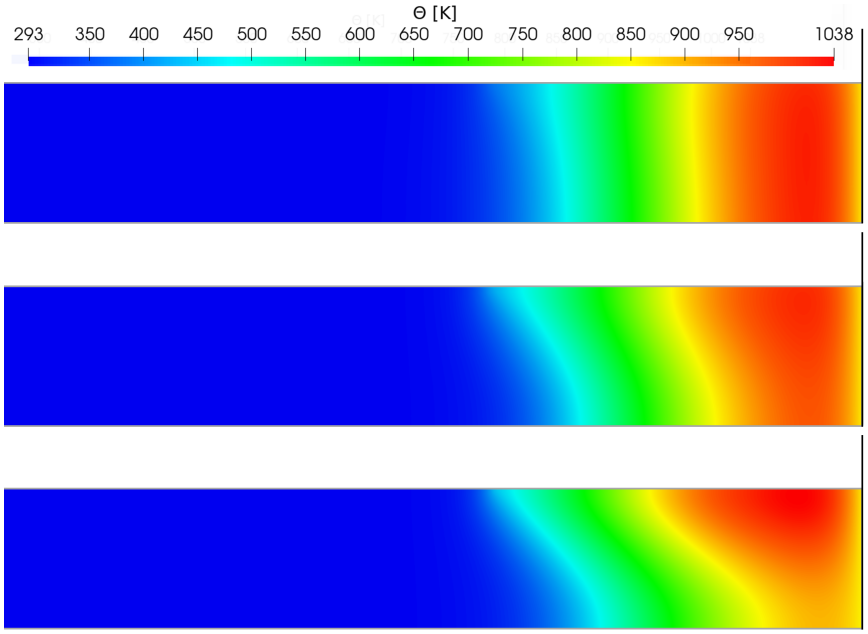

Figure 5.43: Free electric upsetting: temperature and deformed domain (the reference domain is outlined in gray) at $t = 30$ s for $f \approx 0$ Hz (top), $f = 50$ Hz (middle) and $f = 100$ Hz (bottom).

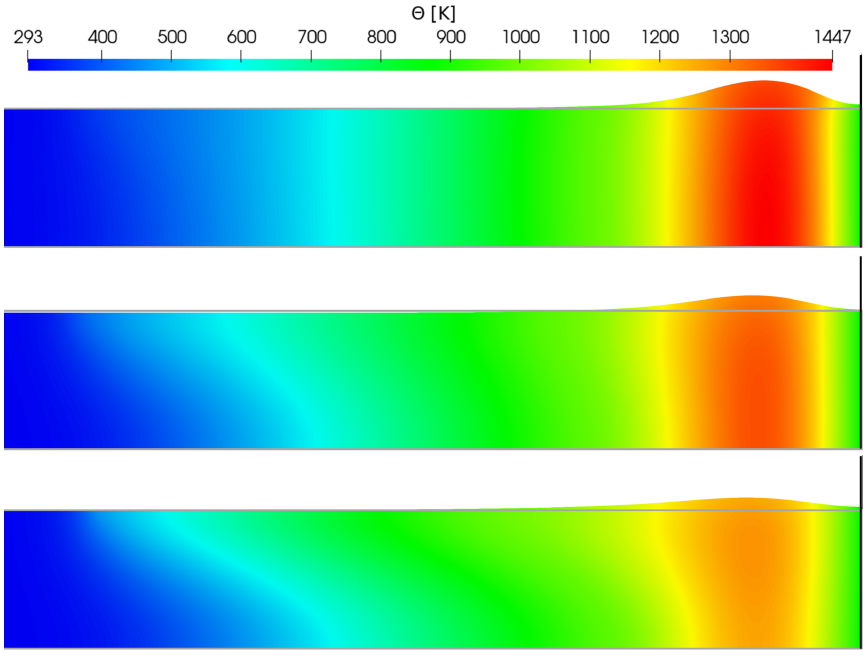

Figure 5.44: Free electric upsetting: temperature and deformed domain (the reference domain is outlined in gray) at $t = 62$ s for $f \approx 0$ Hz (top), $f = 50$ Hz (middle) and $f = 100$ Hz (bottom).

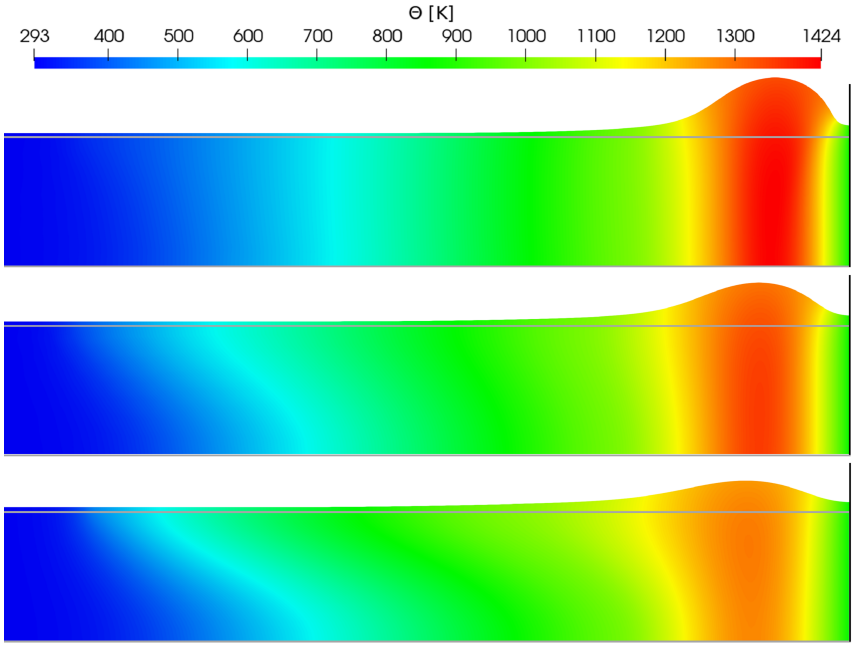

Figure 5.45: Free electric upsetting: temperature and deformed domain (the reference domain is outlined in gray) at $t = 66$ s for $f \approx 0$ Hz (top), $f = 50$ Hz (middle) and $f = 100$ Hz (bottom).

value observed at 100 Hz. Moreover, Figure 5.46 compares the modulus of the viscoplastic deformation gradient at the final time.

These results indicate that lower frequencies promote faster free electric upsetting processes for the same amount of active power. However, the skin effect becomes significantly less relevant above the Curie temperature, as illustrated in Figure 5.47, which shows the final distribution of $\tilde{\mathcal{H}}_\theta$. Beyond the Curie point, the temperature distributions under AC current tend to homogenise. Consequently, the final deformation obtained with DC current is expected to be attainable with low-frequency AC current within a reasonable time frame.

Let us recall that the total active power supplied through $\widehat{\Gamma}_3$ is prescribed data and, therefore, the electrical current entering through this boundary and the potential drop with respect to $\widehat{\Gamma}_1$ are unknowns of the problem. The magnitudes of both the input current and the voltage drop are shown in Figures 5.48 and 5.49, respectively.

It is observed that the input current decreases with frequency, whereas the voltage drop increases. This behaviour can be qualitatively explained in terms of the skin effect, since the metal bar can essentially be regarded as a resistor opposing the current flow. The effective resistance is higher under AC supply: when the current is confined near the surface of the conductor (skin effect), the effective cross-sectional area available for conduction is reduced, thereby increasing the resistance. As the supplied power remains constant across different frequencies, but the resistance rises with frequency, less current is required for resistive heating (Joule effect) at higher frequencies. Moreover, since the supplied active power is given by (4.17), and the behaviour of $\mathrm{Re}(V)$ closely follows that of $|V|$, maintaining constant active power while the current decreases with frequency necessarily requires a corresponding increase in voltage. This trend is clearly illustrated in Figure 5.49.

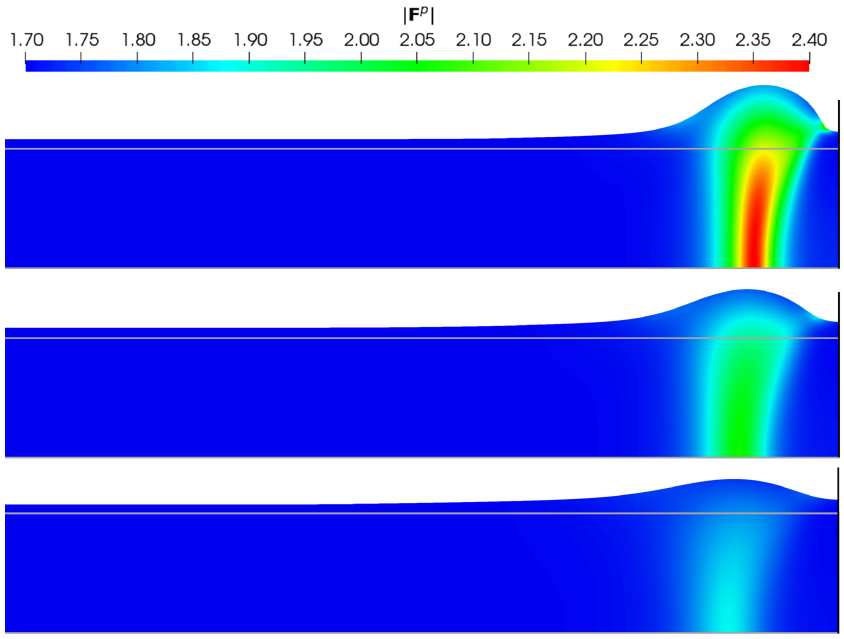

Figure 5.46: Free electric upsetting: $|\mathbf{F}^p|$ and deformed domain (the reference domain is outlined in gray) at $t = 66$ s for $f \approx 0$ Hz (top), $f = 50$ Hz (middle) and $f = 100$ Hz (bottom).

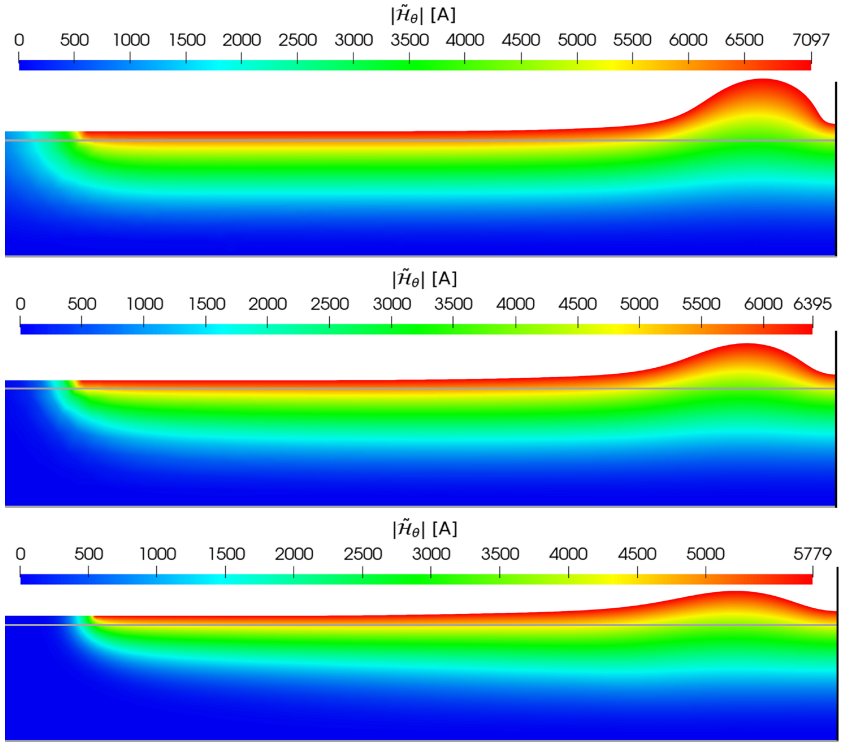

Figure 5.47: Free electric upsetting: $\tilde{\mathcal{H}}_\theta$ and deformed domain (the reference domain is outlined in gray) at $t = 66$ s for $f \approx 0$ Hz (top), $f = 50$ Hz (middle) and $f = 100$ Hz (bottom).

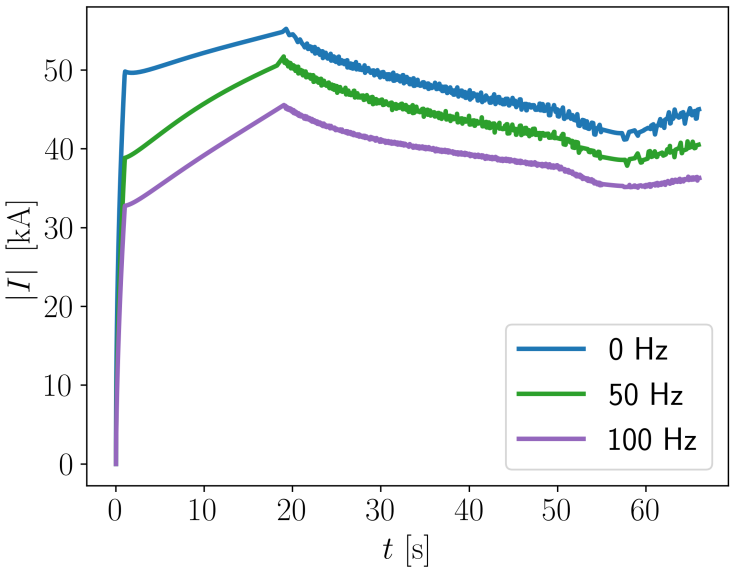

Figure 5.48: Free electric upsetting: time evolution of $|I|$ for different frequencies.

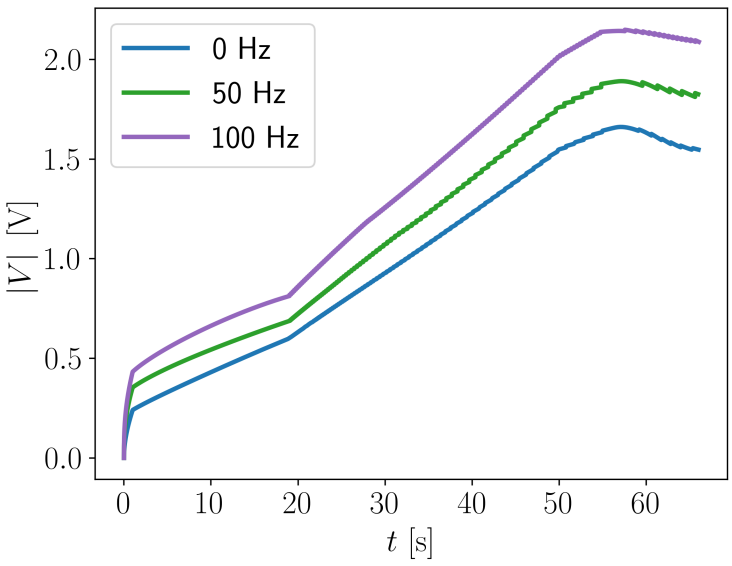

Figure 5.49: Free electric upsetting: time evolution of $|V|$ for different frequencies.

Chapter 6

Conclusions and further work

The objective of this thesis was the mathematical modelling and numerical simulation of electric upsetting, a multiphysics forming process. Consistent mathematical models were developed to describe the coupled thermal, electrical, magnetic, and mechanical phenomena involved.

In the electromagnetic framework, two types of electrical sources were addressed: a direct current (DC) model for DC supply, and an eddy-current model for alternating current (AC). In the latter case, particular attention was devoted to the nonlinearities arising from the magnetic properties of the materials, as well as to the treatment of electrical ports, both of which represented key challenges in the formulation. Furthermore, the option of prescribing electrical power as input was investigated for both DC and AC cases, thereby providing greater flexibility for practical applications and simulation setups.

On the mechanical side, a large strain framework was introduced to model the elasto-viscoplastic deformations occurring during electric upsetting. This framework incorporates the complex Anand constitutive law to accurately capture the material response under high temperature and high strain-rate conditions. A particularly challenging aspect of the mechanical model was the treatment of contact between the deforming metal bar and the surrounding components, a difficulty further compounded by the strong multiphysics coupling in those regions, which also involves thermal and electrical/electromagnetic interactions.

The formulation of the aforementioned models was developed within a purely Lagrangian framework, in which all equations are expressed with respect to a fixed reference configuration. While standard in solid mechanics, this approach is less common in fully coupled thermal, electrical (or electromagnetic), and mechanical problems. Its main advantages are that it avoids updating the computational domain and eliminates the treatment of convective terms. Suitable weak formulations were derived for the three coupled models, which were then spatially discretised using the finite element method. For time integration, high-order schemes were employed to ensure temporal accuracy.

The numerical implementation was carried out using an in-house code based on Python-FEniCS. A series of axisymmetric tests were performed to validate the implementation, including comparisons with analytical solutions and commercial software, as well as several convergence studies. The final section of the numerical results focused on the simulation of realistic in-die

and free electric upsetting processes. In particular, the solution obtained with our in-house code for in-die DC electric upsetting was compared against the commercial codes Marc and Ansys, showing good agreement. For the free electric upsetting case, simulations with prescribed AC electrical power were performed, and the influence of different frequency values on the process behaviour was analysed.

This thesis opens the way to several potential future developments. First, the proposed methodology for electric upsetting could be adapted and extended to other forming processes. In particular, the modelling of large elasto-viscoplastic deformations, addressed through the mechanical framework developed here, is highly relevant for many high-temperature forming applications and could be directly reused or suitably adapted. On the electromagnetic side, the time-harmonic eddy current model proposed for electric upsetting can be naturally extended to the transient regime, which would be especially valuable for modelling electromagnetic forming (EMF) processes [33, 74]. In this case, enlarging the computational domain to include the surrounding dielectric air would likely be necessary. More generally, coupling with lumped electrical circuit models would also be of great interest, as it would enable more realistic representations of industrial power supply systems and control strategies.

It should also be noted that the in-house implementation developed in this thesis is restricted to axisymmetric problems, although the proposed models can be extended to general three-dimensional cases. For the DC setting, the extension to 3D is relatively straightforward, since the thermo-electro-mechanical formulation remains valid for non-axisymmetric geometries without major modifications. By contrast, the extension of the AC electromagnetic model to 3D would require a more substantial reformulation. In particular, it would involve a computational domain encompassing both conducting and dielectric regions, together with the introduction of additional unknowns.

Several additional research directions could be pursued:

- Incorporation of alternative viscoplastic constitutive laws, such as the Johnson–Cook model [45, 46].
- Development of more robust reinitialisation and remeshing strategies, which become essential when severe mesh distortion occurs, even within purely Lagrangian frameworks.
- Improvement of numerical convergence and memory management in the implementation, aiming at more competitive computation times.
- A rigorous theoretical analysis of the proposed models from the standpoint of numerical analysis, which remains a challenging but valuable line of future work.

Appendix A

Function spaces

Several function spaces and their corresponding norms are used in Chapter 5 to compute numerical errors. To this end, this appendix includes the main definitions regarding the function spaces introduced in that chapter.

Let Ω be a bounded open set in $\mathbb{R}^3$. The Lebesgue space $L^p(\Omega)$ is the function space of measurable functions whose absolute value raised to the power of p is integrable. More precisely,

$$L^p(\Omega) := \left\{ w : \Omega \longrightarrow \mathbb{R} \,\middle|\, \int_\Omega |w|^p \, \mathrm{d}V < \infty \right\}, \tag{A.1}$$

where $1 \leq p < \infty$. The corresponding L^p-norm is

$$\|w\|_{L^p(\Omega)} := \left(\int_\Omega |w|^p \, \mathrm{d}V \right)^{1/p}. \tag{A.2}$$

The particular case $p = 2$, i.e., the function space of square-integrable functions $L^2(\Omega)$, is of special interest in this work. As a natural extension, vector-valued function spaces are distinguished using bold fonts, specifically $\mathbf{L}^2(\Omega)$, and tensor-valued function spaces are denoted by $\mathbb{L}^2(\Omega)$.

Moreover, if the first order weak derivatives of a square-integrable function w are also square-integrable, then w belongs to the Sobolev space $H^1(\Omega)$, namely,

$$H^1(\Omega) := \left\{ w \in L^2(\Omega) \,\middle|\, \operatorname{grad} w \in \mathbf{L}^2(\Omega) \right\}. \tag{A.3}$$

Similarly to Lebesgue spaces, vector and tensor Sobolev function spaces are respectively denoted by $\mathbf{H}^1(\Omega)$ and $\mathbb{H}^1(\Omega)$. The corresponding H^1-norm is given by

$$\|w\|_{H^1(\Omega)} := \left(\|w\|^2_{L^2(\Omega)} + \|\operatorname{grad} w\|^2_{L^2(\Omega)} \right)^{1/2}. \tag{A.4}$$

Furthermore, we denote by $H^1_{\Gamma^P}(\Omega)$ the subspace of $H^1(\Omega)$ defined by

$$H^1_{\Gamma^P}(\Omega) := \left\{ w \in H^1(\Omega) : \; w_{|\Gamma^P} = 0 \right\}, \tag{A.5}$$

where Γ^P is a subset of the boundary of Ω of non-null measure.

When $\Omega \subset \mathbb{R}^3$ is obtained by rotating a bounded domain $\widehat{\Omega} \subset \mathbb{R}^2$ around the axis of symmetry and w is θ-independent (further details in Section 2.2), the L^2 and H^1 norms can be explicitly written as

$$\|w\|_{L^2(\Omega)} = \left(2\pi \int_{\widehat{\Omega}} |w(r,z)|^2 \, r \, \mathrm{d}r \, \mathrm{d}z\right)^{1/2}, \tag{A.6}$$

and

$$\|w\|_{H^1(\Omega)} = \left[2\pi \int_{\widehat{\Omega}} \left(|w(r,z)|^2 + \left(\frac{\partial w(r,z)}{\partial r}\right)^2 + \left(\frac{\partial w(r,z)}{\partial z}\right)^2\right) r \, \mathrm{d}r \, \mathrm{d}z\right]^{1/2}. \tag{A.7}$$

These norms are closely related to those of the weighted Lebesgue $L^2(\widehat{\Omega})$ and Sobolev $H^1(\widehat{\Omega})$ spaces defined in $\widehat{\Omega}$ with the axisymmetric weight r, and thus verify $\|w\|^2_{L^2(\Omega)} = 2\pi \|w\|^2_{L^2(\widehat{\Omega})}$ and $\|w\|^2_{H^1(\Omega)} = 2\pi \|w\|^2_{H^1(\widehat{\Omega})}$.

A natural extension to weighted spaces $L^{2,\alpha}(\widehat{\Omega})$ and $H^{1,\alpha}(\widehat{\Omega})$, with weight r^α ($\alpha \in \mathbb{R}$), for sufficiently smooth fields, leads to the norms

$$\|w\|_{L^{2,\alpha}(\widehat{\Omega})} = \left(\int_{\widehat{\Omega}} |w(r,z)|^2 \, r^\alpha \, \mathrm{d}r \, \mathrm{d}z\right)^{1/2}, \tag{A.8}$$

and

$$\|w\|_{H^{1,\alpha}(\widehat{\Omega})} = \left[\int_{\widehat{\Omega}} \left(|w(r,z)|^2 + \left(\frac{\partial w(r,z)}{\partial r}\right)^2 + \left(\frac{\partial w(r,z)}{\partial z}\right)^2\right) r^\alpha \, \mathrm{d}r \, \mathrm{d}z\right]^{1/2}, \tag{A.9}$$

that fulfil $\|w\|^2_{L^{2,\alpha}(\Omega)} = 2\pi \|w\|^2_{L^{2,\alpha}(\widehat{\Omega})}$ and $\|w\|^2_{H^{1,\alpha}(\Omega)} = 2\pi \|w\|^2_{H^{1,\alpha}(\widehat{\Omega})}$.

Nomenclature

Greek symbols

Γ	Boundary of a 3D Lagrangian domain
$\Gamma(t)$	Boundary of a 3D Eulerian domain
ϵ	Emissivity
ε	Electric permittivity
$\boldsymbol{\varepsilon}$	Infinitesimal strain tensor
$\dot{\varepsilon}^p$	Inelastic strain rate
ζ	Contact multiplier
Θ	Temperature
Θ^{C}	Convection temperature
Θ^{R}	Radiation temperature
λ	Lagrange multiplier associated to electromagnetic isolated boundaries
λ_{M}	Lamé's first parameter
μ	Magnetic permeability
μ_{M}	Lamé's second parameter
ν	Poisson's ratio
ξ	Multiplier of stress
ρ	Mass density
ρ_{V}	Electric charge density
σ	Electric conductivity
σ_{SB}	Stefan-Boltzmann constant
$\boldsymbol{\Sigma}$	Second Piola-Kirchhoff stress tensor
ω	Angular frequency
Ω	3D Lagrangian domain
$\Omega(t)$	3D Eulerian domain

Latin symbols

a	Strain rate sensitivity of hardening/softening
$\mathbf{a}$	Spatial description of the acceleration
A	Pre-exponential factor in Anand's model
$\mathbf{b}$	Volumetric force density
$\mathbf{B}$	Magnetic induction (in the context of electromagnetism)

$\mathbf{B}$	Left Cauchy-Green tensor (in the context of solid mechanics)
$\mathcal{B}$	Deformable body
c_p	Specific heat
$\mathbf{C}$	Right Cauchy-Green tensor
C	Rigid obstacle region
$\mathbf{D}$	Electric displacement (in the context of electromagnetism)
$\mathbf{D}$	Stretching tensor (in the context of solid mechanics)
$\tilde{\mathbf{D}}^p$	Spatially rotated plastic stretching tensor
E	Young's modulus
$\mathbf{E}$	Electric field
f	Frequency
$\mathbf{F}$	Deformation gradient
$\mathbf{F}^e$	Elastic deformation gradient
$\mathbf{F}^p$	Plastic deformation gradient
g	Normal component of the current density in the electrical model
$\mathbf{G}$	Green-Lagrange (Green–Saint-Venant) strain tensor
h	Heat transfer coefficient
h_0	Hardening/softening constant
$\mathbf{h}$	Stress vector
$\mathbf{H}$	Magnetic field
$\boldsymbol{\mathcal{H}}$	Unknown for the Lagrangian electromagnetic model (modified magnetic field)
$\mathbf{H_L}$	Left Hencky strain tensor
$\mathbf{H_R}$	Right Hencky strain tensor
I	Current intensity
$\mathbf{I}$	Identity tensor
$\mathbf{J}$	Current density
k	Thermal conductivity
$\mathbf{K}$	Kirchhoff stress tensor
$\mathbf{L}$	Velocity gradient tensor
m	Strain rate sensitivity of stress
n	Strain rate sensitivity for deformation resistance saturation
$\mathbf{n_p}$	Material normal vector
$\mathbf{n_x}$	Spatial normal vector
p	Material point
P	Heat source due to Joule effect
P	Reference map of the motion
$\mathbf{P}$	Resultant force
Q	Activation energy
R	Universal constant for ideal gases
$\mathbf{R}$	Rotation tensor
s	Deformation resistance
$\tilde{s}$	Deformation resistance saturation

$\mathbf{s}$	Surface force density
$\mathbf{S}$	First Piola-Kirchhoff stress tensor
t	Time
T	Final time
$\mathbf{T}$	Cauchy stress tensor
$\mathcal{T}$	Trajectory of the motion
$\mathbf{u}$	Displacement
$\mathbf{U}$	Right stretch tensor
V	Electric potential
$\mathbf{v}$	Spatial description of the velocity
$\mathbf{V}$	Left stretch tensor
x	Spatial point
X	Motion
$\dot{\mathsf{X}}$	Material velocity
$\ddot{\mathsf{X}}$	Material acceleration
$\mathbf{W}$	Spin tensor

Subscripts

θ	Azimuthal component
τ	Intermediate configuration element
CM	Contact mechanical boundary
D	Axis of symmetry
DE	Dirichlet electrical boundary
DM	Dirichlet mechanical boundary
DT	Dirichlet thermal boundary
$\mathbf{E}$	Electromagnetic boundary with reference potential
$\mathbf{J}$	Electromagnetic boundary with known currents or voltages
m	Material field
N	Isolated electromagnetic boundary
NE	Neumann electrical boundary
NM	Neumann mechanical boundary
p	Material element
r	Radial component
RT	Robin thermal boundary
s	Spatial field
x	Spatial element
z	Axial component

Superscripts

0	Initial value
DE	Dirichlet electrical boundary condition
DM	Dirichlet mechanical boundary condition

^{DT}	Dirichlet thermal boundary condition
^{e}	Elastic element
^{p}	Viscoplastic element
$\check{}$	Function dependent on specific variables
$\widehat{}$	Axisymmetric element
$\dot{}$	Material time derivative

Acronyms

3D	Three-dimensional
AC	Alternating current
DC	Direct current
EAF	Electrically assisted forming
EMF	Electromagnetic metal forming
NCP	Nonlinear complementarity problem

Bibliography

[1] B. E. Abali and A. F. Queiruga. Theory and computation of electromagnetic fields and thermomechanical structure interaction for systems undergoing large deformations. *J. Comput. Phys.*, 394:200–231, 2019. doi:10.1016/j.jcp.2019.05.045.

[2] S. Abhyankar, J. Brown, E. M. Constantinescu, D. Ghosh, B. F. Smith, and H. Zhang. PETSc/TS: A Modern Scalable ODE/DAE Solver Library. *arXiv preprint arXiv:1806.01437*, 2018. URL: https://arxiv.org/abs/1806.01437.

[3] J. Alves, S. Acevedo, S. Marie, B. Adams, K. Mocellin, and F. Bay. Numerical modeling of electrical upsetting manufacturing processes based on Forge® environment. *AIP Conf. Proc.*, 1896(1):120003, 10 2017. doi:10.1063/1.5008141.

[4] L. Anand. Constitutive Equations for the Rate-Dependent Deformation of Metals at Elevated Temperatures. *J. Eng. Mater.-T. ASME*, 104:12–17, 1982. doi:10.1115/1.3225028.

[5] L. Anand. Constitutive equations for hot-working of metals. *Int. J. Plasticity*, 1(3):213–231, 1985. doi:10.1016/0749-6419(85)90004-X.

[6] S. Balay, S. Abhyankar, M. F. Adams, S. Benson, J. Brown, P. Brune, K. Buschelman, E. Constantinescu, L. Dalcin, A. Dener, V. Eijkhout, J. Faibussowitsch, W. D. Gropp, V. Hapla, T. Isaac, P. Jolivet, D. Karpeev, D. Kaushik, M. G. Knepley, F. Kong, S. Kruger, D. A. May, L. C. McInnes, R. T. Mills, L. Mitchell, T. Munson, J. E. Roman, K. Rupp, P. Sanan, J. Sarich, B. F. Smith, H. Suh, S. Zampini, H. Zhang, H. Zhang, and J. Zhang. PETSc/TAO Users Manual. Technical Report ANL-21/39 - Revision 3.23, Argonne National Laboratory, 2025. doi:10.2172/2476320.

[7] S. Balay, S. Abhyankar, M. F. Adams, S. Benson, J. Brown, P. Brune, K. Buschelman, E. M. Constantinescu, L. Dalcin, A. Dener, V. Eijkhout, J. Faibussowitsch, W. D. Gropp, V. Hapla, T. Isaac, P. Jolivet, D. Karpeev, D. Kaushik, M. G. Knepley, F. Kong, S. Kruger, D. A. May, L. C. McInnes, R. T. Mills, L. Mitchell, T. Munson, J. E. Roman, K. Rupp, P. Sanan, J. Sarich, B. F. Smith, S. Zampini, H. Zhang, H. Zhang, and J. Zhang. PETSc Web page. https://petsc.org/, 2025.

[8] S. Balay, W. D. Gropp, L. C. McInnes, and B. F. Smith. Efficient Management of Parallelism in Object Oriented Numerical Software Libraries. In E. Arge, A. M. Bruaset, and

H. P. Langtangen, editors, *Modern Software Tools in Scientific Computing*, pages 163–202, Boston, MA, 1997. Birkhäuser Press. doi:10.1007/978-1-4612-1986-6_8.

[9] C. Bell, J. R. Corney, N. Zuelli, and D. Savings. A state of the art review of hydroforming technology. *Int. J. Mater. Form.*, 13:789–828, 2020. doi:10.1007/s12289-019-01507-1.

[10] M. Benítez and A. Bermúdez. A second order characteristics finite element scheme for natural convection problems. *J. Comput. Appl. Math.*, 235(11):3270–3284, 2011. doi:10.1016/j.cam.2011.01.007.

[11] M. Benítez and A. Bermúdez. Numerical Analysis of a Second Order Pure Lagrange-Galerkin Method for Convection-Diffusion Problems. Part I: Time Discretization. *SIAM J. Numer. Anal.*, 50(2):858–882, 2012. doi:10.1137/100809982.

[12] M. Benítez and A. Bermúdez. Numerical Analysis of a Second Order Pure Lagrange-Galerkin Method for Convection-Diffusion Problems. Part II: Fully Discretized Scheme and Numerical Results. *SIAM J. Numer. Anal.*, 50(6):2824–2844, 2012. doi:10.1137/100809994.

[13] M. Benítez and A. Bermúdez. Pure Lagrangian and Semi-Lagrangian Finite Element Methods for the Numerical Solution of Convection-Diffusion Problems. *Int. J. Numer. Anal. Mod.*, 11(2):271–287, 2014. URL: https://journal.global-sci.org/intro/article_detail.html?journal=undefined&article_id=525.

[14] M. Benítez and A. Bermúdez. Pure Lagrangian and semi-Lagrangian finite element methods for the numerical solution of Navier-Stokes equations. *Appl. Numer. Math.*, 95:62–81, 2015. doi:10.1016/j.apnum.2014.01.005.

[15] M. Benítez and A. Bermúdez. Second-Order Pure Lagrange-Galerkin Methods for Fluid-Structure Interaction Problems. *SIAM J. Sci. Comput.*, 37(5):B744–B777, 2015. doi:10.1137/141001081.

[16] M. Benítez, A. Bermúdez, and P. Fontán. Non-Eulerian Newmark Methods: A Powerful Tool for Free-Boundary Continuum Mechanics Problems. *J. Sci. Comput.*, 83(3):Paper No. 44, 27, 2020. doi:10.1007/s10915-020-01207-y.

[17] A. Bermúdez, D. Gómez, M. C. Muñiz, and P. Salgado. Transient numerical simulation of a thermoelectrical problem in cylindrical induction heating furnaces. *Adv. Comput. Math.*, 26(1):39–62, 2007. doi:10.1007/s10444-005-7470-9.

[18] A. Bermúdez, D. Gómez, and P. Salgado. *Mathematical Models and Numerical Simulation in Electromagnetism*, volume 74 of *UNITEXT*. Springer, New York, 2014. doi:10.1007/978-3-319-02949-8.

[19] A. Bermúdez, B. López-Rodríguez, F. J. Pena, R. Rodríguez, P. Salgado, and P. Venegas. Numerical Solution of an Axisymmetric Eddy Current Model with Current and

Voltage Excitations. *J. Sci. Comput.*, 91(1):Paper No. 8, 26, 2022. doi:10.1007/s10915-022-01780-4.

[20] A. Bermúdez, B. López-Rodríguez, R. Rodríguez, and P. Salgado. Numerical solution of transient eddy current problems with input current intensities as boundary data. *IMA J. Numer. Anal.*, 32(3):1001–1029, 2012. doi:10.1093/imanum/drr028.

[21] A. Bermúdez. *Continuum Thermomechanics*, volume 43 of *Progress in Mathematical Physics*. Birkhäuser Basel, 2005. doi:10.1007/3-7643-7383-0.

[22] A. Bermúdez, J. Bullón, F. Pena, and P. Salgado. A numerical method for transient simulation of metallurgical compound electrodes. *Finite Elem. Anal. Des.*, 39(4):283–299, 2003. doi:10.1016/S0168-874X(02)00069-0.

[23] A. Bermúdez, C. Reales, R. Rodríguez, and P. Salgado. Numerical analysis of a finite-element method for the axisymmetric eddy current model of an induction furnace. *IMA J. Numer. Anal.*, 30(3):654–676, 03 2009. doi:10.1093/imanum/drn063.

[24] A. Bermúdez, R. Rodríguez, and P. Salgado. Numerical solution of eddy current problems in bounded domains using realistic boundary conditions. *Comput. Method. Appl. M.*, 194(2):411–426, 2005. Selected papers from the 11th Conference on The Mathematics of Finite Elements and Applications. doi:10.1016/j.cma.2004.05.016.

[25] A. Bossavit. *Computational Electromagnetism. Variational Formulations, Complementarity, Edge Elements.* Academic Press Inc., San Diego, CA, 1998. doi:10.1016/B978-0-12-118710-1.X5000-4.

[26] A. Bossavit and J. Verite. The "TRIFOU" Code: Solving the 3-D eddy-currents problem by using H as state variable. *IEEE T. Magn.*, 19(6):2465–2470, 1983. doi:10.1109/TMAG.1983.1062817.

[27] K. Boukir, Y. Maday, B. Métivet, and E. Razafindrakoto. A high-order characteristics/finite element method for the incompressible Navier-Stokes equations. *Int. J. Numer. Meth. Fl.*, 25:1421–1454, 1997. doi:10.1002/(SICI)1097-0363(19971230)25:12\%3C1421::AID-FLD334\%3E3.0.CO;2-A.

[28] X. Chen, G. Chen, and M. Sakane. Prediction of stress-strain relationship with an improved Anand constitutive model for lead-free solder Sn-3.5Ag. *IEEE T. Compon. Pack. T.*, 28(1):111–116, 2005. doi:10.1109/TCAPT.2004.843157.

[29] Z. N. Cheng, G. Z. Wang, L. Chen, J. Wilde, and K. Becker. Viscoplastic Anand model for solder alloys and its application. *Solder. Surf. Mt. Tech.*, 12(2):31–36, 2000. doi:10.1108/09540910010331428.

[30] E. A. de Souza Neto, D. Perić, and D. R. J. Owen. *Computational Methods for Plasticity: Theory and Applications.* John Wiley & Sons, Ltd., 2008. doi:10.1002/9780470694626.

[31] H. R. Dong, X. Q. Li, Y. Li, Y. H. Wang, H. B. Wang, X. Y. Peng, and D. S. Li. A review of electrically assisted heat treatment and forming of aluminum alloy sheet. *Int. J. Adv. Manuf. Tech.*, 120(11):7079–7099, 2022. doi:10.1007/s00170-022-08996-6.

[32] J. Douglas Jr. and T. F. Russell. Numerical Methods for Convection-Dominated Diffusion Problems Based on Combining the Method of Characteristics with Finite Element or Finite Difference Procedures. *SIAM J. Numer. Anal.*, 19(5):871–885, 1982. doi:10.1137/0719063.

[33] A. El-Azab, M. Garnich, and A. Kapoor. Modeling of the electromagnetic forming of sheet metals: state-of-the-art and future needs. *J. Mater. Process. Tech.*, 142(3):744–754, 2003. doi:10.1016/S0924-0136(03)00615-0.

[34] R. E. Ewing and T. F. Russel. Multistep Galerkin methods along characteristics for convection-diffusion problems. *IMACS Publications. Advances in Computer Methods for Partial Differential Equations IV*, pages 28–36, 1981.

[35] R. E. Ewing and H. Wang. A summary of numerical methods for time-dependent advection-dominated partial differential equations. *J. Comput. Appl. Math.*, 128(1):423–445, 2001. doi:10.1016/S0377-0427(00)00522-7.

[36] J. Fang, L. Ran, W. Huang, K. Pan, and Y. Gong. Prediction of BGA solder joint array shape using improved Perzyna model and Anand model. *Weld. World*, 67:2765 – 2778, 2023. doi:10.1007/s40194-023-01596-2.

[37] N. Firouzi, T. Rabczuk, J. Bonet, and K. K. Zur. A computational framework for large strain electromechanics of electro-visco-hyperelastic beams. *Comput. Method. Appl. M.*, 426:116985, 2024. doi:10.1016/j.cma.2024.116985.

[38] P. Fontán. *Mathematical analysis and numerical simulation with pure Lagrangian and semi-Lagrangian methods of problems in continuum mechanics*. PhD thesis, Universidade de Santiago de Compostela, 2021. URL: http://hdl.handle.net/10347/27661.

[39] M. Franke, R. Ortigosa, J. Martínez-Frutos, A. J. Gil, and P. Betsch. A thermodynamically consistent time integration scheme for non-linear thermo-electro-mechanics. *Comput. Method. Appl. M.*, 389:114298, 2022. doi:10.1016/j.cma.2021.114298.

[40] A. Galantai. Properties and construction of NCP functions. *Comput. Optim. Appl.*, 52(3):805–824, 07 2012. doi:10.1007/s10589-011-9428-9.

[41] K. H. Grote and H. Hefazi. *Springer Handbook of Mechanical Engineering*. Springer Handbooks. Springer Cham, 2021. doi:10.1007/978-3-030-47035-7.

[42] M. E. Gurtin. *An Introduction to Continuum Mechanics*, volume 158 of *Mathematics in Science and Engineering*. Academic Press, New York, 1981.

[43] M. E. Gurtin and L. Anand. The decomposition $\mathbf{F} = \mathbf{F}^e\mathbf{F}^p$, material symmetry, and plastic irrotationality for solids that are isotropic-viscoplastic or amorphous. *Int. J. Plasticity*, 21(9):1686–1719, 2005. doi:10.1016/j.ijplas.2004.11.007.

[44] X. Hu and D. Ju. Application of Anand's constitutive model on twin roll casting process of AZ31 magnesium alloy. *T. Nonferr. Metal. Soc.*, 16:s586–s590, 2006. doi:10.1016/S1003-6326(06)60261-6.

[45] G. R. Johnson and W. H. Cook. A constitutive model and data for metals subjected to large strains, high strain rates, and high temperatures. In *Proc. 7th Int. Symp. on Ballistics*, pages 541–547, The Hague, 1983. URL: https://api.semanticscholar.org/CorpusID:211107144.

[46] G. R. Johnson and W. H. Cook. Fracture characteristics of three metals subjected to various strains, strain rates, temperatures and pressures. *Eng. Fract. Mech.*, 21(1):31–48, 1985. doi:10.1016/0013-7944(85)90052-9.

[47] C. A. Kennedy and M. H. Carpenter. Additive Runge–Kutta schemes for convection–diffusion–reaction equations. *Appl. Numer. Math.*, 44(1):139–181, 2003. doi:10.1016/S0168-9274(02)00138-1.

[48] K. Lange. *Handbook of Metal Forming*. Society of Manufacturing Engineers, 1985. URL: https://books.google.es/books?id=npXgAAAAMAAJ.

[49] E. H. Lee. Elastic-Plastic Deformation at Finite Strains. *J. Appl. Mech.*, 36(1):1–6, 1969. doi:10.1115/1.3564580.

[50] E. H. Lee and D. T. Liu. Finite-Strain Elastic-Plastic Theory with Application to Plane-Wave Analysis. *J. Appl. Phys.*, 38(1):19–27, 1967. doi:10.1063/1.1708953.

[51] H. Li, L. F. Peng, B. Meng, Z. T. Xu, L. L. Wang, G. Ngaile, and M. W. Fu. Energy field assisted metal forming: Current status, challenges and prospects. *Int. J. Mach. Tool. Manu.*, 192:104075, 2023. doi:10.1016/j.ijmachtools.2023.104075.

[52] Z. Li, C. Kadapa, M. Hossain, and J. Wang. A numerical framework for the simulation of coupled electromechanical growth. *Comput. Method. Appl. M.*, 414:116128, 2023. doi:10.1016/j.cma.2023.116128.

[53] A. Logg, K.-A. Mardal, and G. N. Wells, editors. *Automated Solution of Differential Equations by the Finite Element Method. The FEniCS Book*, volume 84 of *Lecture Notes in Computational Science and Engineering*. Springer-Verlag Berlin, Heidelberg, 2012. doi:10.1007/978-3-642-23099-8.

[54] A. F. D. Loula and J. Zhu. Finite element analysis of a coupled nonlinear system. *Comput. Appl. Math.*, 20(3):321–339, 2001.

[55] C. Miehe, D. Vallicotti, and S. Teichtmeister. Homogenization and multiscale stability analysis in finite magneto-electro-elasticity. Application to soft matter EE, ME and MEE composites. *Comput. Method. Appl. M.*, 300:294–346, 2016. doi:10.1016/j.cma.2015.10.013.

[56] P. Monk. *Finite Element Methods for Maxwell's Equations*. Numerical Mathematics and Scientific Computation. Oxford University Press, Oxford, 2003. doi:10.1093/acprof:oso/9780198508885.001.0001.

[57] P. Moreno-Navarro, A. Ibrahimbegovic, and J.L. Pérez-Aparicio. Plasticity coupled with thermo-electric fields: Thermodynamics framework and finite element method computations. *Comput. Method. Appl. M.*, 315:50–72, 2017. doi:10.1016/j.cma.2016.10.038.

[58] D. J. Mynors and B. Zhang. Applications and capabilities of explosive forming. *J. Mater. Process. Tech.*, 125-126:1–25, 2002. doi:10.1016/S0924-0136(02)00413-2.

[59] I. Niyonzima, Y. Jiao, and J. Fish. Modeling and simulation of nonlinear electro-thermo-mechanical continua with application to shape memory polymeric medical devices. *Comput. Method. Appl. M.*, 350:511–534, 2019. doi:10.1016/j.cma.2019.03.003.

[60] P. Nuasri and Y. Aue-u-lan. Investigation of the "surface dimple" defect occurring during the production of an electric upsetting process by viscoplastic finite element modeling. *Int. J. Adv. Manuf. Tech.*, 98(1):1047–1057, 2018. doi:10.1007/s00170-018-2275-4.

[61] G. Paoli, O. Biro, and G. Buchgraber. Complex representation in nonlinear time harmonic eddy current problems. *IEEE T. Magn.*, 34(5):2625–2628, 1998. doi:10.1109/20.717607.

[62] L. Pareschi and G. Russo. Implicit-Explicit Runge–Kutta Schemes and Applications to Hyperbolic Systems with Relaxation. *J. Sci. Comput.*, 25:129–155, 2005. doi:10.1007/s10915-004-4636-4.

[63] T. Petzold. *Modelling, Analysis and Simulation of Multifrequency Induction Hardening*. PhD thesis, Technischen Universität Berlin, 2014. doi:10.14279/depositonce-4118.

[64] O. Pironneau. On the transport-diffusion algorithm and its applications to the Navier-Stokes equations. *Numer. Math.*, 38:309–332, 1982. doi:10.1007/BF01396435.

[65] G. Quan, G. Luo, and H. Wen. Influence of electric upsetting process variables on temperature field evolution by multi-field coupling finite element analysis. *Int. J. Precis. Eng. Man.*, 16:1525–1531, 2015. doi:10.1007/s12541-015-0202-2.

[66] G. Quan, L. Zhang, C. An, and Z. Zou. Multi-Variable and Bi-Objective Optimization of Electric Upsetting Process for Grain Refinement and Its Uniform Distribution. *Int. J. Precis. Eng. Man.*, 19(6):859–872, 2018. doi:10.1007/s12541-018-0102-3.

[67] G. Quan, Z. Zou, Z. Zhang, and J. Pan. A Study on Formation Process of Secondary Upsetting Defect in Electric Upsetting and Optimization of Processing Parameters Based

on Multi-Field Coupling FEM. *Mater. Res.*, 19(4):856–864, 2016. doi:http://dx.doi.org/10.1590/1980-5373-MR-2015-0678.

[68] B. Ramesh and A. M. Maniatty. Stabilized finite element formulation for elastic–plastic finite deformations. *Comput. Method. Appl. M.*, 194(6-8):775–800, 2005. doi:10.1016/j.cma.2004.06.025.

[69] H. Rui and M. Tabata. A second order characteristic finite element scheme for convection-diffusion problems. *Numer. Math.*, 92(1):161–177, 2002. doi:10.1007/s002110100364.

[70] G. Shao, H. Li, and M. Zhan. A Review on Ultrasonic-Assisted Forming: Mechanism, Model, and Process. *Chin. J. Mech. Eng.*, 34:Paper No. 99, 24, 2021. doi:10.1186/s10033-021-00612-0.

[71] J. C. Simo. Numerical analysis and simulation of plasticity. In *Numerical Methods for Solids (Part 3) Numerical Methods for Fluids (Part 1)*, volume 6 of *Handbook of Numerical Analysis*, pages 183–499. Elsevier, 1998. doi:10.1016/S1570-8659(98)80009-4.

[72] E. Süli. Stability and convergence of the Lagrange-Galerkin method with non-exact integration. In *The Mathematics of Finite Elements and Applications VI*, pages 435–442. Academic Press, London, 1988.

[73] Y. Sun, T. Liu, Z. Zhang, T. Zhang, and T. Luo. Optimum control of process parameters in electrical upsetting. *Proc. Inst. Mech. Eng. B-J. Eng.*, 217(9):1259–1263, 2003. doi:10.1243/095440503322420188.

[74] J. D. Thomas and N. Triantafyllidis. On electromagnetic forming processes in finitely strained solids: Theory and examples. *J. Mech. Phys. Solids*, 57(8):1391–1416, 2009. doi:10.1016/j.jmps.2009.04.004.

[75] G. Weber and L. Anand. Finite deformation constitutive equations and a time integration procedure for isotropic, hyperelastic-viscoplastic solids. *Comput. Method. Appl. M.*, 79(2):173–202, 1990. doi:10.1016/0045-7825(90)90131-5.

Copyright and permissions

- M. Benítez, A. Bermúdez, P. Fontán, I. Martínez, P. Salgado (2024). *A Lagrangian approach for solving an axisymmetric thermo-electromagnetic problem. Application to time-varying geometry processes.* Advances in Computational Mathematics, 50, 45. Electronic ISSN: 1572-9044, Print ISSN: 1019-7168. DOI: 10.1007/s10444-024-10121-y

  Permissions: this is an open access article distributed under the terms of a CC BY 4.0 license. The publisher, Springer Nature, grants the right to reuse the contents of the article in the author's thesis (see https://www.springernature.com/gp/partners/rights-permissions-third-party-distribution).

- M. Benítez, A. Bermúdez, P. Fontán, I. Martínez, P. Salgado (2025). *A pure-Lagrangian finite element approach for solving thermo-electrical-mechanical models. Application to electric upsetting.* Finite Elements in Analysis and Design, 251, 104433. Electronic ISSN: 1872-6925, Print ISSN: 0168-874X. DOI: 10.1016/j.finel.2025.104433

  Permissions: this is an open access article distributed under the terms of a CC BY 4.0 license. The publisher, Elsevier, grants the right to reuse the contents of the article in the author's thesis (see https://www.elsevier.com/about/policies-and-standards/copyright).

- Figure 1.9a is reproduced with the permission of ETA Technology, granted via a private request.

- Figure 1.9c is reproduced with the permission of CEMSA International, granted via a private request.

- Figure 1.11b is adapted from the original by Amanjosan2008, with a license CC BY-SA 4.0.

  The remaining graphic material included in this thesis is my own work.

Resumo

A historia do conformado de metais comeza hai varios milenios, evolucionando xunto á civilización humana e converténdose en indispensable na sociedade actual. O obxectivo dun proceso de conformado é a deformación permanente dunha peza ata lograr que esta teña unha forma xeométrica determinada. É fundamental conservar a cohesión e a masa da peza durante o proceso, e que a forma final se manteña unha vez retiradas as forzas aplicadas. Os procesos de conformado de metais presentan vantaxes en comparación con outros procesos de fabricación, como a fundición ou o mecanizado, entre as que destacan o pouco desperdicio de materiais durante o proceso, tempos de produción relativamente baixos, pezas cunha forma final precisa ou a mellora global das propiedades mecánicas. Pola contra, estes procesos tamén teñen algúns inconvenientes, como a necesidade de forzas considerables para a deformación das pezas, o elevado custo dos equipos de traballo ou a fabricación limitada de xeometrías complexas debido ás restricións para a deformación de certos metais.

Cada ano créanse novos procesos de conformado de metais, que adoitan ser complexos e involucran múltiples tipos de esforzos. Existen diversos criterios para a clasificación dos procesos de conformado, atendendo ao tipo de esforzo dominante na zona da deformación, á temperatura das pezas involucradas ou ás súas características (partes macizas ou chapas delgadas). Na literatura especializada [41] podemos atopar máis de 250 procesos de conformado distintos, desde os clásicos ata os máis modernos.

As técnicas convencionais de conformado empregan unha combinación de fenómenos térmicos e mecánicos para deformar as pezas da maneira desexada. No referente a pezas macizas, un destes procesos é a *laminación*, utilizada para reducir o espesor das pezas ao facelas pasar polo medio de dous rolos que xiran en sentidos opostos. Outro método clásico é a *forxa*, que utiliza ferramentas como martelos neumáticos, prensas ou moldes para aplicar forzas compresivas localizadas sobre pezas metálicas, sendo amplamente empregada en multitude de industrias. Tamén son comúns os procesos de *extrusión* e de *estiramento*, dedicados a reducir a sección dun bloque metálico cando é forzado a pasar por unha abertura, e que se empregan na fabricación de diversos produtos como marcos de ventás, varandas, tubos ou cables de distinto grosor.

No referente ao conformado de láminas delgadas atopamos procesos como o *dobrado*, consistente na deformación dunha chapa para darlle forma curva. Temos tamén o *repuxado ao torno*, no que se aplican forzas localizadas sobre unha peza que rota nun torno e que se deforma contra un mandril pola acción dun rolo móbil. Esta técnica utilízase para producir todo tipo de elementos con simetría cilíndrica, como tanques de gas, utensilios de cociña ou partes de instrumentos musicais. Outros dous procesos con características similares entre si son a *embutición* e

o *estiramento*, nos que se deforman láminas mediante a acción dun punzón.

Nos procesos anteriores, a forma final das pezas lógrase mediante contacto mecánico con certas ferramentas, como prensas, moldes ou punzóns. Non obstante, tamén existen técnicas de conformado que se valen das diferenzas de presión entre distintos puntos dun medio material para lograr a deformación. Inclúense nesta categoría o *hidroconformado*, que permite deformar pezas grazas á acción dun líquido a gran presión; ou o *conformado por explosión*, que emprega as ondas de choque producidas por detonacións controladas de certas cargas explosivas para darlle forma a determinadas pezas.

Aínda que as técnicas convencionais de conformado son amplamente utilizadas hoxe en día, presentan certas desvantaxes, como son os altos custos, capacidades de conformado limitadas ou importantes emisións contaminantes. Neste contexto xorden os procesos de conformado asistidos enerxeticamente, consistentes na integración de novas fontes de enerxía no ámbito do conformado, con resultados exitosos en canto á mellora da calidade das pezas e das súas propiedades. Estes métodos clasifícanse en función do tipo de enerxía empregada no proceso, que pode provir, entre outros, de campos electromagnéticos (conformado electromagnético), de vibracións ultrasónicas ou de corrente eléctrica. Neste último caso –os procesos de conformado asistidos electricamente (EAF)–, a corrente circula polo material e fai que a peza se quente por efecto Joule, reducindo así a súa resistencia a ser deformada. Como a corrente pasa directamente pola peza, a eficiencia aumenta en comparación coas tecnoloxías convencionais, reducindo tamén a complexidade e o custo dos equipos involucrados. Esta tese céntrase nun tipo concreto dentro dos procesos asistidos electricamente: o *electro-recalcado*. O interese da industria por estas tecnoloxías creceu moito nos últimos anos, especialmente na fabricación de pezas para o sector aeronáutico e para a automoción. De feito, cómpre salientar que a investigación actual estivo motivada pola colaboración coa empresa CIE Galfor, que emprega o electro-recalcado na fabricación de palieres para vehículos. A colaboración desenvolveuse no marco dun proxecto financiado polo Centro para o Desenvolvemento Tecnolóxico e a Innovación (CDTI) e formalizouse mediante un acordo entre a empresa e ITMATI (hoxe en día integrado en CITMAga).

En síntese, o electro-recalcado é un método de conformado capaz de ensanchar localmente o diámetro dunha barra metálica no seu extremo. Durante este proceso, unha barra a temperatura ambiente é situada nunha máquina horizontal de electro-recalcado e suxeitada por medio de mordazas. Por elas faise entrar unha corrente eléctrica de baixa voltaxe e alta amperaxe, dirixida cara a un dos extremos da barra, que se atopa apoiado nun soporte metálico. Debido ao efecto Joule, o paso da corrente eléctrica polo material metálico da barra produce calor no seu extremo, adquirindo un comportamento plástico. Cando se alcanza unha temperatura suficiente, desde o extremo oposto aplícase unha forza que leva á deformación do extremo quente contra o soporte metálico. Como consecuencia, o diámetro aumenta no extremo quente da barra. Atendendo ao tipo de deformación producida no extremo quente pódense distinguir dúas variantes do proceso: *libre* e *en matriz pechada*. Se o diámetro pode aumentar sen unha limitación expresa, estamos no caso de electro-recalcado libre (Figura A.1a), dando lugar no extremo quente á formación dunha preforma, tipicamente denominada *cebola* pola súa forma. En posteriores etapas, é posible someter esa preforma a outros procesos de conformado, como pode ser a estampación no caso da fabricación de palieres. Estas pezas, que son de vital importancia no sistema de transmisión

de distintos tipos de vehículos, teñen dous extremos ben diferenciados: o *prato*, obtido logo dun proceso combinado de electro-recalcado libre e estampación; e o *piñón*, resultado do electro-recalcado en matriz pechada (Figura A.1b). Neste último caso, a deformación no extremo quente da barra vese limitada por un volume pechado que rodea esa zona, dando lugar directamente a unha barra cun diámetro localmente máis grande.

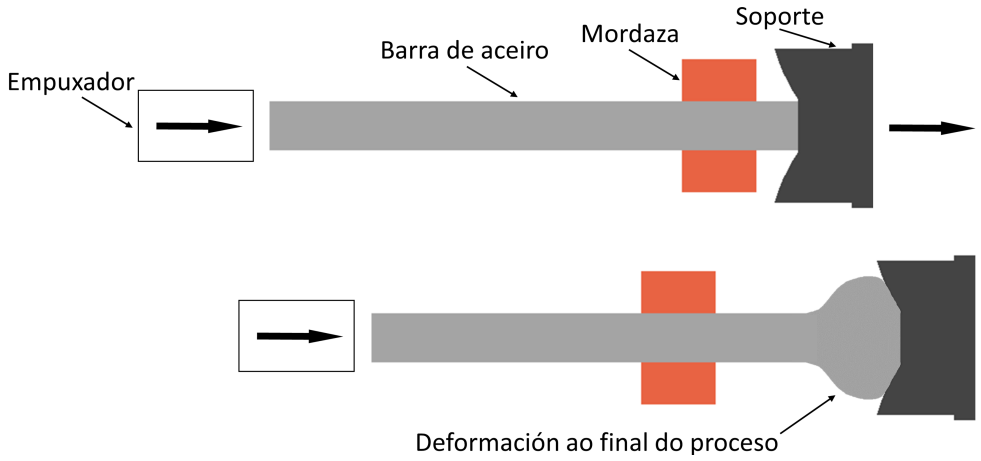

(a) Electro-recalcado libre.

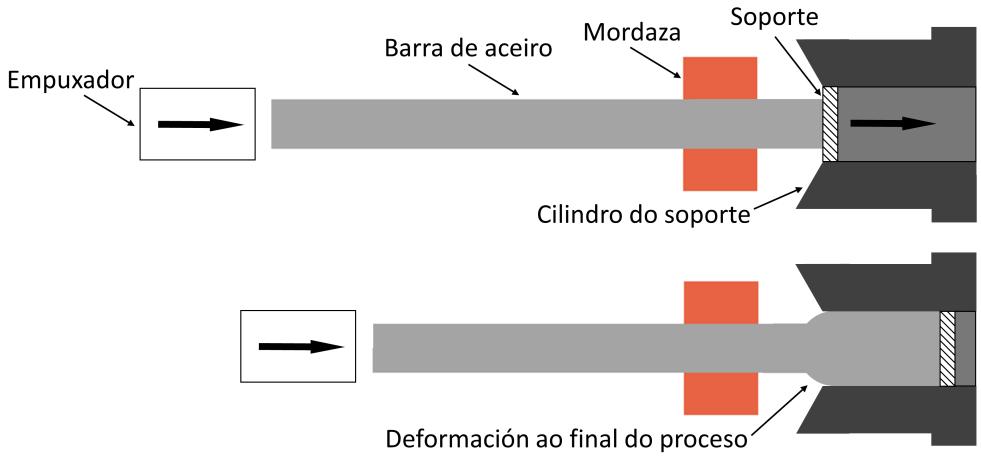

(b) Electro-recalcado en matriz pechada.

Figura A.1: Esquemas dos procesos de electro-recalcado.

Os procesos de electro-recalcado adoitan involucrar fenómenos físicos complexos, polo que o seu control e optimización a escala industrial vén recaendo historicamente na experiencia. Este tipo de procesos vese influenciado por moitos parámetros, entre os que se inclúen a fonte de corrente eléctrica, a forza de recalcado ou o material, dimensións e temperatura inicial da barra metálica. Neste contexto, a simulación numérica é quen de proporcionar información relevante sobre os procesos, xa que considera moitas posibles configuracións que doutra maneira serían custosas de probar en termos de tempo e diñeiro. Hai diferentes publicacións na literatura que abordan a simulación numérica deste tipo de procesos no caso libre. En particular, en [65]

analízase a influencia das variables do proceso na temperatura; en [60, 67] abórdanse posibles defectos na preforma final; e en [66, 73] considérase a optimización de distintos parámetros. Pola súa banda, o único traballo sobre o proceso en matriz pechada atopámolo en [3]. O denominador común destes traballos é a simulación con fontes de corrente continua (DC) e con paquetes de cálculo comerciais, onde os modelos matemáticos non se presentan con detalle. Ademais, descoñecemos a existencia de estudos que traten o problema con fontes de corrente alterna (AC).

En principio, o electro-recalcado pode levarse a cabo tanto con corrente continua como alterna, dependendo do caso. En xeral, a utilización de corrente alterna vese limitada polo diámetro da barra, posto que podería dar lugar a quentamentos lentos e pouco uniformes se o efecto pel é moi pronunciado na súa superficie. Neste traballo elabóranse modelos matemáticos acoplados que permiten considerar fontes de corrente de ambos tipos. No caso de corrente continua, os fenómenos magnéticos non están presentes e a modelización restrínxese á parte eléctrica. Pola contra, se a corrente empregada é alterna, son necesarios modelos electromagnéticos con termos fortemente non lineais e condicións de contorno máis complexas.

En calquera caso, os procesos de electro-recalcado involucran fenómenos mecánicos, térmicos e eléctricos ou electromagnéticos, e o seu acoplamento débese a distintos factores. En primeiro lugar, a deformación da barra modifica o dominio computacional de todos os modelos. Por outra parte, as propiedades mecánicas e electromagnéticas dos materiais dependen da temperatura, polo que existe un acoplamento co modelo térmico nese sentido. Ademais, a fonte de calor do problema térmico vén dada pola potencia disipada por mor do efecto Joule na barra, á súa vez calculada a partir do modelo electromagnético. E, tamén en relación coas propiedades dos materiais, en corrente alterna a permeabilidade magnética é fortemente non lineal e depende tanto da temperatura como do módulo do campo magnético. Os esquemas de acoplamento para os modelos de corrente continua (eléctrico) e corrente alterna (electromagnético) ilústranse na Figura A.2.

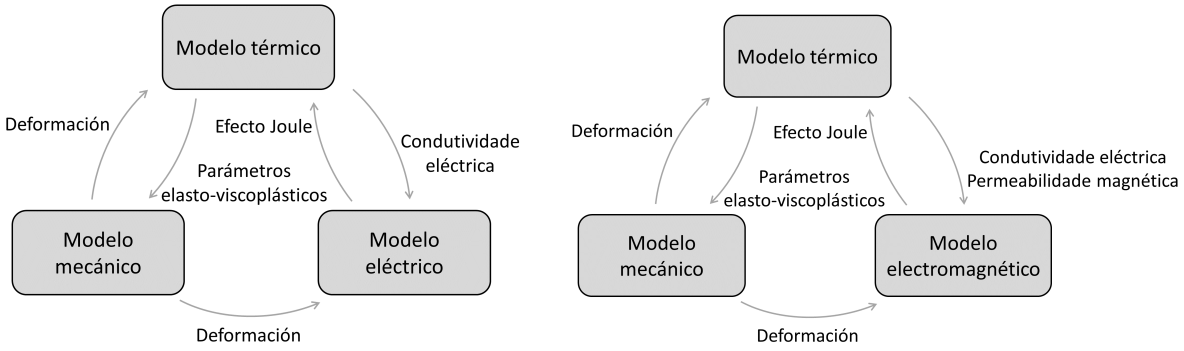

(a) Acoplamento co modelo eléctrico. (b) Acoplamento co modelo electromagnético.

Figura A.2: Esquemas do acoplamento entre modelos.

No caso concreto do modelo mecánico, dada a magnitude dos desprazamentos e das deformacións observadas na práctica nos procesos de electro-recalcado, a habitual teoría infinitesimal para as deformacións non é suficiente á hora de describilas adecuadamente. Pola contra, é nece-

saria a teoría de grandes deformacións, incluíndo a modelización das deformacións elásticas e das viscoplásticas, para as cales son considerados habitualmente na literatura modelos complexos e con moitos parámetros de entrada. Outra parte fundamental da modelización matemática é a relativa ao contacto entre a barra e os elementos circundantes, principalmente as mordazas e o soporte metálico, que son cruciais para alcanzar unha boa deformación final. Para abordar axeitadamente estas cuestións, necesítanse técnicas que permitan modelar e simular o contacto, non só a súa compoñente mecánica senón tamén as contribucións propias dos modelos térmico e eléctrico/electromagnético.

O cálculo de aproximacións á solución deste problema fortemente acoplado presenta retos significativos, que esixen o desenvolvemento de métodos numéricos fiables e precisos. En definitiva, esta tese pretender contribuír ao desenvolvemento de modelos de acoplamento multifísico para a simulación numérica de procesos de electro-recalcado, abordando os seguintes obxectivos: a modelización matemática do problema de electro-recalcado, tanto en corrente continua como alterna; a modelización dos fenómenos multifísicos térmicos, eléctricos (ou electromagnéticos) e mecánicos fortemente acoplados presentes no problema; a implementación nun código informático propio dos modelos desenvoltos, incluíndo grandes deformacións e contacto; a validación do modelo mediante tests numéricos axeitados e a súa aplicación a procesos de electro-recalcado.

A metodoloxía proposta para o cumprimento destes obxectivos vén motivada pola modificación substancial que sofre o dominio de cálculo inicial ao longo do tempo, como consecuencia das grandes deformacións asociadas ao electro-recalcado. Neste sentido, para obter resultados suficientemente precisos, a configuración xeométrica inicial debería actualizarse con frecuencia. Para superar este e outros desafíos específicos desta clase de problemas, como a distorsión da malla ou a forte interacción entre os diferentes modelos, nesta tese introdúcense novas estratexias de resolución baseadas nunha formulación puramente Lagrangiana. Polo tanto, todas as ecuacións están sempre escritas na configuración de referencia e a evolución do dominio tense en conta a través do gradiente da deformación, que forma parte da formulación matemática.

Na mecánica de sólidos, os modelos matemáticos baséanse habitualmente nunha formulación Lagrangiana, en contraste co enfoque Euleriano que se emprega de maneira máis común en mecánica de fluídos ou en problemas termo-eléctricos e electromagnéticos. As dificultades tradicionais da descrición Euleriana inclúen o tratamento dos termos convectivos e a modelización e seguimento de superficies libres, dificultades que desaparecen no marco Lagrangiano. Os métodos puramente Lagrangianos presentan vantaxes adicionais, como un dominio computacional independente do tempo e predefinido, maior precisión en rexións con fortes gradientes ou descontinuidades da solución, e a ausencia de termos de erro que inclúan o paso de tempo no denominador, propios dos métodos semi-Lagrangianos.

Na bibliografía de problemas termo-electro-mecánicos son comúns os algoritmos de resolución numérica con acoplamento secuencial, que empregan un enfoque Lagrangiano para a parte mecánica e un enfoque Euleriano para a parte termo-electromagnética (véxase, por exemplo, [1]). Recentemente, en [38] avanzouse no desenvolvemento de formulacións Lagrangianas para resolver problemas termo-electro-mecánicos con fontes de corrente continua e asumindo pequenas deformacións. Por outra banda, en [59] introduciuse unha formulación puramente Lagrangia-

na para certos procesos de conformado asistidos electricamente e con aplicación en medicina. Baseándonos no marco Lagrangiano introducido en [59], o presente traballo amplía ese enfoque en varias direccións clave para afrontar os retos específicos dos procesos de electro-recalcado. En primeiro lugar, introdúcense esquemas de integración temporal de tipo Runge-Kutta de alta orde, que melloran substancialmente a precisión temporal fronte ao método de Euler empregado en [59]. En segundo lugar, substitúese o modelo constitutivo elasto-plástico máis sinxelo empregado nese traballo por unha formulación elasto-viscoplástica, axeitada para grandes deformacións e baseada nos fundamentos teóricos clásicos de [75]. Ademais, impleméntanse condicións de contacto robustas e unha formulación axisimétrica, ambos aspectos esenciais para modelar con precisión o proceso. En conxunto, estas contribucións establecen un marco de simulación puramente Lagrangiano unificado e libre de remallado para problemas acoplados termo-electro-mecánicos, que opera integramente na configuración de referencia e permite tratar de maneira natural os dominios dependentes do tempo.

En canto á estrutura da tese, no Capítulo 2 comezamos recordando algúns conceptos fundamentais da mecánica de medios continuos, que sentan as bases para os posteriores desenvolvementos matemáticos presentados na tese. Adicionalmente, introdúcese a notación necesaria para a escritura dos modelos baixo a hipótese de simetría cilíndrica, que vai ser aplicable aos problemas de electro-recalcado abordados neste traballo.

No Capítulo 3 descríbense os modelos acoplados térmico, eléctrico e mecánico, asumindo fontes eléctricas de corrente continua. Para cada modelo pártese naturalmente das ecuacións físicas en configuración Euleriana e lévanse a cabo as transformacións pertinentes ata a escritura final da formulación Lagrangiana débil para problemas con simetría cilíndrica. Neste capítulo ponse o foco de maneira especial no modelo mecánico, incluíndo deducións detalladas no marco da teoría das grandes deformacións e das leis constitutivas elasto-viscoplásticas. En concreto, nos procesos de electro-recalcado, as deformacións permanentes (asociadas a un comportamento plástico) son predominantes e ademais dependen da velocidade á que se aplican as cargas. Para describir adecuadamente estes efectos é preciso un modelo viscoplástico, para o cal utilizaremos o de Anand, habitual na literatura de conformado de metais. A modelización mecánica levada a cabo nesta tese faise desde unha perspectiva hiperelástica, considerando a descomposición multiplicativa do gradiente de deformación como base para superar de xeito natural as limitacións tradicionalmente asociadas aos métodos de xeneralización baseados en hipoelasticidade. Así mesmo, neste capítulo ponse de manifesto o carácter puramente Lagrangiano da formulación proposta, xa que evita a necesidade, inherente aos métodos Eulerianos, de actualizar o dominio de cálculo en cada paso de tempo. A pesar disto, pode haber casos nos que as deformacións sexan tan grandes como para necesitar un cambio na configuración de referencia. Co propósito de complementar a información dada neste capítulo, tamén se inclúen cálculos formais relacionados coa aproximación puramente Lagrangiana nunha nova configuración de referencia. Por outra parte, no apartado eléctrico inclúese a formulación do modelo de corrente continua en termos do potencial eléctrico, engadindo condicións de contorno apropiadas de tipo Dirichlet e Neumann, así como a posibilidade de proporcionar a potencia subministrada ao sistema como dato. En canto ao modelo térmico, descríbese a conservación da enerxía xunto con condicións de contorno axeitadas de tipo Dirichlet e Robin, detallando tamén o cálculo da fonte de calor

debida ao efecto Joule.

No caso de fontes eléctricas de corrente alterna faise necesaria a utilización dun modelo electromagnético, de maior complexidade que o eléctrico, especialmente debido ás non linealidades intrínsecas ao comportamento ferromagnético dos materiais e ás condicións de contorno. No Capítulo 4 proponse unha formulación do modelo electromagnético, baseada na utilización dun modelo de correntes inducidas co campo magnético como incógnita principal. Ademais, as correntes e as caídas de potencial incorpóranse ao modelo a través da imposición de condicións de contorno adecuadas nos portos eléctricos, considerando tamén a posibilidade de proporcionar como dato o total de potencia activa subministrada ao sistema. A maiores, a fonte de calor do modelo térmico modifícase axeitadamente para ter en conta o cambio de réxime da corrente.

Os modelos acoplados descritos ao longo da tese impleméntanse nun código informático propio desenvolto en Python e baseado na librería FEniCS, que está orientada á resolución de ecuacións en derivadas parciais mediante o método de elementos finitos. Esta librería fundaméntase na escritura da formulación variacional do problema no código, o cal pode facerse a través da linguaxe UFL incluída en FEniCS. O problema discretízase en espazo mediante o método de elementos finitos e considéranse esquemas de integración temporal de alta orde de tipo Runge-Kutta. Deste xeito, o Capítulo 5 contén os principais resultados numéricos obtidos con este código propio, incluíndo casos de estudo reais e exemplos de validación por comparación con códigos comerciais robustos, como son Marc e Ansys. En particular, resólvense distintos tests para avaliar as ordes de converxencia das incógnitas dos diferentes modelos. Debido á dificultade para atopar solucións analíticas, xeralmente procédese á comparación con solucións obtidas para discretizacións de referencia suficientemente finas en tempo e en espazo. Dada a complexidade dos modelos, inicialmente considéranse de forma separada e vanse engadindo acoplamentos progresivamente, analizando en cada caso os erros obtidos para as solucións numéricas.

En canto á simulación do problema de electro-recalcado, considérase o caso de matriz pechada en condicións realistas e para unha fonte eléctrica de corrente continua. Neste caso, compárase a solución obtida en código propio co mesmo problema resolto cos paquetes de software comercial Marc e Ansys, dando lugar a unha boa concordancia entre os diferentes resultados. A maiores, considérase a simulación do proceso de electro-recalcado libre en corrente alterna, sendo coñecida a potencia activa total subministrada. Compáranse diferentes escenarios atendendo á relevancia do efecto pel no proceso, considerando frecuencias de corrente entre os 0 Hz (corrente continua) e os 100 Hz. Dos resultados conclúese que a redución do efecto pel dá lugar a distribucións de temperatura máis uniformes que facilitan a deformación da barra.

A partir do traballo levado a cabo nesta tese de doutoramento, tivemos ocasión de publicar dous artigos de investigación en revistas científicas indexadas no JCR. No primeiro artigo presentamos o modelo termo-electromagnético para corrente alterna, con aplicación a procesos con deformación ao longo do tempo. No segundo artigo describimos o modelo termo-electro-mecánico para corrente continua, con aplicacións a procesos de electro-recalcado:

- M. Benítez, A. Bermúdez, P. Fontán, I. Martínez, P. Salgado (2024). *A Lagrangian approach for solving an axisymmetric thermo-electromagnetic problem. Application to time-varying geometry processes.* Advances in Computational Mathematics, 50, 45. Electronic ISSN: 1572-9044, Print ISSN: 1019-7168. DOI: 10.1007/s10444-024-10121-y

- M. Benítez, A. Bermúdez, P. Fontán, I. Martínez, P. Salgado (2025). *A pure-Lagrangian finite element approach for solving thermo-electrical-mechanical models. Application to electric upsetting.* Finite Elements in Analysis and Design, 251, 104433. Electronic ISSN: 1872-6925, Print ISSN: 0168-874X. DOI: 10.1016/j.finel.2025.104433

Forming processes are fundamental to modern industry, as they enable workpieces to be permanently deformed into desired geometries while preserving cohesion and mass. Conventional forming techniques primarily rely on mechanical contact and remain challenged by high cost, energy use, and environmental impact. Energy-assisted forming methods have been developed to address these issues, including electrically assisted processes such as electric upsetting.

This thesis focuses on this method, in which the diameter of a metal bar is locally enlarged at one end. The process may occur freely, producing an onion-shaped preform, or within a closed die. It is of particular relevance in the automotive and aerospace sectors. Electric upsetting involves strongly coupled multiphysics phenomena -thermal, electrical, electromagnetic, and mechanical- governed by factors such as current source, bar geometry, and applied force.

The aim of this thesis is the mathematical modelling and numerical simulation of electric upsetting under both direct and alternating current excitations. This work incorporates large-deformation theory, viscoplastic constitutive laws, and detailed contact modelling within a fully Lagrangian framework. These models are implemented in a proprietary finite element code and validated against commercial solvers. The resulting computational framework enables simulation and optimisation of electric upsetting, underscoring its industrial relevance and advantages over conventional forming processes.